

The non-invasive assessment of the condition
of paved areas using electrical resistivity
techniques

by

Ting Yan

A thesis submitted to the University of Birmingham for the degree of
DOCTOR OF PHILOSOPHY

School of Engineering
Electronic, Electrical and System Engineering
University of Birmingham

May 2019

UNIVERSITY OF
BIRMINGHAM

University of Birmingham Research Archive

e-theses repository

This unpublished thesis/dissertation is copyright of the author and/or third parties. The intellectual property rights of the author or third parties in respect of this work are as defined by The Copyright Designs and Patents Act 1988 or as modified by any successor legislation.

Any use made of information contained in this thesis/dissertation must be in accordance with that legislation and must be properly acknowledged. Further distribution or reproduction in any format is prohibited without the permission of the copyright holder.

Abstract

This work to detect wet areas below a paved surface is part of a 10-year research programme “ATU” (Assessing the Underworld), sponsored by EPSRC to assess the condition of the underworld by various techniques [1]. A low-frequency (5 kHz to 15 kHz) non-invasive electrical resistivity technique was applied to a paved surface to assess the condition of upper layers of the asphalt. Generally, the paved surface (e.g. an asphalt pavement) is constructed using a base layer, a sub-base layer and a sub-grade layer or the natural soil foundation. The thickness of the upper typically ranges from 18 mm to 40 mm according to the standards for highway construction in the UK [2].

The electrical resistivity technique applied in this research has been implemented using a capacitive-coupled resistivity (CCR) system. Four square-plate electrodes C1, P1, P2 and C2, of large dimensions compared to the electrode spacing, are operated as inline capacitive sensors: electrodes C1 and C2 act as current sources coupling electrical current into the pavement; while electrodes P1 and P2 operate as receiver sensors to measure the voltage in the media. By this method, the quantity of electrical impedance could be estimated. It is assumed that as the moisture content of the wearing layer increases, its resistivity decreases and its dielectric constant increases. It is believed that this is the first time that this capacitive-coupled resistivity technique has been researched and applied to the condition assessment of asphalt pavement. The separation between the electrode plate and the ground surface affects the capacitance value, and hence, the coupling of the electrical signal into the ground. Thus, the surface roughness of the wearing layer could reasonably be expected to influence the capacitance. Surface roughness effects on capacitors have been studied in the nanoscale integrated circuit (IC) application area. However, no research has been published about the impact of the pavement surface roughness on the impedance measurements, obtained by the capacitive-coupled resistivity technique. In this research a laser profiling instrument with an along-track resolution of 0.125 mm and a typical height resolution of 50 μm has been utilised to measure the asphalt pavement surface roughness height distribution of the areas surveyed using the

capacitive-coupled resistivity technique. These surface roughness height distribution data will be incorporated into the measurement data processing as correction factors, to achieve more accurate survey results. The moisture content of the wearing layer of asphalt pavements will be estimated using the Cole-Cole model for these corrected results.

According to the experiments conducted within the laboratory and field surveys on asphalt pavements in different locations, it is concluded that the measured reactance is an indication of surface roughness (with a typical maximum peak-peak roughness of 1.2 cm for the results presented within this thesis); while the real part of the measured impedance indicates the moisture content of the wearing layer of the asphalt pavement. A larger measured reactance indicates a rougher pavement surface. A smaller real part of the measured impedance indicates a higher moisture content within the sub-surface layer.

Acknowledgment

I wish to show my appreciation to Philip Robert Atkins who is my supervisor and Farzad Hayati who is the research fellow in my group. Sincerely, thanks for their support and help during my PhD research studies. Special thanks to Phil, who gave me the opportunities to attend an intensive continuing education course on underwater acoustics and sonar systems and part-time employment as a research associate on an underwater sonar systems project. With their help, I have developed the skills of researching, critical analysis, organising and team work. Thanks to my dad, my mom and Lu who always listened to me carefully and encouraged me when I faced difficulties or when I was having a hard time. And finally I would like to thank the School for providing me with a scholarship, without that, my PhD would not have happened.

I wish to acknowledge the support provided by the Engineering and Physical Science Research Council (EPSRC) through the grants EP/F065973 (Mapping the Underworld) and EP/K021699/ (Assessing the Underworld).

I also wish to acknowledge Janet Hingley for her care in proofreading this thesis.

Contents

CHAPTER 1.....	1
INTRODUCTION.....	1
1.1 Background.....	1
1.2 Aims.....	4
1.3 Thesis Structure.....	6
References.....	7
CHAPTER 2.....	9
ASPHALT PAVEMENT	9
2.1 Pavement Structure and Asphalt Layer Materials	9
2.1.1 Pavement Structures	9
2.1.2 Pavement Deterioration	11
2.1.3 Asphalt Layer Materials	13
2.2 Electrical Properties of Surfacing Layer Materials	15
2.2.1 Electrical Conductivity.....	19
2.2.2 Relative Permittivity.....	20
References.....	21
CHAPTER 3.....	23
CURRENT INVESTIGATION TECHNIQUES FOR PAVEMENT EVALUATION	23
3.1 Non-Geophysical Techniques.....	23
3.2 Geophysical Techniques on Pavements.....	24
3.2.1 GPR.....	24
3.2.2 Electromagnetic Induction.....	26
3.2.3 Electrical Techniques	31
Reference	56

CHAPTER 4	59
NON-INVASIVE CAPACITIVE-COUPLED RESISTIVITY SYSTEM	59
4.1 Introduction	59
4.2 Capacitive-Coupled Resistivity System	62
4.2.1 Capacitive-coupled resistivity system introduction	62
4.2.2 Source signal	72
4.2.3 Capacitive-Coupled Resistivity System Correction	74
4.2.4 Dielectric Polypropylene Material Parameters	80
4.3 Geometric Factor	83
4.3.1 Analytical model using a resistor-capacitor network	86
4.3.2 Practical experiments using test resistors	98
4.3.3 COMSOL modelling of a mirrored capacitive-coupled resistivity system using test resistors	130
4.3.4 Four-rods experiment using black foam and its COMSOL model	134
4.3.5 Capacitive-coupled resistivity system on black foam and its COMSOL model 138	
References.....	141
CHAPTER 5	142
SURFACE ROUGHNESS EFFECTS ON CAPACITIVE COUPLED RESISTIVITY SYSTEM	142
5.1 Surface roughness	143
5.1.1 Surface roughness model	143
5.1.2 The mechanisms of the self-affine rough pattern	144
5.1.3 Parameters describing pavement surface roughness	146
5.2 Roughness impacts on the capacitance	173
5.2.1 Analytical equations.....	174
5.2.2 Experimental tests	178

5.3	Field surveys and a summary	192
	References.....	197
CHAPTER 6.....		199
PAVEMENT DATA INTERPRETATION BY DEBYE MODEL		199
6.1	Introduction.....	199
6.2	Empirical models used to describe Maxwell-Warburg polarization in the asphalt pavement mixture.....	206
6.3	Dielectric dispersion experiments at frequencies (0.1 kHz – 0.1 MHz)	209
6.4	Field survey data interpretation (asphalt pavement)	214
	References.....	218
Conclusion.....		221
Appendix 1: Main roughness parameters		224
Appendix 2: Key Codes.....		226

List of Abbreviation and Variables

σ	Electrical conductivity with units of Siemens/meter
ρ	Electrical resistivity with units of $\Omega \cdot m$
ρ_e	Effective resistivity with units of $\Omega \cdot m$
$\Phi_{AirVoidsContent}$	Air-void content
$S_{WaterContent}$	Proportion of voids filled with water
ρ_{water}	Resistivity of water
m	Constant
n	Constant of typical value as 2
a	A coefficient
R	Resistance with units of Ω
L	Length with units of m
V	Voltage with units of V
$Area$	Cross-section area with units of m^2
I	Current with units of <i>Ampere</i>
E	The intensity of the electric field with units of V/m
J	Current density with units of A/m^2
ϵ_r	Relative permittivity
ϵ_{rl}	Relative loss factor
ϵ_o	The permittivity of the vacuum with the value of $8.854 * 10^{-12} F/m$
c	The velocity of light in the vacuum with the value of $3 * 10^8 m/s$
t	The two-way travel time of the reflected pulse signal with units of s
∇	Gradient operator

List of Illustrations

Figure 1: ATU project work streams	5
Figure 2: Structure of typical rigid pavement and flexible pavement	10
Figure 3: A 2D field survey conducted adjacent to a car park of Southampton University in 2015 [Photo: Author private archive]	33
Figure 4: A 3D field survey in a car park of Southampton University using AC resistivity methods in 2015 [Photo: Author private archive]	33
Figure 5: A sketch of the field survey in a car park of Southampton University using AC resistivity methods in 2015	34
Figure 6: Electric field strength of point source electrode at the surface of the homogeneous earth	36
Figure 7: Electric potential distribution (2D) of point source electrode at the surface of the homogeneous earth	37
Figure 8: Potential distributions of a simple case: a single current electrode implanted on homogeneous earth	38
Figure 9: Sketch of a pole-dipole configuration	41
Figure 10: Sketch of the Wenner configuration	43
Figure 11: Sketch of the Schlumberger configuration	44
Figure 12: Sketch of dipole-dipole configuration	45
Figure 13: Sketch of line electrode in a Wenner configuration	47
Figure 14: Sketch of dipole-dipole in square configuration	48
Figure 15: Sketch of the prototype of capacitive resistivity technique	51
Figure 16: Sketch of a towed CCR technique by Kuras [35]	53
Figure 17: Sketch of current and voltage relation of a non-ideal capacitor (at frequencies less than 10 MHz [1])	59
Figure 18: Robotic platform carrying the capacitive-coupled resistivity system on the pavement behind the old library at the University of Birmingham	63
Figure 19: A high-level view of the capacitive-coupled resistivity system	63
Figure 20: A low-level view of the electrode configuration of the capacitive-coupled resistivity system	64
Figure 21: The diagram of the capacitive-coupled resistivity system	64

Figure 22: Simplified circuit sketch of four electrodes coupled to the pavement	65
Figure 23: Sketch of sensor electrode array configuration with a guard ring	65
Figure 24: Circuit sketch of the sensor electrode configuration of the capacitive-coupled resistivity system.....	66
Figure 25: Complete capacitive-coupled resistivity system circuit diagram	67
Figure 26: The electrical circuit model of the capacitive-coupled resistivity system using SIMULINK in MATLAB (Gnd1 and Gnd2 are ground; System Earth are System Earth1 are the system earth)	68
Figure 27: Sub-surface equivalent circuit model	68
Figure 28: Half-circuit of capacitive-coupled system applying current loops (denoted by I_1 to I_4) and closed networks	69
Figure 29: Output voltage (V_{out}) relationship to sub-surface equivalent capacitance	71
Figure 30: Output voltage (V_{out}) relationship to capacitance between electrodes and rough surface.....	71
Figure 31: Amplitude response of operating frequency using stepped frequency CW signal (left side); stepped frequency versus the time (right side)	73
Figure 32: Amplitude response with respect to operating frequency (single-side) using a linear frequency modulated signal (left side); linear frequency function to the time (right side).....	74
Figure 33: Amplifier gain characteristics of two voltage amplifiers (amplifier1 and amplifier2) operating from 50 Hz to 21 kHz	75
Figure 34: Diagram of the test system used to estimate the performance of the amplifiers.	76
Figure 35: Practical resistor (5Ω) resistance test after systematic error correction factor applied operating from 50 Hz to 21 kHz	78
Figure 36: Practical resistor (50Ω) resistance test after systematic error correction factor applied operating from 50 Hz to 21 kHz	78
Figure 37: Practical resistor (100Ω) resistance test after systematic error correction factor applied operating from 50 Hz to 21 kHz	79
Figure 38: Practical resistor ($2 \text{ k}\Omega$) resistance test after systematic error correction factor applied operating from 50 Hz to 21 kHz	79
Figure 39: Self-capacitance value test of an HP4921 impedance analyser	81

Figure 40: A single parallel-plate capacitor with a yellow polypropylene sheet as a dielectric material.....	81
Figure 41: Side view of a single parallel plate capacitor with yellow polypropylene sheet as a dielectric material	81
Figure 42: Measured capacitances of a single parallel plate capacitor with a yellow polypropylene sheet as a dielectric material.....	82
Figure 43: Dielectric constant of the yellow polypropylene sheet as a dielectric material (y-axis of Experimental Frequency is in units of Hz).....	83
Figure 44: Flow chart for deriving the geometric factor of the capacitive-coupled resistivity system	84
Figure 45: Diagram of predicting the geometric factor of the capacitive-coupled resistivity system by experimental method using test resistors (R in this diagram ranges from 4 Ω to 680 k Ω).....	85
Figure 46: A side-view diagram of the mirrored system	86
Figure 47: 1D Resistor-capacitor (RC) network of the electrode P1 with an extra resistor and a coupling capacitance (dashed line: potential RC components depending on number of meshes; solid arrows: assumed network-current flow)	88
Figure 48: 1D mirrored system circuit model using a resistor-capacitor network with extra components from the complete system circuit (dashed line: potential RC components depending on number of meshes; arrows: assumed network-current flow)	89
Figure 49: Potential distributions at 5 kHz on the material surface by analytical and network methods (107 Ωm)	92
Figure 50: Current distributions at 5 kHz on the material surface by analytical and network methods (107 Ωm)	93
Figure 51: Potential distributions at 5 kHz on the material surface by analytical and network methods (109 Ωm)	94
Figure 52: Current distributions at 5 kHz on the material surface by analytical and network methods (109 Ωm)	94
Figure 53: Potential distributions at 5 kHz on the material surface by analytical and network methods (1010 Ωm).....	95

Figure 54: Current distributions at 5 kHz on the material surface by analytical and network methods (1010 Ωm)	96
Figure 55: The relationship curve of predicted resistance related to the resistivity (black curve: assumed centre point electrodes of four plate-electrodes of the system; blue curve: from the in-line plate electrodes of the capacitive system)	97
Figure 56: The geometrical factor for materials with resistivity values ranging from 1 Ωm to 1010 Ωm (black curve: assumed centre point electrodes of four plate-electrodes of the system; blue curve: from the in-line plate electrodes of the capacitive system)	98
Figure 57: An example of the electric field including the fringing effect of a parallel plate capacitor (upper figure – the circuit shows the topology of the fringing effect of a parallel plate capacitor which is illustrated by the lower-figure)	99
Figure 58: Standard parallel plate capacitor without fringing effects	100
Figure 59: Analytical capacitances of a parallel plate capacitor by three methods	102
Figure 60: Analytical circuit diagram by placing a capacitive-coupled resistivity system in free space	103
Figure 61: Analytical half-mirrored circuit diagram by placing a capacitive-coupled resistivity system in free space	103
Figure 62: Analytical half-mirrored circuit model by placing a capacitive-coupled resistivity system in free space	104
Figure 63: COMSOL modelling of the capacitive-coupled resistivity system in free space ...	104
Figure 64: Fitted impedance of the capacitive-coupled resistivity system operated in free space (FS)	106
Figure 65: Analytical circuit diagram formed by placing the capacitive-coupled resistivity system onto a copper sheet	107
Figure 66: Analytical half mirrored circuit diagram by placing the capacitive-coupled resistivity system onto a copper sheet	107
Figure 67: Analytical half mirrored circuit model generated by placing the capacitive-coupled resistivity system onto a copper sheet	108
Figure 68: COMSOL modelling of the capacitive-coupled resistivity system placed on a copper sheet	108

Figure 69: Fitted impedance of the capacitive-coupled resistivity system when placed on a copper sheet (CS).....	110
Figure 70: The resistance relationship of copper to operating frequencies (1 Hz-10 MHz) when an AC signal is applied.....	112
Figure 71: Fitted impedance of capacitive-coupled resistivity system on copper sheet (CS) by using AC copper resistance	112
Figure 72: Sketch of practical experiments using test resistors connected to a set of electrodes used to simulate materials of varying resistivity	114
Figure 73: Circuit model of the capacitive-coupled resistivity system placed on discrete test resistors.....	115
Figure 74: Impedance fitting result of test resistor 4 Ω	116
Figure 75: Impedance fitting result of test resistor 10 Ω	116
Figure 76: Impedance fitting result of test resistor 22 Ω	117
Figure 77: Impedance fitting result of test resistor 33 Ω	117
Figure 78: Impedance fitting result of test resistor 47 Ω	118
Figure 79: Impedance fitting result of test resistor 100 Ω	118
Figure 80: Impedance fitting result of test resistor 671 Ω	119
Figure 81: Impedance fitting result of test resistor 1 * 10 ³ Ω	119
Figure 82: Impedance fitting result of test resistor 3 * 10 ³ Ω	120
Figure 83: Impedance fitting result of test resistor 5 * 10 ³ Ω	120
Figure 84: Impedance fitting result of test resistor 7.47 * 10 ³ Ω	121
Figure 85: Impedance fitting result of test resistor 11.6 * 10 ³ Ω	121
Figure 86: Impedance fitting result of test resistor 14.7 * 10 ³ Ω	122
Figure 87: Impedance fitting result of test resistor 21 * 10 ³ Ω	122
Figure 88: Impedance fitting result of test resistor 30 * 10 ³ Ω	123
Figure 89: Impedance fitting result of test resistor 46 * 10 ³ Ω	123
Figure 90: Impedance fitting result of test resistor 62 * 10 ³ Ω	124
Figure 91: Impedance fitting result of test resistor 82 * 10 ³ Ω	124
Figure 92: Impedance fitting result of test resistor 99 * 10 ³ Ω	125
Figure 93: Impedance fitting result of test resistor 120 * 10 ³ Ω	125

Figure 94: Impedance fitting result of test resistor $150 * 10^3 \Omega$	126
Figure 95: Impedance fitting result of test resistor $180 * 10^3 \Omega$	126
Figure 96: Impedance fitting result of test resistor $270 * 10^3 \Omega$	127
Figure 97: Impedance fitting result of test resistor $680 * 10^3 \Omega$	127
Figure 98: Circuit model of pavement materials with the addition of boundary layer capacitors.....	128
Figure 99: Circuit model of pavement materials with the addition of boundary layer capacitors and associated leakage currents	129
Figure 100: Relationship curve of the predicted resistance of the test resistors and their practical resistance (RMS value of test resistors is $2.5 * 10^5 \Omega$; RMS value of predict resistance is $0.9 * 10^4 \Omega$)	130
Figure 101: COMSOL model of mirrored capacitive-coupled resistivity system using discrete test resistors at the frequency of 5 kHz.....	131
Figure 102: Extra circuit connection hidden in the COMSOL model	132
Figure 103: Electric potential spatial distribution of a slice of the mirrored capacitive-coupled resistivity system used to measure test resistors at 5 kHz	133
Figure 104: The relationship curve between the predicted resistances using COMSOL modelling and the value of the test resistors at 5 kHz	133
Figure 105: Relationship curves of the test resistances and the predicted measured resistance obtained by two methods (blue curve-from practical experiments; red curve-from COMSOL modelling) at 5 kHz	134
Figure 106: Experiment using four rods weighted on 5 cm thick conductive foam.....	135
Figure 107: Measured resistance value of the foam by using four rods vs. operating frequency (the spiking value at very low frequency could be the internal resistance of the instrument itself)	136
Figure 108: COMSOL model of the experiment using four rods placed on 10 cm thick conductive foam (5 kHz)	137
Figure 109: Measured impedance and predicted impedance curves when the capacitive-coupled resistivity system is placed on the conductive foam (10 cm)	138
Figure 110: COMSOL model of the capacitive-coupled resistivity system measurement when placed on the black foam with a thickness of 10 cm.....	139

Figure 111: Height distribution measurement of an area of degraded pavement behind the Gisbert Kapp building using a laser profiling instrument	142
Figure 112: Surface height distribution of the good pavement between the North Car Park and the Gisbert Kapp building	147
Figure 113: Surface height distribution of the poor pavement behind the Gisbert Kapp building	147
Figure 114: Cumulative distribution function of the amplitude surface roughness of a good pavement and a poor pavement, numerically obtained from data used in Figure 112 and Figure 113	148
Figure 115: Amplitude probability density function of a good pavement	150
Figure 116: Global autocorrelation function (ACF) of a good pavement	151
Figure 117: Amplitude probability density function of a poor pavement.....	151
Figure 118: Autocorrelation function (ACF) of a poor pavement.....	152
Figure 119: One example of a local autocorrelation function of a good pavement in final survey position where four electrodes are placed in Figure 112	154
Figure 120: One example of a local autocorrelation function of a poor pavement in final survey position where four electrodes are placed in Figure 113	155
Figure 121: Local correlation lengths of a good pavement	157
Figure 122: Local correlation lengths of a poor pavement	158
Figure 123: Local power spectral density (upper: in linear scale; lower: in log-log scale) of good pavement surface profiles covered by each electrode for the last scan	160
Figure 124: Local power spectral density (upper: in linear scale; lower: in log-log scale) of bad pavement surface profiles covered by each electrode for the last scan.....	162
Figure 125: Global power spectral density of a good pavement surface profile (Upper: X and Y are in linear scale; Lower: X and Y are in log-log scale)	164
Figure 126: Global power spectral density of a poor pavement surface profile (Upper: X and Y are in linear scale; Lower: X and Y are in log-log scale)	165
Figure 127: Probability density function of both pavements (X-coordinate represents current height probability and Y-coordinate describes current height)	166
Figure 128: Amplitude probability cumulative distributions of a good pavement and a poor pavement (The four colour curves represent the analytical and measured results of both pavements)	168

Figure 129: Normal probability plots of a good pavement (Left side: normal probability plot; Right side: a Z-test box-plot).....	170
Figure 130: Normal probability plots of a poor pavement (Left side: normal probability plot; Right side: a Z-test box-plot).....	170
Figure 131: Typical Allan variance analysis results [16] [17]	171
Figure 132: Allan variance analysis result of a good pavement	172
Figure 133: Allan variance analysis result of a poor pavement.....	173
Figure 134: Diagram of the capacitive coupled resistivity technique system placed on the pavement with a rough surface (a side view).....	174
Figure 135: An example of the effects of the reference heights on the capacitance of a rough-capacitor.....	178
Figure 136: Varying surface heights by using multiple dielectric-layers	179
Figure 137: The relationship curve between the reactance and the resistance of a varying dielectric-layer-thicknesses at 5 kHz.....	180
Figure 138: Measured impedance data on foam at various heights fitted with analytical data using the resistor-capacitor network method	181
Figure 139: Normalized capacitance on the foam at various heights at 5 kHz	182
Figure 140: Normalised first differentiation of rough capacitance to the height	183
Figure 141: Sand bag located on an acrylic squared, perforated sheet to model a surface roughness layer.....	184
Figure 142: Acrylic squared, perforated sheet placed on the soft foam inside a vacuum bag and used to model a rough surface layer	185
Figure 143: Three-square-layers with copper tapes to model deeper roughness (left side: front view; right side: back view).....	186
Figure 144: Rough capacitor formed by a square-roughness-model and copper plate connected to the HP4921	187
Figure 145: Normalised capacitance of one-layer-roughness-model with spacer heights...	188
Figure 146: Comparison between the predicted capacitances of a single-layer-roughness-model of varied heights and the measured capacitances.....	190
Figure 147: The normalised capacitances of three layer-roughness models using copper tapes.....	191
Figure 148: The impedance results of three roughness models	192

Figure 149: Field survey on good pavement between the North Car Park and the Gisbert Kapp building	193
Figure 150: Field survey on the poor pavement at the rear of the Gisbert Kapp building ...	193
Figure 151: Raw impedance data collected on a good asphalt pavement, a dry old asphalt pavement and a wet old pavement with overlaid polynomial curve fits.....	194
Figure 152: Corrected impedance data collected on a good asphalt pavement, a dry old asphalt pavement and a wet old pavement after applying a roughness correction factor ..	195
Figure 153: Corrected impedance data collected on a good asphalt pavement, a dry old asphalt pavement and a wet old pavement by roughness correction factor and geometric factor.....	196
Figure 154: Debye model describing typical dispersion phenomenon (derived from the Debye equation: the relaxation frequency may change as the dielectric materials; the complex permittivity and complex conductivity of asphalt pavement materials can be described by Debye model may have same curve tendency as this example depending on the operating frequencies)	201
Figure 155: Sketch of three polarizations of a pore between two grains [11] [12]	203
Figure 156: Conceptual diagram illustrating the process of interfacial polarization [1]	204
Figure 157: A sketch view of polarization mechanisms in different porous dielectrics	206
Figure 158: Example of comparison between Debye curve and experimental behaviour (both curves were derived from synthetic data to illustrate results from the literature [9])	208
Figure 159: Test rig including epoxy fillers surrounded by water	210
Figure 160: Experimental capacitance and conductance of epoxy experiment	210
Figure 161: Case 1-using epoxy and copper powder.....	211
Figure 162: Case 2-using epoxy, copper powder and 50% water-fill	212
Figure 163: Case 3-using epoxy, copper powder and 100% water-fill	212
Figure 164: Fitting results between the dataset from the epoxy experiment (epoxy fillers with 100% water-fill) and the analytical Cole-Cole model (broader frequency range factor set as zero; X-axis: operating frequency in unit of Hz; Y-axis of the upper figure: Experimental Capacitance in unit of Farads; Y-axis of the lower figure: Experimental Conductance in unit of Siemens)	213
Figure 165: Fitting results between the measured resistivity of a poor asphalt pavement and analytical resistivity predicted using the Debye model at 10 kHz.....	215

Figure 166: Fitting results between the measured reactance of a poor asphalt pavement (after applying geometric factor and roughness factor) and calculated reactance predicted by the Debye model at 10 kHz	216
Figure 167: Relaxation time of a poor asphalt pavement at 161 positions predicted by the Debye model at 10 kHz	216
Figure 168: Fitting results between the measured resistivity of a good asphalt pavement and analytical resistivity predicted using the Debye model at 10 kHz	217
Figure 169: Fitting results between the measured reactance of a good asphalt pavement (after applying geometric factor and roughness factor) and calculated reactance predicted by the Debye model at 10 kHz	217
Figure 170: Relaxation time of a good asphalt pavement at 164 positions predicted by the Debye model at 10 kHz	218

List of Tables

Table 1: Deterioration types of flexible pavements [6]	12
Table 2: Typical asphalt base layer properties (in the UK) [7]	15
Table 3: Typical relative permittivity and electrical resistivity of pavement materials [9] [10] [12] [13] [14] [15] [16]	17
Table 4: The GPR applications on pavements [3] [4] [5] [6]	25
Table 5: Typical electrode array configurations and their properties [32] [33]	50
Table 6: Experiment data of normal parallel capacitor	82
Table 7: Components of predicted values for both cases of free space and copper sheet ..	113
Table 8: Configuration of practical experiment using four rods	135
Table 9: A summary of the properties of the self-similar rough pattern and the self-affine rough pattern.....	144
Table 10: A summary of random deposition models and ballistic deformation models from fractal theories [1] [2] [3] [4] [5]	145
Table 11: Main effective parameters describing the roughness of a good and a poor pavement (Y_i : measured raw height distribution data).....	149
Table 12: Mean correlation length for each electrode in all survey positions.....	159
Table 13: Two constants of power law decay function obtained from the global power spectral density ($PSDf = B f\beta$)	166
Table 14: Kolmogorov-Smirnov test of both pavements.....	168
Table 15: Parametric Z-test of both pavements	169
Table 16: Predicted foam resistivity and foam equivalent capacitance.....	181
Table 17: Polypropylene squared sheet's dimension	185
Table 18: The dimension of a single layer roughness-model	186
Table 19: Various air-filled separation configurations above a single square-roughness-layer	187
Table 20: Roughness parameters of the single-layer-roughness-model.....	189
Table 21: Cylinder geometry.....	209

CHAPTER 1

INTRODUCTION

1.1 Background

Over time new pavement layers gradually deteriorate; as the asphalt base becomes more brittle and the pavement surface texture fractures due to age hardening. Typical failure modes in the pavement are bound-layer cracking (fatigue cracking, low temperature cracking, and shrinkage cracking) and permanent deformation such as wheel-track rutting. These failures result from traffic loading and environmental conditions such as temperature or moisture levels, contributing to all the other under-lying degradation mechanisms. Sub-surface moisture is probably the dominant factor, within the base layer, in the weakening of the pavement structure and speeding up the aging process of pavements or the degradation of buried assets. The moisture content of cracks increases as the cracks become wider and deeper. The road condition becomes worse as the water content increases. In winter, as wet areas become frozen, expand and later shrink, the endurance ability to cope with heavy traffic loads is greatly reduced. According to [3] “the cost of immediate reconstruction without any prior pavements fixes could be three times or even more than the cost of frequent maintenance on aging pavements”. Thus, maintenance needs to be employed, to extend the service life of ageing or damaged pavements and to reduce total maintenance costs, before seriously damaged pavements become irreparable.

Furthermore, according to a BBC report by Martin Cassidy in Northern Ireland in 2012 [4] “there were 700 underground cables hit in 2012 in Northern Ireland alone. Though much effort of using more accurate mapping techniques was applied to avoid high-voltage electricity cables during pavement rehabilitation, maintenance workers continued to accidentally hit them”. Such failures can potentially lead to serious injuries or even death as workmen excavate roads to repair them. Another failure case of digging underground cables can be found from the report written by the Royal & Sun Alliance Insurance Company of Canada. It pointed out that about 70% of underground cross-linked polyethylene

insulation (XLPE) power cables failed because of water ingress caused by roots and the high-level moisture content of the sub-soil layer [5]. These examples indicate that without knowing the exact location of buried assets (e.g. electricity cables) during rehabilitation, digging very likely results in excavating the wrong location during the asphalt pavement repair process. Such location uncertainty during rehabilitation work usually results in a huge waste of time and money, public transportation disruption and sometimes even a threat to the life of maintenance workers. Given this background, the moisture condition assessment of sub-surface layers using non-invasive geophysical methods becomes highly desirable.

Traditional invasive methods including drilling into the ground for road condition evaluation; to provide estimates such as thickness, moisture levels, clay content and porosity. Such measurements, based on point-to-point investigations, are limited to small spatial survey coverage areas and are time-consuming in a large field survey. Though these conventional destructive techniques are not effective over large pavement survey areas, they could be combined with some prior non-invasive geophysical mapping techniques, as these non-destructive techniques could provide indicative prior information about problematic areas. Therefore, before any pavement remediation is undertaken, pavement condition assessment operations using non-destructive (NDT) geophysical mapping techniques become indispensable. Non-destructive testing methods are usually applied to the investigation of highway structures or pavements because of the lack of damage to the structures thus reduce costs. Meanwhile, traditional invasive methods such as borehole and drilling methods could be combined with the non-destructive methods to verify the measured results. Non-invasive investigations are helpful in reducing the number of boreholes necessary in pavement maintenance operation; while rapid survey techniques greatly reduce the number of road closures required, thus reducing the inconvenience to transportation. A single geophysical method generally returns one parameter data set; thus, a number of techniques tend to be combined together to provide more accurate mapping.

Over the past three to four decades, the use of ground penetrating radar (GPR) [6] as a non-destructive testing method has proved to be a very popular and useful technique for pavement condition evaluation, considering its real-time measurement with rapid speed

and high resolution. Ground penetrating radar (GPR) operating at very high frequencies, e.g. GHz, to achieve high resolution at the expense of penetrating depth are used for pavement condition assessment. The higher the frequency that is used, the higher will be the spatial resolution and the shallower the penetration depth will be. It effectively works by detecting the changes in echo strength (an echo is the reflected signal that arrives at the receiver with a delay after the initial transmitted signal; the strength is usually quantified in units of decibels which is the ratio of the intensity of the reflected signal to the transmitted signal) between layers constructed using materials with different dielectric and conductive properties. In addition, a GPR signal will be highly attenuated due to the presence of conductive materials such as water and metal-filled media. It was stated within the American Society for Testing and Materials (ASTM) guidance [7] that “a typical GPR system usually has a resolution sufficient to determine a minimum layer thickness of 40 mm to an accuracy of 5 mm”. The wearing layer of a flexible pavement typically ranges from 20 mm to 50 mm. If a typical GPR system is applied to such a wearing layer, its resolution will probably be insufficient to estimate the layer thickness and condition. It is therefore seldom used for the investigations of the wearing layer. The GPR system has been most commonly applied to pavement investigations such as binding layer thickness estimation, void location and bridge deck delamination. Since 1998, GPR techniques have been developed for applications such as crack detection in the bound upper asphalt layer, and moisture estimation in the unbound sub-base layer. Misleading results have been observed because of buried moisture barriers detected when processing various subsurface reflections from asphalt layers, as the echo level is dependent on the moisture content [8] [9].

Resistivity techniques have been well used in the archaeological application field [10] [11] [12] for detecting buried cultural relics and have proved to be effective when applied to estimate the clay content, or the water content, in pavement layers. Traditional DC/AC resistivity techniques rely on inserting electrodes into the ground; thus, survey costs are higher and measurement times are longer than a GPR survey investigating the same area. The electrode deployment restricts its applications associated with pavements because of the hardness of the surface – usually manual electrode insertion is impossible. Though deployments could sometimes be achieved practically, the galvanic resistance between the

electrodes and the surface results in small values of injected current and a correspondingly poor signal-to-noise ratio of the received signal. A dense electrode deployment on an asphalt pavement will cause damage to the surface and probably require road closure and reinstatement. Considering these disadvantages of conventional resistivity techniques, the extended geophysical method of a capacitive-coupled resistivity technique has been studied and applied to an assessment of pavement condition. A capacitive-coupled resistivity technique with wide electrode spacing of 1 metre was first discussed by Kuras [13] in his PhD research. In his research, four electrode sensors could be recognized as four point-sources operating in an electrostatic state where the spatial resolution was not high. Under such a situation of wide electrode spacing, the moisture level in a small localised area could not be estimated accurately enough and its measuring depth might include the sub-base of a flexible pavement instead of the wearing layer [13]. Since then, non-invasive resistivity techniques have been developed significantly.

1.2 Aims

The “ATU” (Assessing the Underworld) was a large cooperative research programme incorporating many universities and industrial stakeholders. It aimed to assess the condition of buried infrastructure such as pipes, cables, tree roots, and cracks by applying target-specific sensor techniques, which can be seen in Figure 1. This figure illustrates the big picture of the “ATU” including five work streams that are denoted by WS. Different work streams implement condition-assessments using different sensor methods. The research described within this thesis (WS3c) was part of the work stream WS3, and aims to detect wet areas of the wearing layer due to leaks from aging water utilities and water ingress from the surface, using an automated electrical resistivity technique employing a capacitive-coupled sensor system.

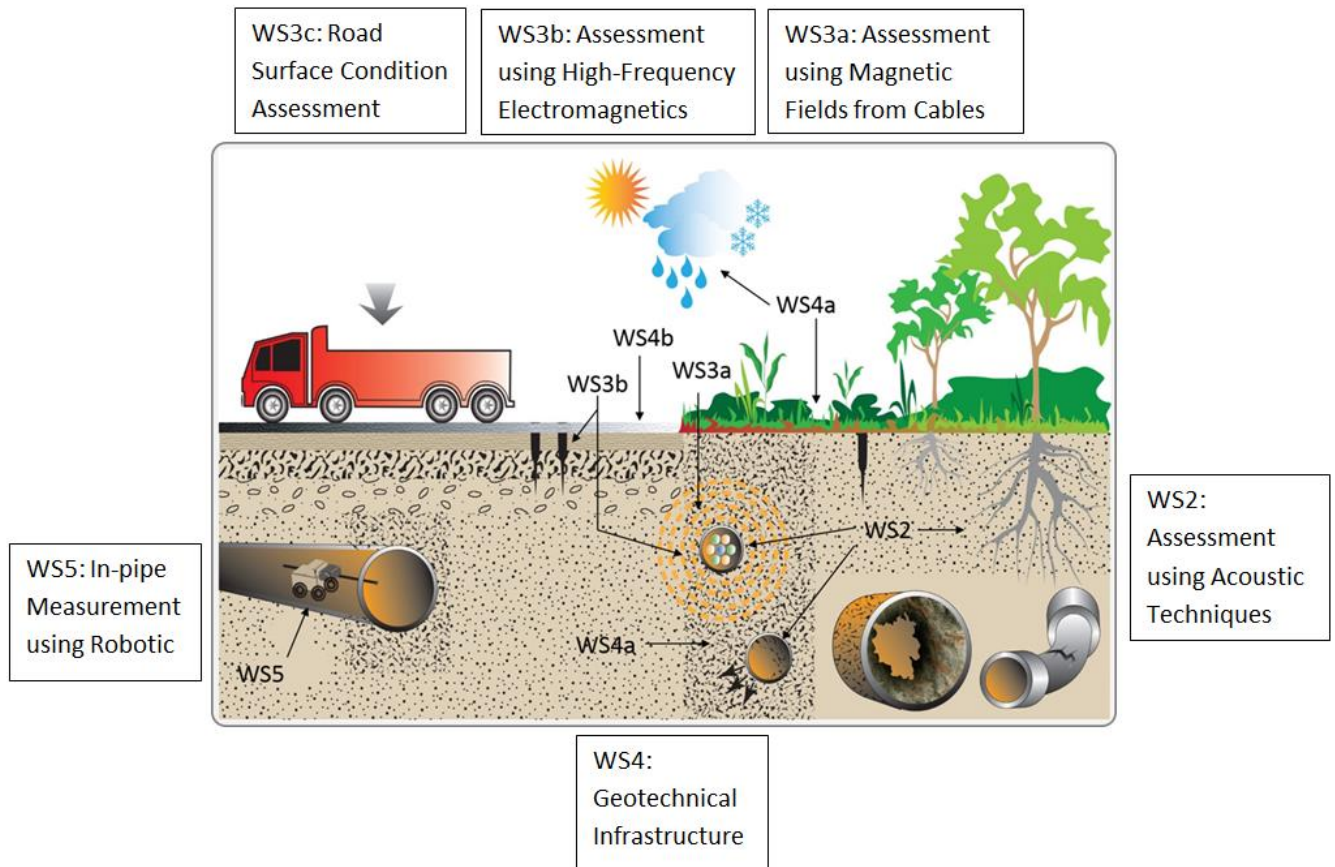


Figure 1: ATU project work streams

The scope of the thesis and main objectives are:

- To describe the fundamental concepts, the physical properties and the structures of a typical asphalt pavement.
- To provide a review of the geophysical methods used in pavement condition assessment.
- To describe an automated capacitive-coupled resistivity technique system.
- To model, measure and correct systematic instrumentation errors.
- To provide an analytical model of the capacitive-coupled system; to calculate and verify the geometric factor; to verify the efficacy of the analytical model by conducting practical experiments and comparing it with numerical models implemented using COMSOL.
- To set up experiments to assess the impact of surface roughness on system performance; to conduct surface roughness surveys; and to provide calculations of

the impact on the capacitance or reactance estimates as a result of surface roughness.

- To conduct field surveys on asphalt pavements including new pavements in good condition and old pavements in poor condition.
- To provide appropriate roughness correction factors to be applied to measured data and to calculate the true electrical resistivity or electrical conductivity; to verify the hypotheses that the measured electrical reactance mainly reflects the surface roughness, and the measured resistance or electrical resistivity mainly reflects the moisture level of the wearing surface layer of the asphalt pavement.
- To assess the moisture level of pavements using the Cole-Cole model and to provide appropriate data interpretation.

1.3 Thesis Structure

To achieve the goals listed in the previous section, the asphalt pavement structure and the physical properties of the construction materials will be introduced in Chapter 2. A good understanding of the target is necessary and no single geophysical method is suitable to assess the condition of the pavement. Non-invasive measurement techniques are required; and these have been chosen to rapidly measure the electrical properties of resistance and permittivity primarily in the wearing surface layer due to the induced signal energy taking the easiest route that is likely to be near the surface. Chapter 3 illustrates current non-destructive geophysical testing techniques used for pavement evaluation. The merits and limitations of different techniques used in field survey applications are considered. The conclusion is reached that electrical resistivity techniques using capacitive-coupled systems are a suitable method for assessing the moisture content of the wearing surface layer of a pavement. Chapter 4 includes detailed technical information about capacitive-coupled systems, the geometric factor, and the system error factors, COMSOL modelling and experimental verification. The electrode sensors described in this work cannot be considered as point sources and therefore need to be appropriately modelled. Similarly, the roughness factor associated with the contact between the electrode sensors and the surface of the pavement cannot be ignored. Therefore, surface roughness theories and their impact on the measured data (e.g. capacitance) are studied by theoretical analysis and verified experimentally in Chapter 5. Suitable roughness correction factors are then

derived and applied to field and laboratory-derived data. Finally, in Chapter 6, the Cole-Cole model will be used to interpret measured resistivity data to derive parameters of chargeability and relaxation time of pavement materials, which can infer water content. The conclusions of this research are also provided in Chapter 6.

References

- [1] www.assessingtheunderworld.org (access within 2017-2019).
- [2] Design Manual for Roads and Bridges, <http://standardsforhighways.co.uk/ha/standards/index.htm> (access within 2016-2019).
- [3] AASHTO, <https://www.transportation.org/> (accessed 2016).
- [4] M. Cassidy, <https://www.bbc.co.uk/news/uk-northern-ireland-16970715> (accessed in 2016).
- [5] Y. Huang, "Extruded underground cables failure and testing," RSA, Oct.2012.
- [6] D. J. Daniels, *Ground Penetrating Radar*. The institute of engineering and technology, 2nd Edition, August 20, 2004.
- [7] <https://www.astm.org/Standards/D6432.htm> (accessed 2016).
- [8] R. D. Evans, M. Frost, M. S. Jones and N. Dixon, "A review of pavement assessment using ground penetrating radar," presented at the 12th International Conference on Ground Penetrating Radar, Birmingham, The UK, June 16-19, 2008.
- [9] T. Saarenketo and T. Scullion, "Road evaluation with ground penetrating radar," in *Journal of Applied Geophysics*, 43 (2000) 119-138.
- [10] A. A. Tabbagh, A. Hesse and R. Grard., 1993, Determination of electrical properties of the ground at shallow depth with an electrostatic quadrupole: field trials on archaeological sites: *Geophysical prospecting*, 41, 579 - 597.
- [11] J. M. Reynolds., 1997, *An introduction to applied and environmental geophysics*: John Wiley & Sons Ltd.
- [12] K. Zonge, J. Wynn and S. Urquhart., 2005, *Resistivity, induced polarization and complex resistivity: Near-Surface Geophysics*, No. 13, 265.
- [13] O. Kuras, "The Capacitive Resistivity Technique for Electrical Imaging of the Shallow Surface," Ph.D. dissertation, Dipl.-Phys. FGS., University of Nottingham, 2002.
- [14] W. M. Telford, L. P. Geldart, R. E. Sheriff and D. A. Keys, *Applied Geophysics*. Cambridge University Press, Cambridge, 1976.

[15] Design Manual for Roads and Bridges (DMRB), Volume 7: Surfacing and Surfacing Materials (HD37/99). The Stationary Office, London, 2019. [Online]. Available: <http://www.standardsforhighways.co.uk/ha/standards/dmr/vol7/>

[16] W. E. Wightman, "application of geophysical methods to highway related problems," Federal Highway Administration, Central Federal Lands Highway Div., Contract No. DTFH68-02-p-00083, Sep. 2003.

CHAPTER 2

ASPHALT PAVEMENT

2.1 Pavement Structure and Asphalt Layer Materials

2.1.1 Pavement Structures

The “pavement” is defined as an engineering structure to carry transportation loadings, which could be a motorway, an airport runway or a trunk road. Pavements in the UK are categorized into flexible pavements and rigid pavements (or concrete pavements). From Figure 2, it is seen that these two kinds of pavements are basically constituted of three layers: an upper base layer, a middle sub-base layer (generally formed of unbounded granular materials), and a sub-grade foundation layer (generally natural soil ground). The upper layer of a rigid pavement could be recognized as one single layer, constructed using different kinds of concrete slabs including continuously reinforced concrete pavement (CRCP) or joined concrete pavement (JCP). Generally, the upper bound asphalt layer of a flexible pavement consists of three individual courses of slightly varying material composition. Currently, flexible pavements in the UK are composed of an upper asphalt layer, involving a surfacing course to provide riding surface skid-resistance and prevent the entire pavement from weakening when exposed to water; a wearing course and an asphalt base, a sub-base layer of hydraulically bound material (HBM), and a sub-grade foundation layer. Based on four stiffness classes (class 1, 2, 3 and class 4) of a flexible pavement foundation design, the equivalent thickness limitations of the base layer and the sub-base layer used during pavement design are defined in the Highways Agency design manual for roads and bridges [1]. According to the standards set for the design of flexible pavements in the UK, the foundation layer corresponds to stiffness class-2, requiring the equivalent 225 mm of sub-base on a sub-grade ground layer. It is stated by [2] “to give enough resistance to reflection cracking for hydraulically bound material crack spacing of 3 meters and a lifetime in excess of 80 million standard axles (msa), the asphalt cover should be of thickness 180 mm”. A TRL report in published 2004 states that an asphalt layer consists of 35 mm of a thin asphalt surfacing course and another 145 mm of dense bitumen macadam, incorporating 100 penetration grade bitumen [3]. For lower traffic loads, the minimum

permitted thickness of the sub-base is 150 mm and the minimum allowed asphalt layer thickness is 100 mm [4].

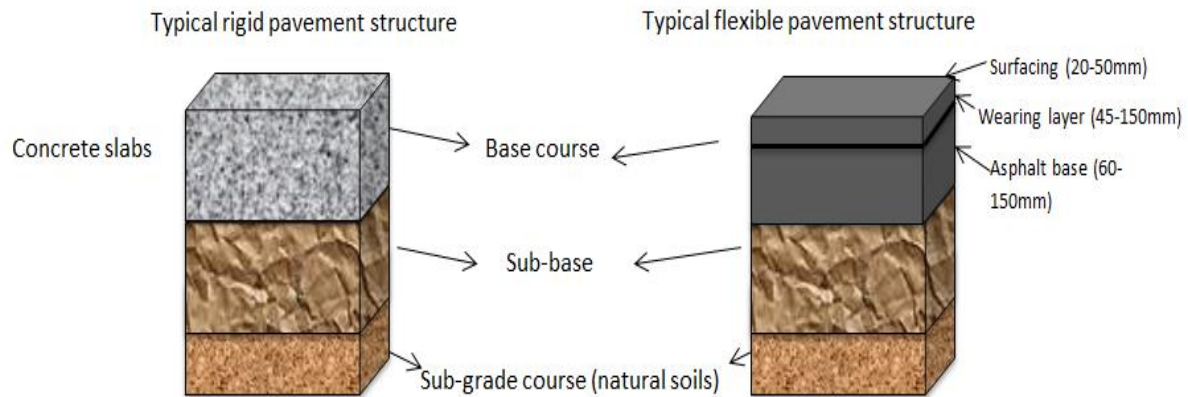


Figure 2: Structure of typical rigid pavement and flexible pavement

According to reports published by the Transportation Research Laboratory [4, page 1] and the transportation standards in the UK [5, page 2]:

“The performance of a rigid pavement is mainly affected by the condition of the surface including cracking and defects in the surfacing layer of continuously reinforced concrete pavement (CRCP), where such cracking patterns are mainly influenced by the aggregate type in continuously reinforced concrete pavement (CRCP) more than the sub-base type. However, the Government noticed that traffic noise associated with concrete pavements is much higher than hot rolled asphalt pavements. Considering another additional problem of the high initial construction cost of continuously reinforced concrete pavement (CRCP) construction, such kinds of rigid pavement have very limited application in the UK.”

“Joined concrete pavement (JCP) rigid pavement is also generally unsuitable for trunk roads including motorway construction in the UK because of the surfacing requirement that leads joined concrete pavement (JCP) to surfacing reflection cracking, which very likely increases future maintenance costs.”

Flexible pavement is the most commonly applied technique in practical engineering construction in the UK. Though rigid pavements do have limited applicability for transportation in the UK, it is still allowed to be used in trunk roads; generally only if it has

asphalt surfacing, which is usually the top course in the upper bound asphalt layer of a flexible pavement. Based on these considerations, this thesis will target the condition of moisture content within the surfacing course of flexible pavements.

2.1.2 Pavement Deterioration

For new pavements, failures will happen resulting from traffic loading and environmental conditions such as temperature or moisture ingress. As the pavement properties (e.g. resistance to deformation, durability, and skid resistance) are related to each other, the pavement design should be based on rules to achieve the best compromise between these properties. For example, excessive moisture induces environmental damage to the pavement surfaces or even generates extended damage to the foundations. Water entry is largely dependent on the air-void content or the extent of the cracking. Certain levels of air-voids and moisture content are indispensable to retain the good deformation resistance and durability performance of the pavement.

Too low a void content ($< 3\%$) would cause pavement distress resulting in decreased durability, and rutting. Too high a water content ($> 8\%$) results in a decrease in the stiffness and strength, resulting in a decreased fatigue life of the pavement, the ravelling (dislodging) of the binder and stripping of the aggregates. The moisture level increasing through interconnected air voids and water enters the pavement more easily. These types of deteriorations related to flexible pavements are summarized in Table 1.

Table 1: Deterioration types of flexible pavements [6]

Deterioration types	Deterioration forms	Layer where deterioration happened	Causes
Common deterioration	Loss of skidding resistance	Surfaces of all pavements	
	Loss of texture	Surfacing with high binder content materials	
	Rutting	Surfacing with high binder content materials	
Environmental deterioration (mainly on thin flexible pavements)	Aggregates loss	Surface courses	Hardening of the bitumen; less cohesion of the mixture
	Binder hardening; fatigue resisting properties of asphalt	Surface of pavements: propagates downward from surface to the base of bound layers	Oxidation of bitumen; strains by thermal cycling and vehicle loading
	Non-structural permanent deformation of rutting	Surfacing layer	Service temperature, like hot weather and stationary traffic
	Variation in foundation strength	Cracked thin pavements	Seasonal changes in moisture content; freeze-thaw cycle
Environmental deterioration (thick flexible pavements with strong foundations)	Cracking	Only at the surface, gradually increasing in depth	
	Non-structural deformation	Only at the surfacing layers	
Traffic loading deterioration	Fatigue cracks	Propagates upwards through underside of asphalt base to upper side of asphalt base	Tensile strains within the bound layers (thin pavements)
	Structural deformation of rutting	Subgrade or foundation and the entire pavement structure	Due to permanent deformation of one or more various layers, including foundation

Moreover, the separation caused by ravelling and stripping of the binder, leads to poor cohesion and adhesion in the mixture of aggregates, fillers and binders. Such poor adhesion without maintenance causes aggregation loss, crack formation beginning from the

surface and then gradually increasing in depth to the underlying layers and expansion of air-voids. Again and again, the pavement will be significantly damaged [6] [7]. Above all, both cases corresponding to insufficient air contents and excessive moisture would lead to a significant reduction of the pavement service life. Therefore, void content and moisture level detection or monitoring become necessary before, or during, maintenance procedures.

2.1.3 Asphalt Layer Materials

For flexible pavements, the basic types of bituminous surfacing materials include stone mastic asphalt (SMA), dense bitumen macadam (DBM) and hot mix asphalt (HMA). These are generally formed by a mixture of aggregates (crushed rock 30%-55%, slag or gravel), sand, fillers such as hydrated lime or cement, a bituminous binder, voids, some moisture and some reinforcement materials such as fibres, rubber, resins or polymers. Bitumen macadam materials are not usually utilised in the surface course because of their low texture depth, suspected durability and lower resistance to deformation [7].

Stone Mastic Asphalt Surfacing

A stone mastic asphalt surfacing layer typically consists of 70–80% gap-graded coarse aggregates; the voids between these coarse aggregate particles are filled with a few percent of mastic fine sand, 8–12% fillers such as hydrated lime or cement, 6.0–7.0% binder and 0.3% fibres (cellulose fibres or mineral fibres), or polymers, or resins. Graded coarse aggregates are commonly used with sizes of 5 mm, 8 mm and 11 mm. Sometimes, 14 mm-sized aggregates are applied to achieve a specific performance, such as high-speed skid resistance [7].

Three types of wearing course layer (type A, type B and type C) have been classified by the British Board of Agrément. Considering their thickness limitations, type A wearing course thickness should be smaller than 18 mm; type B wearing course thickness should be from 18 mm to 25 mm; and type C is the thin surfacing with a thickness limit of 25 mm to 40 mm. The type C wearing course system of stone mastic asphalt (SMA) has been commonly applied in UK pavement constructions.

Hot Rolled Asphalt Surfacing (Asphalt Concrete)

Hot rolled asphalt (HRA) surfacing uses a dense mixture of nominal 55% stone content aggregate, sand, fillers of cement or limestone dust and a binder mortar of bitumen for road works. The proportions of these mixture materials could vary based on different design standards to be used in the road network construction (in BS 594, 30% stone content aggregate materials are required). Typically, a hot rolled asphalt wearing course has a thickness of 45 mm or 50 mm. A 50 mm thickness is recommended [7].

In summary, all pavement materials are composite media that are formed by aggregates, a bituminous binder, fillers and reinforcement materials, but in various proportions. Every section of new pavement will be slightly different from others. Typical asphalt base layer materials and layer thicknesses are summarized in Table 2.

Table 2: Typical asphalt base layer properties (in the UK) [7]

Layer Name	General Materials	Aggregate Sieve Size	Thickness	Compositions
Surfacing	Hot rolled asphalt (HRA)	14 mm	20-45 mm	aggregates (crushed rock 30%-55%, slag or gravel), 7% voids filled with sand and fillers (hydrated lime or cement), 15% bituminous binder, some moisture and some reinforcement materials (fibres, rubber, resins or polymers)
	Stone mastic asphalt (SMA)	5 mm/8 mm/11 mm	15-60 mm	gap-graded coarse aggregates (70-80% crushed rock or crushed gravel), voids (2%-4%) between these coarse aggregate particles filled with mastic fine sand and 8-12% fillers (hydrated lime or cement), binder (6.0-7.0%), and 0.3% fibres (cellulose fibres or mineral fibres) or polymers or resins
Binder Course	Dense bitumen macadam (DBM)	10 mm-32 mm	45-150 mm	
Base	Dense bitumen macadam (DBM) and hot rolled asphalt (HRA)	10 mm-32 mm	60-150 mm	

2.2 Electrical Properties of Surfacing Layer Materials

The response of a pavement material to an electrical current from a current source at low frequencies (< 20 kHz) is related to the electrical impedance expressed in complex form; which is a function of operating frequency, electrical permittivity and electrical conductivity. Most of the materials used in pavements are electrical insulators with very high resistivity. From the experimental data provided in McNeill's research [8], the resistivity for dry aggregate (crushed stone) is around $10^6 \Omega \cdot m$ to $10^8 \Omega \cdot m$ with a dielectric constant around 2.6. The resistivity of bituminous bound is around $2 * 10^6 \Omega \cdot m$ to $10^9 \Omega \cdot m$ with a

dielectric constant of around 2.7 at room temperature [8]. At room temperature, pure water has electrical resistivity of $2 * 10^5 \Omega \cdot m$ and relative permittivity of 80. In practice, any water encountered is likely to be more conductive due to dissolved solids e.g. salts. The typical dielectric permittivity of water containing impurities is 7.8. Under some circumstances, pavement materials assumed to be poor conductors would become conductive because of the temperature, conductive minerals (e.g. magnetite, carbon, and graphite), water content, and operating frequency. For example, a typical basalt rock has a DC resistivity on the order of $10^{12} \Omega \cdot m$ in the complete absence of water. However, this same basalt sample with a single absorbed layer of water vapour has a DC resistivity that dramatically drops to $10^3 \Omega \cdot m$. At room temperature, some rock materials have similar DC resistivities of around $10^{10} \Omega \cdot m$; whilst a change of nine orders of magnitude could be caused by the temperature increasing from room temperature to temperatures above those experienced during pavement construction (900 degrees). Such temperature effects can be equivalently replaced by adding a little water to those rock samples or by increasing the operating frequency from DC to a few megahertz [9] [10] [11]. In summary, the water content and temperature are the primary variables determining the electrical properties of the materials.

Thus, a question has to be considered that during moisture condition assessment of the pavement, will temperature, operating frequency and chemical composition influence the measurement? According to the temperature effects on DC resistivity results [9][11], the effects on electrical conductivity can be assumed as constant when the temperature floats up and down within few degrees, typically 2% percent per degree. The operating frequency was assumed as fixed within these studies. Therefore, during field surveys and experimental tests, it could be stated that a wetting area assessment by measured electrical resistivity is independent of other environmental factors. Typical relative permittivity and electrical resistivity of the pavement materials are summarized in Table 3 [9] [10] [12] [13] [14] [15] [16]. The definitions and introductions of relative permittivity and electrical resistivity will be discussed in the following paragraphs.

Table 3: Typical relative permittivity and electrical resistivity of pavement materials [9] [10] [12] [13] [14] [15] [16]

Material		Typical dielectric constant		Typical electrical resistivity ($\Omega \cdot m$)	
				Dry	Wet
Concrete in service		5-9		10^6 to 10^9	21-100
Asphalt overlays		6 to 6.5		$2 * 10^6$ to 10^9	10^4 - $6 * 10^6$
Pure water		81		$2 * 10^5$	
Natural water with impurities		7.8		$2 * 10^3$ for water of permissible impurities	
Air		1			
Sand (wet to a predominantly dry)		3-30		20-200	
Dry asphalt		2-6.1	100 MHz	10^4 to 10^9	
		6.0 +/- 0.15	8-900 MHz		
Wet asphalt		6-12	100 MHz		
Asphalt		3-6			
Asphalt (4% binder plus sand aggregate)		3.8-4.4	11 GHz	10^4 to 10^9	
Asphalt (8% binder plus sand aggregate)		4.75			
Asphalt (4% binder plus crushed rock aggregate)		6.5-6.7			
Asphalt (8.5% binder plus crushed rock aggregate)		5.7-6.3			
Rock samples					
	Limestones	4-8		50 - 10^7	
	Sandstones	6		1 - $6.4 * 10^8$	
	Granite	5-7		Water (0%), 10^{11}	
				Water (0.06%), $1.3 * 10^8$	
				Water (0.19%), $1.8 * 10^6$	
				Water (0.31%), $4.4 * 10^3$	
	Basalt	(saturated) 8		Water (0%), $1.3 * 10^8$	
				Water (0.26%), $3 * 10^7$	
				Water (0.49%), $9 * 10^5$	
				Water (0.95%), $4 * 10^4$	

The electrical resistivity of pavement materials due to the ionic electrical conduction is determined by many parameters e.g. constituent materials, sizes and shapes of the components. When the ionic electrical conduction takes place through water-filled pores and the passages between the aggregates within the asphalt, the current flow is known as a percolation process. Among all those parameters, only the parameters of porosity (shape, size and number of pores), moisture level (extent of water-filled pores) and the level of dissolved electrolytes (e.g. salinity) are dominant [8]. For instance, it is seen from Table 3 that introducing slight moisture into the pavement could bring enormous changes to the resistivity of the material. Analytically, the effective resistivity ρ_e can be estimated by the empirical formula of Archie's law [8] [15] [17]:

$$\rho_{\text{effective}} = a \phi_{\text{AirVoidsContent}}^{-m} S_{\text{WaterContent}}^{-n} \rho_{\text{water}} \quad \text{for } 0.5 \leq a \leq 2.5, \quad 1.3 \leq m \leq 2.5 \quad (2-1)$$

Where, $\phi_{\text{AirVoidsContent}}$ is the air-void content (porosity); $S_{\text{WaterContent}}$ is the proportion of voids filled with water (water saturation); ρ_{water} is the resistivity of water; m and n (typical value is 2) are constants; a is a coefficient.

The electrical conductivity in porous media (e.g. rocks) is generally described by two empirical mixing laws. The first is Archie's law (used to predict the electrical conductivity of the porous media) and the second is the use of the geometric mean (to accurately predict the effective physical properties of a mixture of heterogeneous materials). Mixing models can be further sub-divided into parallel models, perpendicular models and random networks [18; 19]. Currently available electrical conductivity mixing models were summarized by Glover in 2010 [19]. The classical Archie's law is applicable for a material of two phases and only when the matrix is non-conducting (e.g. it relates the electrical conductivity of a small number of the clean rock samples to a small range of porosities and pore fluids) [20]. It was also stated by Glover [19], that the classical Archie's law becomes inapplicable when the materials are of more than one conducting phases or when the conducting phase does not fully fill the available pore space; furthermore, the surface conduction due to ions is not included within the classical Archie's law. A modified Archie's law (e.g. two-phase Archie's law) was applied for materials including clay-rich rocks. The electrical conductivities are now dependent on the fluid conductivity which is due to ions attracted to mineral surfaces

with net charges inside the materials [20]. This is important when the fluid solutions are salt-saturated [18]. The successful applications of two-phase Archie's law in modelling materials (e.g. enhanced porosity concretes, partially crystallized basaltic samples) of significant matrix conductivity were also summarized by Glover. Moreover, considering those limitations of the original Archie's law, a generalized form of the classical Archie's law has been developed for materials of any number of phases by Glover [19]. Taking account of the complex and changeable elements of the asphalt materials and the lack of applications of Archie's law in the asphalt pavement, the generalized form of the Archie's law is not applied in this work. Instead, the models of Cole-Cole or Debye are discussed (details are shown in Chapter 6) to describe the electrical properties of asphalt pavement materials at low operating frequencies (< 20 kHz).

2.2.1 Electrical Conductivity

Electrical conductivity σ (with units of S/m) is the reciprocal of electrical resistivity ρ (with units of $\Omega \cdot m$) such that:

$$\sigma = \frac{1}{\rho} \quad (2-2)$$

The resistance R (with units of Ω) between two cross-section faces of a solid with a dimension of length L (with units of m) and cross-section area of A (with units of m^2) is

$$R = \frac{\rho L}{A} \quad (2-3)$$

When a voltage V (with units of V) is applied across the solid and the resultant current I (with units of **Amps**) through it,

$$R = \frac{V}{I} \quad (2-4)$$

Then, electrical conductivity becomes

$$\sigma = \frac{L}{R A} = \frac{L}{\frac{V A}{I}} = \frac{L I}{V A} = \frac{\frac{I}{A}}{\frac{V}{L}} = \frac{J}{E} \quad (2-5)$$

Where E (with units of V/m) is the electric field; J (with units of Amps/m²) is the current density such that $J = \sigma E$.

2.2.2 Relative Permittivity

The charging current and the loss current stemming from charge carrier migration, are energy consuming processes e.g. due to dipole molecule rotation or friction, and are experienced when an AC voltage is applied to dielectric materials. Considering the existence of a loss current and a charging current, the complex permittivity ϵ^* and the complex impedance Z^* are introduced:

$$\epsilon^* = \epsilon_r \epsilon_0 - j \epsilon_{rl} \epsilon_0 \quad (2-6)$$

For a simple dielectric capacitor,

$$Z^* = \frac{1}{j\omega\epsilon^*} = \frac{1}{j\omega\epsilon_r\epsilon_0 + \omega\epsilon_{rl}\epsilon_0} \quad (2-7)$$

The complex admittance is $Y^* = (\omega\epsilon_{rl} + j\omega\epsilon_r)\epsilon_0$

Where ϵ_{rl} relates to the energy loss because of attenuation and dispersion of the signal; ϵ_0 is the permittivity of the vacuum.

Relative permittivity is an essential and very important parameter in GPR and Induced Polarization (see Chapter 3) applications, as the relative permittivity partially determines the wave propagation velocity v and the penetration depth d

$$v_{propagation} = \frac{c}{\sqrt{\epsilon_r}} \quad (2-8)$$

$$d_{penetration} = v_{propagation} t \quad (2-9)$$

Where t the two-way travel is time of the reflected pulse signal and $c = 3 * 10^8$ m/s is the velocity of light in the vacuum.

The properties of relative permittivity and electrical conductivity in the context of DC or low frequency techniques are introduced in Chapter 3.

References

- [1] <http://www.standardsforhighways.co.uk/ha/standards/dmr/>(accessed within 2016-2019).
- [2] Standards for highways, <http://www.standardsforhighways.co.uk/ha/standards/> (accessed within 2016-2019).
- [3] M. Nunn, "Development of a more versatile approach to flexible and flexible composite pavement design: Prepared for Highways Agency," TRL Rep. TRL615, 2004. [Online]. Available: <https://trl.co.uk/reports/TRL615>
- [4] <https://trl.co.uk/reports/TRL630> (accessed within 2016-2019).
- [5] Design Manual for Roads and Bridges (DMRB), Volume 7: Pavement design (HD26/06), the Stationary Office, London, 2019. [Online]. Available: <http://www.standardsforhighways.co.uk/ha/standards/dmr/vol7/>
- [6] Design Manual for Roads and Bridges (DMRB), Volume 7, Section 3: maintenance assessment procedure (HD30/08), the Stationary Office, London, 2019. [Online]. Available: <http://www.standardsforhighways.co.uk/ha/standards/dmr/vol7/>
- [7] Design Manual for Roads and Bridges (DMRB), Volume 7, Section 5: pavement design (HD37/99), the Stationary Office, London, 2019. [Online]. Available: <http://www.standardsforhighways.co.uk/ha/standards/dmr/vol7/>
- [8] J.D. McNEILL, "Electromagnetic terrain conductivity measurement at low induction numbers," GEONICS LIMITED Technical Note TN-6, 1980.
- [9] G.R. Olhoeft, "Electrical properties of rocks and minerals with permittivity statics," U.S. Geological Survey, Denver, Colorado 80225, May. 1979, Open file report 79-993.
- [10] G.R. Olhoeft, "Low frequency electrical properties," in Geophysics, Vol. 50 (1985), pp. 2492-2503.
- [11] Y.S. TOULOUKIAN and W.R. JUDD, "Physical properties of rocks and minerals" in chapter 1 and chapter 9 of "*Data series on material properties*," New York, Washington 1970.
- [12] R.D. Evans, M. Frost, M.S. Jones and N. Dixon, "Assessment of the in-situ dielectrical constant of bituminous pavement materials," in Journal of the Transportation Research Board, 2037(2007), pp. 128-135.
- [13] Design Manual for Roads and Bridges (DMRB), Volume 7: Pavement Design and Construction, the Stationary Office, London, 2019. [Online]. Available: <http://www.standardsforhighways.co.uk/ha/standards/dmr/vol7/>
- [14] Design Manual for Roads and Bridges (DMRB), Volume 7, Section 3: Data for Pavement Assessment (HD29/08), the Stationary Office, London, 2019. [Online]. Available: <http://www.standardsforhighways.co.uk/ha/standards/dmr/vol7/>

- [15] W.M. Telford, L.P. Geldart, R.E. Sheriff and D.A. Keys, *Applied Geophysics*, Cambridge University Press, Cambridge, 1976.
- [16] S.S. Hubbard, J.E. Peterson, J. Roberts, R. Wobber, "Estimation of permeable pathways and water content using tomographic radar data," in *The Leading Edge*, Nov. 1997, pp. 1623-1628.
- [17] J.D. McNEILL, "Electromagnetic conductivity of soils and rocks," GEONICS LIMITED Technical Note TN-5, 1980.
- [18] T. R. Madden, "Random networks and mixing laws", *Geophysics*, Vol. 41, No. 6A, P. 1104-1125, 1976.
- [19] P. W. J. Glover, "A generalized Archie's law for n phases", *Geophysics*, Vol. 75, No. 6, P. E247-E265, 2010.
- [20] G. E. Archie, "The electrical resistivity log as an aid in determining some reservoir characteristics", *Transactions of the American Institute of Mechanical Engineers*, 146, 54-67, 1942.

CHAPTER 3

CURRENT INVESTIGATION TECHNIQUES FOR PAVEMENT EVALUATION

3.1 Non-Geophysical Techniques

Deflectography and use of the falling weight deflectometer (FWD) are two non-geophysical methods used for evaluating pavement strength or layer stiffness, according to the standard for highway construction in the UK [1]. Deflectography, a technique to estimate the structural condition of a flexible pavement, operates on the principle that the extension of the pavement's deflection reflects the pavement's strength. The pavement's deflection results from excessive traffic loads passing over the pavement. The deflection data is collected by beams installed on a survey vehicle moving at a slow speed. Such an operation has its own limitations; firstly, it largely depends on the temperature. Field surveys, obtained by the method of deflectography, have to be temporarily stopped if the rate-of-change of the temperature exceeds 2.5 degrees per hour. Secondly, drillings into the pavement are required to record the variation of the pavement's temperature before the survey. In previous chapters it was discussed that borehole drillings are not suitable for large area field surveys because of possible damage generated to the pavement.

Similar to deflectography, the falling weight deflectometer method works by measuring the deflection of the pavement relative to its stiffness. This method also measures the ability of the pavement to distribute traffic loads. Similar to the limitations of using deflectography, the falling weight deflectometer also requires temperature recording and prior coring into the pavements. Moreover, the measurements of the stiffness are critically influenced by the estimation of the layer thickness. An underestimate of the thickness of the bound layer results in an overestimate of the stiffness of that layer [2].

In summary, deflectography and the falling weight deflectometer have restricted applications for estimating the condition of a large area pavement because of their slow investigation speeds, their strict requirements on the necessary temperature recording and

the coring of the pavement. To achieve more accurate stiffness information, these techniques should be supplemented by using geophysical methods.

3.2 Geophysical Techniques on Pavements

Common geophysical evaluation methods for pavements including ground penetrating radar (GPR), impact echo (IE) and the seismic method are discussed by Wightman [3]. These methods are applied for the quality control of new pavements and the quality assessment or condition evaluation of old pavements. The condition of old pavements includes segregation into categories: hot mastic asphalt extent (by methods such as GPR, IE and acoustic ultrasonic); the moisture level (GPR); the detection of voids beneath the pavements (GPR and IE); crack detection (GPR); the location of the cavities (resistivity, GPR and seismic); and the structural changes (GPR, IE and seismic methods). Dielectric permittivity and electrical conductivity are stated as much better indicators and predictors for the physical properties of road aggregates and potential road problems according to surveys that have mainly been conducted at high frequency e.g. 500 MHz to 2.5 GHz [4]. This is because their natural properties reflect the arrangement of water molecules between ions dissociated from free water in materials and aggregate mineral surfaces. When an electromagnetic wave and field exists in a dielectric material, the energy travelling through the dielectric decreases as the wave propagates because of the ohmic losses, when the ratio of conduction current density to the displacement current density in a dielectric ($\frac{\sigma}{\omega\epsilon}$) is much larger than 1. Considering the general electrical properties of asphalt pavements and typical measurement frequencies, GPR is more sensitive to the dielectric permittivity of materials; whilst electromagnetic induction and the resistivity technique are primarily sensitive to the electrical conductivity of materials [4] [5] [6]. Three geophysical methods of GPR, electromagnetic induction, and resistivity, as used for pavement condition evaluation, are introduced in this chapter.

3.2.1 GPR

As a sensing and non-destructive technique, GPR [7] works on the principle that a transmitted electromagnetic pulsed signal would be partially reflected back to the receiver antenna from any interfaces between two layers which have a dielectric permittivity

contrast. The operating frequencies of GPR usually range from MHz to a few GHz. The penetration depth is a function of electrical conductivity and the dielectric constant of the materials. The higher the transmitted frequency that is applied, the higher the resolution of the sub-surface measurements, due to the increased bandwidth available from the antenna. However, the penetration depth inside the ground decreases with transmitted frequency. The penetration depth also decreases when the electrical conductivity of the ground increases.

The GPR geophysical method has been used for the condition estimation of pavements for over 30 years due to its high resolution, cost efficiency, rapid speed and efficient field surveys without traffic closure. Impulse GPR systems, frequency modulated continuous waveform (FMCW) GPR systems and stepped frequency continuous waveform (SFCW) GPR systems are used for applications ranging from environmental and agricultural monitoring, sedimentary study, civil engineering and landmine detection [8]. Since 1998, GPR has been developed for the assessment of pavement conditions as summarized in Table 4.

Table 4: The GPR applications on pavements [3] [4] [5] [6]

GPR technique	Bridge deck survey (1 GHz–1.5 GHz)		Since 1994
	Pavement design and quality control	Mix segregation detection	Since 1998
		Air-void content estimation	
		Layer thickness estimation	
		Subsurface defects detection	
		Base course quality	
	Pavement subgrade soil type assessment		Since 2000
Pavement base-course moisture assessment			

Earlier than the research published by Wightman [3], Saarenketo [4] conducted some GPR research on road evaluation including moisture level assessment. According to Saarenketo’s research on moisture impact on the base layer comprising unbound aggregate materials, it was said that water content is one of the most important factors affecting the strength and deformation properties of the base layer [4] [5] [6]. A few years later, Evan [9, page 9] reviewed the usage of GPR for moisture assessment of the sub-base of pavements stating that:

“Although GPR has an established application in monitoring sub-base moisture level, the ability of GPR to determine moisture in bound materials is less developed. Some work has been reported showing the ability of GPR to classify and interpret different subsurface reflections from asphalt layers containing a buried moisture barrier, depending on the presence of moisture within individual layers”.

When considering the detection of wetting patches in the wearing layer, Qadi’s practical research [10] pointed out that the three sub-layers (wearing layer, binder course and asphalt base) of the asphalt layer cannot be simply assumed as one homogeneous layer during GPR data interpretation, because of spurious reflections due to the overlap between reflections from the pavement surface and the wearing surface. Eight years later, Plati [11] discussed the GPR application for moisture evaluation of a hot mastic asphalt (HMA) pavement layer, with the assumption that a HMA pavement acts as a homogeneous layer. Hence, it is likely that the spurious reflections not only make it difficult to find the three sub-layer interfaces using GPR, but also adds difficulties in locating the possible reflections as a result of potential moisture patches within the asphalt layer.

3.2.2 Electromagnetic Induction

Electromagnetic (EM) induction, with its broadest range of geophysical applications e.g. mineral and hydrocarbon exploration, is one method of measuring the electrical conductivity of the sub-surface media. Electromagnetic methods are categorized into passive (e.g. magnetic-telluric techniques) or active methods, depending on whether an extra transmitting source is included. The basic principle of an active electromagnetic technique is to induce an electromagnetic field which is composed of two orthogonal vector components (an electric field **E** and a magnetic force **H**) in a plane perpendicular to the wave propagation direction.

Application of Maxwell’s equations in a dielectric material layer yields [12]:

$$\nabla \cdot E = \frac{\rho_{free}}{\epsilon'} \quad (3-1)$$

$$\nabla \times E = -\frac{\partial B}{\partial t} \quad (3-2)$$

$$\nabla \cdot B = 0 \quad (3-3)$$

$$\nabla \times B = \mu' \sigma E + \mu' \varepsilon' \frac{\partial E}{\partial t} \quad (3-4)$$

Where

ρ_{free} is free charge density; μ' is real permeability of materials; E is electric field strength; B is magnetic field strength; $\mu_0 = 4\pi * 10^{-7} \text{N/A}^2$

Substituting the free current within the continuity equation

$$\nabla \cdot J_{free} = -\frac{\partial \rho_{free}}{\partial t} \quad (3-5)$$

Together with Gauss's law and Ohm's law

$$\frac{\partial \rho_{free}}{\partial t} = -\nabla \cdot (\sigma E) = -\sigma (\nabla \cdot E) = -\sigma \frac{\rho_{free}}{\varepsilon'} \quad (3-6)$$

The solution of this equation is:

$$\rho_{free} = e^{-\left(\frac{\sigma}{\varepsilon'}\right)t} \rho_{free}(0) \quad (3-7)$$

Where $\rho_{free}(0)$ is the initial free charge density;

From this solution, we can see that the free charge density is going to dissipate in a characteristic time which equals to $\frac{\varepsilon'}{\sigma}$. And after a while, the free charge density will be attenuated to zero. So the Maxwell equations become

$$\nabla \cdot E = 0 \quad (3-8)$$

$$\nabla \times E = -\frac{\partial B}{\partial t} \quad (3-9)$$

$$\nabla \cdot B = 0 \quad (3-10)$$

$$\nabla \times B = \mu' \sigma E + \mu' \varepsilon' \frac{\partial E}{\partial t} \quad (3-11)$$

Apply the curl operations on (3-9) and (3-11), the equations become

$$\nabla^2 E = \mu' \sigma \frac{\partial E}{\partial t} + \mu' \varepsilon' \frac{\partial}{\partial t} \left(\frac{\partial E}{\partial t} \right) \quad (3-12)$$

$$\nabla^2 B = \mu' \sigma \frac{\partial B}{\partial t} + \mu' \varepsilon' \frac{\partial}{\partial t} \left(\frac{\partial B}{\partial t} \right) \quad (3-13)$$

The solutions of these two curl-curl equations are:

$$E(x, t) = E_0 e^{i(kx - \omega t)} \quad (3-14)$$

$$B(x, t) = B_0 e^{i(kx - \omega t)} \quad (3-15)$$

Where k is the wave number and it is described by

$$k^2 = i\mu' \sigma \omega + \mu' \varepsilon' \omega^2 \quad (3-16)$$

$$k = k_+ + ik_- \quad (3-17)$$

Now replacing k with a complex form, we get

$$E(x, t) = E_0 e^{i(k_+ x - \omega t) - k_- x} \quad (3-18)$$

$$B(x, t) = B_0 e^{i(k_+ x - \omega t) - k_- x} \quad (3-19)$$

From these two equations, we see there is an attenuation component caused by the imaginary part of wave number k_- .

According to the electric skin depth definition, when $x = \frac{1}{k_-}$, the electric field and magnetism field amplitudes are reduced by a factor of $\frac{1}{e}$. Denote the skin depth using d

$$d = \frac{1}{k_-} \quad (3-20)$$

The physical meaning of skin depth is related to the depth that the electromagnetic wave can pass through the material.

Then we can solve for the real part and the imaginary part of the wave number

$$k_+ = \omega \sqrt{\frac{\mu' \epsilon'}{2}} \left[\sqrt{1 + \left(\frac{\sigma}{\omega \epsilon'}\right)^2} + 1 \right]^{1/2} \quad (3-21)$$

$$k_- = \omega \sqrt{\frac{\mu' \epsilon'}{2}} \left[\sqrt{1 + \left(\frac{\sigma}{\omega \epsilon'}\right)^2} - 1 \right]^{1/2} \quad (3-22)$$

The attenuation of the electromagnetic wave amplitude in the distance *dis* of the medium is given by

$$Atten[dB] = 20k_- * dis * \log(e) \quad (3-23)$$

We could see that the higher the frequency, the higher the attenuation and the smaller the penetration depth.

So the imaginary part of wave number influences the skin depth, whilst the real part determines the wavelength

$$\lambda = \frac{2\pi}{k_+} \quad (3-24)$$

And the propagation speed *v*

$$v = \lambda f = \frac{2\pi}{k_+} * f = \frac{\omega}{k_+} \quad (3-25)$$

If a very low frequency is applied such that $\sigma \gg \omega \epsilon'$ then $k_+ \cong k_- = \sqrt{\frac{\sigma \omega \mu'}{2}}$. This means that the electrical conductivity becomes the dominant factor instead of the dielectric permittivity, and

$$\lambda = \frac{2\pi}{k_+} \approx \frac{2\pi}{k_-} \equiv \frac{2\pi}{\frac{1}{d}} = 2\pi d \quad (3-26)$$

If a very high frequency is applied such that $\sigma \ll \omega \epsilon'$ then the dielectric permittivity becomes the dominant factor rather than electrical conductivity.

The electromagnetic field is induced using a small coil or a large loop of wire depending on the application. The received response is caused by the induced drift of mobile charges within the ground media, acting as a secondary source of the electromagnetic field. Neither bound charges confined to individual atoms, nor mobile charges trapped at material interfaces, make any significant contribution to the electromagnetic induction response [13]. During the late twentieth century, electromagnetic methods used in shallow-surface geophysical applications developed rapidly because of the available accuracy in detecting conductivity variations of as little as 3%, and its effective sensitivity to clay content, porosity and fluid type [13] [14] [15] [16]. In research that used a roller-mountable microwave asphalt pavement density sensor, Jaselskis [17] studied the dielectric properties of asphalt pavement samples with different densities, when the operating frequencies ranged from 100 Hz to 12 GHz. For comparison, the penetration depth of the microwave signal in an asphalt pavement is about 12-14 cm at an operating frequency of 8 GHz and only about 4 cm at a frequency of 30 GHz. It was found that the permittivity and loss factor are strongly frequency-dependent when the operating frequency is less than 10 MHz. Whilst at microwave frequencies e.g. 8 GHz to 12 GHz, both permittivity and loss are almost independent of the frequency because of electronic and atomic polarization mechanisms. Electronic polarization is a result of the movements of the electrons and the distorted paths of the electrons against the direction of an applied external electric field. Atomic polarization arises because of a relative change in the mean positions of the atomic nuclei within the molecules when an external electric field is applied. Moisture level strongly influences the permittivity and the loss factor at low frequencies; whereas water content only slightly affects electrical permittivity in the microwave frequency region. Different materials within the pavement with different water content values could have the same electrical permittivity or electrical conductivity at very high operating frequencies.

3.2.3 Electrical Techniques

Electrical techniques have been most commonly applied to the measurement of earth resistivity since the development of conventional DC resistivity methods in the early 1900s. They have been developed to support applications including groundwater monitoring, subsurface condition surveys and archaeology mapping. Electrical techniques normally include: DC (or AC with a very low operating frequency) resistivity methods; their extended methods such as capacitive resistivity technique; and induced polarisation methods. Considering the nature of electrical techniques to conduct electric current through pavement aggregates, the three categories of electronic conduction, dielectric conduction and electrolytic conduction are to be covered. Electronic conduction usually occurs within very conductive materials (e.g. copper) with the current applied by the rapid movement of electrons. Dielectric conduction generally occurs on poorly conductive materials or even insulators, by the shift of bound charges, which becomes dominant when a capacitive resistivity technique is applied to the wearing course condition assessment of the pavements. Electrolytic conduction is a predominant method of electric current conduction in most pavement aggregate materials, with fluids contained in voids acting as the electrolyte when conventional DC resistivity methods are applied. The current relates to the movement of ions, their type and their concentration in the electrolyte [18].

3.2.3.1 Induced Polarisation Methods

The induced polarisation (IP) method, typically operating at a frequency from a few hertz to 1 kHz, is categorized into a time-domain-induced polarization method and a frequency-domain-induced polarization method (SIP). Time-domain IP methods measure the resulting voltage after the turn-off of a current injection signal; while SIP injects alternating currents (AC) to induce electric charges into the subsurface with the resulting voltage and apparent conductivity measured at different AC frequencies. The IP methods are used to identify electrical chargeability through the pore-water-mineral interface of sub-surface materials [19] [20]. The SIP has been widely used in applications of hydrogeological and environmental, hydrogeology [21]; bio-geophysics [22]; minerals and environments; and biological and geophysical [20] [21] investigations. The fluid-flow characteristics of rocks, fluid content and fluid chemistry are of major interest. The SIP is

also called a complex resistivity technique, as a polarization mechanism in the sub-surface materials produces energy loss and storage mechanisms that form both real and imaginary parts of a measured impedance. This technique is developed from DC resistivity methods and shares the field implementation of an electrical resistivity technique (ERT). Four polarization mechanisms exist: Maxwell-Wagner interfacial, dipole, ionic and electronic. A significant contribution to a low-frequency phenomenon in asphalt samples is that of the Maxwell-Wagner interfacial polarization [24] [25]. The bound charges are confined to individual atoms, and the mobile charges trapped at a material interface are causes of interfacial and orientation polarisations, which occur at low frequencies of less than 1 MHz [26]. Tabbagh [19] discussed Maxwell-Wagner interfacial polarisation effects in clayey materials using laboratory tests and SIP methods at operating frequencies from 1 kHz to 1 MHz, and modelled the Maxwell-Wagner effect in heterogeneous media. It was also pointed out that dielectric permittivity is more sensitive to platelet roughness than electrical conductivity. Therefore, electrical conductivity is a more reliable indicator in predicting wetting patches inside pavements as it is less sensitive to the roughness of the particles. For low frequencies less than 1 kHz, it was reported by Revil [27] that effective permittivity is at least six-to-eight orders of magnitude larger than the dielectric permittivity of materials measured at high frequencies, because of electrochemical effects.

3.2.3.2 Electrical Resistivity Techniques

Traditional electrical resistivity techniques emerged from DC/AC resistivity methods. The principle of DC/AC resistivity methods is based on two installed current electrodes used to transmit a current into the ground and a pair of moveable potential electrodes on the surface of the ground to measure the voltage. The first utilization of electrical methods was tried on Cornish copper mines by Robert W. Fox. (1830). Decades later, Dr. Carl Barus (1882) conducted experiments which showed the prospection of applying the electrical method for hidden sulphide ores [48]. A few years later, Schlumberger (1912, 1920) and Wenner (1912) developed this idea to four moveable electrodes in a similar operation principle but in different electrode array configurations [28] [29]. An electrical resistivity 2D imaging survey, developed from the research of Schlumberger and Wenner, was conducted in a field survey in Southampton (Figure 3). Current sources C1 and C2 were inserted into the soil and placed at two ends of a variable length array to transmit a current into the grass

land. Meanwhile, other electrodes acted as potential receivers to measure the potentials of the grass land media. The investigation depth varied as the separation between the two current injection electrodes changed. The transmitted current and the received potential values were sampled, processed and stored on a laptop computer.

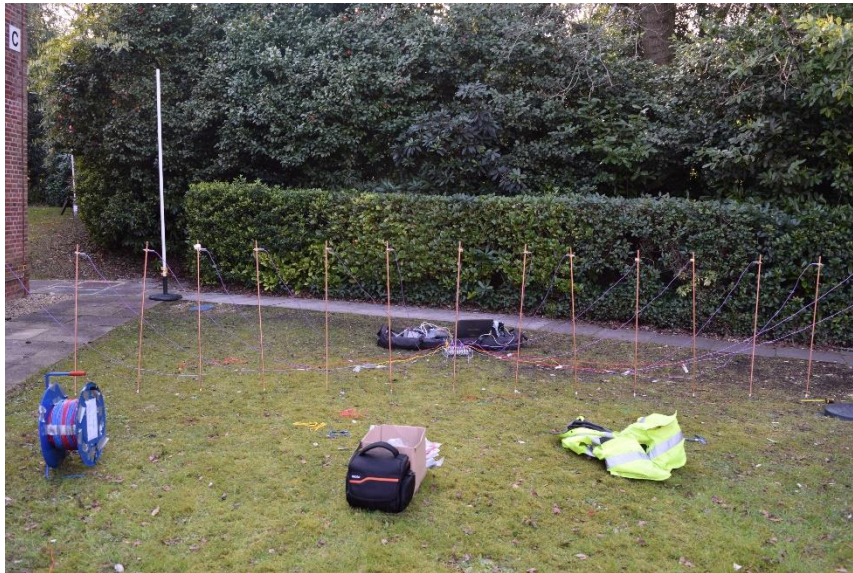


Figure 3: A 2D field survey conducted adjacent to a car park of Southampton University in 2015 [Photo: Author private archive]

Considering the hardness of the asphalt pavement surface, non-contact potential sensors were used instead of inserting into the ground. This is illustrated in Figure 4 and Figure 5.

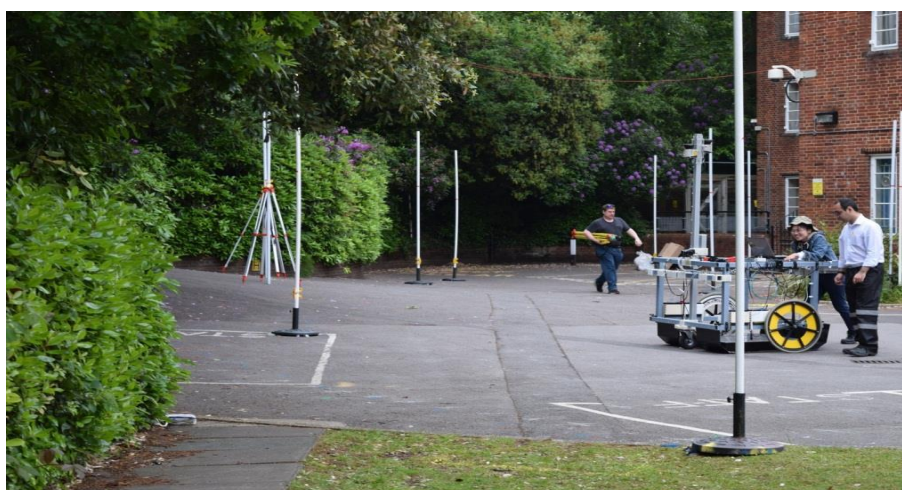


Figure 4: A 3D field survey in a car park of Southampton University using AC resistivity methods in 2015 [Photo: Author private archive]

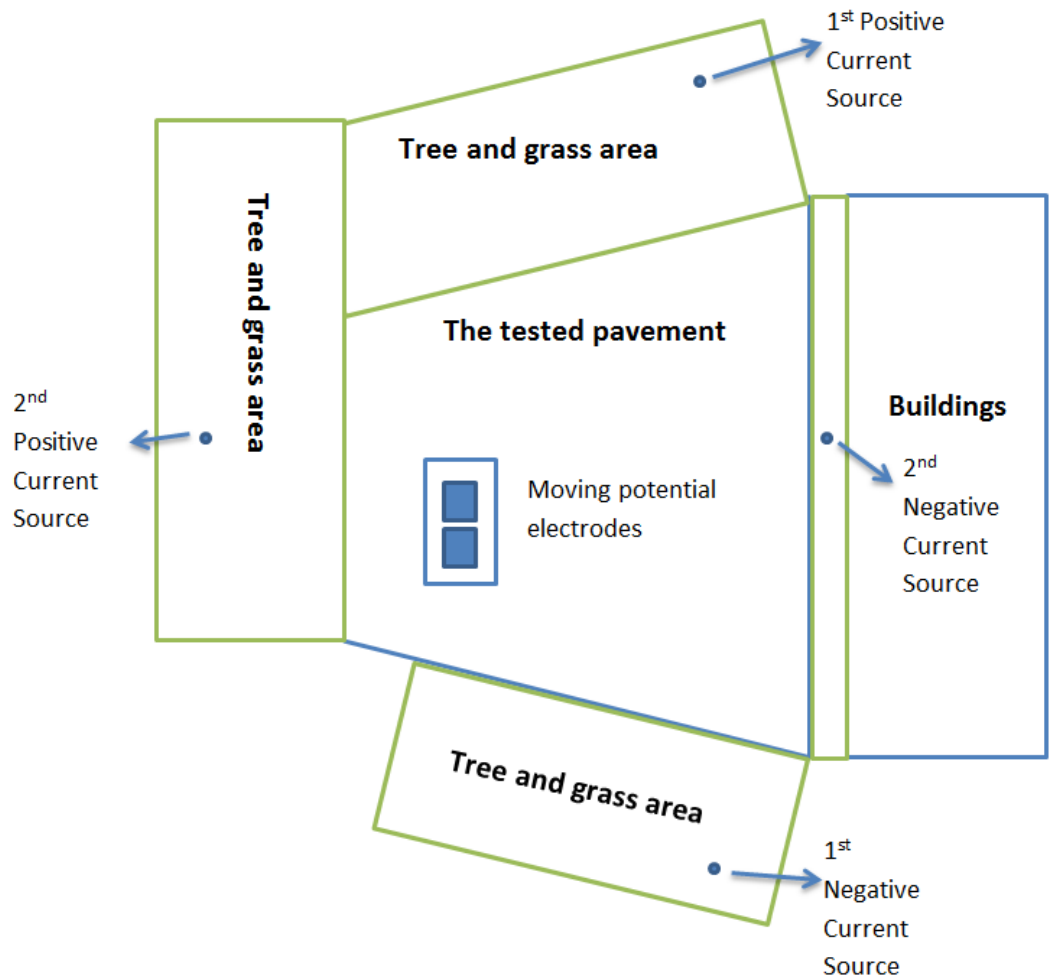


Figure 5: A sketch of the field survey in a car park of Southampton University using AC resistivity methods in 2015

Figure 4 shows a field survey conducted at Southampton University applying a low-frequency AC resistivity technique with its operation principle sketched in Figure 5. Two pairs of current sources (Current1 and Current2 in Figure 5) were implanted into soil areas outside the pavement section to transmit current signals into the ground. These two current sources operate at different frequencies to permit simultaneous surveying with different electrode geometries. A set of two movable potential electrodes, as illustrated in Figure 5, was integrated onto a manually controlled system to measure the induced surface voltages of the pavement media between pairs of potential electrodes.

With 3D modelling and data interpretation (e.g. an open source like RESINV3D, MATLAB package, or BERT), electrical resistivity of materials could be interpreted by an iterative algorithm. The depth of an investigation depends on the electrical resistivity of the earth

material, electrode array configuration and electrode spread. The penetrating depth is expected to increase if the electrode spacing is larger. To apply such traditional electrical resistivity techniques, surface hardness and galvanic contact resistance have to be considered. Regarding the hardness of pavement surfaces, it is difficult to manually insert electrodes into the pavements. Even if insertions can be undertaken, such activities would cause damage to the pavement structure thus requiring rehabilitation. Furthermore, as the pavement materials generally have high resistivity, higher contact resistance between electrodes and their surrounding pavement media would exist. To avoid these limitations, current electrodes were implanted into soil areas surrounding the pavement. This method generates poor spatial resolution mapping and it is not good for the condition evaluation of the shallow layer (e.g. the asphalt layer).

The estimated resistance R (with units of Ω) is obtained by a division of the measured voltage by the measured current, corrected by a geometric factor. Different surveys usually utilise different electrode array configurations (e.g. Wenner [28]; Schlumberger [29]; pole-dipole, and dipole-dipole), which have impacts on the prediction of the electrical resistivity. The geometric factor k is defined as a parameter used to describe the geometric relationship between electrical resistance and electrical resistivity ρ (with units of $\Omega \cdot \text{m}$).

$$\rho = kR \tag{3-27}$$

Before discussing the derivation of the geometric factor in a complex electrode array configuration, a simple case of a current electrode, implanted on a single and homogeneous layer, is studied to provide some theoretical foundation. Its current flow and potential distribution are modelled by a classical field-plotting iterative method [30] on a surface of a hemisphere using MATLAB. They are illustrated in Figure 6 and Figure 7. Meanwhile, some analysis will be conducted to achieve the geometric factor for this case.

An assumption is made that the resistivity of the homogeneous earth is ρ_{homo} ; the voltage at the centre point is V ; the voltage difference between each two points is defined by δV ; the current density is J ; the electric field strength is given by E ; the injected current is I ; and the distance from the centre current source to the measured location is r . The 2D

models are implemented using MATLAB with the results displayed in Figure 6 and Figure 7 and give us a basic understanding of how the current flows and what the potential distribution looks like. For the modelling of the electric field and potential distribution of the point source shown in Figure 6 and Figure 7, the voltage at the centre point is assumed as 3 V; The 2D space is divided into 301 meshes in both X and Y directions. The initial electric field, potentials and charges are assumed as zero. The boundary conditions are given by equations (3-41) to (3-44).

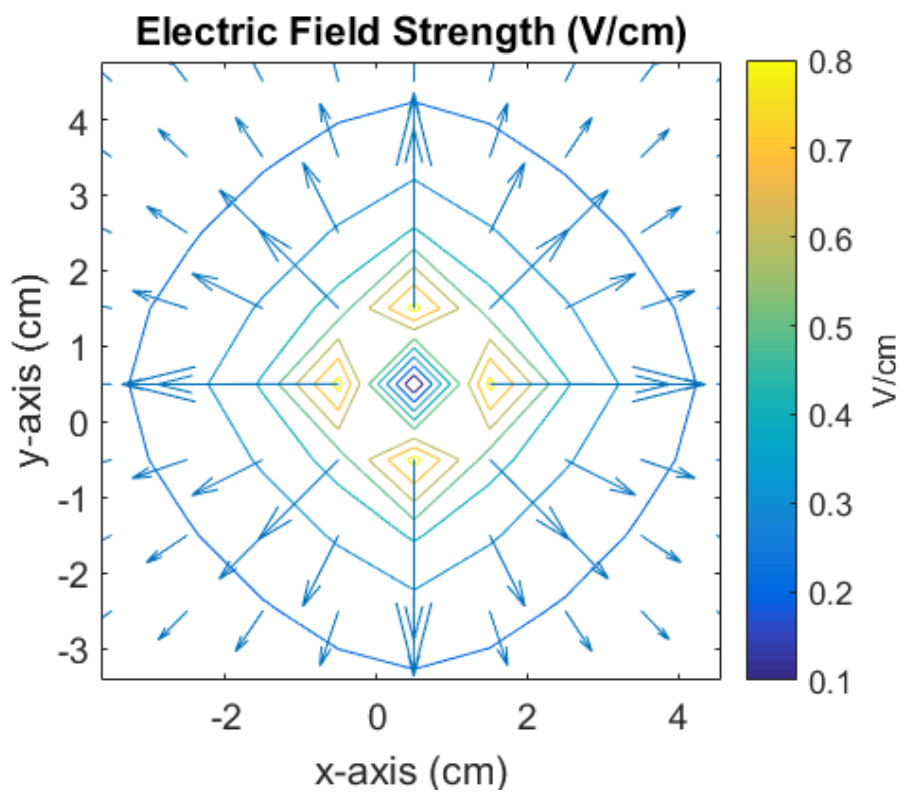


Figure 6: Electric field strength of point source electrode at the surface of the homogeneous earth

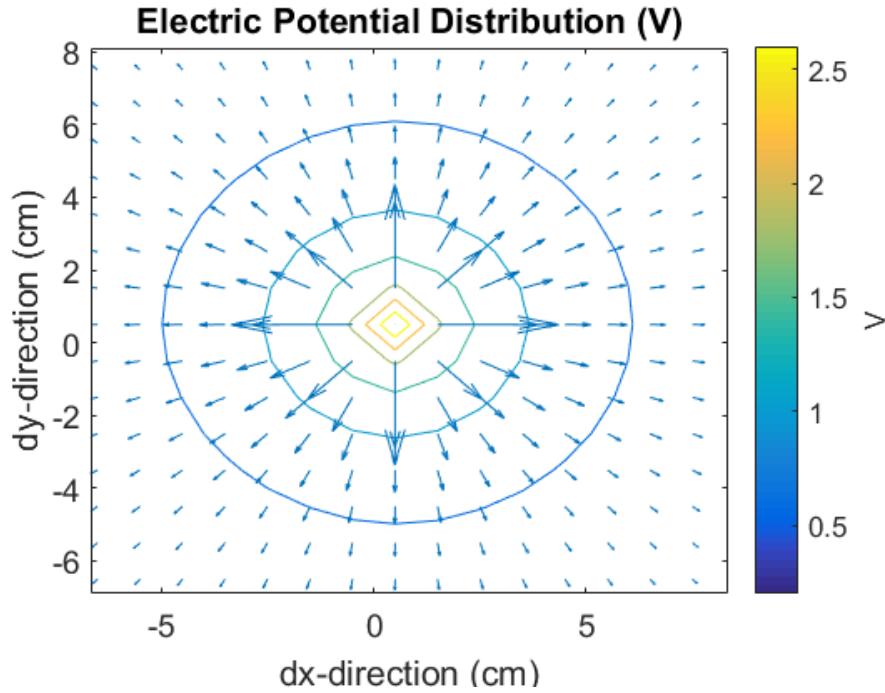


Figure 7: Electric potential distribution (2D) of point source electrode at the surface of the homogeneous earth

Note: A singularity exists in the centre of the diagrams. In Figure 6 and Figure 7, the electric field vectors originate from the centre point. The intensity of the electric field decreases towards the edges of the figure. The circles represent the equipotential positions. It is seen from the figures that the electric field strength and the potential distribution decrease from the centre source to the outside locations.

The potential distribution and electric field result from the analytical modelling method, using a finite element method and an iterative algorithm [30], which is introduced below.

As a vector field $E = -\nabla V = -\left(\frac{\partial V}{\partial x}, \frac{\partial V}{\partial y}\right)$, in order to model the electric field, the potential distribution in 2D form in the X and Y directions is calculated. The space surrounding the central source is divided into meshes with the length of each mesh as Δh in both the X and Y directions. It is assumed that the internal region within the electric field is charge-free and the dielectric constant of this region is homogeneous. Then,

$$\nabla \cdot D = 0 \quad (3-28)$$

By Gauss' law

$$\nabla \cdot E = \frac{\rho_{free}}{\epsilon'} \quad (3-29)$$

Under the assumption of charge-free, Gauss' law becomes:

$$\nabla \cdot E = 0 \quad (3-30)$$

Replacing equation (3-30) with the derivative forms, it becomes:

$$\frac{\partial E}{\partial x} + \frac{\partial E}{\partial y} = 0 \quad (3-31)$$

Replace E by $-\nabla V$:

$$\frac{\partial}{\partial x} \left(\frac{\partial V}{\partial x} \right) + \frac{\partial}{\partial y} \left(\frac{\partial V}{\partial y} \right) = 0 \quad (3-32)$$

According to the mathematical definition of the partial derivative, the partial derivatives of the potentials on the x-direction at points a and c approximately equal to:

$$\left. \frac{\partial V}{\partial x} \right|_{x=a, \Delta h \rightarrow 0} \cong \frac{V_1 - V_0}{\Delta h} \quad (3-33)$$

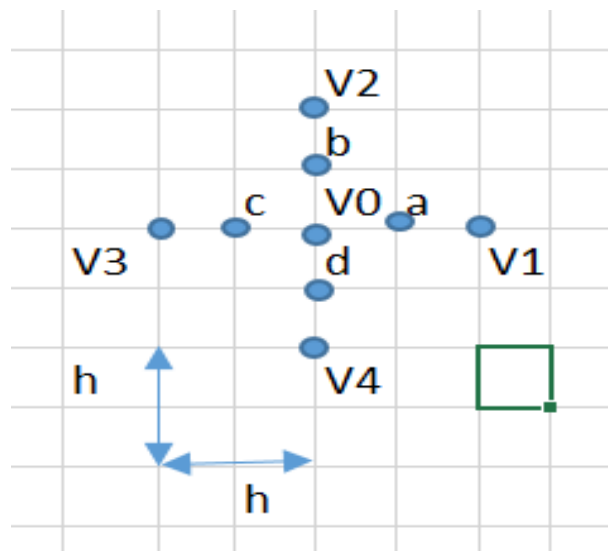


Figure 8: Potential distributions of a simple case: a single current electrode implanted on homogeneous earth

Note: V_0 in the centre location is the voltage source of value 3 V; V_1 , V_2 , V_3 and V_4 are potentials of points surrounding the centre source with radial separation $2 * \Delta h$; a , b , c and d represent the points in the X and Y directions with radial separation Δh ;

And

$$\left. \frac{\partial V}{\partial x} \right|_{x=c, \Delta h \rightarrow 0} \cong \frac{V_0 - V_3}{\Delta h} \quad (3-34)$$

So, the second partial derivative of the potential at the centre point can be solved by applying the first partial derivatives of the potential at node a and c . It is given by:

$$\left. \frac{\partial}{\partial x} \left(\frac{\partial V}{\partial x} \right) \right|_{X_{centre, \Delta h \rightarrow 0}} = \frac{\left. \frac{\partial V}{\partial x} \right|_{x=a, \Delta h \rightarrow 0} - \left. \frac{\partial V}{\partial x} \right|_{x=c, \Delta h \rightarrow 0}}{\Delta h} \quad (3-35)$$

Then substitute the partial derivatives using the approximation equation (3-33) and equation (3-34)

$$\left. \frac{\partial}{\partial x} \left(\frac{\partial V}{\partial x} \right) \right|_{X_{centre, \Delta h \rightarrow 0}} = \frac{\frac{V_1 - V_0}{\Delta h} - \frac{V_0 - V_3}{\Delta h}}{\Delta h} = \frac{V_1 - V_0 - V_0 + V_3}{\Delta h^2} \quad (3-36)$$

$$\left. \frac{\partial}{\partial y} \left(\frac{\partial V}{\partial y} \right) \right|_{Y_{centre, \Delta h \rightarrow 0}} = \frac{\frac{V_2 - V_0}{\Delta h} - \frac{V_0 - V_4}{\Delta h}}{\Delta h} = \frac{V_2 - V_0 - V_0 + V_4}{\Delta h^2} \quad (3-37)$$

Hence, equation (3-32) turns into

$$\frac{V_1 + V_3 + V_2 + V_4 - 4V_0}{\Delta h^2} = 0 \quad (3-38)$$

This yields:

$$V_0 = \frac{V_1 + V_2 + V_3 + V_4}{4} \quad (3-39)$$

Similarly, we could derive the potential distribution of a 3D situation

$$V_0 = \frac{V_1 + V_2 + V_3 + V_4 + V_5 + V_6}{6} \quad (3-40)$$

Applying boundary conditions that:

$$V_{-\infty(x)} = 0 \quad (3-41)$$

$$V_{+\infty(x)} = 0 \quad (3-42)$$

$$V_{-\infty}(y) = 0 \quad (3-43)$$

$$V_{+\infty}(y) = 0 \quad (3-44)$$

Where $V_{-\infty}(x)$, $V_{+\infty}(x)$, $V_{-\infty}(y)$, and $V_{+\infty}(y)$ are potentials at infinite positions with X and Y coordinates; X_{centre} and Y_{centre} are the positions of the central point source on X and Y coordinates.

Finally, applying equation (3-39) or equation (3-40) with boundary conditions in an iterative algorithm, the 2D or 3D potential distribution of the central source in homogeneous earth is estimated and displayed in Figure 7.

The Calculation of Geometric Factor

According to the definition of electric field strength $E = -\nabla V = -\left(\frac{\partial V}{\partial x}, \frac{\partial V}{\partial y}\right)$, and Ohm's

Law $J = E \sigma_{homoo}$ such that $E = J \rho_{homoo}$,

$$E = -\frac{\delta V}{\delta r} = J \rho_{homoo} \quad (3-45)$$

The current density is defined as the electric current per cross-sectional area at a given point:

$$J = \frac{I}{2\pi r^2} \quad (3-46)$$

Hence,

$$\frac{\delta V}{\delta r} = -\frac{I \rho_{homoo}}{2\pi r^2} \quad (3-47)$$

Through integration, the potential at a point at a distance of r from the centre point is given by

$$V = -\int_{r1}^{r2} \frac{I \rho_{homoo}}{2\pi r^2} dr = \frac{I \rho_{homoo}}{2\pi r1} - \frac{I \rho_{homoo}}{2\pi r2} \quad (3-48)$$

When the other electrode is at a location with infinite radial distance ($r_2 = \infty$) from the centre point source (as the example discussed above)

$$\rho_{homo} = \frac{2\pi V r_1}{I} = 2\pi r_1 R \quad (3-49)$$

So, the geometric factor for this single electrode (the other electrode is assumed to be placed infinitely far away from that electrode) on the surface of a homogeneous layer is

$$k_{pole-pole} = 2\pi r_1 \quad (3-50)$$

Pole-Dipole Configuration

The previous example (equation 3-50) can be recognized as a pole-pole configuration with one current source electrode placed in the centre and the other electrode acting as a potential electrode (the word pole in this thesis means a point-electrode which is inserted into the ground or the earth; a dipole means the combination of a positive and a negative point-electrodes that are inserted into the earth). The pole-dipole configuration is developed from the pole-pole case: electrode C1 acts as a current source and the other two electrodes P1 and P2 act as potential receivers (e.g. P1 is the positive electrode and P2 is the negative one). An illustrative diagram is given in Figure 9.

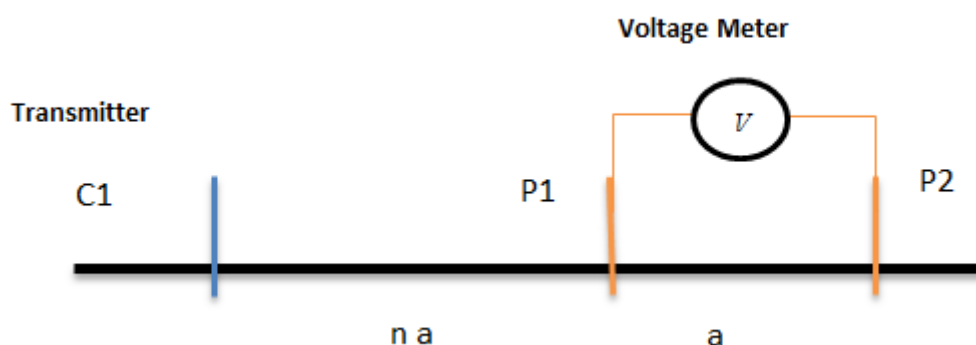


Figure 9: Sketch of a pole-dipole configuration

Note: C1 is the current source electrode inserted into the earth; C1 would have the electric field illustrated in Figure 6 but in 3D formation; According to the equipotential lines shown

in Figure 7, positive and negative electrodes P1 and P2 would have the potentials corresponding to their equipotential lines; a is the separation between the two potential electrodes; n is a constant representing how many times larger the spacing is between C1 and P1 compared to the separation between the potential electrodes.

Based on previous knowledge, the potentials at P1 and P2 are

$$V_{p1} = \frac{I \rho_{homo}}{2\pi n a} \quad (3-51)$$

$$V_{p2} = \frac{I \rho_{homo}}{2\pi(n+1)a} \quad (3-52)$$

Therefore,

$$V = V_{P1} - V_{P2} = \frac{I \rho_{homo}}{2\pi a} \left[\frac{1}{n} - \frac{1}{n+1} \right] \quad (3-53)$$

The geometric factor of a pole-dipole configuration in homogeneous earth is

$$k_{\text{pole-dipole}} = 2\pi a n(n + 1) \quad (3-54)$$

Wenner Configuration

The Wenner electrode configuration is illustrated by a diagram in Figure 10 indicating that two electrodes C1 and C2 act as current sources and the other two electrodes P1 and P2 are potential receivers. The separation between neighbouring electrodes is a . In this example, C1, C2, P1 and P2 are electrodes inserted into the earth.

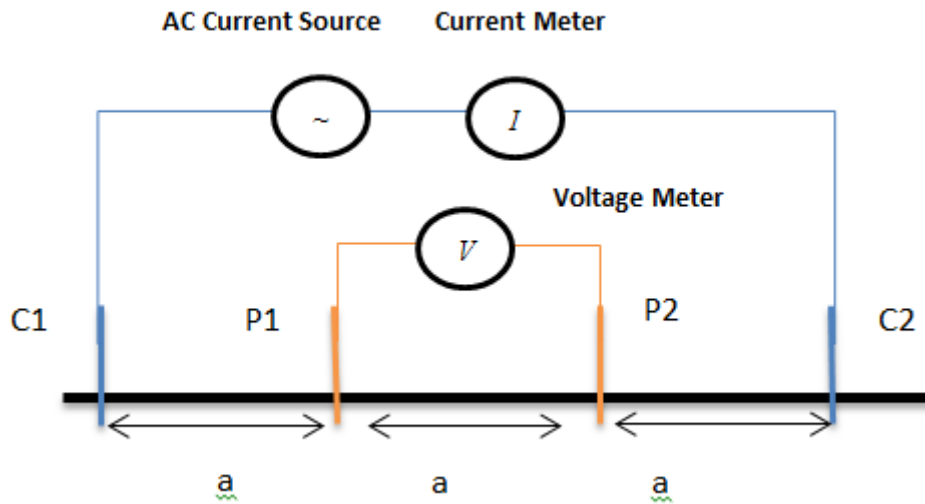


Figure 10: Sketch of the Wenner configuration

Note: the transmitted current is generated by the AC current source and it is recorded by the current meter. A voltage meter is used to record the voltage of the media.

The potentials at P1 and P2 are respectively given by

$$V_{p1} = \frac{I \rho_{homo}}{2\pi a} - \frac{I \rho_{homo}}{2\pi 2a} \quad (3-55)$$

$$V_{p2} = \frac{I \rho_{homo}}{2\pi 2a} - \frac{I \rho_{homo}}{2\pi a} \quad (3-56)$$

Therefore,

$$V = V_{P1} - V_{P2} = \frac{I \rho_{homo}}{2\pi a} \quad (3-57)$$

$$k_{Wenner} = 2\pi a \quad (3-58)$$

All discussions above assume the condition of an infinite earth. However, additional correction factors also have to be considered for the case of finite depth layers. It should be noted that these correction factors will vary with different layer thicknesses. When a thick homogeneous layer is considered, the correction factor of a Wenner array is:

$$K_{thick} = f_{thick} \left(\frac{thickness}{a} \right) k_{Wenner} \quad (3-59)$$

For a thin homogeneous layer $\frac{\text{thickness}}{a} \leq 0.5$

$$K_{thin} = 4.5324 \text{ thickness } f_{thin} \left(\frac{\text{thickness}}{a} \right) \quad (3-60)$$

Where $f_{thick} \left(\frac{\text{thickness}}{a} \right)$ and $f_{thin} \left(\frac{\text{thickness}}{a} \right)$ are correction factors related to the ratio of the thickness and the electrode separation, as listed by Topsoe [31].

Schlumberger

An illustrative diagram, describing the Schlumberger electrode configuration, is given in Figure 11. Similar to the Wenner configuration, two electrodes, C1 and C2, act as current sources and the other two electrodes, P1 and P2, act as potential receivers. All these electrodes in this example are inserted into the earth. The spacing between the current electrode and the potential electrode is n times the separation of a between the two potential electrodes (n is much larger than 1). Though the Schlumberger configuration includes the Wenner configuration when n equals to 1, in geophysics, the Wenner configuration is separately introduced, possibly because these two configurations were developed by two researchers at approximately the same time.

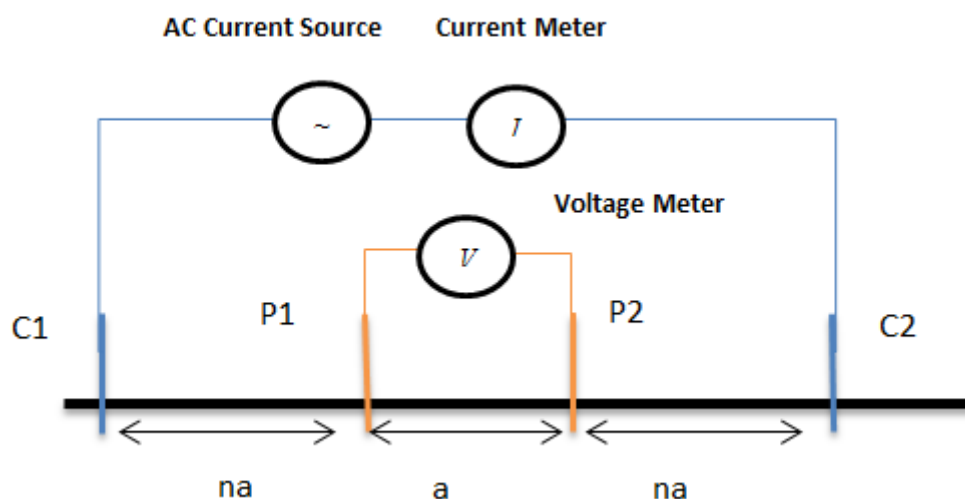


Figure 11: Sketch of the Schlumberger configuration

The potentials at electrode P1 and electrode P2 are respectively given by

$$V_{p1} = \frac{I \rho_{homo}}{2\pi n a} - \frac{I \rho_{homo}}{2\pi(n+1)a} \quad (3-61)$$

$$V_{p2} = \frac{I \rho_{homo}}{2\pi(n+1)a} - \frac{I \rho_{homo}}{2\pi n a} \quad (3-62)$$

Therefore,

$$V = V_{P1} - V_{P2} = \frac{I \rho_{homo}}{\pi a n(n+1)} \quad (3-63)$$

$$k_{Schlumberger} = \pi a n(n+1) \quad (3-64)$$

Dipole-Dipole Configuration

Two electrodes, C1 and C2, act as current sources and the other two electrodes, P1 and P2, act as potential receivers. Here, the C1 is the positive electrode and the C2 is assumed as the negative electrode; P1 is assumed as the positive potential electrode and the P2 is assumed as the negative potential electrode. The current electrodes and potential electrodes are usually separated by a large distance compared to their individual separations, as illustrated in Figure 12.

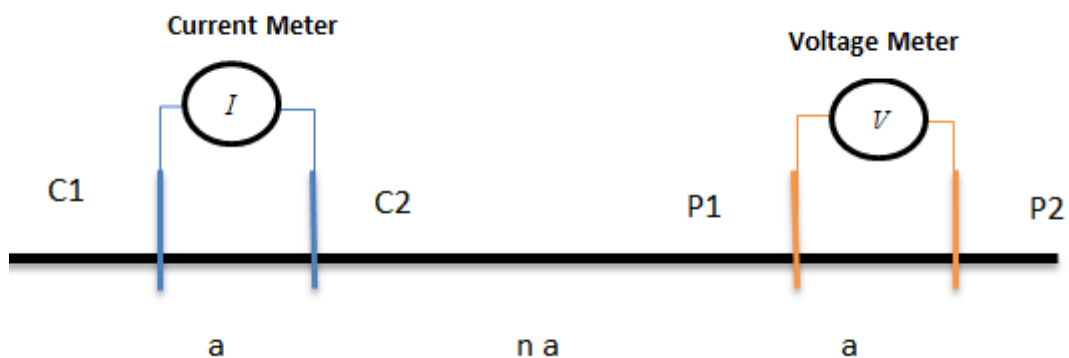


Figure 12: Sketch of dipole-dipole configuration

Note: a is the separation of current sources and potential electrodes; n represents the multiplication factor which is much larger than 1. The current meter is used to record the transmitted current and the voltage meter is used to record the voltage of the media.

The potentials at electrode P1 and electrode P2 are given by

$$V_{p1} = \frac{I \rho_{homo}}{2\pi n a} - \frac{I \rho_{homo}}{2\pi(n+1)a} \quad (3-65)$$

$$V_{p2} = \frac{I \rho_{homo}}{2\pi(n+1)a} - \frac{I \rho_{homo}}{2\pi(n+2)a} \quad (3-66)$$

Therefore,

$$V = V_{P1} - V_{P2} = \frac{I \rho_{homo}}{2\pi a} \left(\frac{1}{n} - \frac{2}{n+1} + \frac{1}{n+2} \right) = \frac{I \rho_{homo}}{\pi a n(n+1)(n+2)} \quad (3-67)$$

$$k_{dipole-dipole} = \pi a n(n+1)(n+2) \quad (3-68)$$

Line Electrode in Wenner Configuration

Considering that the free charge density dissipates to the edges of plate electrodes after a characteristic time, it was thought that it may be possible to assume plate electrodes may be modelled as line electrodes to reflect the geometric factors of plate electrodes in a Wenner configuration. Hence, a line electrode case was studied. An illustrative diagram of this configuration is given in Figure 13. A current, generated by the AC current source, passes through two conducting lines, C1 and C2; while two potential electrodes, P1 and P2, are placed in any positions between the two current conducting lines. In a Wenner configuration, all electrode separations are exactly the same which is of the value a .

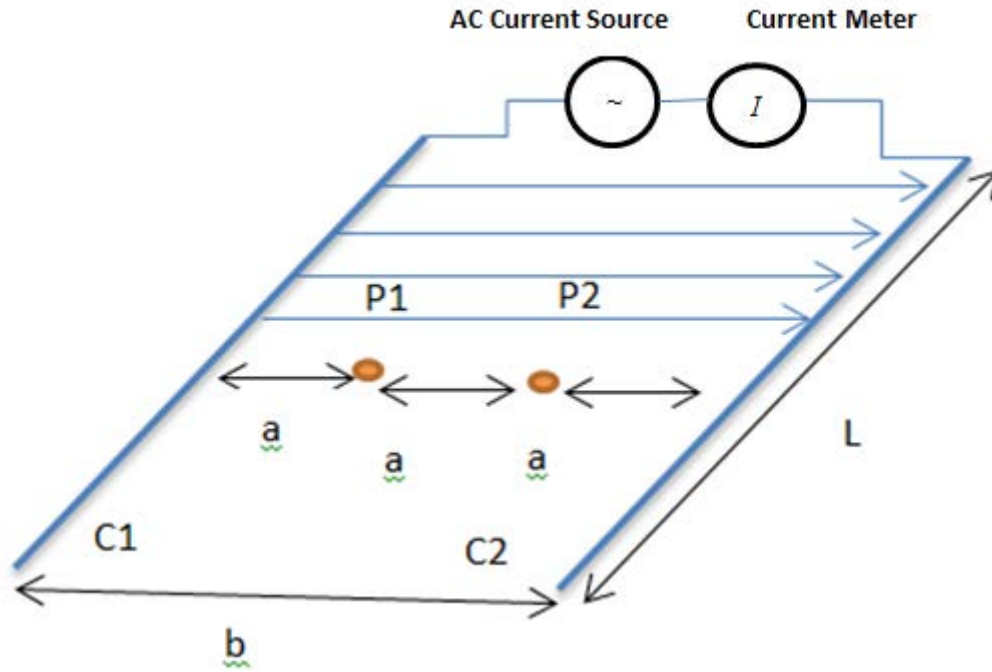


Figure 13: Sketch of line electrode in a Wenner configuration

Note: the length of the conducting lines are of value L and the separation between two conducting lines is given by b ; A current meter is used to record the transmitted current.

The current density at the position of potential electrode P1 is

$$J = \frac{\frac{I}{L}}{\frac{2\pi a L}{2L}} = \frac{I}{\pi a} = \frac{I}{L\pi a} \quad (3-69)$$

Then

$$V = - \int \frac{I \rho_{homo}}{L\pi a} da = - \frac{I \rho_{homo}}{L\pi} \log(a) \quad (3-70)$$

The potentials at electrode P1 and electrode P2 are given by

$$V_{p1} = - \frac{I \rho_{homo}}{L\pi} \log(a) + \frac{I \rho_{homo}}{L\pi} \log(2a) = \frac{I \rho_{homo}}{L\pi} \log 2 \quad (3-71)$$

$$V_{p2} = - \frac{I \rho_{homo}}{L\pi} \log(2a) + \frac{I \rho_{homo}}{L\pi} \log(a) = \frac{I \rho_{homo}}{L\pi} \log 0.5 \quad (3-72)$$

Therefore,

$$V = V_{P1} - V_{P2} = \frac{I \rho_{hom\sigma}}{L\pi} \log 4 \quad (3-73)$$

$$k_{LineElectrode} = \frac{\pi L}{\log 4} \quad (3-74)$$

Equatorial Configuration

The Equatorial dipole-dipole array configuration (dipole-dipole represents positive and negative current point-electrodes inserted into the earth, and positive and negative potential point-electrodes inserted into the earth) when arranged in a square is based on the dipole-dipole configuration but with the potential electrodes moved to positions parallel to the current sources, as illustrated in Figure 14.

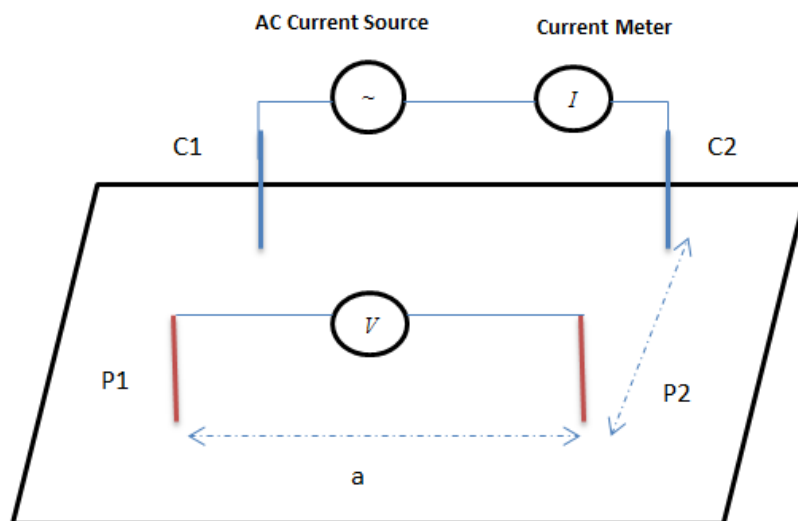


Figure 14: Sketch of dipole-dipole in square configuration

Note: point electrodes C1 and C2 acted as the current electrodes to transmit current (generated by the AC current source and recorded by the current meter) into the material layer; P1 and P2 are potential electrodes to collect potential. The voltage would be recorded by the voltage meter. a is the separation of the potential electrodes, it is also the separation between C1 and P1, C2 and P2, C1 and C2.

The potentials at P1 and P2 are given by

$$V_{p1} = \frac{I \rho_{homo}}{2\pi * a} - \frac{I \rho_{homo}}{2\pi * \sqrt{2}a} \quad (3-75)$$

$$V_{p2} = \frac{I \rho_{homo}}{2\pi * \sqrt{2}a} - \frac{I \rho_{homo}}{2\pi a} \quad (3-76)$$

Therefore,

$$V = V_{p1} - V_{p2} = \frac{I \rho_{homo}(\sqrt{2}-1)}{\pi a \sqrt{2}} \quad (3-77)$$

$$k_{square} = \frac{\pi a \sqrt{2}}{\sqrt{2}-1} \quad (3-78)$$

These typical electrode array configurations are utilised on lateral profiling, vertical sounding, or 3D mapping surveys. Their properties including limitations and advantages are summarized in Table 5.

Table 5: Typical electrode array configurations and their properties [32] [33]

Electrode array configuration (homogeneous semi-infinite earth)		Geometric factor K	Advantages	Limitations
2D	Wenner	$2\pi a$	Good depth determination; less noise contamination than Schlumberger; high SNR	Poor spatial resolution; sensitive to spacing errors
	Schlumberger	$\pi n(n + 1)a$	Good depth determination; better spatial resolution than Wenner	In multichannel applications
	Pole-Pole	$2\pi a$	Wide horizontal coverage and deep depth of investigation.	Remote electrode limits the surveys to accessible sites; high noise at the remote potential electrode; very poor resolution.
	Pole-dipole	$2\pi n(n + 1)a$	Better spatial resolution images	Remote electrode limits the surveys to accessible sites; high noise at the remote potential electrode; low SNR.
	Dipole-dipole	$\pi n(n + 1)(n + 2)a$	Had high anomaly effects; better imaging resolution for vertical and dipping structures	Lower SNR (signal noise ratio); poor depth resolution; sensitive to spacing errors
	Equatorial	$\frac{2\pi a}{2 - \sqrt{2}}$	Good spatial resolution	Time consuming deployment
	Line electrode	$\frac{\pi l}{\log 4}$	Simple deployment	Acutely non-isotropic response

All of these configurations, used for traditional electrical resistivity techniques, have one thing in common in that the current and potential electrodes are inserted into the ground. Such implanting introduces non-negligible galvanic contact resistance between the

electrodes and the resistive sub-surface. Furthermore, invasive electrical resistivity methods require drillings into the sub-surface. Besides these limitations, traditional electrical resistivity methods require much more time and generate practical difficulties e.g. electrodes require plugging and dragging. Therefore, non-invasive techniques using capacitive coupling and adapted from DC resistivity techniques have been developed by Ogilvy [34] and Kuras [35] [36].

3.2.3.3 Capacitive-Coupled Resistivity Methods

The principle of capacitive-coupled resistivity (CCR) techniques is to employ non-contact current electrodes coupling an alternating current into the ground, whilst other electrodes act as potential receivers measuring the voltages. The prototype of the capacitive-coupled resistivity technique, using an electrostatic quadrupole and operating at a frequency of 128 kHz, was introduced by Gard and Tabbagh [33]. The system in this configuration at this frequency could be considered as electrostatic, which was detailed by Gard in his research. Four square electrodes were placed at the corners of a rectangle with a length of 1.17 metres and a width of 1 metre, as sketched in Figure 15. These four electrodes were treated as point sources because of the smaller dimensions of these electrodes compared to the electrode separations and the scale of the site (20 m by 30 m).

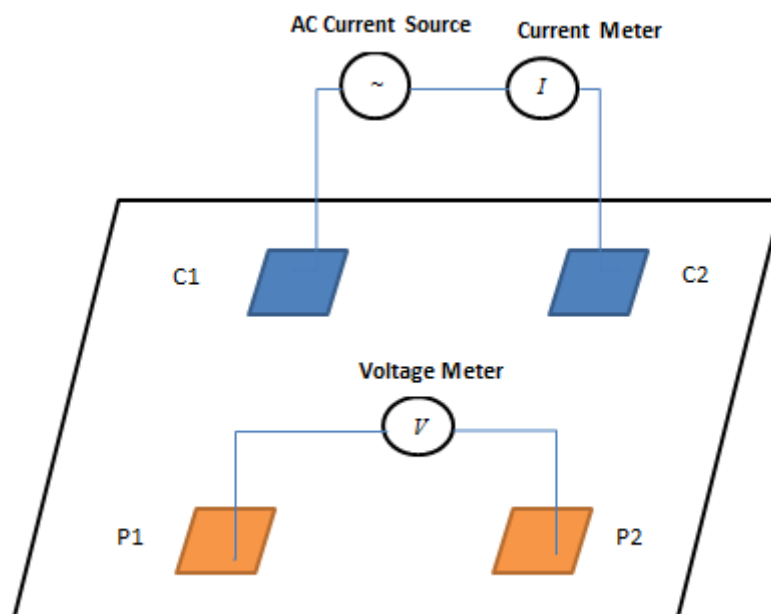


Figure 15: Sketch of the prototype of capacitive resistivity technique

Note: current electrodes C1 and C2 are used to induce the current signal into the ground or the material layer; P1 and P2 are potential electrodes to measure the voltage of the media using a voltage meter.

From 1998 to 2002, the capacitive-coupled resistivity technique was developed in the PhD thesis work presented by Ogilvy and the patent was granted in 2009 [34]. Following Ogilvy's work, Kuras conducted a very detailed theoretical analysis on the physical principle of the capacitive-coupled resistivity technique and provided detailed analysis on measured data collected from different surfaces including concrete roads [35] [36] [37]. A towed capacitive-coupled resistivity (CCR) array arranged in a square dipole-dipole configuration using operating frequencies from 1.6 kHz to 25 kHz was applied in his surveys. Six pairs of receiver electrodes (25 cm by 25 cm and 2 mm thickness) and one pair of current source electrodes were deployed, see Figure 16. Its maximum depth investigation was around 2.3 metres. These sensors are recognized as point sources in comparison with the wavelength and the electrode separations.

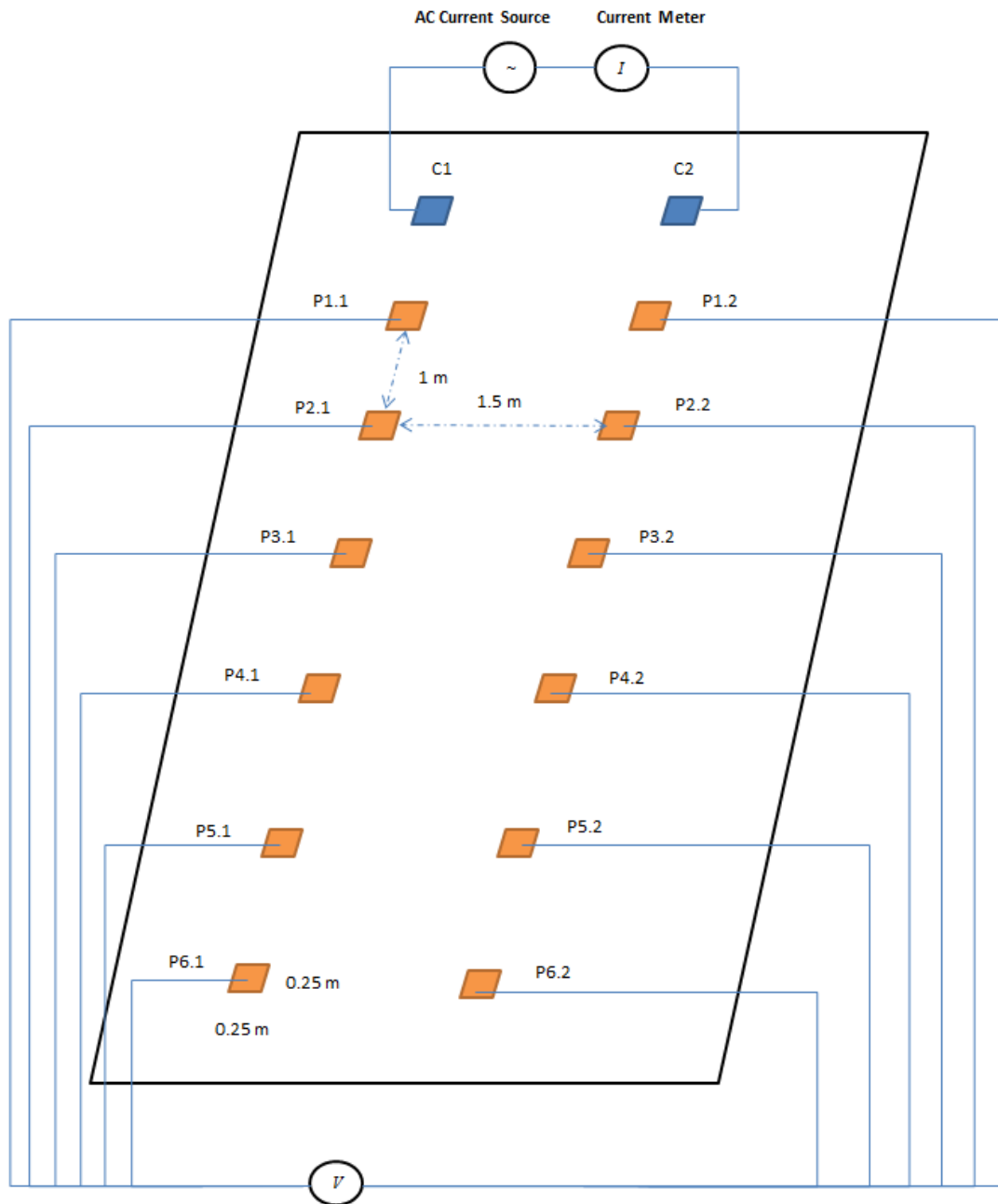


Figure 16: Sketch of a towed CCR technique by Kuras [35]

Note: C1 and C2 are current electrodes inducing the current signal, that is measured by the current meter, into the ground or the material layer; charges on the current electrodes would generate a 3D electric field distribution in the space; as a result, the equipotential is yielded (a basic understanding of the 3D electric field and the equipotential can refer to the modelling of the electric field and the equipotential of a point source). Other potential electrodes, of different separation to the current electrodes, are used to measure voltages of materials at different depths (the couple of current electrodes and each pair of potential

electrodes forms a square-electrode configuration; in total, there are six electrode configurations; the measurement depth for each configuration is different from the others).

There are many advantages of this method, including that it can be used for various depth investigations by changing the electrode separations; it is non-destructive and can be used for repeatable field surveys; it can continuously collect data and form 2D/3D images of the underground. Geometric factors are predicted, using the same methods as calculating the geometric factors of a dipole-dipole configuration operating in a semi-homogeneous layer. Surface roughness has not been discussed in Kuras' research, possibly because of the assumption that the capacitive sensor electrodes can be recognized as point sources. Although the surface roughness is important, its effect can be ignored due to the wider spatial resolution of the method.

Following Kuras' initial research using towed capacitive-coupled resistivity techniques, the performance of non-contact capacitive-coupled resistivity methods with wide electrode separation and at low-frequencies for evaluating high-resistive sites (e.g. asphalt pavements and icy areas), has been discussed and developed in recent years [38] [39] [40]. It was stated by Hordt [39] that over very resistive ground, the capacitive-coupled resistivity source signal is sufficient to enable enough current flow into a highly resistive sub-surface. Therefore, the capacitive-coupled resistivity technique applied at low frequencies and at suitable power levels can be used for the condition assessment of pavements. Dashevsky [38] described a capacitance sounding method (CSM) operating at low frequency (~1 kHz) on asphalt pavements. This was used to measure the capacitance and the thickness by grounding an electrode into the soil adjacent to the side of the road and the other electrode on the top of the pavement surface. The influence of the electrode clearance, the sensitivity of the electrode-to-surface capacitance to the layer thicknesses of the asphalt pavement, and the sensitivity of the electrode-to-surface capacitances to the permittivity of the pavement materials were investigated. It was indicated that the measured signal depends only on the thickness and dielectric permittivity, assuming the thickness of the asphalt pavement is from 6.5 cm to 7.0 cm. Experiments using this method have been conducted in the laboratory by myself, and proved his conclusion that dielectric permittivity is constant when the layer thickness is over 7 cm. Because surface roughness would generate a variation in the electrode clearance, it is believed that a roughness factor should

be considered when capacitive-coupled techniques are applied, and where the dimensions of electrode sensors cannot be ignored. The effects of surface roughness on the capacitance and leakage current have been studied by many researchers, especially in the field of integrated circuit (IC) design [41] [42]. Surface roughness impacts on the capacitance should be similar to the clearance influence on the capacitance, as studied by Dashevsky. An alternative to previous capacitive-coupled resistivity techniques using multi-electrodes was introduced by Przyklenk and Hordt [40], who described a capacitive-coupled resistivity technique named “Chameleon” with an operating frequency from 100 Hz to 100 kHz. This technique was used for the condition assessment of frozen ground. It was pointed out that “Chameleon” is only sensitive to the electrical resistivity on a moderately resistive observation field and it would be sensitive to both the electrical resistivity and the permittivity for particularly resistive ground, such as icy sites. An in-line Wenner array configuration was utilised, where its plate electrodes could not be assumed as point electrodes because of the dimensions of the electrodes and the geometric configuration. Traditional, DC resistivity geometric factor-calculating formulas become ineffective under such circumstances. However, no deduction or theoretical discussion was mentioned or analysed for the geometric factor in that research.

It would appear that non-contact electrical resistivity techniques using a capacitive-coupling method, operating at low frequency in a quasi-static regime, should be effective for the condition assessment of an asphalt layer, by measuring physical properties of electrical resistivity and electrical permittivity. Quasi-static theory was discussed in detail by Kuras [35] in his thesis, to yield bounds for upper and lower operating frequencies. In this work, the operating frequency will be determined by considering pavement materials as “good” conductors ($<10^5$ ohm-meter). Surface roughness has to be measured using a laser profiler and its influences on results need to be analysed. To achieve repeatable and continuous data rapidly, an automatic transportation device carrying a capacitive-coupling technique system has been designed.

Reference

- [1] Standards for highways, <http://www.standardsforhighways.co.uk/ha/standards/> accessed within 2016-2019.
- [2] Design Manual for Roads and Bridges (DMRB), Volume 7, Section 3: Data for Pavement Assessment (HD29/08). The Stationary Office, London, 2019
- [3] W. E. Wightman, "application of geophysical methods to highway related problems," Federal Highway Administration, Central Federal Lands Highway Div., Contract No. DTFH68-02-p-00083, Sep. 2003.
- [4] T. Saarenketo and T. Scullion, "Road evaluation with ground penetrating radar," in *Journal of Applied Geophysics*, 43 (2000), pp. 119 – 138.
- [5] T. Saarenketo, "Electrical properties of water in clay and silty soils," in *Journal of Applied Geophysics*, 40 (1998), 73-88.
- [6] T. Saarenketo and T. Scullion, "Using electrical properties to classify the strength properties of base course aggregates," Texas Transportation Institute, The Texas A&M University System, Rep. FHWA/TX-97/1341-2, Nov. 1995.
- [7] D. J. Daniels, *Ground Penetrating Radar*. The institute of engineering and technology, 2nd Edition, August 20, 2004.
- [8] N. Metje, P. R. Atkins, M. J. Brennan, D. N. Chapman, H. M. Lim, J. Machell, J. M. Muggleton, S. Pennock, J. Ratcliffe, M. Redfern, C.D.F. Rogers, A. J. Saul, A. Shan, S. Swingler and A. M. Thomas, "Mapping the underworld – state of the art review," in *Tunnelling and Underground space technology*, 22 (2007), pp. 568 – 586.
- [9] R. D. Evans, M. Frost, M. S. Jones and N. Dixon, "A review of pavement assessment using ground penetrating radar (GPR)," in 12th International Conference on Ground Penetrating Radar, June 16-19 (2008), Birmingham, UK.
- [10] I. L. Al-Qadi and S. Lahouar, "Measuring layer thicknesses with GPR," in *Theory to practice. Construction and Building Materials*, 19(2005), pp. 763-772.
- [11] C. Plati and A. Loizos, "Estimation of in-situ density and moisture content in HMA pavements based on GPR trace reflection amplitude using different frequencies," in *Journal of Applied Geophysics*, Vol 97 (2013), pp. 3-10.
- [12] D. J. Griffiths, *Introduction to electrodynamics*, Upper Saddle River, N.J.: Prentice Hall, 3rd ed., 1999.
- [13] M. E. Everett, *Near-surface applied geophysics*, Cambridge: Cambridge University Press, 2013.
- [14] J. D. McNEILL, "Electromagnetic terrain conductivity measurement at low induction numbers," GEONICS LIMITED Technical Note TN-6, 1980.
- [15] J. D. McNEILL, "Electromagnetic conductivity of soils and rocks," GEONICS LIMITED Technical Note TN-5, 1980.
- [16] D. C. Nobes, "Troubles waters: Environmental applications of electrical and electromagnetic methods," in *Surveys in Geophysics*, Vol 17, Issue 4 (1996), pp. 393-454.

- [17] E. J. Jaselskis, A. M. ASCE, J. Grigas and A. Brilingas, "Dielectric properties of asphalt pavement," in *Journal of materials in civil engineering*, Sep. 2003.
- [18] J. M. Reynolds, *An Introduction to Applied and Environmental Geophysics*, John Wiley & Sons Ltd, 1997.
- [19] A. Tabbagh, P. Cosenza, A. Ghorbani, R. Guerin, and N. Florsch, "Modelling of Maxwell-Wagner induced polarisation amplitude for clayey materials," in *Journal of Applied Geophysics*, 67 (2009), pp. 109 – 113.
- [20] A. Revil, M. Karaoulis, T. Johnson and A. Kemna, "Some low-frequency electrical methods for subsurface characterization and monitoring in hydrology," in *Hydrogeology Journal*, Vol 20 (2012).
- [21] L. Slater and D. P. Lesmes, "Electrical hydraulic relationships observed for unconsolidated sediments," in *Water resource research*, Vol 38 No. 10 (2002), pp. 1213.
- [22] G. Z. Abdel, E. A. Atekwana, S. Rossbach and D. D. Werkema, "Sensitivity of geoelectrical measurements to the presence of bacteria in porous media," in *Journal of geophysical research*, Vol. 115 (2010).
- [23] A. Revil, M. Karaoulis, T. Johnson and A. Kemna, "Review: Some low-frequency electrical methods for subsurface characterization and monitoring in hydrogeology," in *Hydrogeology Journal*, 20 (2012), pp. 617-658.
- [24] A. Kemna, A. Binley, G. Cassiani, E. Niederleithinger, A. Revil, L. Slater, K. H. Williams, A. F. Orozco, F. H. Haegel, A. Hordt, S. Kruschwitz, V. Leroux, K. Titov and E. Zimmermann, "An overview of the spectral induced polarization method for near surface applications," in *Near surface geophysics*, Vol 10, No 6 (2012).
- [25] H. M. Jol, *Ground Penetrating Radar: Theory and Applications*, ELSEVIER, 2009.
- [26] R. V. Hippel, *Dielectric Materials and Applications*, Artech House, 1952.
- [27] A. Revil, "Effective conductivity and permittivity of unsaturated porous materials in the frequency range 1 mHz – 1 GHz," in *Water resource research*, Vol 49 (2013), pp. 306-327.
- [28] F. Wenner, "The four terminal conductor and the Thomson bridge," *U.S.Bur.Standards Bull*, Vol 8 (1912).
- [29] C. Schlumberger, "Etude sur la prospection électrique du sous-sol", Paris, Gauthier-Villars, 1920.
- [30] H. H. William, *Engineering electromagnetics*, 3rd edition, International student edition, 1974.
- [31] H. Topsoe, *Geometric factors in four point resistivity measurement*, 2nd edition, May 25, 1968.
- [32] T. Dahlin, "The development of DC resistivity imaging techniques," in *Computers and Geosciences*, 27 (2001), pp. 1019 – 1029.
- [33] R. Grard and A. Tabbagh, "A mobile four electrode array and its application to the electrical survey of planetary grounds at shallow depths," in *Journal of geophysical research*, Vol. 96, No.B3 (1991), pp. 4117-4123.

- [34] R. Ogilvy, P. I. Meldrum, O. Kuras, D. Beamish, "Systems and methods for resistivity measurement," Patent Publication Number WO 2004/068172 A1, Natural Environment Research Council, United States, 2009.
- [35] O. Kuras, "The capacitive resistivity technique for electrical imaging of the shallow subsurface," Ph.D dissertation, University of Nottingham, UK, 2002.
- [36] O. Kuras, D. Beamish, P. I. Meldrum and R. D. Ogilvy, "Fundamentals of the capacitive resistivity technique," in British Geological Survey, Kingsley Dunham Centre, Keyworth, Nottingham, United Kingdom, June 17 (2005).
- [37] O. Kuras, P. I. Meldrum, D. Beamish, R. D. Ogilvy and D. Lala, "Capacitive resistivity imaging with towed arrays," British Geological Survey, Kingsley Dunham Centre, Keyworth, Nottingham, United Kingdom, 2007.
- [38] Y. Dashevsky, O. Y. Dashevsky, M. I. Filkovsky and V. S. Synakh, "Capacitance sounding: a new geophysical method for asphalt pavement quality evaluation," in Journal of applied geophysics, Vol 57, Issue 2 (2005), pp. 95-106.
- [39] A. Hordt, P. Weidelt and A. Przyklenk, "Contact impedance of grounded and capacitive electrodes," in Geophysical journal international, Vol 193, Issue 1 (2013), pp. 187-196.
- [40] A. Przyklenk, A. Hordt and T. Radic, "Capacitively coupled resistivity measurements to determine frequency dependent electrical parameters in periglacial environment-theoretical considerations and first field tests," in Geophysical journal international, Vol 206, Issue 2 (2016), pp. 1352-1365.
- [41] Y. P. Zhao, G. C. Wang, T. M. Lu, G. Palasantzas and J. T. M. D. Hosson, "Surface roughness effect on capacitance and leakage current of an insulating film," in Physical review B.60, 12 (1999), pp. 9157-9164.
- [42] T. Jamali, S. V. Farahani, M. Jannesar, G. Palasantzas and G. R. Jafari, "Surface coupling effects on the capacitance of thin insulating films," in Journal of applied physics, Vol 117 (2015).
- [43] H. H. William, *Engineering Electromagnetics*, McGRAW-HILL KOGAKUSHA, LTD, 3rd edition, 1974.
- [44] T. Haldor, "Geometric factors in four point resistivity measurement," Bulletin No. 472-13, 2nd edition, 1966.
- [45] E. Schnebele and B. F. Tanyu, "Review of remote sensing methodologies for pavement management and assessment," in Eur.Transp.Res.Rev, 2015.
- [46] J. D. Jackson, *Classical Electrodynamics*, 3rd edition, John Wiley & Sons, 1998.
- [47] J. Larsson, "Electromagnetics from a quasistatic perspective," in American journal of physics, Vol. 75, 230 (2007).
- [48] GL04108 "HISTORY OF ELECTRICAL METHODS OF EXPLORATION".

CHAPTER 4

NON-INVASIVE CAPACITIVE-COUPLED RESISTIVITY SYSTEM

4.1 Introduction

In a capacitive-coupled regime using sensor electrodes to couple a current signal into the pavement at low frequency, the conductive properties (the ability of a material transmitting current signals) of the pavement materials depend on the operating frequency, the resistivity and the dielectric constant. For investigations on the pavement using a non-invasive electrical resistivity technique, the electrical performance of the pavement materials is described by a non-ideal capacitor as shown in Figure 17, illustrated in a closed circuit with charging current I_{charge} and loss current I_{loss} . The charging current originates from bound charges. The loss current not only stems from the migration of charge carriers, but also comes from some other energy consuming processes such as the rotation and friction of the dipole molecules.

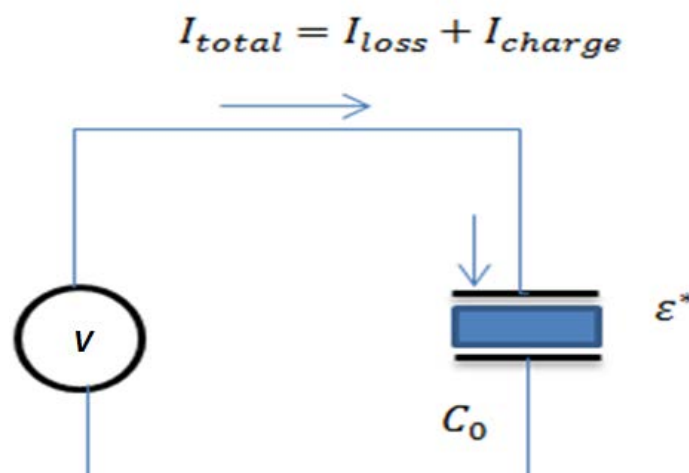


Figure 17: Sketch of current and voltage relation of a non-ideal capacitor (at frequencies less than 10 MHz [1])

Note: V is the input voltage; C_0 is the capacitance of the non-ideal capacitor with air as the dielectric material. This sketch represents a conceptual model of the sub-surface equivalent circuit. It was stated that a sub-surface equivalent capacitor and a sub-surface

equivalent resistor form the sub-surface equivalent circuit, which could be assumed as two components of a resistor and a capacitor of a non-idea capacitor. In this figure, the upper and lower electrodes of the capacitor can be assumed as capacitive sensor electrodes C1 and C2, whilst the dielectric material is assumed as the sub-surface materials (e.g. pavement aggregates). Current signals flow through the sub-surface via both sensor electrodes.

In order to describe the existence of the loss current component, complex permittivity and complex impedance are introduced:

$$\varepsilon^* = \varepsilon' - j\varepsilon'' \quad (4-1)$$

Where ε^* is the complex permittivity and

$$\varepsilon' = \varepsilon_r \varepsilon_0 \quad (4-2)$$

$$\varepsilon'' = \varepsilon_{rl} \varepsilon_0 \quad (4-3)$$

Where $\varepsilon_0 = 8.854 * 10^{-12}$ F/m is the dielectric permittivity of the vacuum; ε' is the relative permittivity of the dielectric; ε'' is the loss factor; ε_r is the relative dielectric constant and ε_{rl} is the relative loss factor.

Thus, the total current flowing through a capacitor with dielectric material contained inside, connected to a voltage source V , would be:

$$I_{total} = j\omega\varepsilon^* \left(\frac{Area}{d} \right) V \quad (4-4)$$

$$C_0 = \varepsilon_0 \frac{Area}{d} \quad (4-5)$$

Where $Area$ is the electrode area of the non-ideal capacitor and d is the non-ideal electrode separation (thickness); V is the driven voltage; $j^2 = -1$ and $\omega = 2\pi f$;

Replace ε^* with equations (4-2) and (4-3), it becomes

$$I_{total} = j\omega(\varepsilon_r - j\varepsilon_{rl})C_0V \quad (4-6)$$

$$I_{total} = (j\omega\varepsilon_r + \omega\varepsilon_{rl})C_0V \quad (4-7)$$

Replace C_0 with equation (4-5), equation (4-7) turns out to be

$$I_{total} = (j\omega\varepsilon_r + \omega\varepsilon_{rl})\varepsilon_0 \left(\frac{Area}{d}\right)V \quad (4-8)$$

Move *Area* to the left side:

$$\frac{I_{total}}{Area} = (j\omega\varepsilon_r + \omega\varepsilon_{rl})\varepsilon_0 \left(\frac{1}{d}\right)V \quad (4-9)$$

According to the definitions of the current density and the electric field strength E ,

$$J_{total} = (j\omega\varepsilon_r + \omega\varepsilon_{rl})\varepsilon_0 E \quad (4-10)$$

Then the current density becomes

$$J_{total} = (j\omega\varepsilon' + \omega\varepsilon'')E \quad (4-11)$$

The first part of current density ($j\omega\varepsilon'E$) is derived from the displacement of bound charges; the second part ($\omega\varepsilon''E$) results from dielectric conductivity which sums over all dissipative effects. As $J_{total} = \sigma^*E$ and $\sigma^* = \sigma + j\sigma''$, the conductivity σ could be described by formula (4-12)

$$\sigma = \omega\varepsilon'' \quad (4-12)$$

To recognize the pavement materials as “good” conductive materials, the dielectric conductivity current density should be much larger than the first part caused by the displacement of bound charges. Therefore,

$$\sigma = \omega\varepsilon'' \gg \omega\varepsilon' \quad (4-13)$$

$$f \ll \frac{\sigma}{2\pi\varepsilon'} \quad (4-14)$$

Conversely for a “poor” conductive material, the charging effect should be the dominant factor instead:

$$\sigma \ll \omega \varepsilon' \quad (4-15)$$

To use the equations defined above to reflect the upper and lower limitations of operating frequency, it is necessary to know general values of dielectric constant and electrical conductivity of pavement materials. According to the properties of pavement materials given in chapter 2, the typical dielectric constant of a new asphalt pavement ranges from 2.6 to 6. The dielectric constant of pavement materials will increase as the water content inside the pavement increases. The electrical conductivity of new asphalt pavement materials ranges from 10^{-8} to 10^{-6} S/m. It is known that the electrical conductivity will significantly increase from 10^{-8} to 10^{-6} S/m (or from 10^{-6} to 10^{-4} S/m) when there is a small increase in water content (0% - 0.31%) which is much less than the typical moisture level (3% - 8%) expected in a designed pavement. Here, the electrical conductivity of normal pavement materials is assumed as 10^{-5} S/m. Therefore, a rough estimation of the operating frequency is derived from:

$$f \ll \frac{1e-5}{2\pi * 4 * 8.854 * 10^{-12}} = 45 \text{ kHz and } f \gg \frac{1e-8}{2\pi * 2.6 * 8.854 * 10^{-12}} = 100 \text{ Hz} \quad (4-16)$$

Considering the upper-limit comparison and harmonics of 50/60 Hz power line noise, the upper limitation of the system’s operating frequency is chosen as half the maximum frequency $f_{system} < 20$ kHz and its lower frequency as 1 kHz. Within this frequency range, pavement materials can be recognized as good conductive materials where electrical conductivity is the dominant factor instead of dielectric permittivity.

4.2 Capacitive-Coupled Resistivity System

4.2.1 Capacitive-coupled resistivity system introduction

A non-destructive and rapid geophysical method using an automatic capacitive-coupling technique operating at low frequencies from 5 kHz to 15 kHz, was applied to assess the moisture related condition of the wearing layer of asphalt pavements. Considering the uncertainty of electrical conductivity and electrical permittivity of pavement materials,

three frequencies (5 kHz, 7.5 kHz and 10 kHz) were applied during site investigations. The high-level view of the capacitive-coupled resistivity system is given in Figure 19, which is carried by a vehicle illustrated in Figure 18. The lower-level view of the capacitive-coupled resistivity system is illustrated in Figure 20. The movement speed, the direction and spatial step-size of this vehicle are controlled by the operator according to the investigation requirements.



Figure 18: Robotic platform carrying the capacitive-coupled resistivity system on the pavement behind the old library at the University of Birmingham

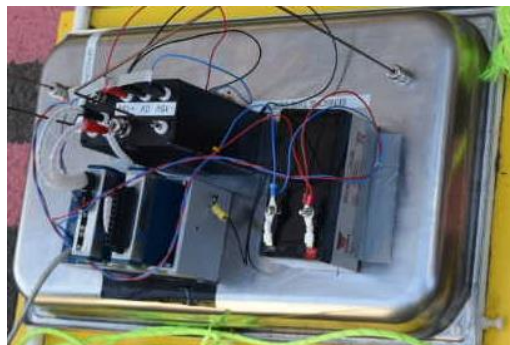


Figure 19: A high-level view of the capacitive-coupled resistivity system

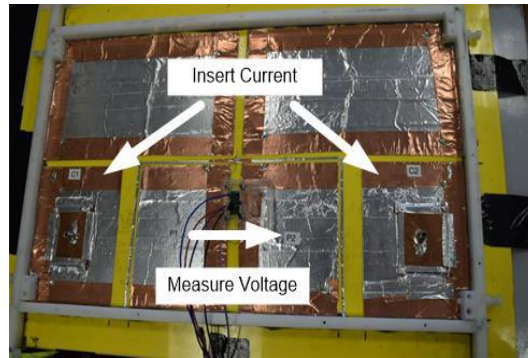


Figure 20: A low-level view of the electrode configuration of the capacitive-coupled resistivity system

The capacitive-coupled resistivity system is composed of sensor electrodes, transmitter signal generation by a NI 9263 DAC, data acquisition using a NI 9239 ADC, data storage and controller functions implemented on a portable workstation. The system diagram is described by Figure 21; its circuit sketch, including four electrodes and the pavement model, is given by Figure 22.

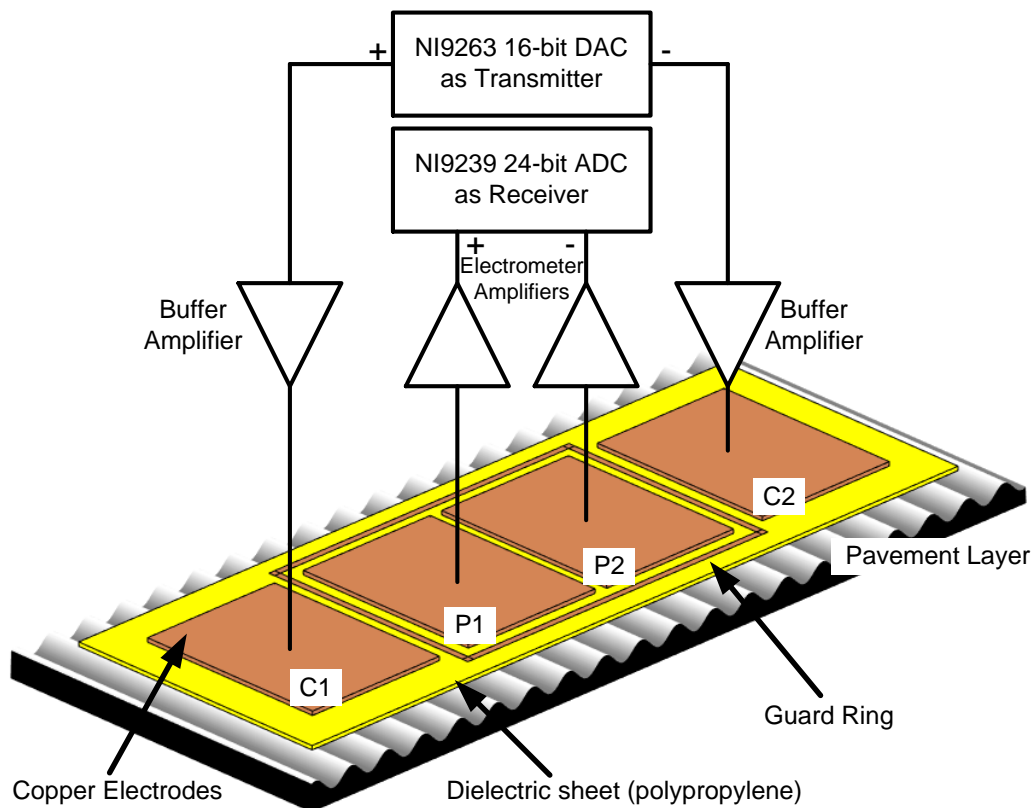


Figure 21: The diagram of the capacitive-coupled resistivity system

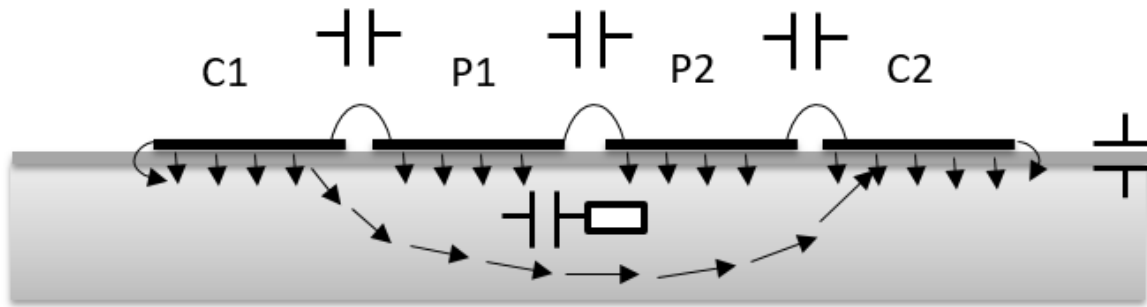


Figure 22: Simplified circuit sketch of four electrodes coupled to the pavement

Note: arrows represent generated electric fields when a four-electrode system is placed on the surface; the sketched capacitors between electrode plates represent the fringing capacitance; the sketched capacitor from C2 to the pavement surface represents the parallel capacitance; the separate sketched capacitor and resistor inside the pavement layer represent components of the sub-surface equivalent circuit model.

Four rectangular plate electrodes C1, C2, P1 and P2 act as current and potential sensors in a Wenner electrode array configuration. The yellow polypropylene sheet, seen in Figure 20, with a thickness of 2.273 mm is utilised as the bottom base layer of the capacitive-coupled resistivity sensor system. It has a dielectric constant of 2.283. All four electrodes have the same dimensions with lengths of 110 mm, widths of 145 mm and thickness of 1 mm. The two outside electrodes, C1 and C2, act as current sources and the remaining electrodes, P1 and P2, are potential receivers. The separation between a current electrode and a potential electrode is 25 mm; the separation between potential electrodes P1 and P2 is 10 mm. To reduce fringing effects between neighbouring plate electrodes, a guard ring of width 5 mm (the black frame seen in Figure 23) is added surrounding the potential electrodes.

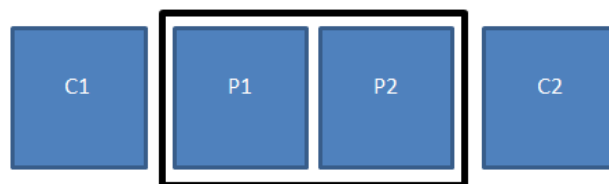


Figure 23: Sketch of sensor electrode array configuration with a guard ring

The spacing between the guard ring and each edge of the potential electrodes is 5 mm. Using such a configuration, the electrodes cannot be considered as point sources. Previous calculations of the geometric factor used in traditional DC resistivity techniques become invalid here. Therefore, a new calculation method for the geometric factor has to be derived, using finite element methods based on the electronic circuit schematic diagram illustrated in Figure 24.

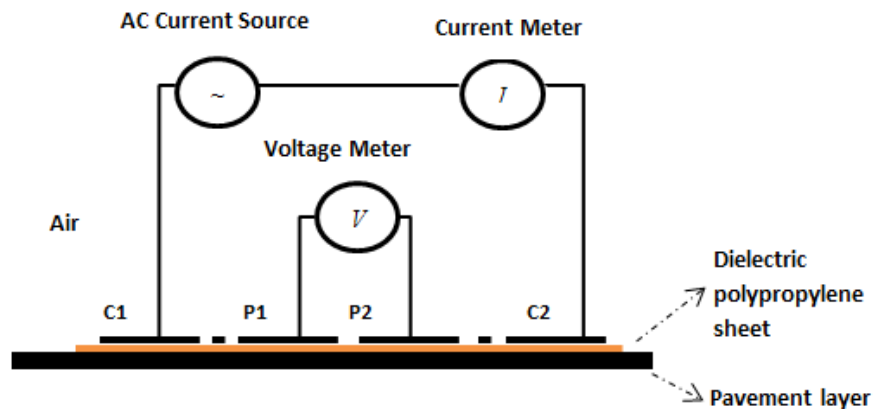


Figure 24: Circuit sketch of the sensor electrode configuration of the capacitive-coupled resistivity system

The system is powered by a 12 V battery. The maximum transmit signal voltage is limited to 9.95 V (19.9 V pk-pk). A 10 kOhm series resistor is used in the transmitting path to limit the maximum current to 1 mA under fault, or unexpected, conditions. The current is measured by estimating the voltage appearing across a low-inductance series resistor. A stepped-frequency, continuous wave (CW) input signal of 5 kHz, 7.5 kHz and 10 kHz is transmitted into the pavement. The received potential signal is processed using a pre-amplifier, voltage amplifier and NI 9239 ADC. This converted digital signal is stored within a PANASONIC workstation. The diagram of this whole system is shown in Figure 25.

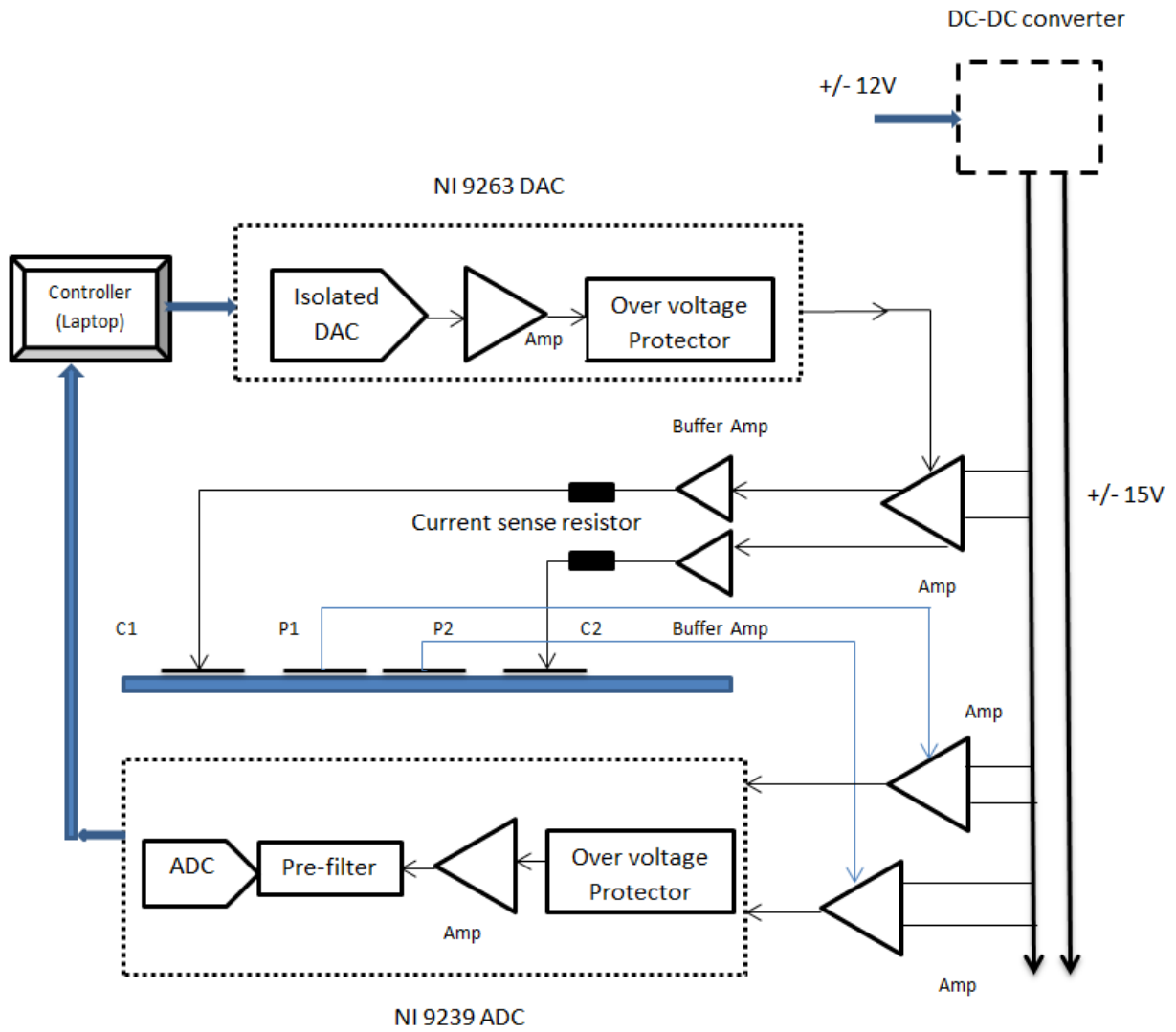


Figure 25: Complete capacitive-coupled resistivity system circuit diagram

The electrical circuit model of the whole system is given in Figure 26.

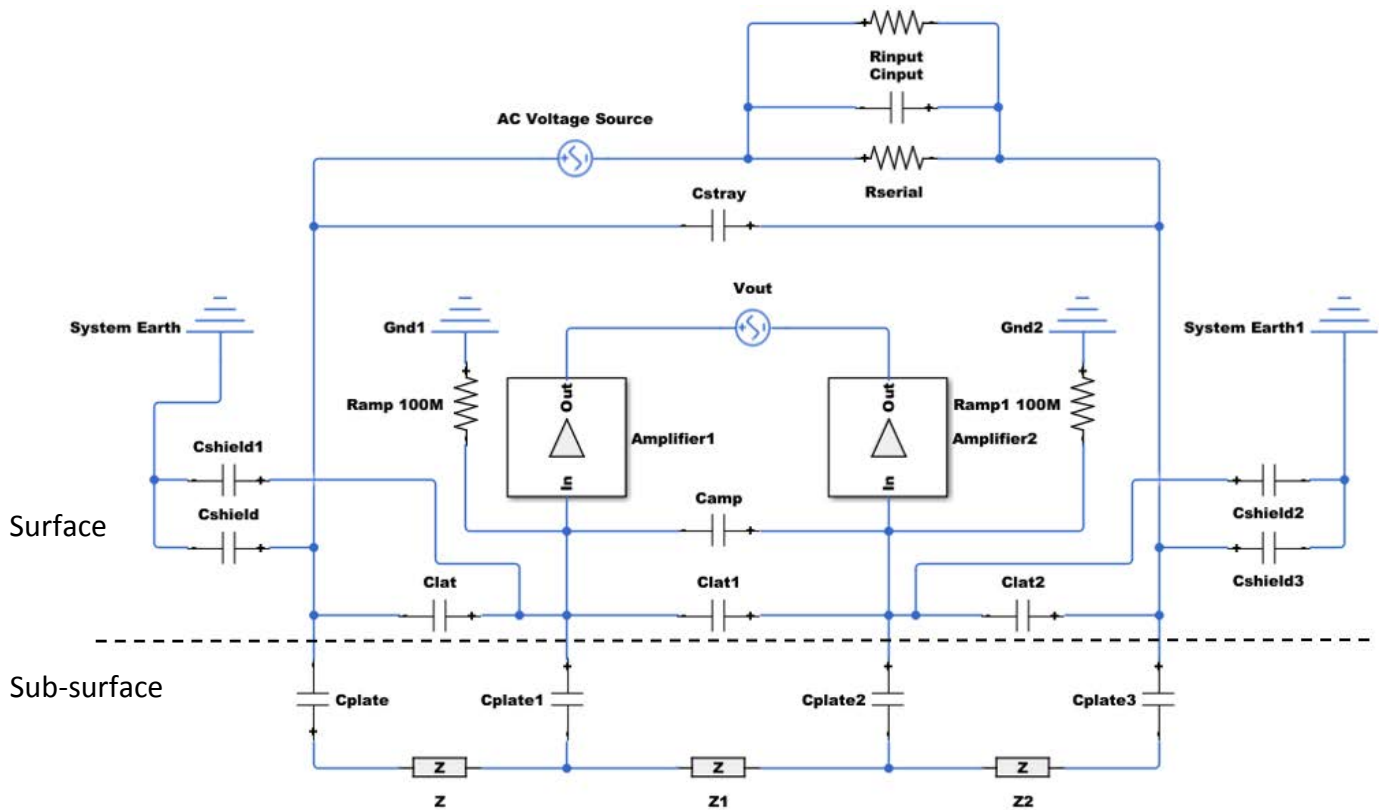


Figure 26: The electrical circuit model of the capacitive-coupled resistivity system using SIMULINK in MATLAB (Gnd1 and Gnd2 are ground; System Earth and System Earth1 are the system earth)

The equivalent electrical circuit model [13] of the sub-surface is denoted by Z or $Z1$ or $Z2$ composed of a resistor (denoted by $R_{\text{sub-surface}}$) and a capacitor (denoted by $C_{\text{sub-surface}}$) in parallel, as illustrated in Figure 27.

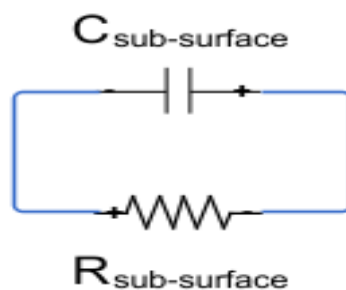


Figure 27: Sub-surface equivalent circuit model

A model fitting scheme was used to predict unknown values of components of the capacitive-coupled system circuit and the sensitivity of the output potential (denoted by V_{out}) to circuit components. The predicted circuit components included the stray capacitance associated with the drive circuitry (C_{stray}), the lateral capacitance between each electrode (C_{lat} , C_{lat1} , C_{lat2}), the capacitance between the outer shielding metal box and the electrodes (C_{shield} , $C_{shield1}$, $C_{shield2}$, $C_{shield3}$), the parallel plate capacitance between the upper sensor electrode and the lower rough surface (C_{plate} , C_{plate1} , C_{plate2} , C_{plate3}) and the equivalent electrical capacitance of the sub-surface material ($C_{sub-surface}$).

Applying a half-mirror method and closed-network analysis methods to the circuit illustrated in Figure 28:

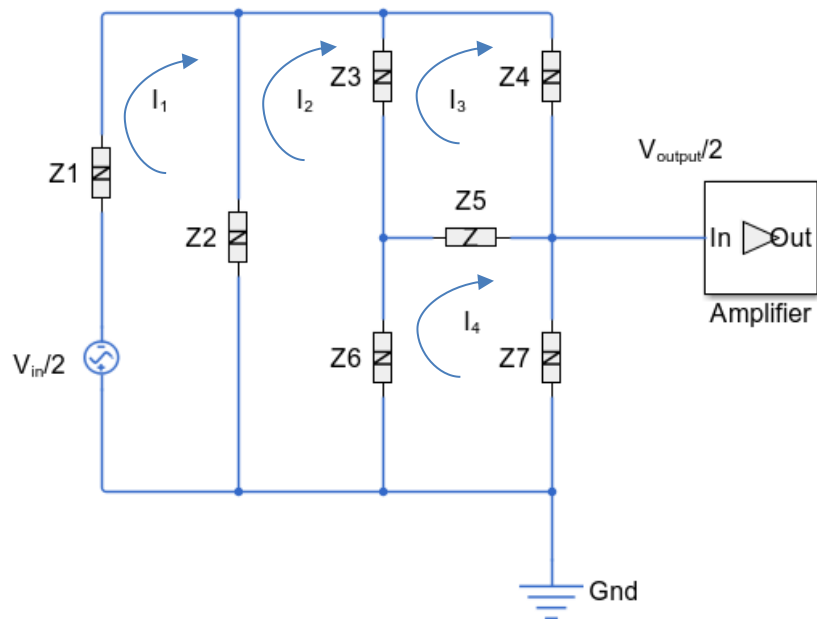


Figure 28: Half-mirrored circuit of a capacitive-coupled system applying current loops (denoted by I_1 to I_4) and closed networks

Note: V_{in} is the input voltage; V_{output} is the measured output voltage; Z_1 , Z_2 , Z_3 , Z_4 , Z_5 , Z_6 and Z_7 are equivalent impedance symbols.

Using Kirchoff's law that states that the sum of all voltages in a closed network is equal to zero (impedance symbols of Z are combinations of components in Figure 26) that,

$$(Z_1 + Z_2)I_1 - Z_2 I_2 = V_{in}/2 \tag{4-17}$$

$$(Z_2 + Z_3 + Z_6)I_1 - Z_3 I_3 - Z_6 I_4 - Z_2 I_1 = 0 \quad (4-18)$$

$$(Z_3 + Z_4 + Z_5)I_3 - Z_5 I_4 - Z_3 I_2 = 0 \quad (4-19)$$

$$(Z_5 + Z_6 + Z_7)I_4 - Z_5 I_3 - Z_6 I_2 = 0 \quad (4-20)$$

$$Z_7 I_4 = V_{\text{out}}/2 \quad (4-21)$$

Where

$$Z_{\text{sub-surface}} = 1/\left(\frac{1}{R_{\text{sub-surface}}} + j\omega C_{\text{sub-surface}}\right) \quad (4-22)$$

$$Z_1 = 1/\left(\frac{2}{R_{\text{input}}} + j2\omega C_{\text{input}} + \frac{2}{R_{\text{serial}}}\right) \quad (4-23)$$

$$Z_2 = \frac{1}{j\omega(2C_{\text{stray}} + C_{\text{shield}})} \quad (4-24)$$

$$Z_3 = \frac{1}{j\omega C_{\text{plate}}} + Z_{\text{sub-surface}} \quad (4-25)$$

$$Z_4 = \frac{1}{j\omega C_{\text{lat}}} \quad (4-26)$$

$$Z_5 = \frac{1}{j\omega C_{\text{plate1}}} \quad (4-27)$$

$$Z_6 = Z_{\text{sub-surface}}/2 \quad (4-28)$$

$$Z_7 = \frac{1}{j\omega(C_{\text{shield1}} + 2C_{\text{lat1}} + 2C_{\text{amp}}) + \frac{1}{R_{\text{amp1}}}} \quad (4-29)$$

The sensitivity relationships of the output voltage to all components were computed and plotted by using equation (4-17) to equation (4-29) (to plot the sensitivity relationship between the output voltage and every component, values of other components are kept constants while the value of that component is varied). It was found that the output voltage remains approximately constant when many of the sensor-related components change their values. However, the output voltage changes significantly, when variations occur in the parameters related to the sub-surface equivalent capacitance (denoted by $C_{\text{sub-surface}}$), or the capacitance between electrodes and a rough surface (including fringing effects) denoted by C_{plate} , C_{plate1} , C_{plate2} and C_{plate3} . Thus, it is proposed that a sub-

surface equivalent capacitance and the capacitance between electrodes and a rough surface (including fringing effects) are key factors. The relationships of the output voltage to these two key factors are illustrated by Figure 29 and Figure 30.

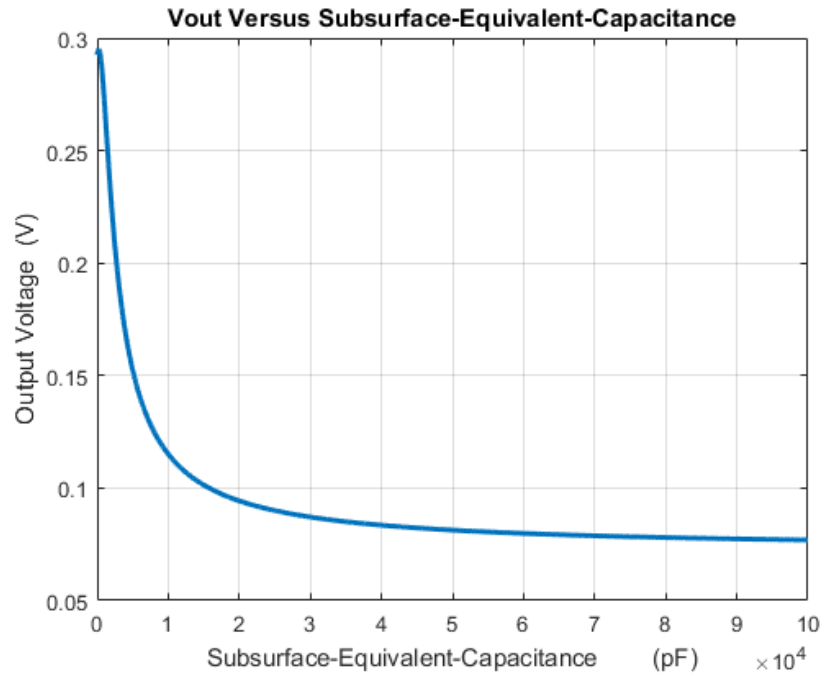


Figure 29: Output voltage (Vout) relationship to sub-surface equivalent capacitance

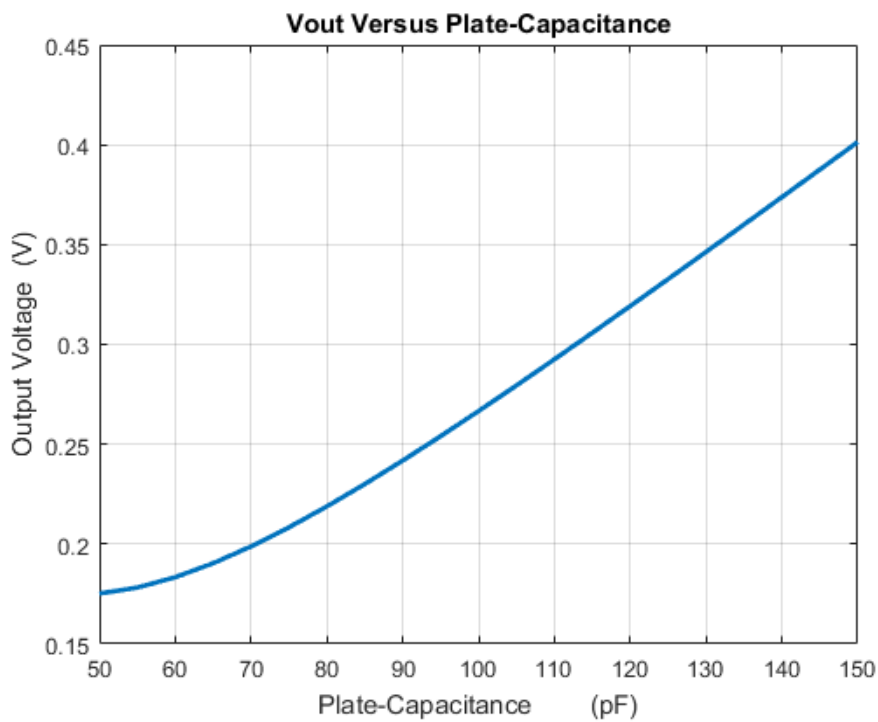


Figure 30: Output voltage (Vout) relationship to capacitance between electrodes and rough surface

4.2.2 Source signal

Stepped-frequency continuous wave (CW) signals and linear frequency modulation (LFM) continuous wave signals are commonly used as source signals because of their advantages of a wider dynamic range and higher mean power. In electronics, dynamic range is defined as a ratio between a maximum level and a minimum detectable value of a parameter e.g. power. The wider dynamic range shows that CW signals and LFM signals are of larger signal power to the noise level of the system. Hence, a CW or LFM signal is good at increasing the signal-to-noise ratio (SNR) and the stability of the system. They are both introduced in detail below.

4.2.2.1 Stepped-frequency continuous wave (CW) signal Equation [2]

$$TX_{CWSignal} = Vmax \cdot e^{j2\pi \cdot SteppedFrequencies \cdot TXIndex} \quad (4-30)$$

Where $Vmax = 9.95 V$ is the maximum transmitted signal voltage; $SteppedFrequencies$ is chosen as 5 kHz, 7.5 kHz and 10 kHz; $TXIndex$ is a time variable.

Frequency Response

Applying a Fourier transform on the CW signal of a time-domain function, the frequency response (Amplitude vs. Frequency) of a CW signal is illustrated in Figure 31. Signals at operating frequencies of 5 kHz, 7.5 kHz and 10 kHz are illustrated as three identifiable peaks with a large signal power spectral density. Significant attenuation of signal energy at other frequencies occurs.

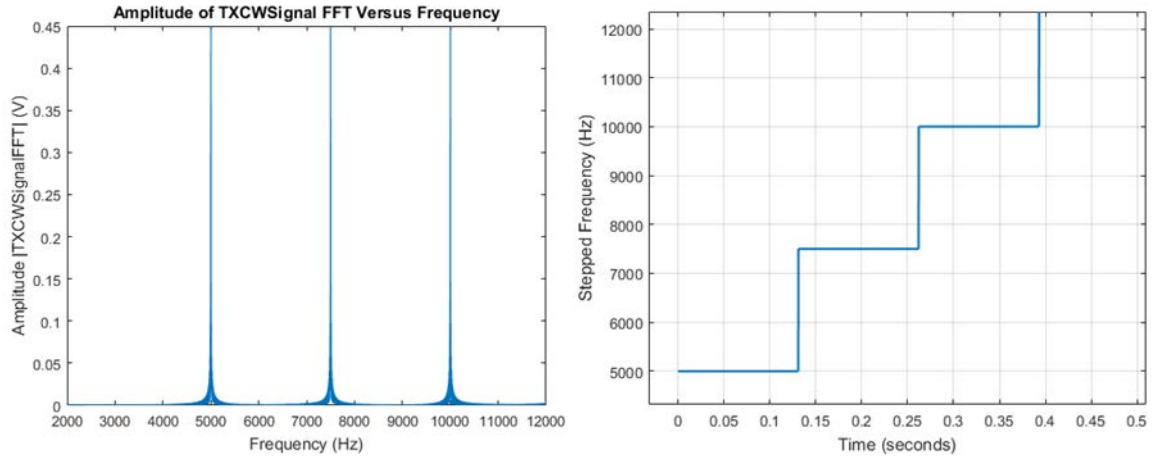


Figure 31: Amplitude response of operating frequency using stepped frequency CW signal (left side); stepped frequency versus the time (right side)

4.2.2.2 Linear frequency modulation (LFM) signal Equation [2]

$$TX_{LFM} = Vmax \cdot e^{j(2\pi \cdot StartFreq \cdot TXIndex + \pi \cdot TXIndex^2 \cdot BW \cdot \frac{InputSampleRate}{InputSamplesPerChannel})} \quad (4-31)$$

Where, $Vmax = 9.95 \text{ V}$ is the maximum transmitted signal voltage; $StartFreq$ is the starting frequency of 100 Hz; $TXIndex$ is the time variable; BW is the bandwidth of 10 kHz; $InputSampleRate$ is the input sampling rate of 50 kHz; $InputSamplesPerChannel$ is the number of transmitted samples.

Frequency Response

Applying a Fourier transform, the single-sided frequency response (amplitude vs. frequency) of the LFM signal is illustrated in Figure 32. The main cause of the ringing evident in the frequency response is due to the parameter of BW which is the bandwidth of LFM signal multiplied by the time duration of the pulse. The frequency domain effect of ringing results from a rectangular function in the time domain which cause ripples in the frequency domain. A stepped-frequency continuous wave signal is good for applications requiring a larger injection power and a LFM signal is good for applications requiring rapid frequency response estimation and where high signal-to-noise ratios are inherently available. In this work, a stepped-frequency continuous wave signal is commonly utilized as a source signal in order to maximise the received signal-to-noise ratio.

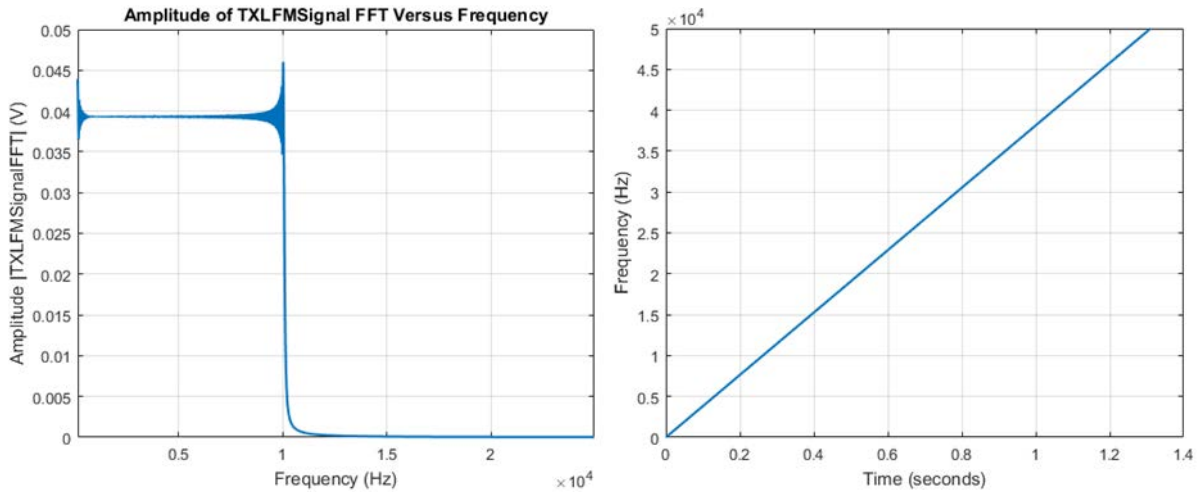


Figure 32: Amplitude response with respect to operating frequency (single-sided) using a linear frequency modulated signal (left side); linear instantaneous frequency as a function of time (right side)

4.2.3 Capacitive-Coupled Resistivity System Correction

Generally, systematic measurement errors are unavoidable and have to be corrected. For example, the multiple receiver voltage amplifiers should all have the same parameters, such as voltage gain; however, in practice, it is unlikely that any two amplifiers contained within the receiver chain will have exactly the same voltage gain and phase response. As a practical example, a measurement was conducted on two amplifiers with theoretically the same gain and phase responses. Their ideal amplifier gain is one. The test results (recorded using an analogue-to-digital converter 'NI 9239') are illustrated in Figure 33 as two, coloured curves representing the magnitude gain relationships of two voltage amplifiers with respect to frequency. It will be observed that both amplifiers have their gains randomly shifted around the ideal gain of unity. The shifted gain errors are within the specified gain error accuracy of a NI 9239 of $\pm 0.13\%$ (gain values may be below or above the ideal gain value). The maximum percentage gain errors of amplifier 1 and amplifier 2 are 0.07% and 0.05% respectively. According to the datasheet, it was found that the post-calibration gain matching from channel to channel is of 1.0257 (which is 0.22 dB maximum). In the capacitive-coupled resistivity system, it is usually the difference between two signals that infers the condition of the pavement; thus, such variations between components become critically important.

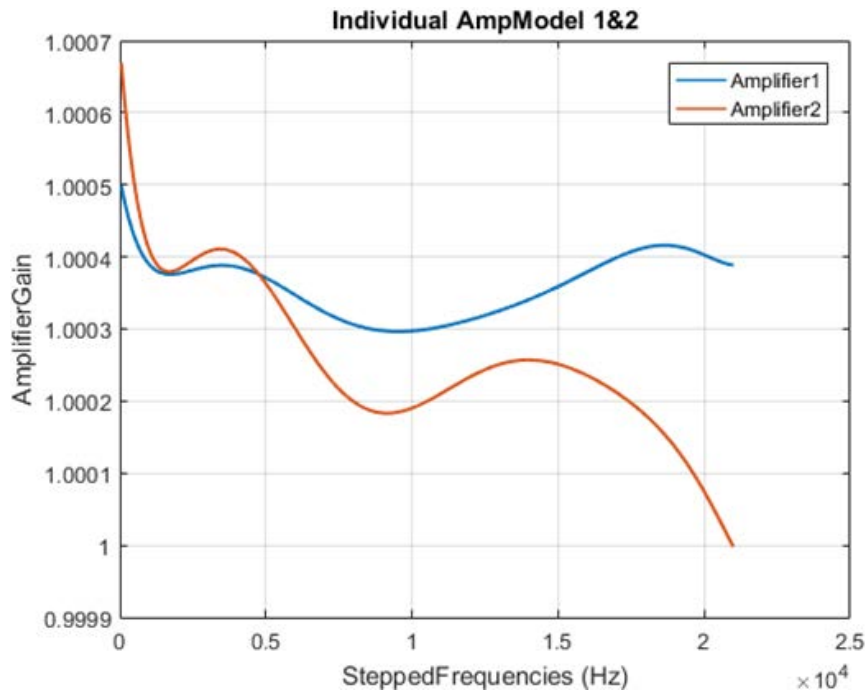


Figure 33: Amplifier gain characteristics of two voltage amplifiers (amplifier1 and amplifier2) operating from 50 Hz to 21 kHz

At low frequencies, the gain of the first amplifier is larger than the second. At high frequencies, the gain of the second amplifier is larger than that of the first one. If the outputs of these two amplifiers are applied to a differential amplifier, negative resistance results may be generated. These two voltage amplifiers connected to the potential electrodes are respectively symbolized as AMP1 and AMP2 (Figure 34) with gains of k_1 and k_2 . Ideally, k_1 is equal to k_2 . Assume the input voltage of AMP1 is V_1 , then the input voltage of AMP2 is $V_1 - \Delta V$.

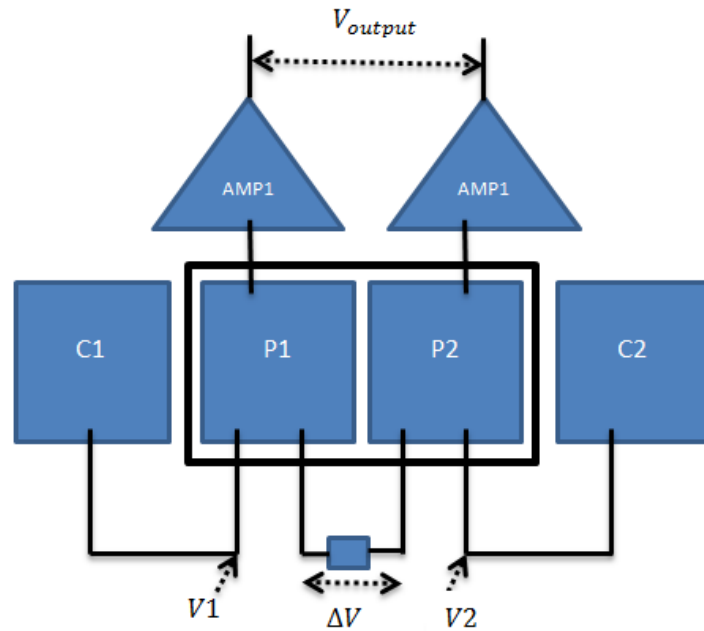


Figure 34: Diagram of the test system used to estimate the performance of the amplifiers

So, the output potential V_{output} after the two voltage amplifiers is:

$$V_{output} = V1 k1 - (V1 - \Delta V)k2 \quad (4-32)$$

As the voltage gain is given by

$$Gain = \frac{V_{output}}{\Delta V} \quad (4-33)$$

Rearranging equation (4-32) to obtain the voltage gain gives

$$Gain = V1 \frac{k1-k2}{\Delta V} + k2 \quad (4-34)$$

Whereas, $\Delta k = k1 - k2$ should be a small value tending towards zero.

Here, when the electrical resistivity of materials inserted between P1 and P2 is high, assuming a constant injected current, the result is that ΔV is large; $V1$ and ΔV tend to be infinite for a material of infinite resistivity with a finite injected current. According to the mathematics of limits and l'Hôpital's rule, the product of infinity and zero cannot be simply recognized as zero; the division value of zero and zero is undefined. As a result, under such an assumption of infinite resistivity, the value of $Gain$ is not equivalent to $k2$. Conversely,

if the potential difference ΔV is very small and tends towards zero, the component of $\frac{k_1 - k_2}{\Delta V}$ becomes a division of zero and zero. Thus, correction factors of gain matched of non-ideal practical amplifiers should be applied to both voltage amplifiers AMP1 and AMP2; and these factors must be incorporated into the calculation of the measured impedance.

4.2.3.1 Analytical Method

For a practical measurement system, the gains k_1 and k_2 of the voltage amplifiers have to be separately recorded and stored. In the frequency domain, the recorded potential values are corrected by multiplicative correction factors. For this capacitive-coupled resistivity system, the correction factors also include internal errors associated with the two channels as a result of the analogue-to-digital conversion processes.

The impedance ($Z = R + jX$) of this capacitive-coupled resistivity system is:

$$Z = \frac{V_1 k_1 - V_2 k_2}{I} \quad (4-35)$$

Instead of $Z = \frac{V_1 - V_2}{I}$

Where V_1 and V_2 are the measured voltages on electrodes P1 and P2; I is the measured current; R is the resistance and X is the reactance.

4.2.3.2 Experimental Tests

Following the analytical method described above, four high-accuracy resistors ranging from very small resistance to high resistance (5 Ω , 50 Ω , 100 Ω and 2 k Ω) were tested. The measured resistances of those four test resistors were then compared with their resistances stated by the manufacturer. Comparisons are shown in Figure 35, Figure 36, Figure 37 and Figure 38. In these figures, measured resistance values tend to randomly vary from the ideal resistance values. This is due to the maximum gain errors of the NI 9239 analogue-to-digital converter which is $\pm 0.13\%$.

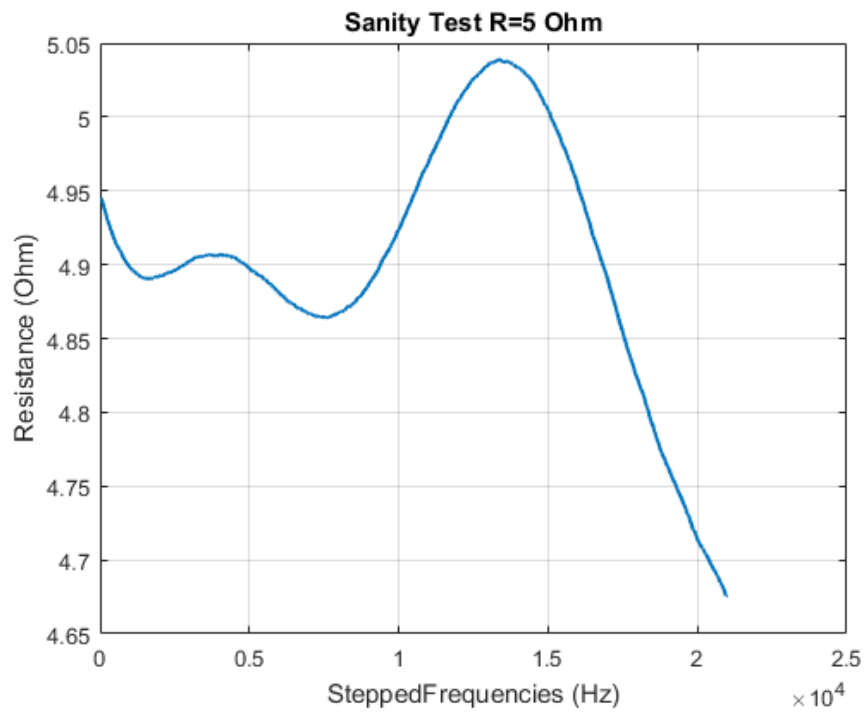


Figure 35: Practical resistor (5 Ω) resistance test after systematic error correction factor applied operating from 50 Hz to 21 kHz

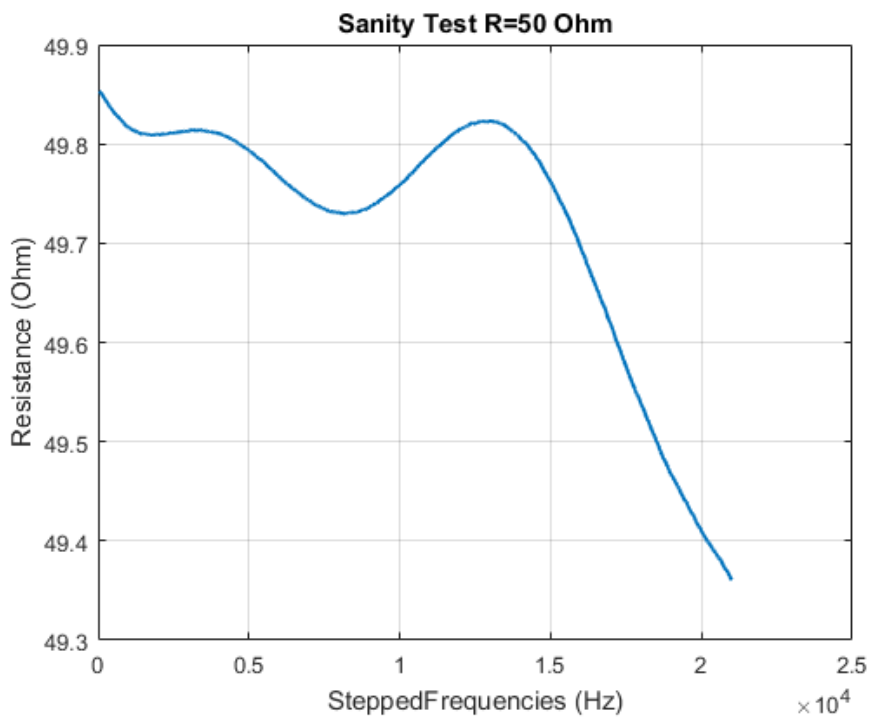


Figure 36: Practical resistor (50 Ω) resistance test after systematic error correction factor applied operating from 50 Hz to 21 kHz

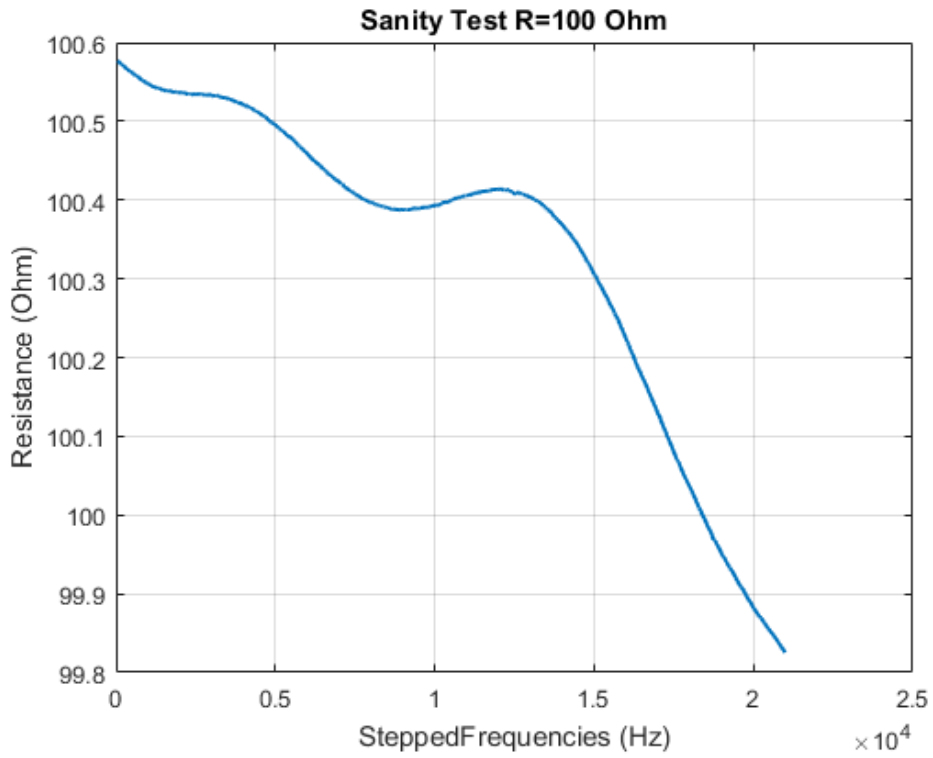


Figure 37: Practical resistor (100 Ω) resistance test after systematic error correction factor applied operating from 50 Hz to 21 kHz

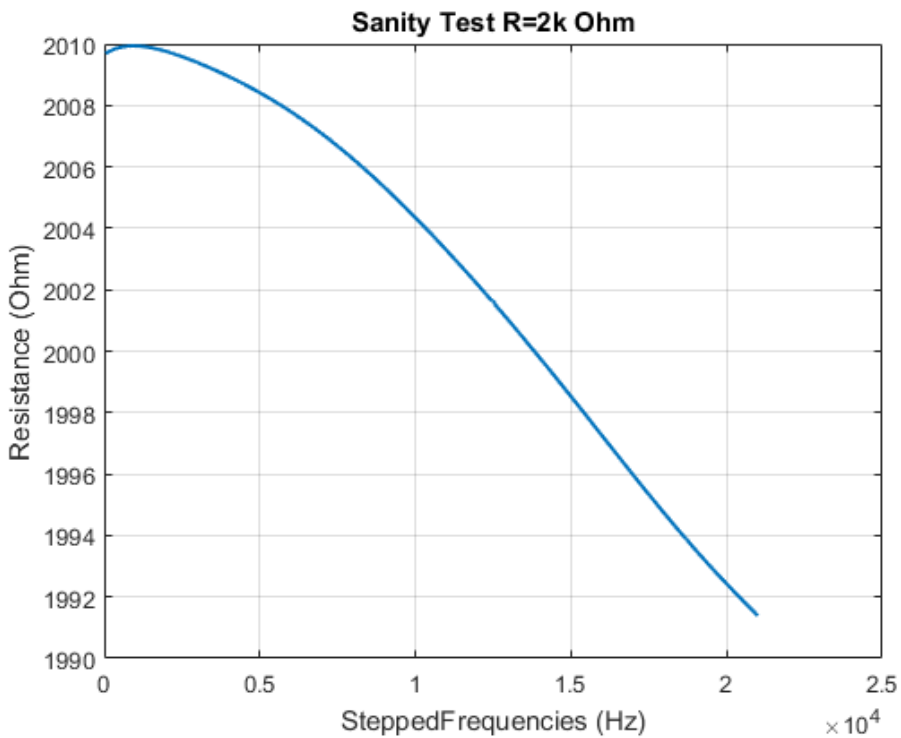


Figure 38: Practical resistor (2 kΩ) resistance test after systematic error correction factor applied operating from 50 Hz to 21 kHz

The measured error for each resistor is:

Resistor (5 Ω) has error from 1% to 7%; resistor (50 Ω) has error from 0.2% to 1.4%; resistor (100 Ω) has error from 0.2% to 0.6%; resistor (2 k Ω) has error smaller than 0.5%. The test resistors were chosen be of a low-reactance foil construction with a tolerance of 0.01%.

As the stated test resistance value becomes higher, the error decreases. Even for very small resistor values, the highest error is 7%, which is acceptable. Considering the typical high resistivity of asphalt pavement materials, a measurement error using this capacitive-coupled resistivity system should be smaller than 1%. It should be noted that the impedance measurement method is that of a ratiometric comparison of a device-under-test with a sense resistor of assumed ideal characteristics. Measurement errors are minimised when the impedance of the device-under-test is approximately the same as the sense resistor, in this case assumed to be $R_{sense} = 10000 + j0 \Omega$. The measurement errors are compounded by the requirement to solder the test resistors directly to the electrode plates, thus adding an unknown value of series contact resistance. Therefore a contact resistance of 1% of 5 Ω is not unreasonable (0.025 Ω per solder joint).

4.2.4 Dielectric Polypropylene Material Parameters

In section 4.2.1 it was mentioned that the yellow polypropylene sheet was used as the base of the capacitive-coupled resistivity system and placed on the surface of the pavement. This polypropylene sheet forms the dielectric material of the capacitors composed of sensor electrodes C1, C2, P1, P2 (upper electrodes of the capacitors) and the surface of the pavement (bottom electrodes of the capacitors). These capacitors are part of the whole system and definitely will influence its performance. An HP4921 impedance analyser was used to measure the electrical permittivity of the yellow polypropylene sheet.

HP4921 self-capacitance values used as an impedance analyser correction

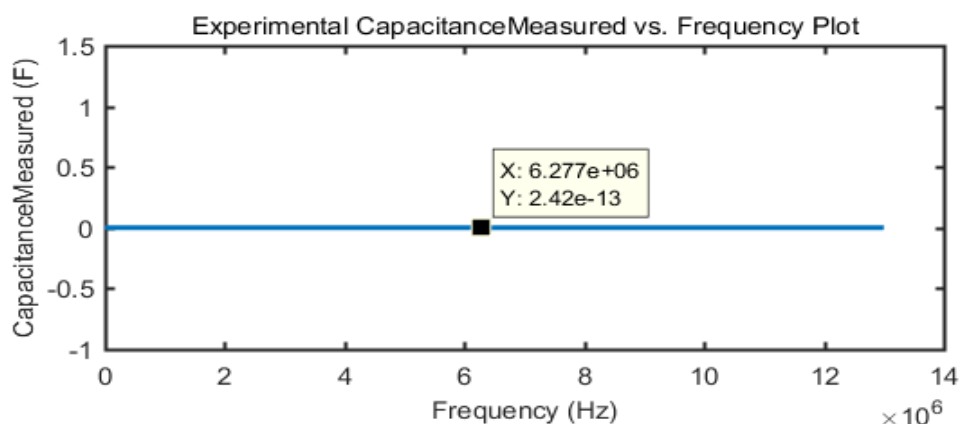


Figure 39: Self-capacitance value test of an HP4921 impedance analyser

According to Figure 39, the impedance analyser's self-capacitance is 0.242 pF. This value should be applied to all measured results obtained using the HP4921.

Capacitance of a single parallel capacitor with a yellow polypropylene sheet as a dielectric material

A single parallel-plate capacitor is shown in Figure 40 with its side view shown in Figure 41. This capacitor is connected to the HP4921 in order to measure its capacitance.

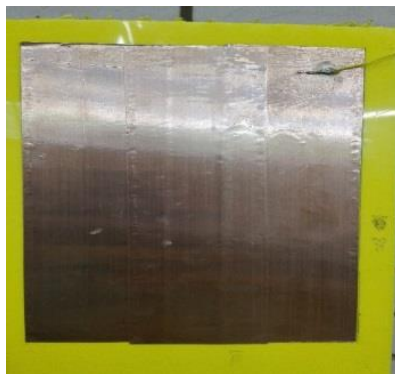


Figure 40: A single parallel-plate capacitor with a yellow polypropylene sheet as a dielectric material



Figure 41: Side view of a single parallel plate capacitor with yellow polypropylene sheet as a dielectric material

The dimensions of the capacitor are given in Table 6 including its length, width, and thickness. The measured capacitances and dielectric constants calculated from those measured results are shown in Figure 42 and Figure 43.

Table 6: Experiment data of normal parallel capacitor

Material	Width/m	Length/m	Thickness/m	Frequency range
Yellow polypropylene	0.12	0.2	0.00273	100 Hz-100 kHz

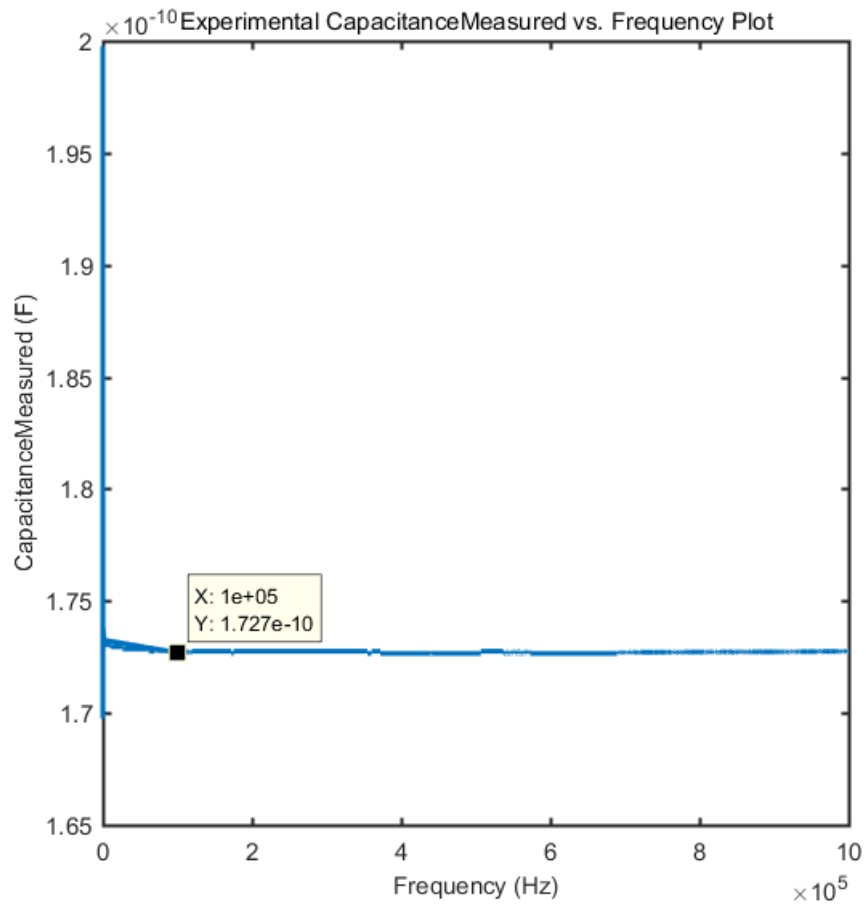


Figure 42: Measured capacitances of a single parallel plate capacitor with a yellow polypropylene sheet as a dielectric material

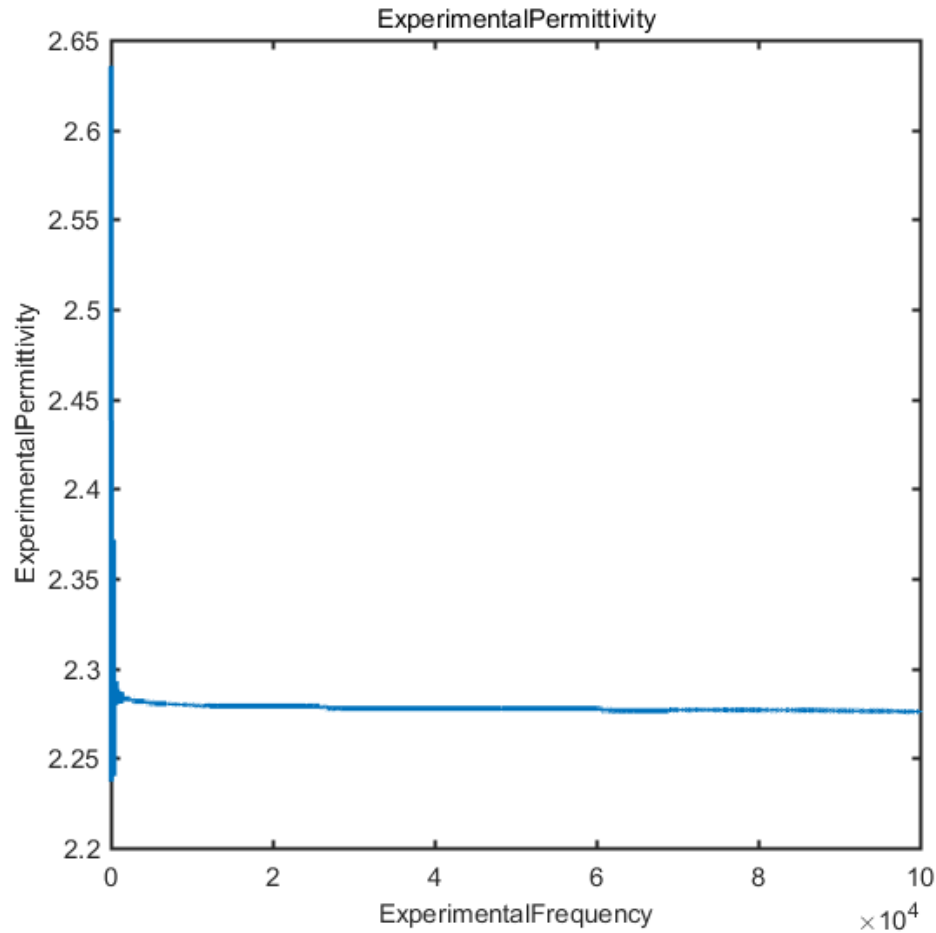


Figure 43: Dielectric constant of the yellow polypropylene sheet as a dielectric material (Y-axis of ExperimentalFrequency is in units of Hz)

Figure 42 shows the capacitance of a single parallel-plate capacitor (approximately 0.1727 nF) over a broad frequency band. The electrical permittivity of the yellow polypropylene sheet is around 2.283 as shown in Figure 43.

4.3 Geometric Factor

Formulas for the geometric factor of traditional DC resistivity array configurations (Wenner array, Schlumberger array, dipole-dipole, pole-pole and in-line rod electrode array) have been introduced and discussed by previous researchers [3] [4] [5]. However, those methods are not appropriate in this research as the four electrodes cannot be assumed to be point sources. Considering the relationship between the electrical resistance and apparent resistivity $\rho = kR$, the geometric factor k can be predicted by using analytical methods, COMSOL modelling and experiments. The derivation of the geometric factor of

this capacitive-coupled resistivity system is introduced by means of a flow chart illustrated in Figure 44.

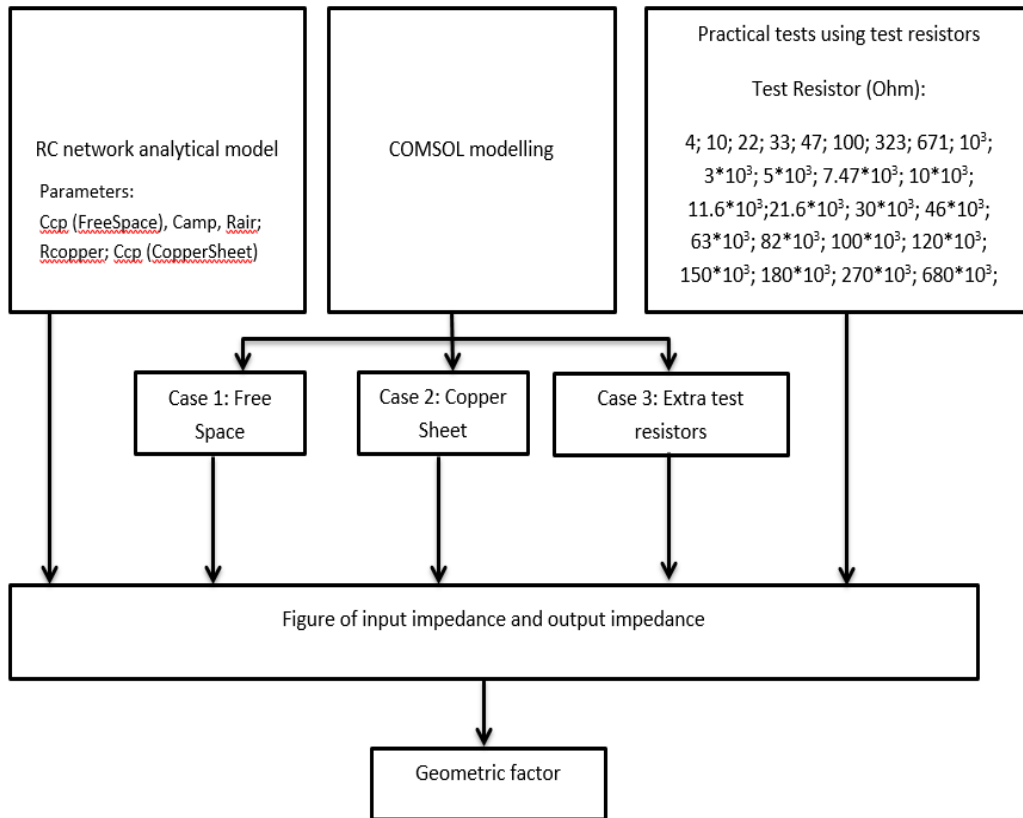


Figure 44: Flow chart for deriving the geometric factor of the capacitive-coupled resistivity system

Before conducting experimental tests, the basic idea is to use the resistor-capacitor network method to validate the analytical model. Following the analytical model development, 26 experiments were conducted using 26 test resistors with their electrical resistances R ranging from $4\ \Omega$ to $680\ k\Omega$. Each time, three test resistors of the same value were connected in-series between C1 and P1, P1 and P2, P2 and C2, as shown in Figure 45.

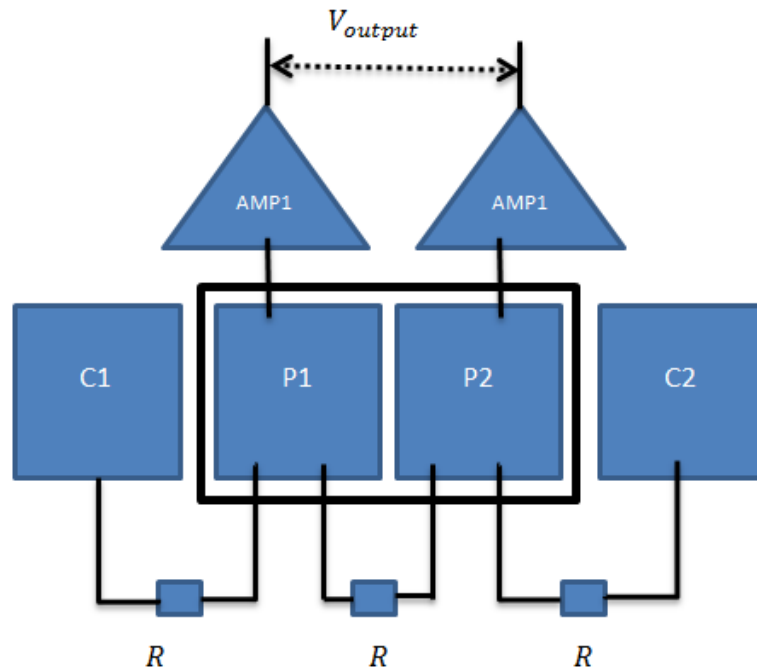


Figure 45: Diagram of predicting the geometric factor of the capacitive-coupled resistivity system by experimental method using test resistors (R in this diagram ranges from 4Ω to $680 \text{ k}\Omega$)

Experiments using a capacitive-coupled resistivity system in free space (air is considered as the material layer) and on a copper sheet were also conducted in order to calculate the coupling capacitances between sensor electrodes. These coupling capacitances will be used later in predictions of other electrical components using appropriate model-fitting schemes. The copper sheet mimics a material of a very low electrical resistivity. Electrical resistivity of the dry air with no distributed conductive ions is very high typically $1.3 * 10^{16} \Omega m$. Considering the hydrated UK weather, some conductive ions very likely exist and will be distributed over the bottom surface of the yellow polypropylene sheet. The measured resistivity of the air should thus be less than the expected dry-air value, but is still of a high value. Furthermore, to prove the efficacy of the analytical model using a resistor-capacitor network, the circuit model of the capacitive-coupled resistivity system tested using practical resistors in free space and on copper sheet, are set up, run and analysed in COMSOL. The analytical model using a resistor-capacitor network, the COMSOL model and practical experiments are introduced and explained in the following sections. Results derived from these three methods will be compared, and finally, the geometric factor of the

capacitive-coupled resistivity technique in a Wenner electrode array configuration will be summarized.

4.3.1 Analytical model using a resistor-capacitor network

Regardless of the materials (copper sheet, black foam, the pavement or free space) to be used in experiments, for a closed circuit there is a vertical potential drop from sensor plate electrodes to the pavement surface. There is also a longitudinal potential drop along the length of the pavement surface. Considering the symmetrical design of the system (Figure 22, Figure 27 and Figure 45), a mirrored equivalent circuit of the system is extracted in order to conduct the circuit analysis, assuming the potential is zero at the central position between P1 and P2. For any sub-surface materials e.g. inhomogeneous or homogeneous in this work, mirrored circuit analysis would be effectively applicable as the zero potential should exist at somewhere within electrodes covered areas; while for homogeneous materials, the zero potential is exactly located at the centre. The circuit diagram of this mirrored system is given in Figure 46.

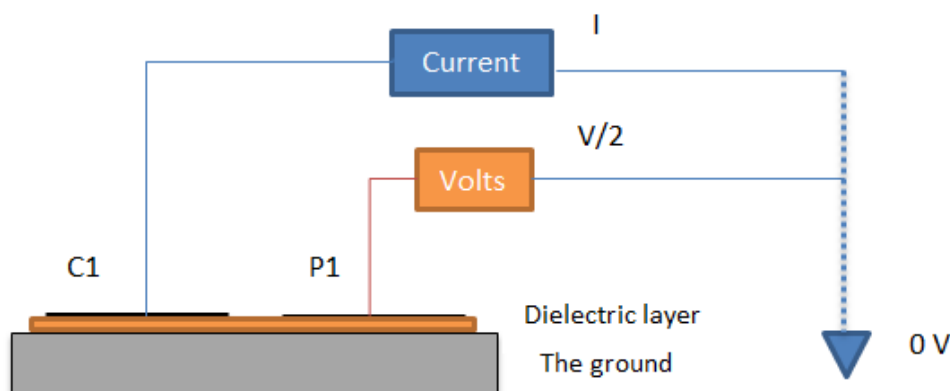


Figure 46: A side-view diagram of the mirrored system

In the mirrored symmetrical system model, electrode C1 is driven by a voltage source of half the potential of the injection source used in the complete system, connected in series with a sense resistor of half the value used in the complete system. The same current I flows through electrode C1 in both the modelled and the experimental systems. The potential at P1 becomes half of original output voltage, which is denoted as $\frac{V}{2}$ in the figure. Electrode P1 is still connected to a receiver amplifier. A large resistor of $100\text{ M}\Omega$ is connected

between the potential electrode and the guard ring which is connected to the referenced earth.

A numerical solution using a 1D finite element method (FEM) was undertaken to derive a solution of this mirrored circuit. It was assumed that a 1D finite element technique would provide similar results to a more realistic 2D model, whilst requiring significantly less computational effort. This assumption is based on the fact that free charge will flow out to the edges of a conductor in a characteristic time when they are placed on a conducting material [6]. Electrode C1, electrode P1, and the surface of the bottom material layer are meshed into finite elements. Each element has a length of 1 mm. Each element and its related surface element, connected by a dielectric material, form a unit capacitor. The vertical current distribution decreases because of the current flow into each unit capacitor, denoted by di . The longitude voltage decreases because of the resistance of the unit resistor of the material layer, denoted by dV . A stray coupling capacitor connects electrodes C1 and P1 together. Thus, the mirrored circuit model using a resistor-capacitor network will be generated and is illustrated in Figure 47. The relationship between the practical resistor values and the predicted output resistance will be derived within the following sections.

4.3.1.1 Analytical Equations Deduction

First, consider only the electrode P1 in the mirrored system model, with its connected amplifier-input capacitance C_{amp} and an extra resistor R_{amp} . Assuming the length of each unit is Δx m, the electrical resistivity of the material layer (copper sheet, hydrated air, black foam test material, or asphalt pavement) is of order $r \Omega m$; the susceptance of a unit capacitor is g Siemens; the input voltage is V_{input} ; and V generally represents the potential at every unit on the surface of the material layer.

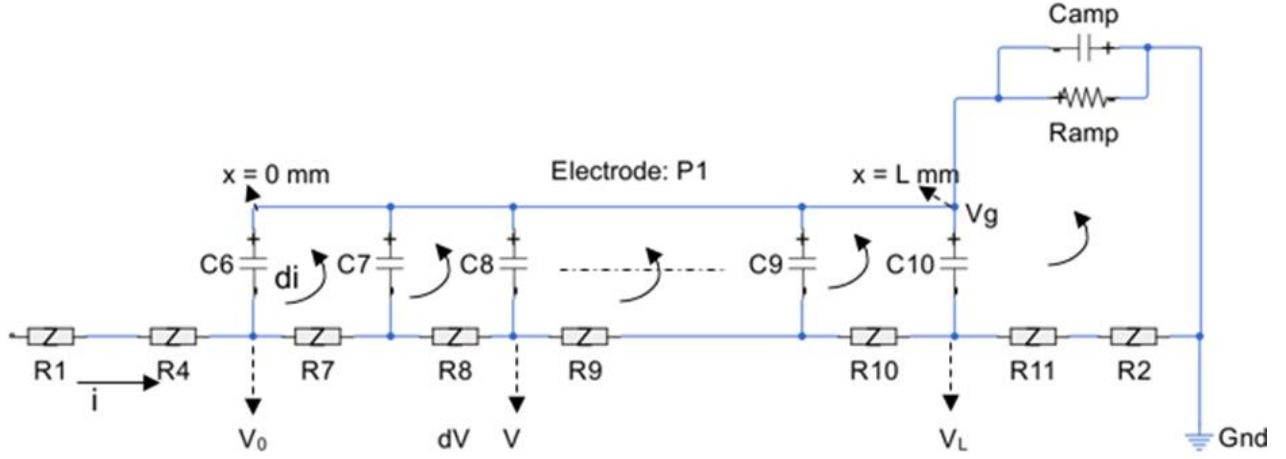


Figure 47: 1D Resistor-capacitor (RC) network of the electrode P1 with an extra resistor and a coupling capacitance (dashed line: potential RC components depending on number of meshes; solid arrows: assumed network-current flow)

Note: C_{amp} is an internal input-capacitance for the receiver amplifier; $R_{amp} = 100 \text{ M}\Omega$ is the internal resistance of the receiver amplifier; all resistances $R1 \dots R11 = \Delta Z$ excluding R_{amp} ; similarly, all capacitances $C6 \dots C10$ except C_{amp} have the same impedance ΔZ_c .

$$\Delta Z = r\Delta x \quad (4-36)$$

$$\Delta Z_c = \frac{1}{g\Delta x} \quad (4-37)$$

$$dV = (i - di)r dx \quad (4-38)$$

$$di = (V - V_g + dV)g dx \quad (4-39)$$

The differentiation of the potential and the current with respect to the length, result from moving dx to the left side (di and dV are very small values and can be ignored in the deductions below):

$$\frac{dV}{dx} = ir \quad (4-40)$$

$$\frac{di}{dx} = (V - V_g)g \quad (4-41)$$

Take a second derivative of equations (4-40) and (4-41):

$$\frac{d^2V}{dx^2} = r \frac{di}{dx} = r(V - V_g)g = rgV - rgV_g \quad (4-42)$$

$$\frac{d^2i}{dx^2} = g \frac{dV}{dx} = gri \quad (4-43)$$

Assume $rg = \lambda^2$ then the two formulae (4-42) and (4-43) become:

$$\frac{d^2V}{dx^2} = \lambda^2V - \lambda^2V_g \quad (4-44)$$

$$\frac{d^2i}{dx^2} = \lambda^2i \quad (4-45)$$

The general solutions of these two equations (4-44) and (4-45) are given by:

$$V = V_1 e^{-\lambda x} + V_2 e^{\lambda x} + V_g \quad (4-46)$$

$$i = i_1 e^{-\lambda x} + i_2 e^{\lambda x} \quad (4-47)$$

Where V_1, V_2, i_1 and i_2 are the coefficients and λ is the characteristic value. The analytical methods used to achieve these general solutions are not only suitable for this single electrode circuit model, but also for the mirrored circuit model as illustrated in Figure 48.

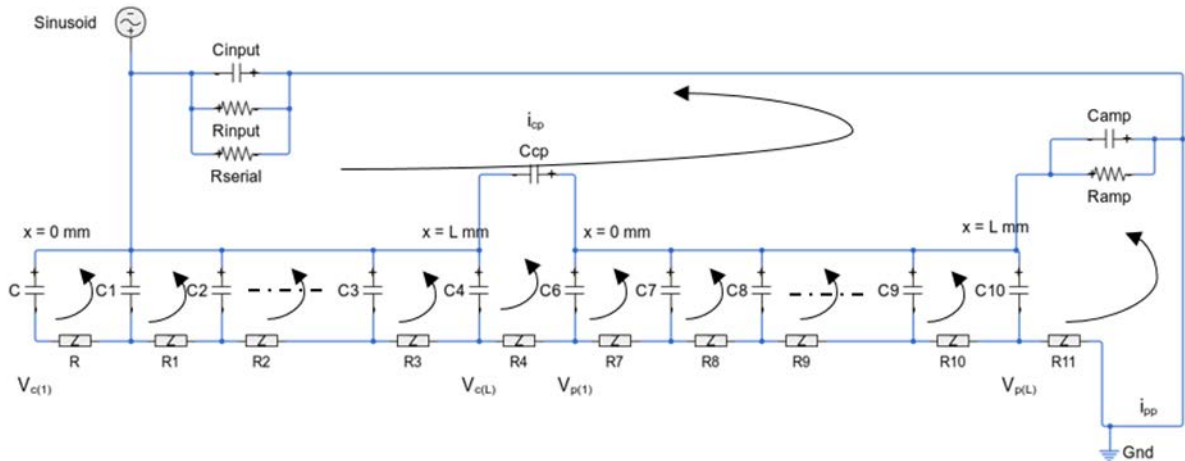


Figure 48: 1D mirrored system circuit model using a resistor-capacitor network with extra components from the complete system circuit (dashed line: potential RC components depending on number of meshes; arrows: assumed network-current flow)

Note: $C_{in} = 4 \text{ pF}$ is the input-capacitance of the NI 9239 ADC; $R_{input} = 1 \text{ M}\Omega$ is the input impedance of the NI 9239 ADC; $R_{serial} = 5 \text{ k}\Omega$ is the series resistor used to limit the input current; the C_{in} and R_{input} are from the NI 9239 ADC which are parallel

connected with the sense resistor R_{serial} . Hence these three components are in-parallel with each other. C_{cp} is the lateral stray capacitance between electrodes C1 and P1. V_{input} is the input potential on the electrode C1.

Specific solutions of this mirrored circuit model are derived from the previous general solutions and will be different because of the altered boundary conditions. Analytical solutions of the mirrored system based on its boundary conditions are given by

$$V_{\text{c}(1)} = V_{\text{c}1} + V_{\text{c}2} + V_{\text{input}} \quad (4-48)$$

$$V_{\text{c}(L)} = V_{\text{c}1} e^{-\lambda L} + V_{\text{c}2} e^{\lambda L} + V_{\text{input}} \quad (4-49)$$

$$i_{\text{c}(1)} = i_{\text{c}1} + i_{\text{c}2} \quad (4-50)$$

$$i_{\text{c}(L)} = i_{\text{c}1} e^{-\lambda L} + i_{\text{c}2} e^{\lambda L} \quad (4-51)$$

$$V_{\text{p}(1)} = V_{\text{p}1} + V_{\text{p}2} + V_{\text{g}} \quad (4-52)$$

$$V_{\text{p}(L)} = V_{\text{p}1} e^{-\lambda L} + V_{\text{p}2} e^{\lambda L} + V_{\text{g}} \quad (4-53)$$

$$i_{\text{p}(1)} = i_{\text{p}1} + i_{\text{p}2} = i_{\text{cp}} \quad (4-54)$$

$$i_{\text{p}(L)} = i_{\text{p}1} e^{-\lambda L} + i_{\text{p}2} e^{\lambda L} = i_{\text{pp}} \quad (4-55)$$

Once the source current, the input voltage, the unit capacitance, and the unit resistance are given, using these equations the current and potential distribution can be calculated. Another method is to use the resistor-capacitor network method, as discussed in the next section. A comparison of the results obtained by the analytical method and the network method will then be given.

4.3.1.2 Resistor-Capacitor Network

For the capacitor formed by electrode C1 and the material surface (Figure 48), the circuit analysis current loops are labelled from left to right as $I_{\text{c}1}$ to $I_{\text{c}N}$; N is the number of cells on the electrode C1. Similarly, the circuit analysis current loops associated with the capacitor formed by P1 are labelled from left to right as $I_{\text{p}1}$ to $I_{\text{p}N}$; $\text{C}(1)$ to $\text{C}(L)$ stand for unit positions on the material surface related to C1, and the potentials are $V_{\text{c}(1)}$ and $V_{\text{c}(L)}$;

$P(1)$ to $P(L)$ are unit positions on the material surface related to P1, and the potentials are $V_{p(1)}$ and $V_{p(L)}$. The equations associated with these current loops are derived using Kirchoff's law that states that the sum of all voltages in a closed network is equal to zero:

$$I_{c1} (2 \Delta Zc + \Delta Z) - I_{c2} \Delta Zc = 0 \quad (4-56)$$

$$I_{c2} (2 \Delta Zc + \Delta Z) - I_{c1} \Delta Zc - I_{c3} \Delta Zc = 0 \quad (4-57)$$

$$I_{cN-1} (2 \Delta Zc + \Delta Z) - I_{cN-2} \Delta Zc - I_{cN} \Delta Zc = 0 \quad (4-58)$$

$$I_{cN} (2 \Delta Zc + \Delta Z) - I_{cN-1} \Delta Zc = I_{cN+1} \Delta Zc \quad (4-59)$$

$$I_{cN+1} = I_{cp} \quad (4-60)$$

$$I_{cN+1} (2 \Delta Zc + Z_{cp} + Z_{tx}) - I_{cN} \Delta Zc - I_{p1} \Delta Zc = I_{source} Z_{tx} \quad (4-61)$$

$$I_{p1} (2 \Delta Zc + \Delta Z) - I_{cN+1} \Delta Zc - I_{p2} \Delta Zc = 0 \quad (4-62)$$

$$I_{pN-1} (2 \Delta Zc + \Delta Z) - I_{pN-2} \Delta Zc - I_{pN} \Delta Zc = 0 \quad (4-63)$$

$$I_{pN} (2 \Delta Zc + \Delta Z) - I_{pN-1} \Delta Zc = I_{pN+1} \Delta Zc \quad (4-64)$$

$$I_{pN+1} = I_{pp} \quad (4-65)$$

$$I_{pN+1} (\Delta Zc + Z_{pp} + Z_{amp}) - I_{pN} \Delta Zc = I_{source} Z_{amp} \quad (4-66)$$

Rearranging these equations into matrix form allows these transformed linear equations to be solved, eventually yielding the output voltage and the dielectric impedance. Thus, the current and potential distributions of three kinds of materials of various resistivity ranges, derived using the analytical method and the network method, are given in Figure 49 to Figure 54. In these three examples, the source current is set as 10^{-3} A. Considering Figure 49 to Figure 54, the X-axis describes the unit position on the material surface. Electrodes C1 and P1 have length of 110 mm and the separation of 25 mm, leading to a processed domain extent of 245 mm. The Y-axis separately shows the potential and the current distributions. The two coloured curves represent the distributions resulting from those two methods.

For the materials having the resistivity from $1 \Omega\text{m}$ to $10^7 \Omega\text{m}$

Figure 49 and Figure 50 show the current and potential distributions on the material surface when the resistivity of the material is $10^7 \Omega\text{m}$. For other resistivity values smaller than $10^7 \Omega\text{m}$, both distributions follow the same curve tendencies as illustrated in Figure 49 and Figure 50 but of different values.

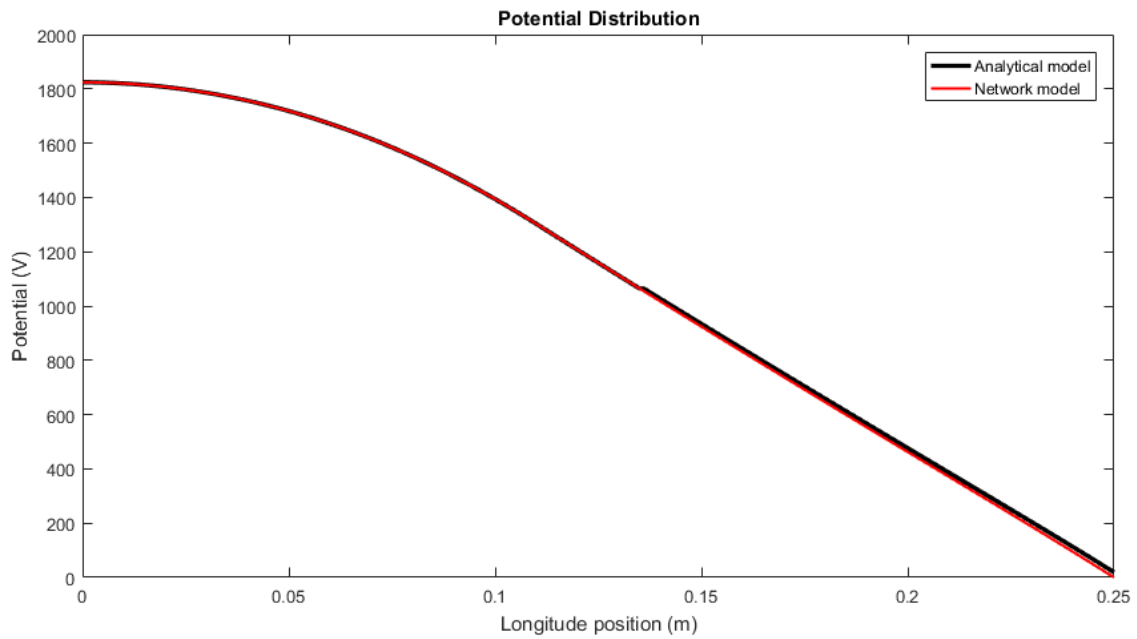


Figure 49: Potential distributions at 5 kHz on the material surface by analytical and network methods ($10^7 \Omega\text{m}$)

Figure 49 shows the potential distribution from the position $C(1)$ to $P(L)$ on the material layer surface, decreasing to zero at the mirrored position-of-symmetry.

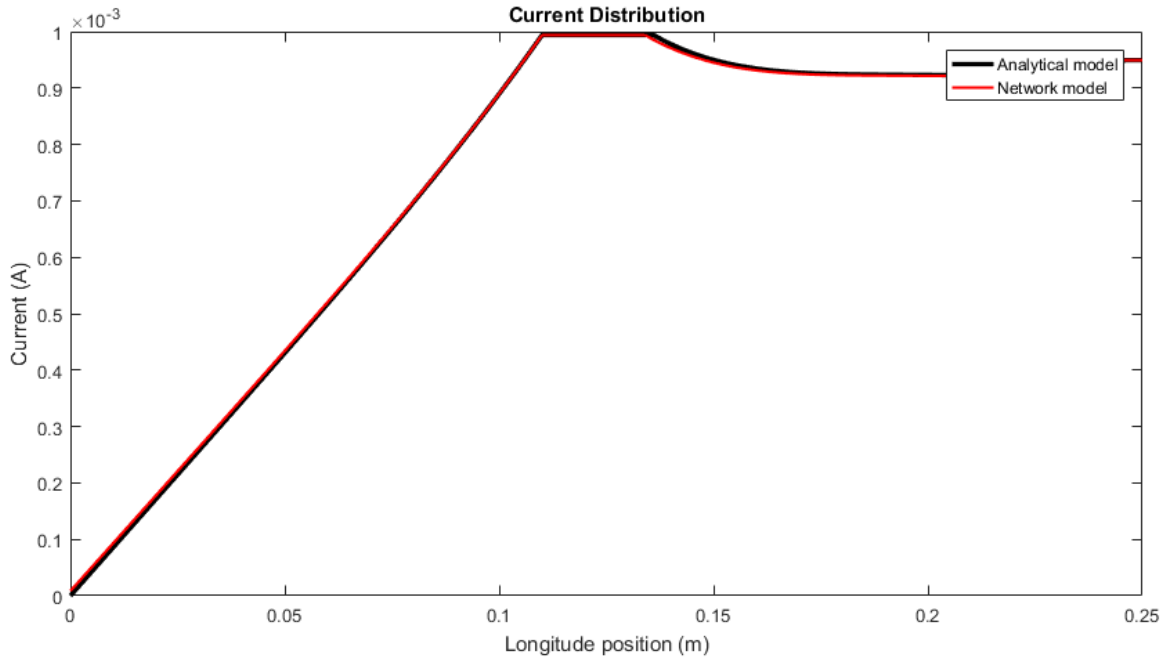


Figure 50: Current distributions at 5 kHz on the material surface by analytical and network methods ($10^7 \Omega\text{m}$)

Figure 50 shows the current distribution from the position $C(1)$ to $P(L)$, with zero current being injected at the outer extremes of the C1 electrode (the specific point, when the X-axis equals 0.11 m, results from the current flow through the spacing area between C1 related material surface and P1 related material surface). In Figure 50, C1 and P1 represent the surface areas related to electrodes C1 and P1, noting that the extent of C1 maps is from 0 m to 0.11 m and the extent of P1 maps is from 0.135 m to 0.245 m. The mirrored system line-of-symmetry occurs at the central position between electrodes P1 and P2, where the separation between P1 and P2 is 10 mm. Thus, an extra 5 mm has to be added to $P(L)$, resulting in the X-axis of all figures being plotted in the range 0 mm to 250 mm.

For the materials having the resistivity from $10^7 \Omega\text{m}$ to $10^9 \Omega\text{m}$

Figure 51 and Figure 52 show the current and potential distributions on the material surface when the resistivity of the material is increased to $10^9 \Omega\text{m}$. For other resistivity values larger than $10^7 \Omega\text{m}$ but smaller than $10^9 \Omega\text{m}$, both distributions follow the same curve tendencies as illustrated in Figure 51 and Figure 52 but with different values.

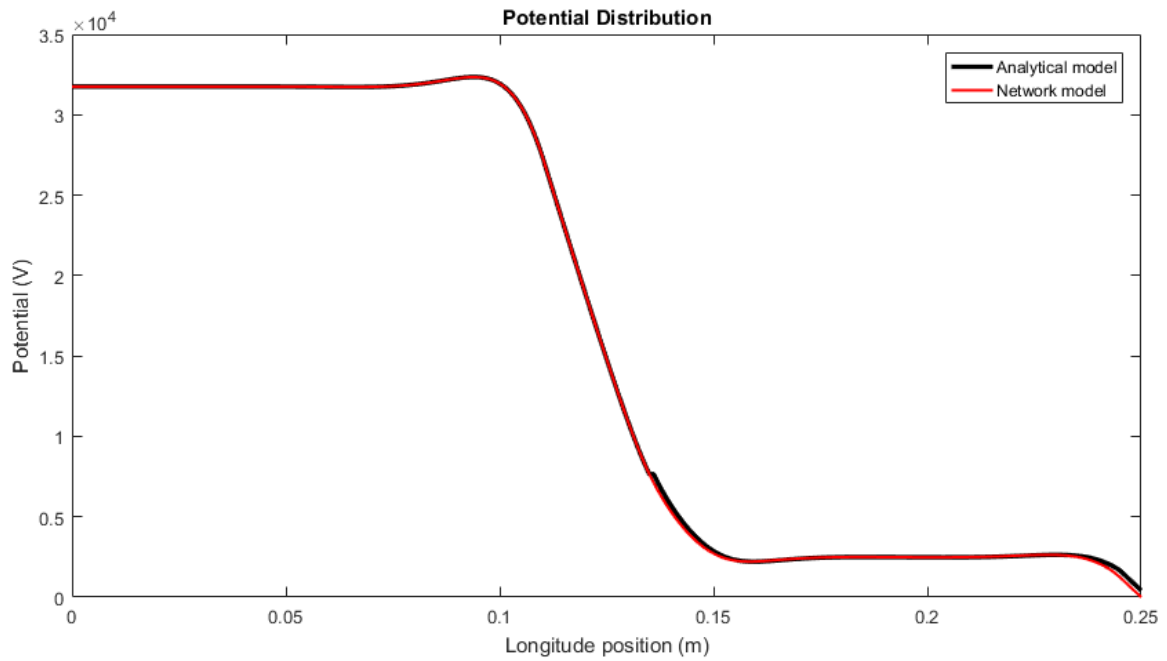


Figure 51: Potential distributions at 5 kHz on the material surface by analytical and network methods ($10^9 \Omega\text{m}$)

Figure 51 shows the potential distribution from the position $C(1)$ to $P(L)$, decreasing to zero at the mirrored position-of-symmetry.

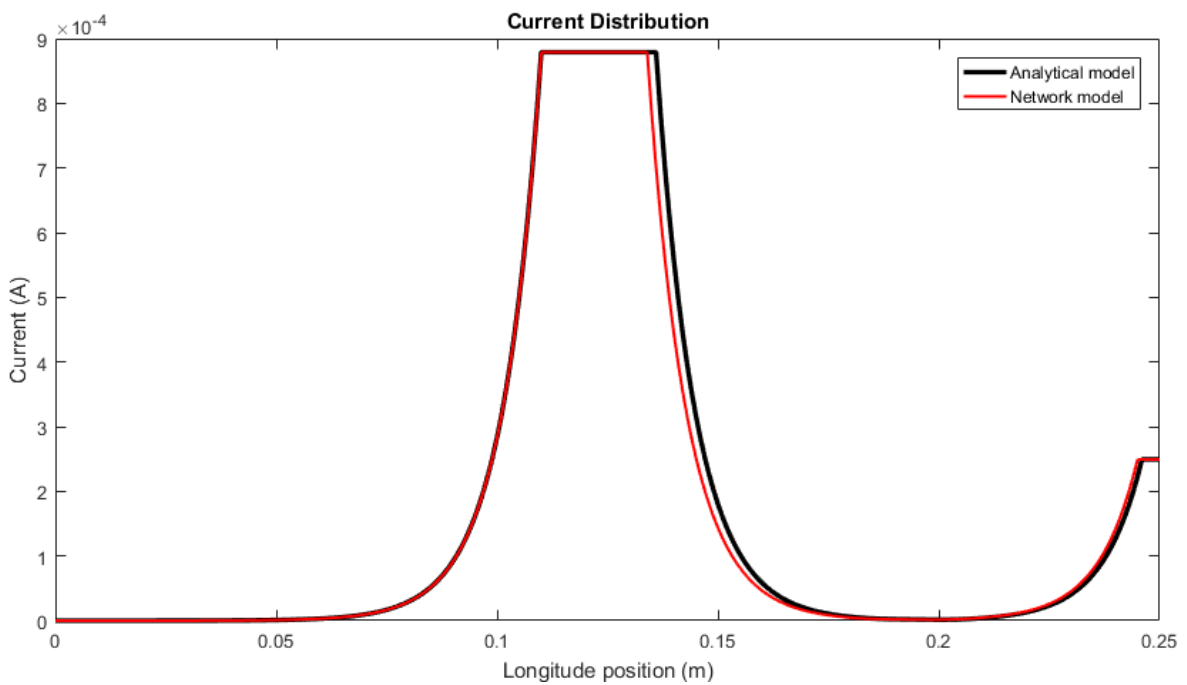


Figure 52: Current distributions at 5 kHz on the material surface by analytical and network methods ($10^9 \Omega\text{m}$)

Figure 52 shows the current distribution from the position $C(1)$ to $P(L)$, with zero current being injected at the outer extremes of the C1 electrode. The potential is almost constant from the position $C(1)$ to $C(L)$ and from the position $P(1)$ to $P(L)$ because of a very small value of injected current. From $C(L)$ to $P(1)$ and from $P(L)$ to the end, the potential drops down quickly because the material has a high resistivity value. The current varies significantly near the edges of the electrodes C1 and P1, which corroborates the expectation that free charges flow out to the edges of the conductor.

For the materials having the resistivity from $10^9 \Omega\text{m}$ to $10^{10} \Omega\text{m}$

Figure 53 and figure 54 show the current and potential distributions on the material surface when the resistivity of the material is increased to $10^{10} \Omega\text{m}$. For other resistivity values larger than $10^9 \Omega\text{m}$ but smaller than $10^{10} \Omega\text{m}$, both distributions follow the same curve tendencies as illustrated in Figure 53 and Figure 54 but with different values.

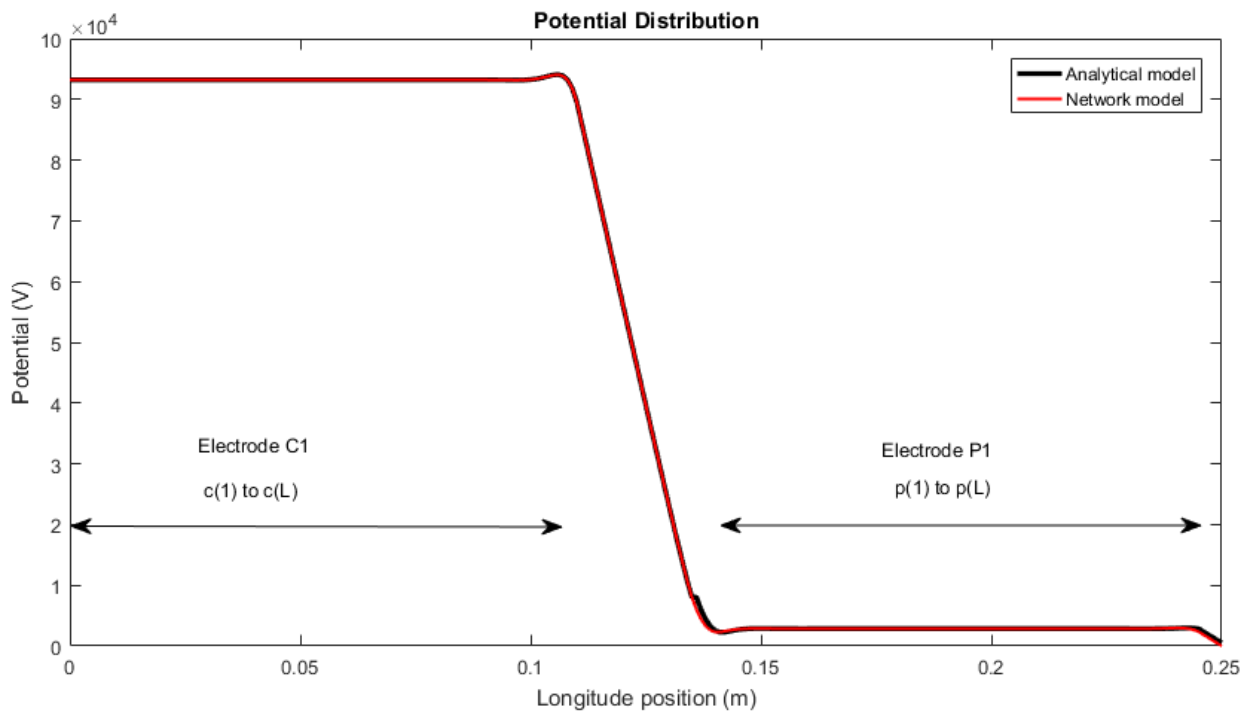


Figure 53: Potential distributions at 5 kHz on the material surface by analytical and network methods ($10^{10} \Omega\text{m}$)

Figure 53 shows the potential distribution from the position $C(1)$ to $P(L)$, decreasing to zero at the mirrored position-of-symmetry.

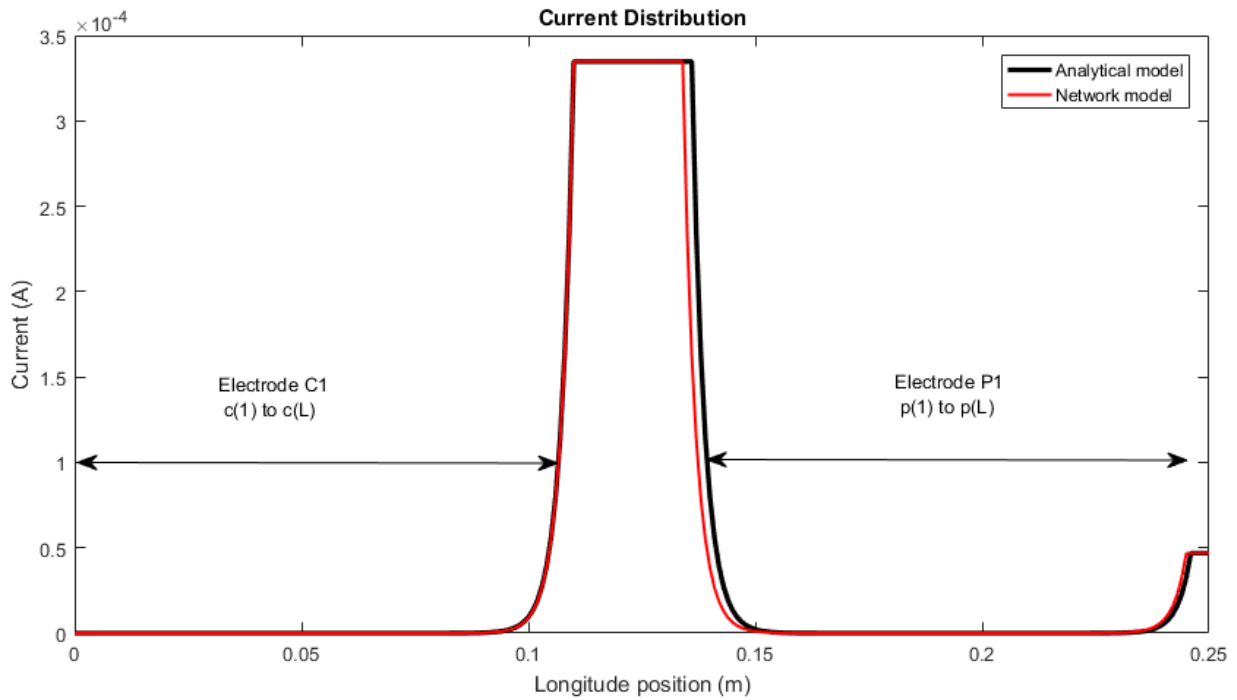


Figure 54: Current distributions at 5 kHz on the material surface by analytical and network methods ($10^{10} \Omega\text{m}$)

Figure 54 shows the current distribution from the position $C(1)$ to $P(L)$, with zero current being injected at the outer extremes of the C1 electrode. A similar conclusion could be made as the conclusion derived from Figure 52.

In summary, as the resistivity of the material increases from $10^7 \Omega\text{m}$ to $10^{10} \Omega\text{m}$, the spatial current distribution in the middle of both electrodes C1 and P1 is almost negligible. However, the spatial current distribution increases sharply on the edges of both C1 and P1 electrodes. The potential distribution on the material surface approaches a constant value as the resistivity of the material increases. The estimated impedance transfer function based on the network method is given by:

$$V_{Out_P1_RightEdge} = (I_{source} - I_{pp}) Z_{amp} \quad (4-67)$$

As the resistivity of the material is assumed and given during the analysis, the relationship curve of predicted resistance related to the resistivity is illustrated in Figure 55.

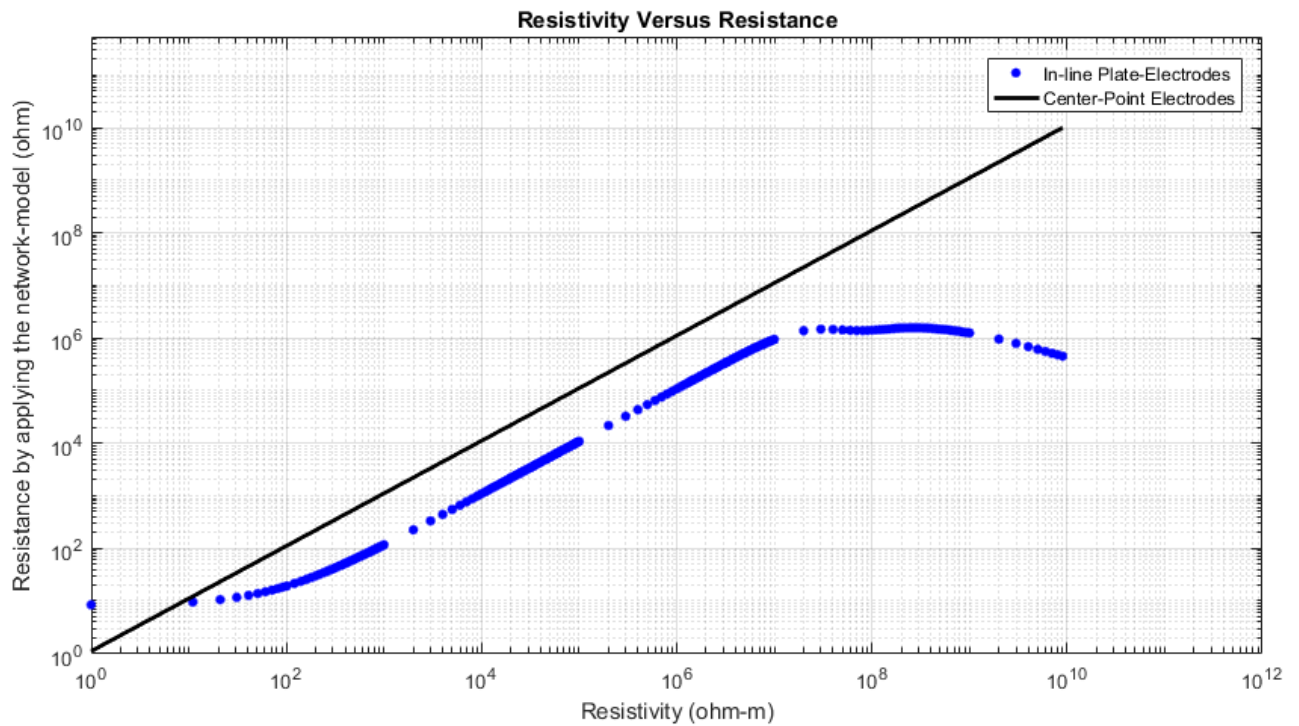


Figure 55: The relationship curve of predicted resistance related to the resistivity (black curve: assumed centre point electrodes of four plate-electrodes of the system; blue curve: from the in-line plate electrodes of the capacitive system)

According to the equation $\rho = kR$, the geometric factor for the material with a resistivity ranging from $1 \Omega\text{m}$ to $10^{10} \Omega\text{m}$ is given in Figure 56. This conveys an important message; that the geometric factor can no longer be assumed to be a constant, but is a function of the properties of the material being measured.

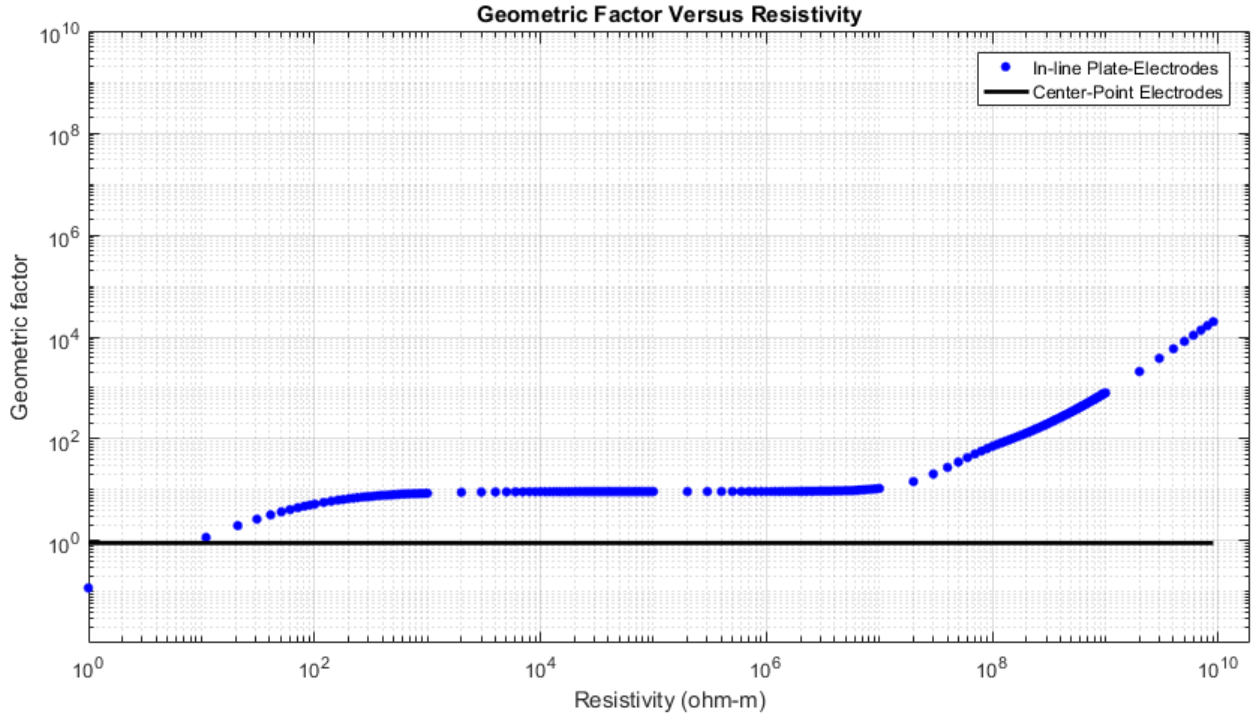


Figure 56: The geometrical factor for materials with resistivity values ranging from $1 \Omega\text{m}$ to $10^{10} \Omega\text{m}$ (black curve: assumed centre point electrodes of four plate-electrodes of the system; blue curve: from the in-line plate electrodes of the capacitive system)

Therefore, once the current and voltage are measured using the capacitive-coupled resistivity system, the electrical resistance and its corresponding geometric factor will be predicted. In this way, the apparent resistivity of pavement materials can be estimated.

4.3.2 Practical experiments using test resistors

To verify the analytical geometric factors, practical experiments applying 26 manufactured resistors of various resistances were conducted. The resistances of these test resistors will be predicted by fitting the predicted resistances and their practical resistances provided by the manufacturer. Here, the practical resistance of a test resistor is denoted as R_{test} and the predicted resistance is denoted as $R_{prediction}$.

$$R_{prediction} = kR_{test} \tag{4-68}$$

The predicted resistance depends on components in the complete circuit model. As the output voltage is sensitive to the parallel-plate capacitance including the fringing capacitances, and the equivalent capacitance of the material before applying the fitting scheme, it is necessary to reduce the number of unknown parameters and obtain an

accurate prediction of these capacitances. First, the fringing effect on the parallel capacitor is discussed. Later on, the fringing capacitances originating from the electrode edges are predicted using a COMSOL model. Thus, the capacitance of the parallel-plate capacitor can be confirmed.

4.3.2.1 Fringing Capacitance

The fringing effect occurs because of the electric field extension out of the overlap area of the two plate electrodes. Figure 57 gives us an overview of the fringing effect because of the edge of the parallel plate capacitor.

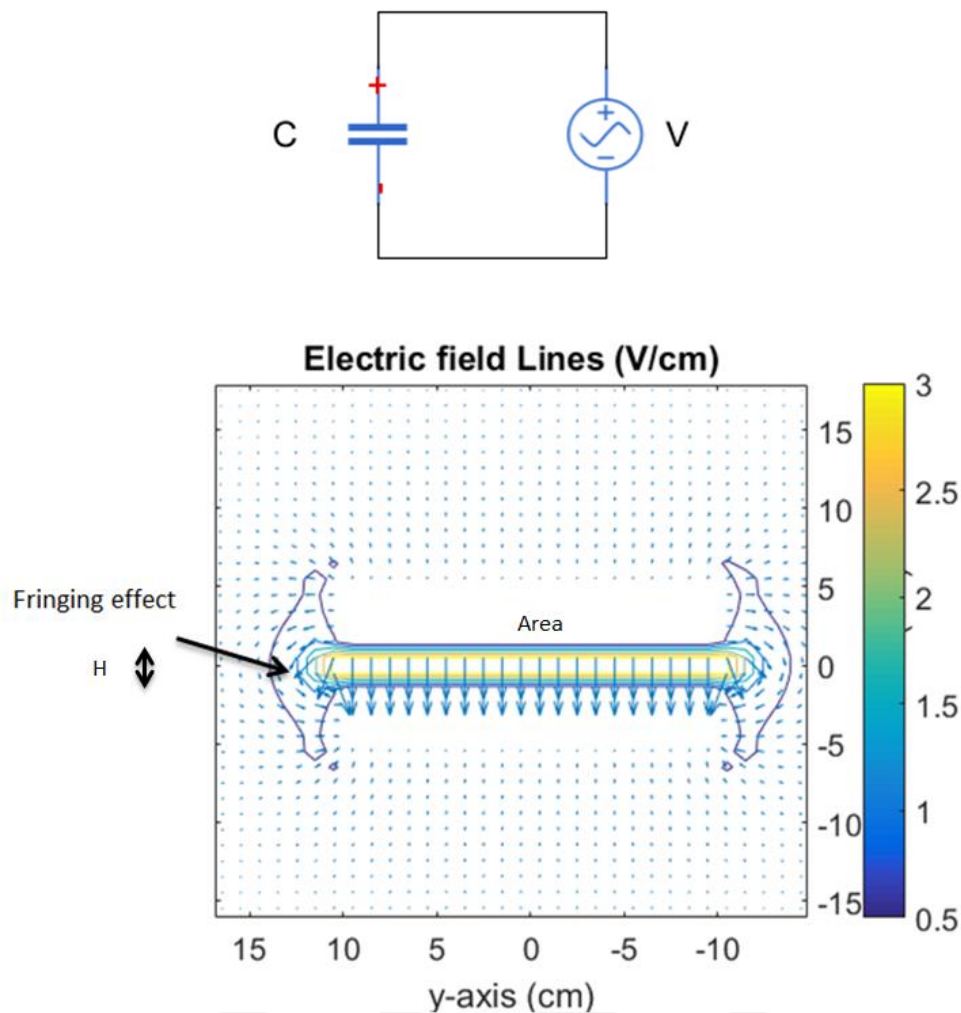


Figure 57: An example of the electric field including the fringing effect of a parallel plate capacitor (upper figure – the circuit shows the topology of the fringing effect of a parallel plate capacitor which is illustrated by the lower-figure)

Note: A 2D finite element method and an iterative method were applied to model the fringing effect of a parallel plate capacitor. The upper and lower electrodes of the capacitor, of length 21 cm, are connected to an AC voltage. The space encompassing the capacitor is divided and meshed into 2D rectangles. Each mesh has both length and width of 1 cm. Figure 57 was generated when a potential of 3 V was applied to the upper electrode and -3 V was applied to the lower electrode. Arrows are used to visualise the electric field. The colour bar on the right side represents electric field strength. The electric field strength gradually decreases from the electrodes of the capacitor to the outer space. The lines at the left and right edges of the capacitor are associated with the fringing effect.

The standard frequently used assumption for the capacitance of a parallel plate capacitor illustrated in Figure 58 is given by

$$C_{parallel} = \epsilon_r \epsilon_0 \frac{Area}{H} \quad (4-69)$$

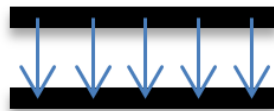


Figure 58: Standard parallel plate capacitor without fringing effects

Where *Area* is the overlap area of the capacitor; *H* is the thickness of the dielectric material between the upper and bottom electrodes.

However, in practice, the measured parallel capacitance is larger than the theoretical value because of the fringing effect. There are many theoretical research papers that discuss fringing effects in detail, especially in the integrated-circuit field. T. Sakurai and K. Tamaru [7] proposed three simple formulas in 1983:

Case 1: a single wire of unit length on a ground plane

$$C = \epsilon_r \epsilon_0 \left(1.15 \left(\frac{W}{H} \right) + 2.80 \left(\frac{T}{H} \right)^{0.222} \right) \quad (4-70)$$

Case 2: three lines of unit length on a ground plane

$$C = \varepsilon_r \varepsilon_0 \left(1.15 \left(\frac{W}{H} \right) + 2.80 \left(\frac{T}{H} \right)^{0.222} \right) + 2\varepsilon_r \varepsilon_0 \left(0.03 \frac{W}{H} + 0.83 \frac{T}{H} - 0.07 \frac{T^{0.222}}{H} \right) \frac{S^{-1.34}}{H} \quad (4-71)$$

Case 3: a single plate of finite dimension on a ground plate

$$C_p = \varepsilon_r \varepsilon_0 \left(1.15 \frac{WL}{H} + 1.40 \frac{T^{0.222}}{H} (2L + 2W) + 4.12 \frac{T^{0.728}}{H} H \right) \quad (4-72)$$

M.I. Elmasry [8] presented a simple equation to calculate the capacitance of the interconnection lines in a MOSFET very-large-scale-integrated-circuit (VLSI) including edge effects:

$$Cp = \varepsilon_r \varepsilon_0 \frac{WL}{H} \left(1 + 2 \frac{H}{W} \ln \left(1 + \frac{T}{H} \right) + 2 \frac{T}{W} \ln \left(1 + \frac{W/2}{T+H} \right) \right) \quad (4-73)$$

Where W is the width; L is the length; T is the thickness.

In 2015, G. Shomalnasab [9] built an analytical model to compute the coupling capacitance between interconnects on the same or different layers, and the substrate capacitance in very-large-scale-integrated-circuits (VLSI). The equation reproduced below described the substrate capacitance of a square metal block with an overlap capacitance and four side-wall fringe components considered.

$$C = \varepsilon_r \varepsilon_0 \frac{WL}{H} + 4 \cdot \frac{2\varepsilon_r \varepsilon_0}{\pi} \ln \left(1 + \frac{T}{H} \right) \left(\frac{H}{T} + 1 + \frac{X}{T} \right) \quad (4-74)$$

For the top, bottom, or side unit capacitance, the formula is going to be:

$$C_{top/bottom/side} = \frac{\varepsilon_r \varepsilon_0}{\pi} \ln \left(1 + \frac{2w_e}{s} \right) \quad (4-75)$$

Where w_e is the effective fringing edge width (this factor is always decided by fitting); s is the separation between two plates.

The measured capacitance of 172.7 pF, in the experiment mentioned in section 4.2.4, is used as a reference here to verify the performances of those equations. The relationship curve of predicted capacitances related to the width computed by equations proposed by Sakurai, Elmasry, Shomalnasab and the standard used equation are displayed in Figure 59.

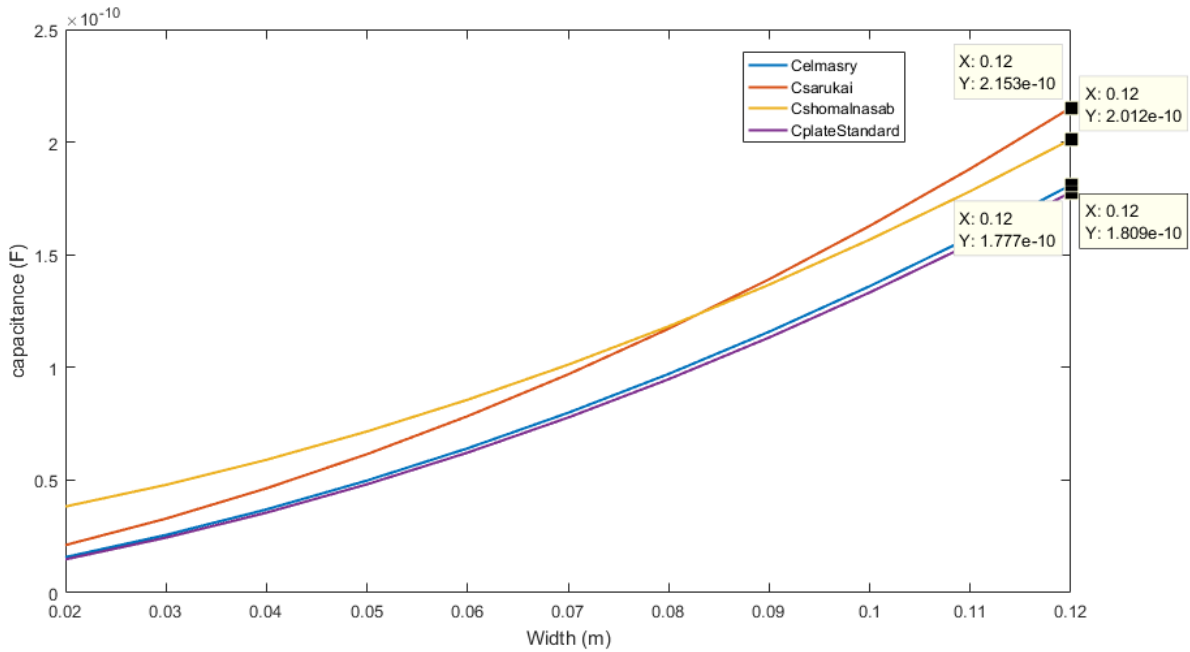


Figure 59: Analytical capacitances of a parallel plate capacitor by three methods

The errors between the measured capacitances and the predicted capacitances using these three methods are 21.14% (Sakurai's method), 1.82% (Elmasry) and 13.2% (Shomalnasab). In this work, equations (4-73) and (4-74) are utilised because of their accuracies. The overlap capacitance C_{c1} from equation (4-69) is 118.0983 pF. Practically, C_{c1} should be larger than that theoretical value. To reduce the fringing effect generated by the edges of the electrodes, a guard ring surrounding electrode P1 and P2 is applied. In this way, the fringing effect from electrodes to the bottom surface will be significantly reduced and the value of the parallel-plate capacitance would be closer to the simplistic model of capacitance. As the capacitive-coupled resistivity system's performance is expected to be very sensitive to the stray coupling capacitance C_{cp} between electrodes C1 and P1 (the capacitance C_{amp} depends on the internal system), it is important to discuss C_{cp} here. The stray coupling capacitance C_{cp} in free space is much larger than the stray capacitance C_{cp} when a copper sheet is placed on the bottom surface.

4.3.2.2 Practical experiment in free space (high resistivity)

The capacitive-coupled resistivity system is placed in free space by placing four corners of the system platform on four chairs. The "pavement layer" here becomes the air and the non-ideal air can be recognized as a material of high resistivity. The parameter resistivity r

is assumed to be a high value in the circuit model, as illustrated in Figure 60, by the network method.

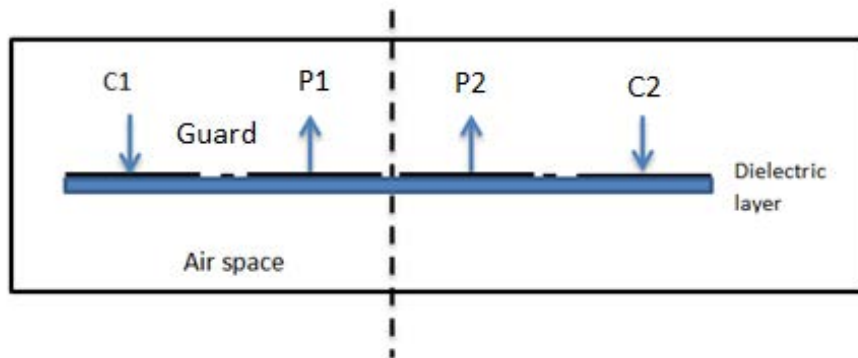


Figure 60: Analytical circuit diagram by placing a capacitive-coupled resistivity system in free space

The circuit diagram of the mirrored system in free space is given by Figure 61. To solve the voltage appearing on the stray coupling capacitance C_{cp} , the circuit model of the mirrored system in free space is given in Figure 62 and the potentials at nodes A and B must be predicted.

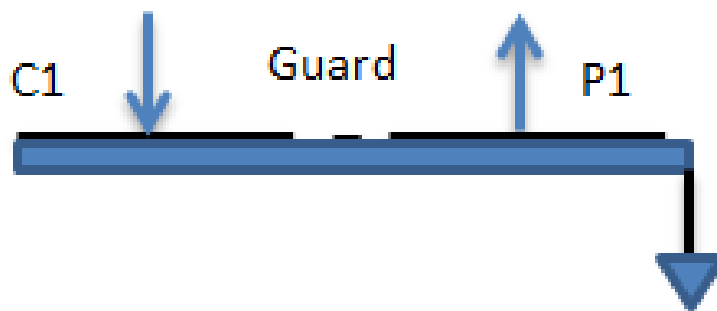


Figure 61: Analytical half-mirrored circuit diagram by placing a capacitive-coupled resistivity system in free space

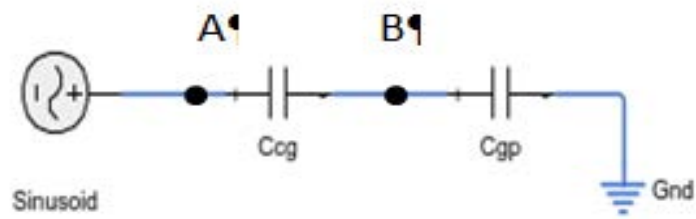


Figure 62: Analytical half-mirrored circuit model by placing a capacitive-coupled resistivity system in free space

In Figure 62 C_{cg} is the coupling capacitance between the electrode C1 and the guard ring; C_{gp} is the coupling capacitance between the electrode P1 and the guard ring. The current is induced by the stray coupling capacitors C_{cg} and C_{gp} . The admittances at nodes A and B are predicted by modelling the capacitive-coupled resistivity system in free space using a COMSOL FEM model (Figure 63) and then comparing the measured voltages and currents' values at these two nodes.

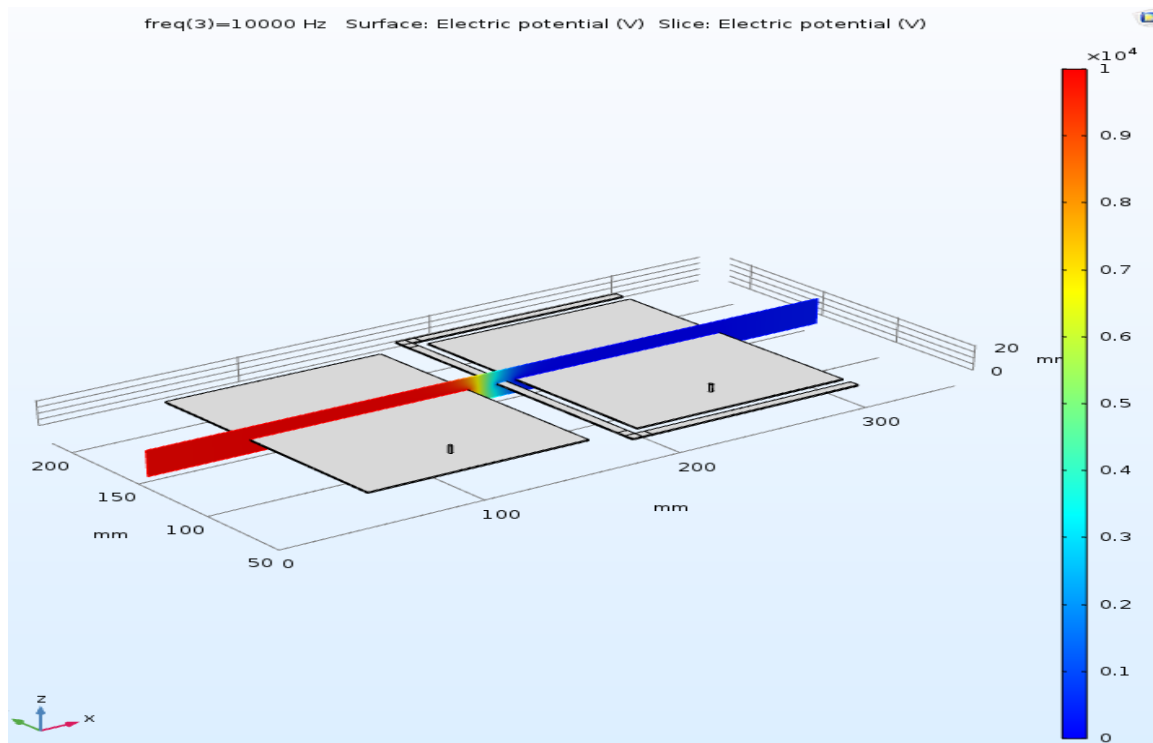


Figure 63: COMSOL modelling of the capacitive-coupled resistivity system in free space

This COMSOL model has the same configuration (e.g. operating frequency and voltage source) as the mirrored system in free space, with extra components of R_{input} , C_{input} and R_{serial} considered. From the COMSOL modelling results, the stray coupling capacitances are:

$$C_{cp} = 1.5885 \text{ pF}$$

$$C_{gp} = 8.7272 \text{ pF}$$

These two values of C_{cp} and C_{gp} come from COMSOL simulation results of admittances, which are calculated by measuring the potential on nodes of A and B and the current flowing through the A-B route, in the Figure 61, Figure 62 and Figure 63 (a COMSOL model of circuits shown in Figure 61 and Figure 62).

$$\text{Since } C_{cp} = \frac{C_{gp} C_{cg}}{C_{gp} + C_{cg}} \tag{4-76}$$

Hence, $C_{cg} = 1.9420 \text{ pF}$ as discussed in the previous sections, the voltage is sensitive to sub-surface equivalent capacitance and parallel plate-electrode capacitance (C_{cg} contributes to this parallel capacitance).

The impedance transfer function is deduced using the network method (Figure 48) on the mirrored system. Note: $R_{input} = 1 \text{ M}\Omega$ is the input impedance of the ADC; $C_{input} = 4 \text{ pF}$ is the input capacitance of NI 9239 ADC; $R_{serial} = 5 \text{ k}\Omega$ is the series resistor connected in-line with the transmitter buffer amplifier; C_{tx} is the capacitance between two current transmit copper wires; $C_{cp} = 1.5885 \text{ pF}$ is the lateral stray capacitance between electrode C1 and electrode P1; R_{air} is the resistance of the air; $R_{amp} = 100 \text{ M}\Omega$ is the internal resistance of the receiver amplifier; C_{amp} is the input capacitance of the receiver amplifiers.

The predicted impedance is estimated by using a least square fitting scheme with three unknown parameters R_{air} , C_{amp} and C_{cp} . Figure 64 shows the comparison of the predicted impedance and the measured impedance when the capacitive-coupled resistivity system operates at frequencies from 50 Hz to 21 kHz in free space with a frequency step of 50 Hz. The X and Y-axis represent the resistance and reactance components of the impedance. In the figure, to compare the resistance and the reactance, the X-axis and Y-

axis are set to be of equal-scale resulting in negative values of the X-axis scale appearing. In practical measurements, all resistances are of positive values.

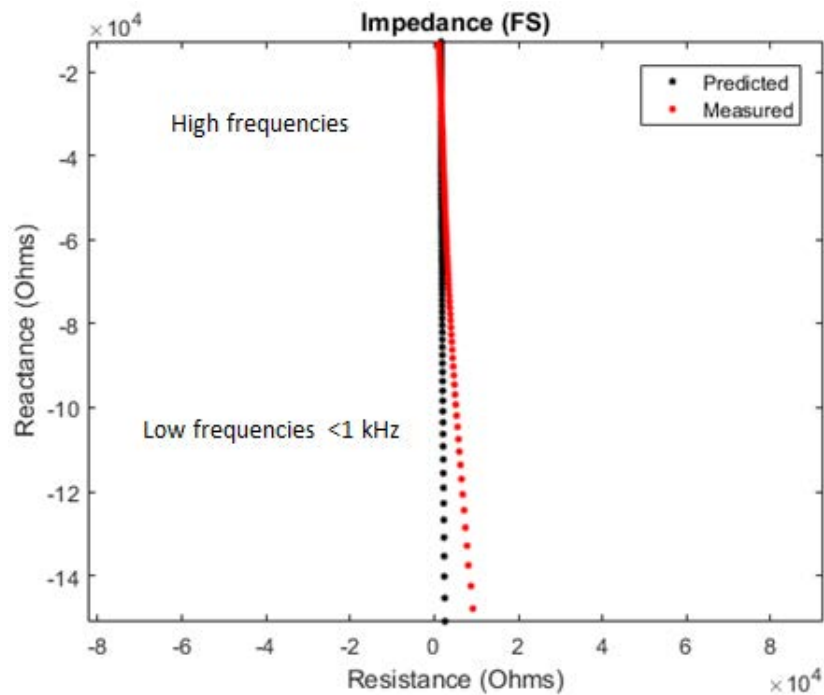


Figure 64: Fitted impedance of the capacitive-coupled resistivity system operated in free space (FS)

From Figure 64, it is seen that the predicted impedance from 1 kHz to 21 kHz fits the practical data well. Points at low frequencies (<1 kHz) are not fitted very well, which makes sense according to the frequency choice discussed in section 4.2. The near vertical line (predicted line in black) indicates that for the measured impedance, its component of reactance is more sensitive to operating frequency than the resistance. This can explain the constant value of fitted resistance and changeable value of fitted reactance during the fitting mechanism. To confirm the value of reactance-corresponding capacitance, other parameters with confirmed values are needed. The predicted resistance of the free space is $12 * 10^3 \Omega$, an artefact of the model. C_{amp} is 13.3 pF. The predicted capacitance of C_{cp} is 1.68 pF. This should be compared with $C_{cp} = 1.5885$ pF calculated using COMSOL, an error of 5.7%.

4.3.2.3 Practical experiment on copper sheet (very low resistivity)

A copper sheet was added to the bottom of the dielectric layer, which is highlighted by a yellow line in Figure 65. Compared to the free space case, there are four parallel capacitors of relatively large value formed by electrodes C1, P1, P2, C2 and the bottom copper sheet.

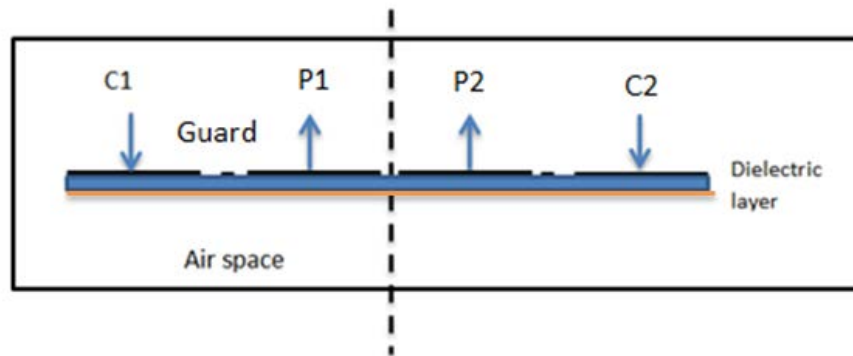


Figure 65: Analytical circuit diagram formed by placing the capacitive-coupled resistivity system onto a copper sheet

In order to simplify the circuit analysis, a mirrored circuit as illustrated in Figure 66 is applied. To calculate fringing capacitances, in this half circuit model, electrode P1 was set as ground (in the practical circuit analysis, all electrodes and dielectrics were of floating potentials) as it was supposed not to affect fringing capacitances; the injected current was provided via electrode C1; the guard ring and the bottom copper sheet were set to have floating potential.

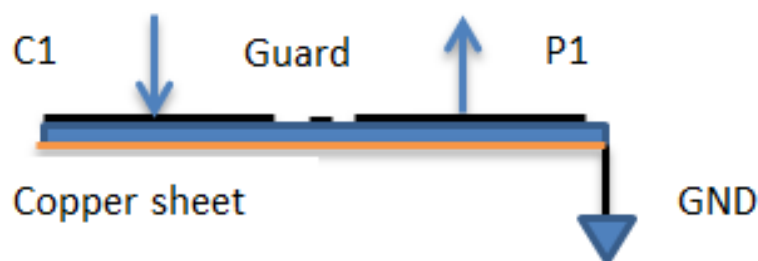


Figure 66: Analytical half mirrored circuit diagram by placing the capacitive-coupled resistivity system onto a copper sheet

The circuit model of this mirrored system is given in Figure 67. Capacitances C_{c1} , C_{p1} , C_{cg} , C_{gp} and C_g are calculated by using two current (I_{c1} , I_{p1}) and voltage networks. In this way, the fringing capacitance C_{cp} is predicted.

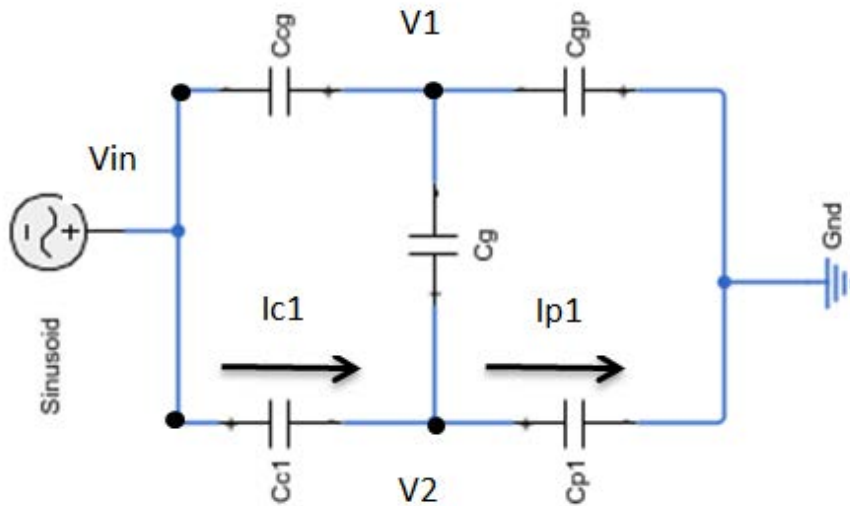


Figure 67: Analytical half mirrored circuit model generated by placing the capacitive-coupled resistivity system onto a copper sheet

The values of the four capacitances are estimated by using COMSOL to model this circuit (Figure 68), and the network method. This COMSOL model has the same configuration (e.g. operating frequency and voltage source) as the mirrored system placed on a copper sheet, with the extra components of R_{input} , C_{input} and R_{serial} considered.

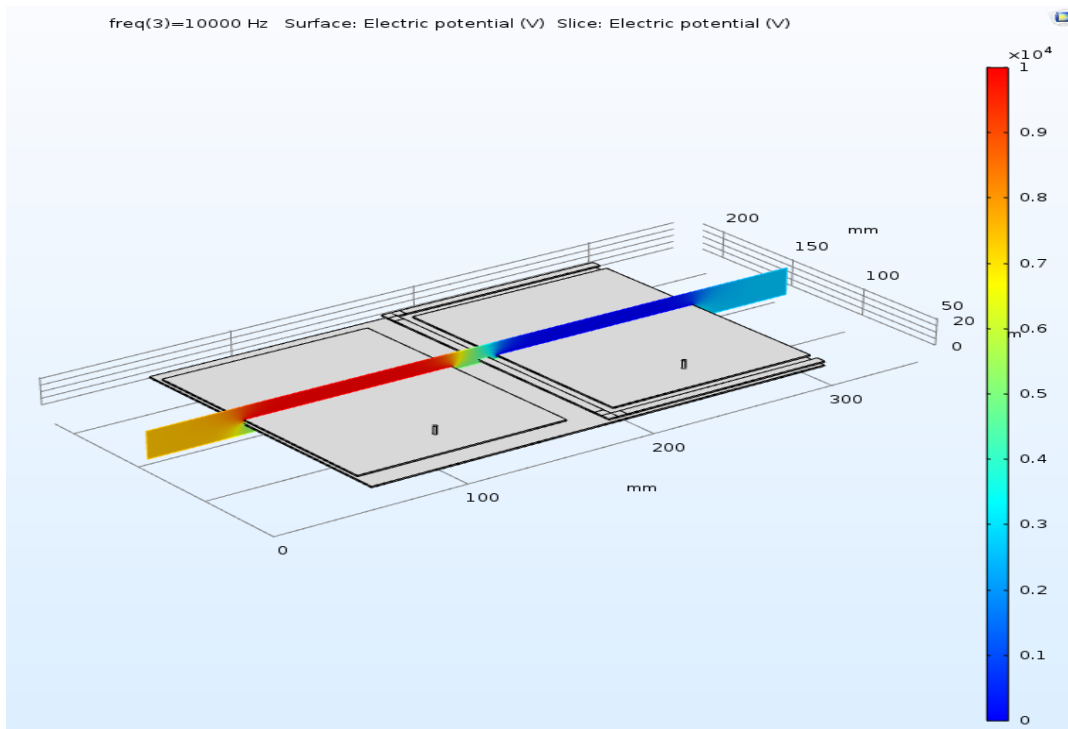


Figure 68: COMSOL modelling of the capacitive-coupled resistivity system placed on a copper sheet

From the COMSOL modelling results, the coupling capacitances are

$$Z_{c1} = \frac{1}{j\omega C_{c1}} = \frac{V_{in}-V_2}{I_{c1}} \quad (4-77)$$

$$Z_{cg} = \frac{1}{j\omega C_{cg}} = \frac{V_{in}-V_1}{I_{in}-I_{c1}} \quad (4-78)$$

$$Z_{gp} = \frac{1}{j\omega C_{gp}} = \frac{V_1}{I_{in}-I_{p1}} \quad (4-79)$$

$$Z_g = \frac{1}{j\omega C_g} = \frac{V_2-V_1}{I_{c1}-I_{p1}} \quad (4-80)$$

So,

$$C_{cg} = 0.39 \text{ pF}$$

$$C_{gp} = 0.56 \text{ pF}$$

$$\text{Hence, } C_{cp} = 0.23 \text{ pF}$$

The value of C_{cp} derived under free space conditions is much larger than the value obtained when the device is placed on a copper sheet. This is because part of the fringing capacitance is blocked when a copper sheet is placed close to the sensor electrodes to form the parallel capacitors. Furthermore, a guard ring around potential electrodes P1 and P2 greatly reduces the fringing effects between electrode C1 and electrode P1 in both situations.

The impedance transfer function for the copper sheet case is also deduced by using a network method (Figure 48) assuming a mirrored system. Note: $R_{input} = 1 \text{ M}\Omega$ is the input impedance of the NI 9239 ADC; $C_{input} = 4 \text{ pF}$ is the input capacitance of the NI 9239 ADC; $R_{serial} = 5 \text{ k}\Omega$ is the series resistor; C_{tx} is the capacitance between two current-transmitting copper wires; $C_{cp} = 0.23 \text{ pF}$ is the lateral capacitance between electrode C1 and electrode P1; R_c is the predicted resistance of the copper sheet; $R_{amp} = 100 \text{ M}\Omega$ is the resistor connecting the potential electrode to the reference earth; $C_{amp} \cong 13.3 \text{ pF}$ is the estimated input capacitance of the amplifiers; $C_{plate} \cong 118 \text{ pF}$ is the capacitance between each electrode plate and the bottom copper sheet.

The predicted impedance is estimated by using a least square fitting scheme with three unknown parameters R_c , C_{amp} and C_{cp} . Figure 69 shows the comparison of the predicted impedance and the measured impedance when the capacitive-coupled resistivity system operates at frequencies from 50 Hz to 21 kHz, placed on a copper sheet with a frequency step of 50 Hz. The X and Y-coordinates represent the resistance and reactance components of the impedance. In the figure, to compare the resistance and the reactance, the X-axis and Y-axis are set as equal-scale resulting in negative values of the X-axis scale appearing. In practical measurements, all resistances are of positive values.

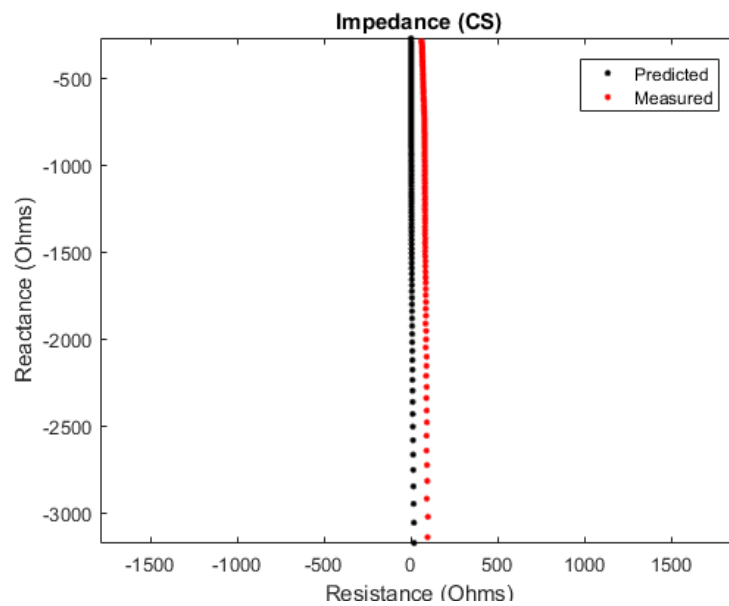


Figure 69: Fitted impedance of the capacitive-coupled resistivity system when placed on a copper sheet (CS)

The predicted resistance of the copper sheet $R_c = 0.06 \text{ m}\Omega$. C_{amp} is equal to 11 pF. The predicted capacitance of $C_{cp}=0.32 \text{ pF}$; compared with the value of $C_{cp}=0.23 \text{ pF}$ calculated from COMSOL, the error is 39%.

The possible reasons for the variations in this fitting result are:

- The copper sheet impedance varies as a function of frequency and also the sheet thickness. The copper sheet impedance estimated at a wide range of frequencies is discussed in the following section. Updated results are then presented when the model of the copper sheet is replaced by a function of frequency and thickness.
- The existence of additional parasitic capacitances.

- The leakage current that may exist in a non-ideal parallel plate capacitor.
- The poor signal-to-noise ratio at low frequencies (<1 kHz) due to very low injection current values.

4.3.2.4 Skin effects on copper sheet impedance over a wide range of frequencies

Ashraf [10] provides a very accurate analytical solution for the AC resistance of rectangular foils at low frequencies and also high frequencies (microwave) using three combined techniques of conformal mapping, power series and asymptotic matching. Two-dimensional methods were applied to these three combined techniques to achieve an accurate solution for the skin effect resistance. Ashraf's research stated that this method is valid over the entire frequency range from zero frequency to high frequencies exceeding 10 MHz.

Approximating a rectangular foil section into an elliptical conductor by a conformal mapping technique, the AC resistance of the foil is given by

$$R_{ac} = \frac{\rho K\left(\frac{h}{a}\right)}{\pi^2 \delta a} \left(1 - e^{-\frac{2b}{\delta}}\right) \quad (4-81)$$

$$\delta = \frac{1}{\sqrt{\pi f \mu_0 \sigma}} \quad (4-82)$$

Where $K\left(\frac{h}{a}\right)$ is the complete elliptic integral of the first kind with modulus $\frac{h}{a}$; a is the major semi-axis of the ellipse and b is the minor semi-axis of the ellipse; $h = \sqrt{a^2 - b^2}$ which is the focal distance of the ellipse; ρ is the resistivity, σ is the conductivity and δ is the skin depth; μ_0 is the permeability in vacuum.

This conformal mapping equation is not only suitable at higher frequencies but also valid at lower frequencies. Another equation derived using power series and asymptotic matching is:

$$R_{ac} = \sqrt{\frac{f_0 \mu_0 \rho}{\pi}} \frac{K\left(\frac{h}{a}\right)}{\pi a} \frac{f}{f_0} \frac{\beta}{r} \quad (4-83)$$

Where f_0 is the upper cut-off frequency; β is half of r ;

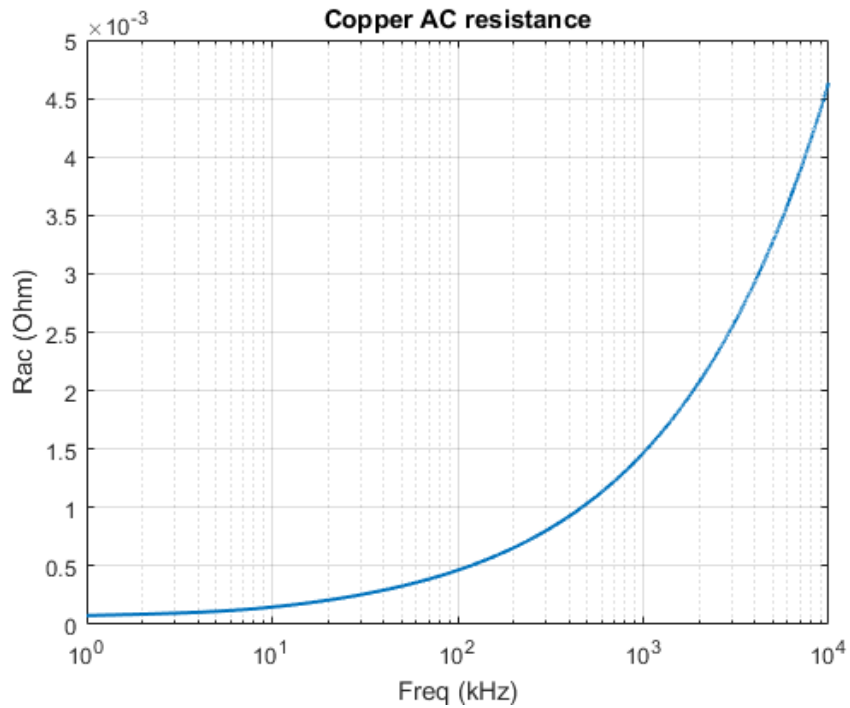


Figure 70: The resistance relationship of copper to operating frequencies (1 Hz-10 MHz) when an AC signal is applied

This AC resistance function ($< 0.5 \times 10^{-3} \Omega$) of the rectangular foil related to the frequencies (Figure 70) is applied to the previous fitting scheme, see Figure 71.

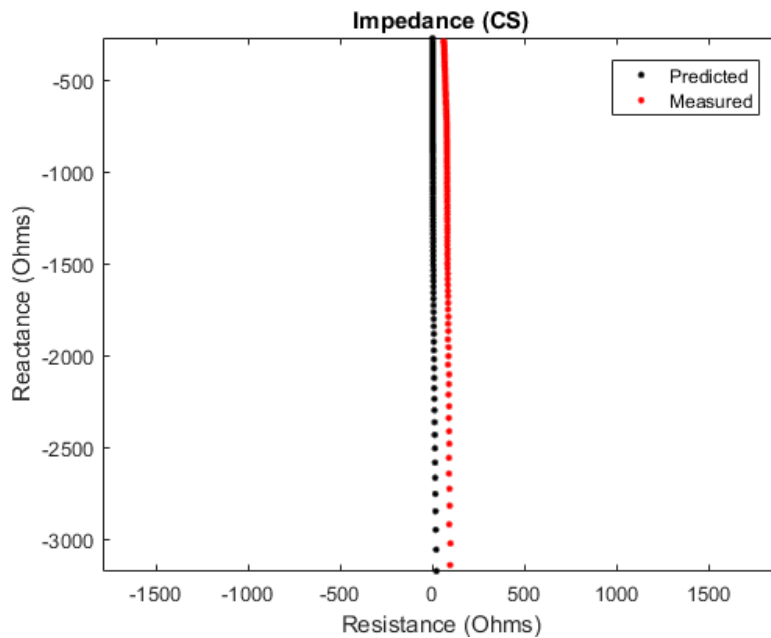


Figure 71: Fitted impedance of capacitive-coupled resistivity system on copper sheet (CS) by using AC copper resistance

From Figure 71, it can be seen that the fitting result does not improve compared to Figure 69. The impact of leakage currents will be introduced later. The components predicted by a least square fitting using measured impedance values obtained from two experiments in free space and on a copper sheet, are summarized in Table 7.

Table 7: Components of predicted values for both cases of free space and copper sheet

Case	C_{input} (pF)	R_{input} (Ω)	R_{serial} (Ω)	C_{stray} (pF)	C_{cp} (pF)	C_{amp} (pF)	r (Ωm)
Free Space (FS)	4	10^6	$5 \cdot 10^3$	1.5	1.68	13.3	$12 \cdot 10^3$
Copper Sheet (CS)	4	10^6	$5 \cdot 10^3$	0.3	0.32	11	$0.0452 \cdot 10^{-3}$

4.3.2.5 Practical experiments using test resistors

Practical experiments using the capacitive-coupled resistivity system in free space and placed on a copper sheet were used to mimic two extreme situations of very low resistivity and very high resistivity. Ideally, a set of materials with known resistivity values would be available to allow rigorous testing of the device. However, the lack of such materials led to the development of a physical analogue based on secondary electrodes and discrete resistors. To verify the performance of the system when operating with resistivity values between these two extremes, 26 resistors with values ranging from 4 Ω to 680 k Ω were measured using the capacitive-coupled resistivity system at operating frequencies from 2 kHz to 20 kHz. The capacitive-coupled resistivity system was placed on a low-density foamed PVC board with four copper electrodes that matched the spatial arrangement of electrodes C1, P1, P2 and C2 (Figure 72). The dimensions of these four electrodes are shown in Table 8.

Table 8: Electrode dimensions

Electrode	Length (mm)	Width (mm)
Copper electrodes on white board	125	90

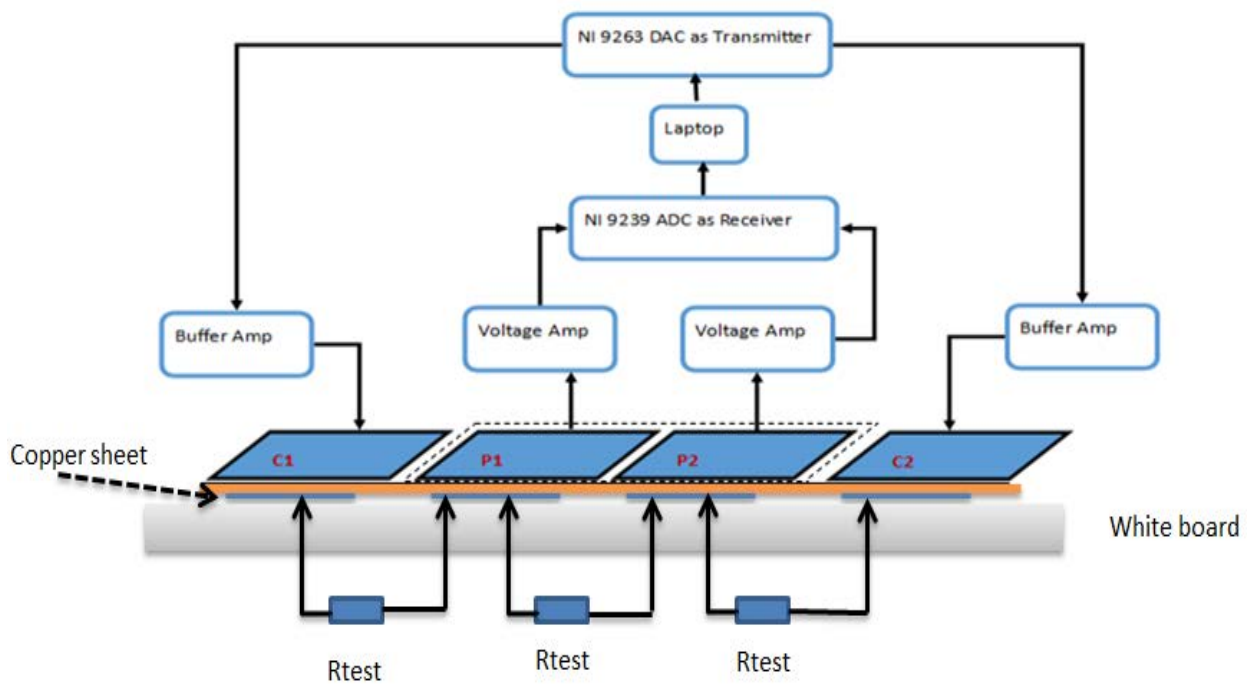


Figure 72: Sketch of practical experiments using test resistors connected to a set of electrodes used to simulate materials of varying resistivity

As indicated in Figure 72 and Figure 73, three resistors were connected between adjacent test electrodes. The circuit model illustrated in Figure 73 assumes that the test resistors are of equal value, $R_{\text{test}} = R_{\text{test1}} = R_{\text{test2}}$. For each measurement, three test resistors of values: 4Ω , 10Ω , 22Ω , 33Ω , 47Ω , 100Ω , 323Ω , 671Ω , $1 * 10^3 \Omega$, $3 * 10^3 \Omega$, $5 * 10^3 \Omega$, $7.47 * 10^3 \Omega$, $10 * 10^3 \Omega$, $11.6 * 10^3 \Omega$, $21.6 * 10^3 \Omega$, $30 * 10^3 \Omega$, $46 * 10^3 \Omega$, $63 * 10^3 \Omega$, $82 * 10^3 \Omega$, $100 * 10^3 \Omega$, $120 * 10^3 \Omega$, $150 * 10^3 \Omega$, $180 * 10^3 \Omega$, $270 * 10^3 \Omega$, $680 * 10^3 \Omega$ were used.

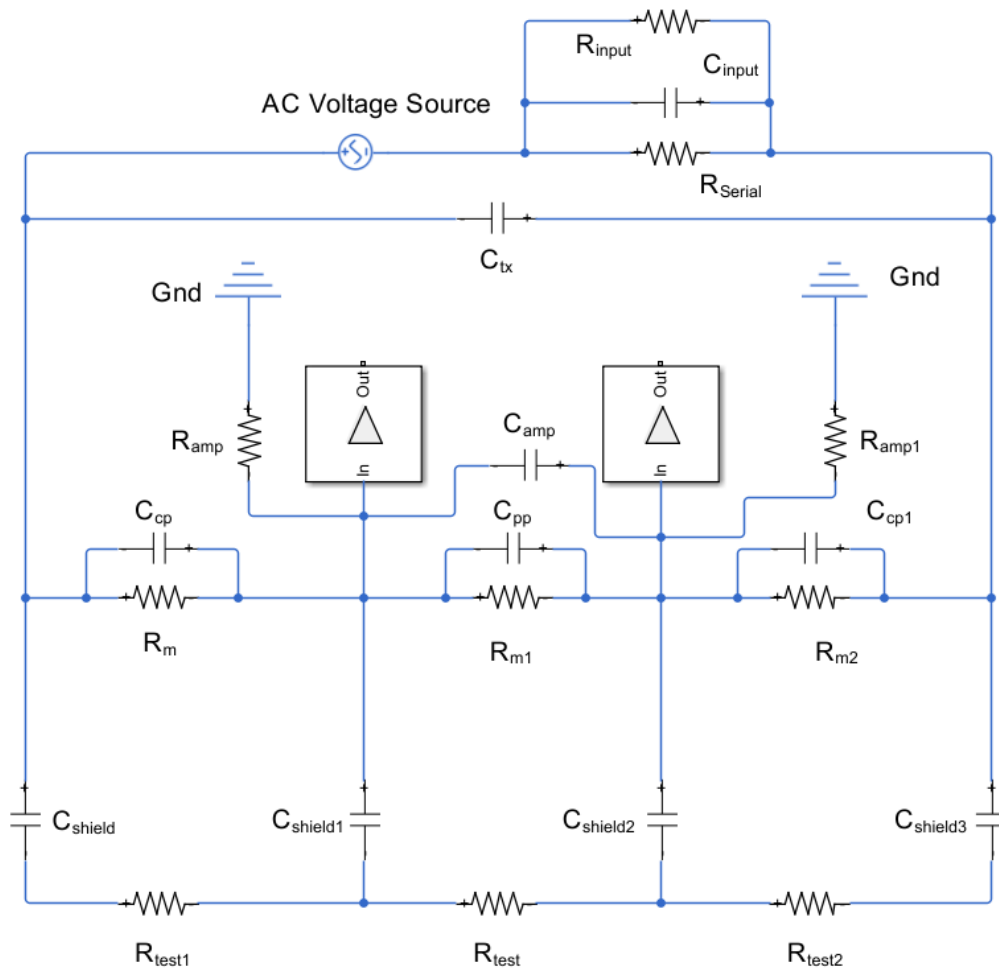


Figure 73: Circuit model of the capacitive-coupled resistivity system placed on discrete test resistors

Note: other components are the same as the case for the capacitive-coupled resistivity system placed on a copper sheet; $R_{\text{test}} = R_{\text{test1}} = R_{\text{test2}}$ are the test resistors.

For each measurement of a test resistor value, the related output impedance function is fitted to the practical impedance measurement by using a least square method and the network method, in a similar manner to that conducted for the free space and the copper sheet cases. Three unknown components $R_{\text{PredictTest}}$, C_{WireCap} and C_{amp} have to be predicted. The $R_{\text{PredictTest}}$ is the predicted resistance of the test resistor; C_{WireCap} is the parasitic capacitance between the connecting wires of the test resistors. The predicted results for all of these test resistors are given in Figure 74 to Figure 97. In these figures, to compare resistances and reactance, the X-axis and Y-axis are set to be of equal-scale resulting in negative values of the X-axis scale appearing. In practical measurements, all resistances are of positive values. Nearly vertical lines (in black) indicate that for measured

impedance, its component of reactance is more sensitive to operating frequency than the resistance. When test resistors are of resistance values larger than $62 \times 10^3 \Omega$, at high frequencies, reactance values tend to increase as resistance values tend to decrease. This is contrary to the phenomena illustrated by previous impedance results when the resistance values were smaller than $62 \times 10^3 \Omega$. One reason is possibly that of high-frequency parasitic components e.g. inductance (these have been ignored at the frequency range used in this work).

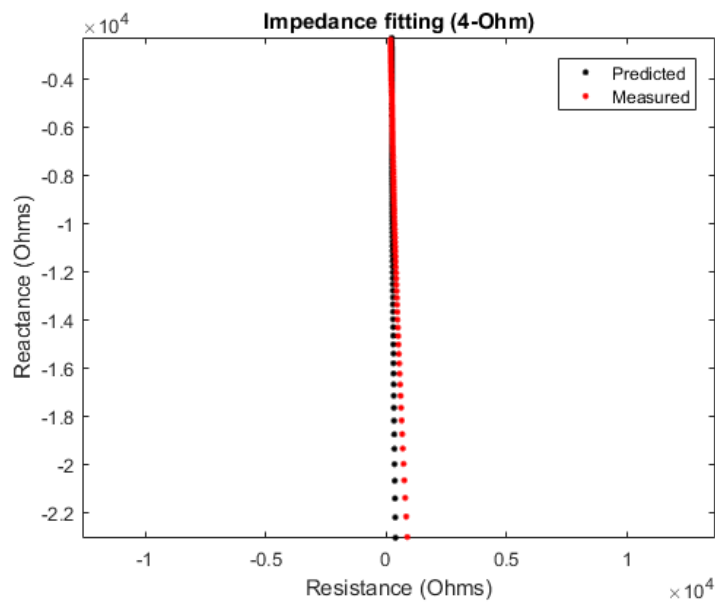


Figure 74: Impedance fitting result of test resistor 4 Ω

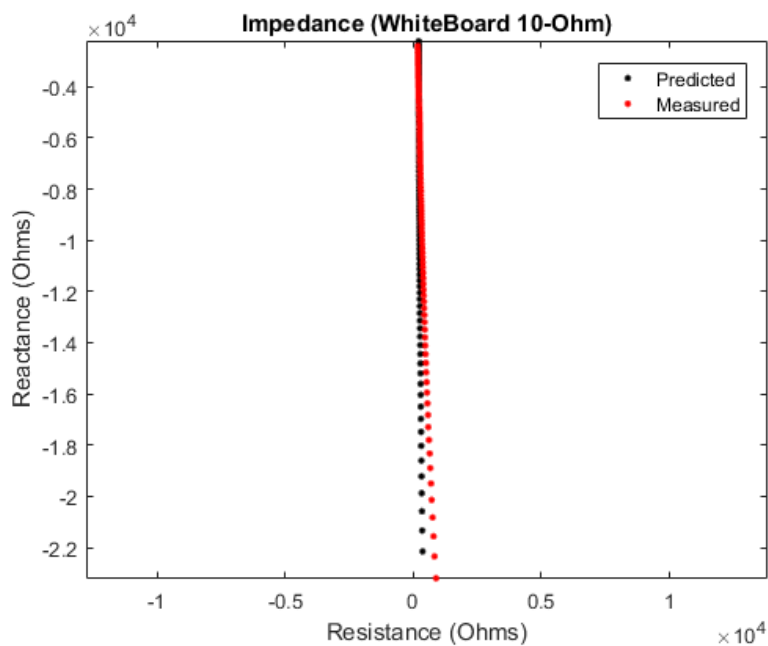


Figure 75: Impedance fitting result of test resistor 10 Ω

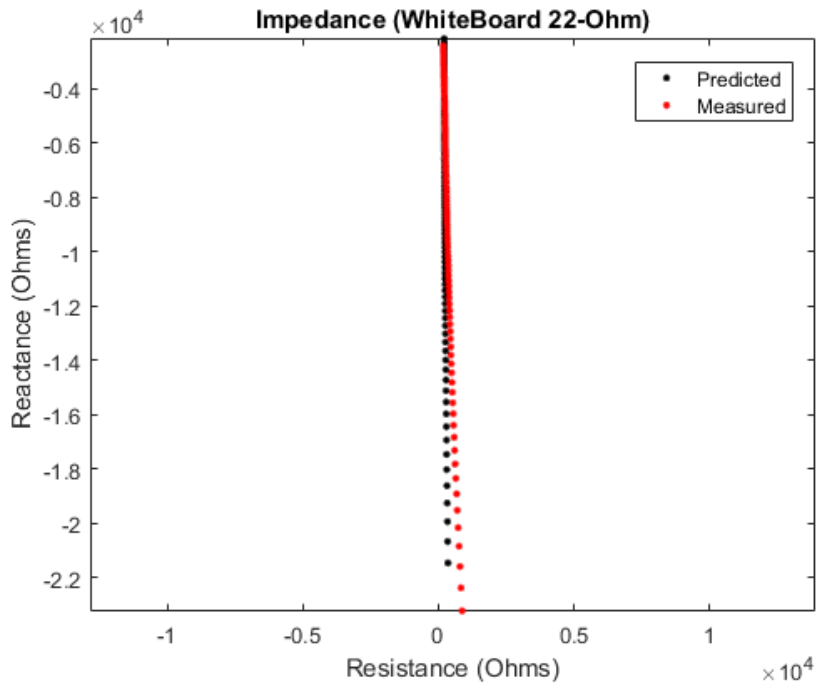


Figure 76: Impedance fitting result of test resistor 22 Ω

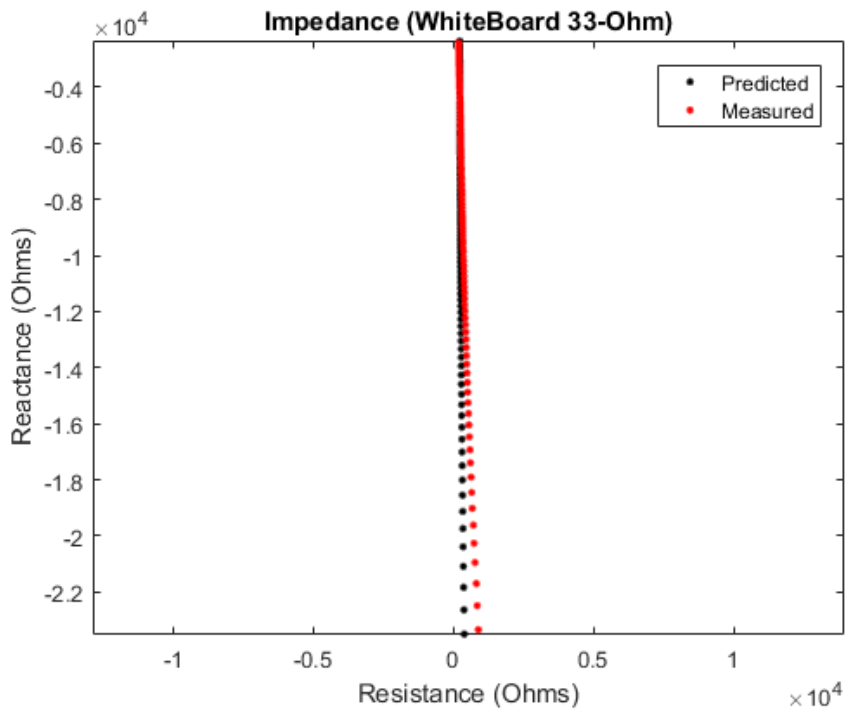


Figure 77: Impedance fitting result of test resistor 33 Ω

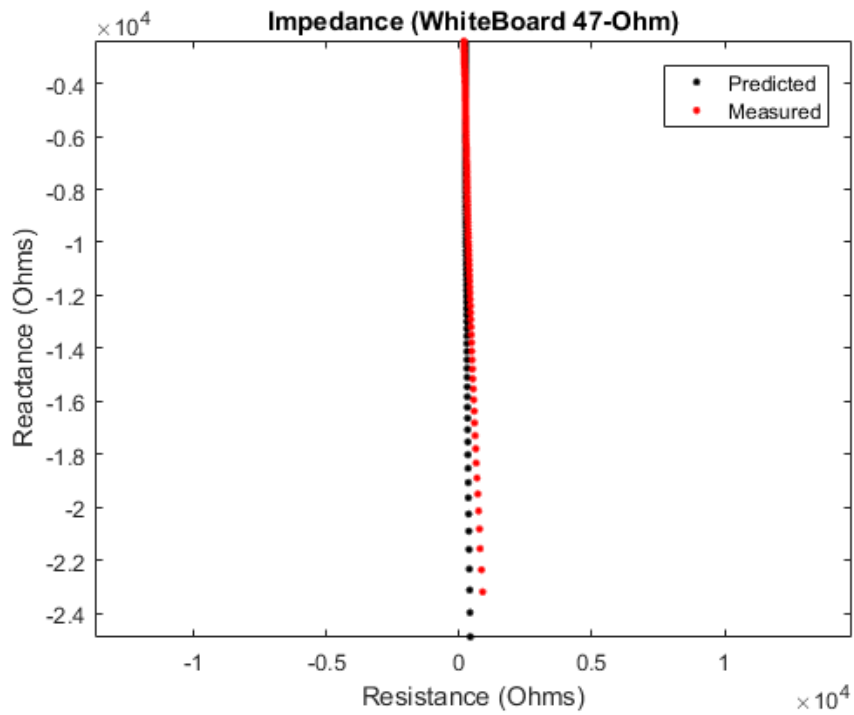


Figure 78: Impedance fitting result of test resistor 47 Ω

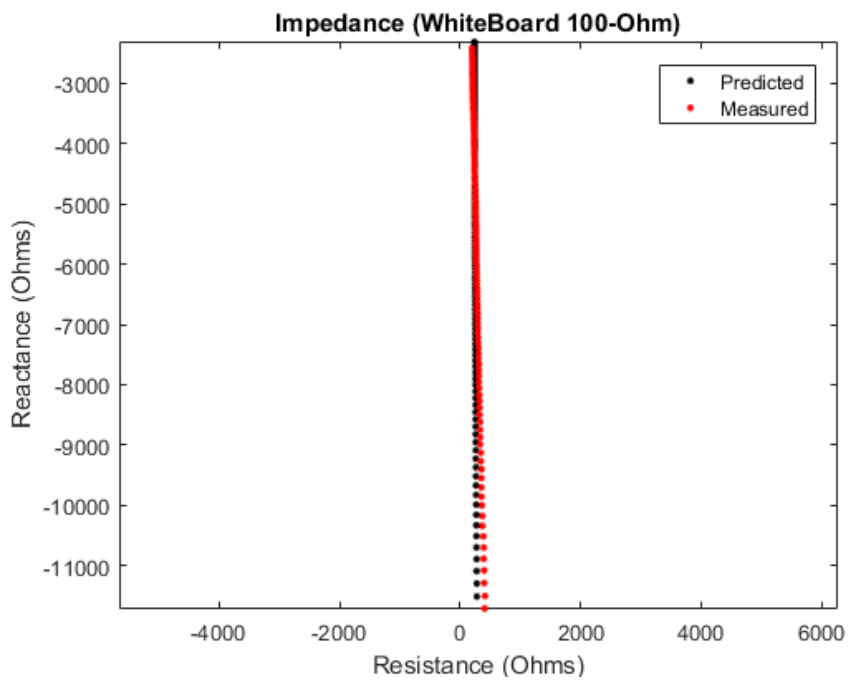


Figure 79: Impedance fitting result of test resistor 100 Ω

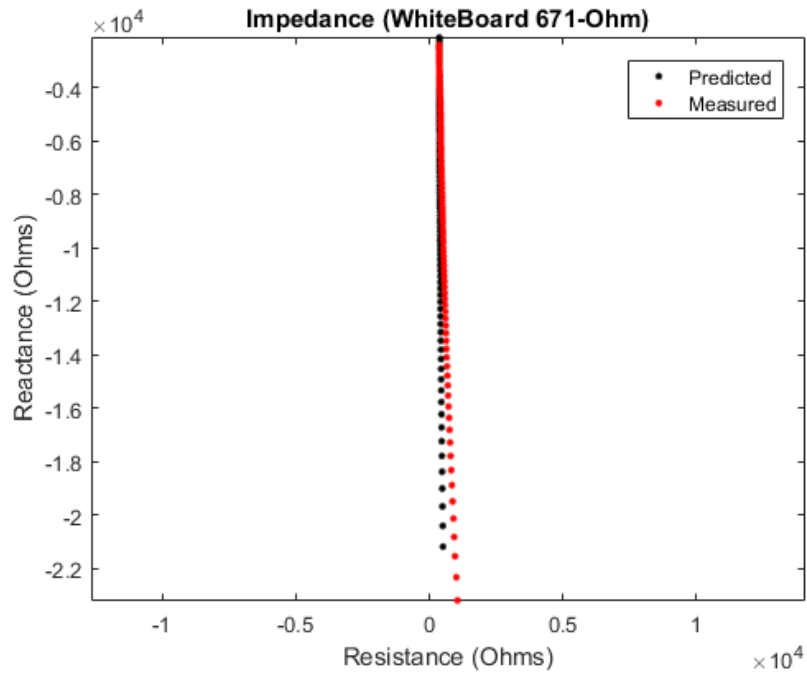


Figure 80: Impedance fitting result of test resistor 671 Ω

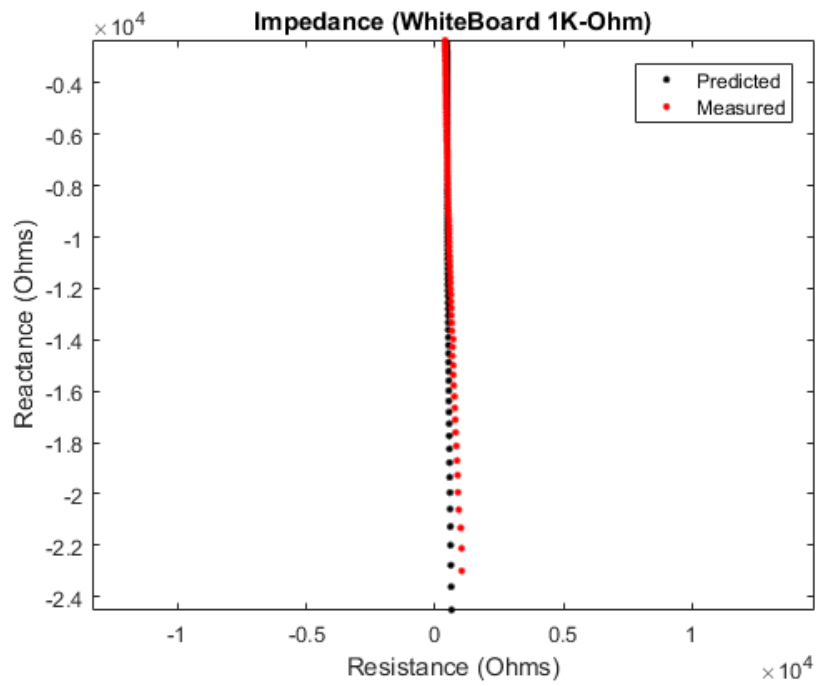


Figure 81: Impedance fitting result of test resistor $1 \times 10^3 \Omega$

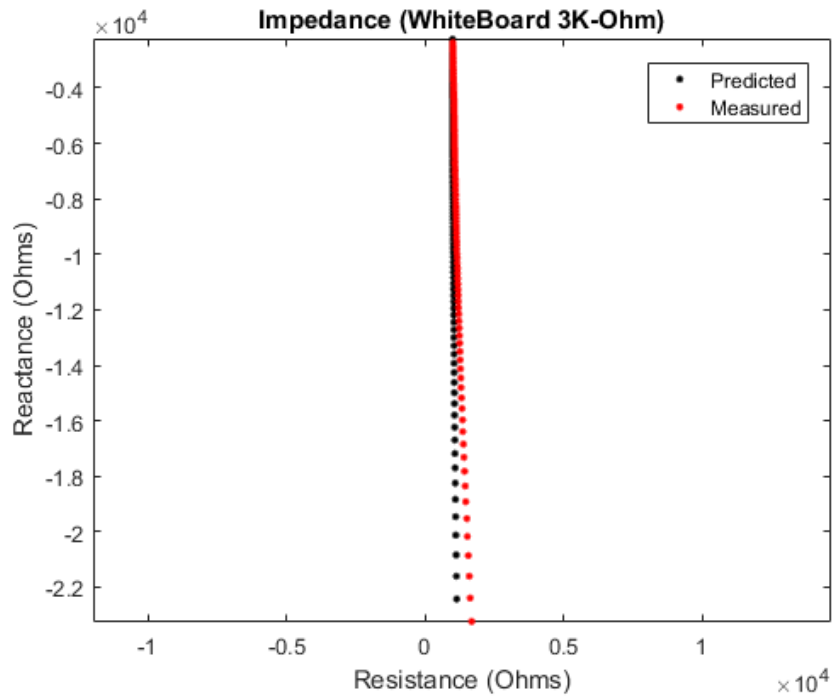


Figure 82: Impedance fitting result of test resistor $3 \times 10^3 \Omega$

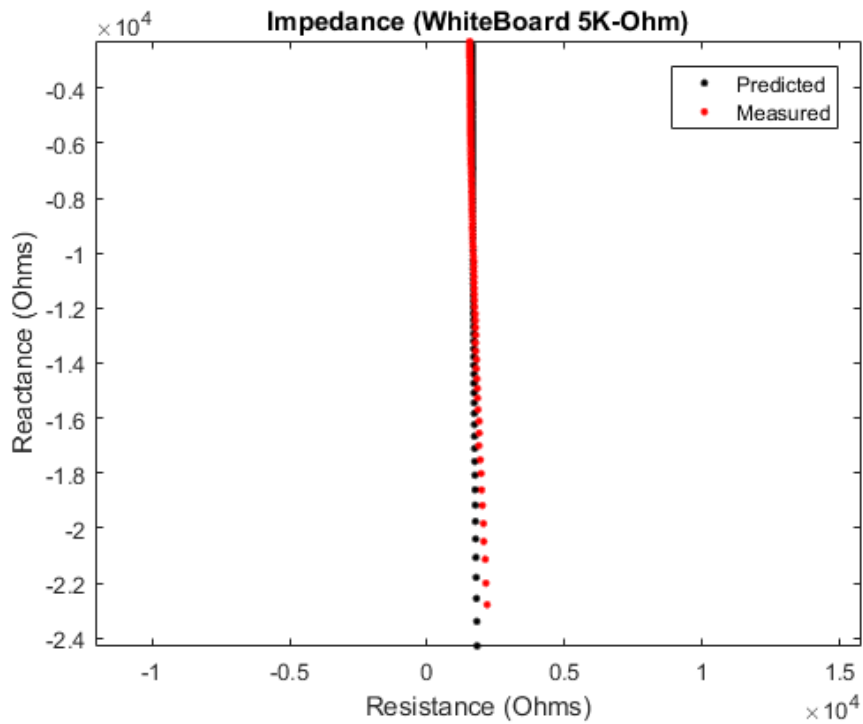


Figure 83: Impedance fitting result of test resistor $5 \times 10^3 \Omega$

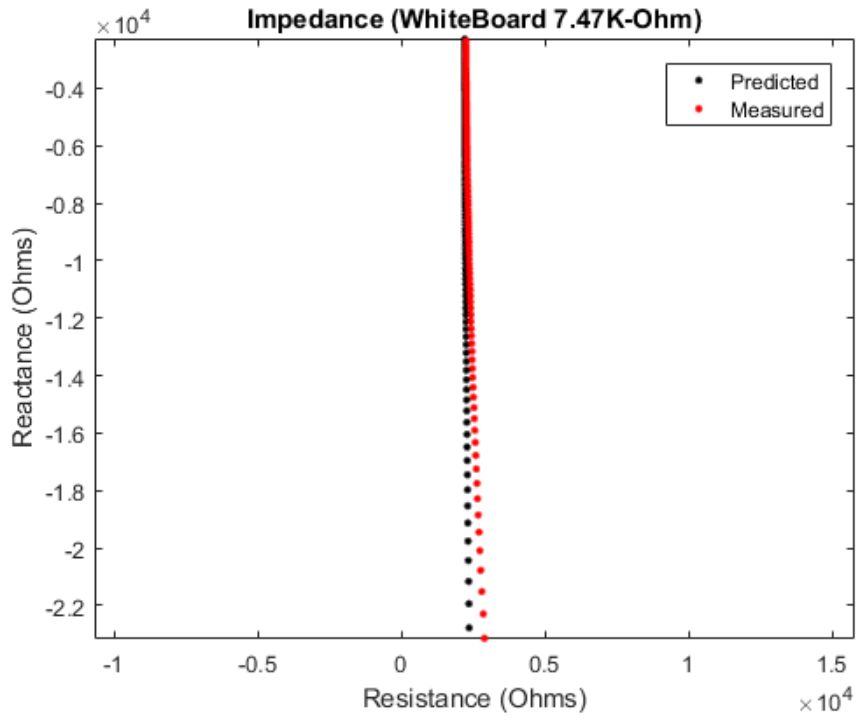


Figure 84: Impedance fitting result of test resistor $7.47 \times 10^3 \Omega$

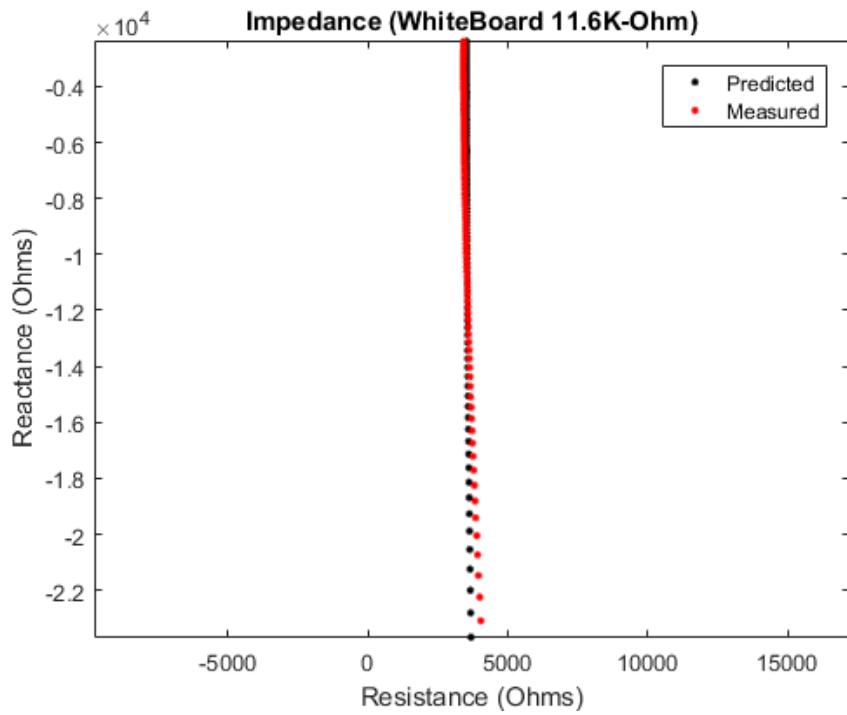


Figure 85: Impedance fitting result of test resistor $11.6 \times 10^3 \Omega$

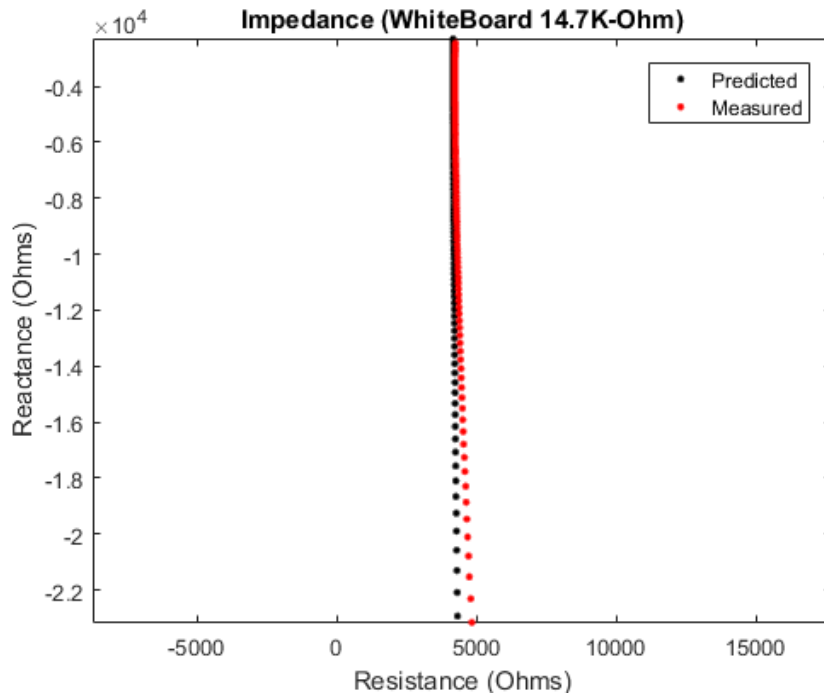


Figure 86: Impedance fitting result of test resistor $14.7 \times 10^3 \Omega$

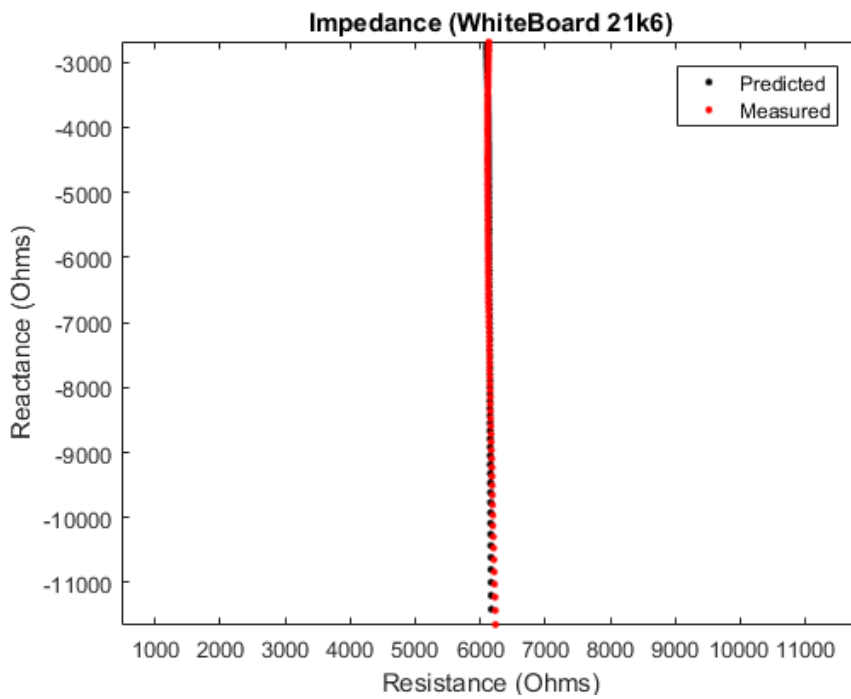


Figure 87: Impedance fitting result of test resistor $21 \times 10^3 \Omega$

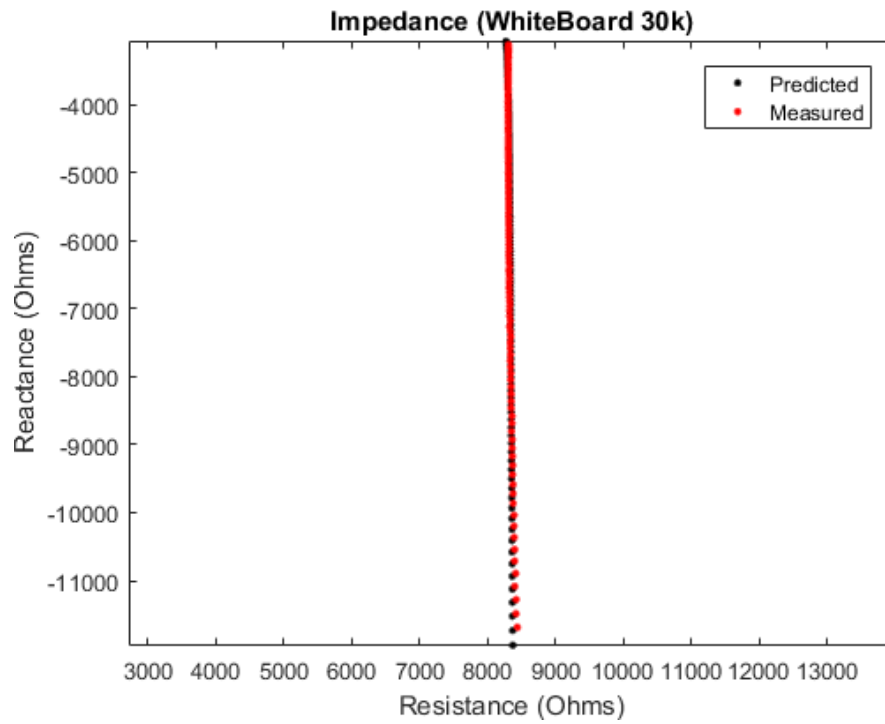


Figure 88: Impedance fitting result of test resistor $30 \times 10^3 \Omega$

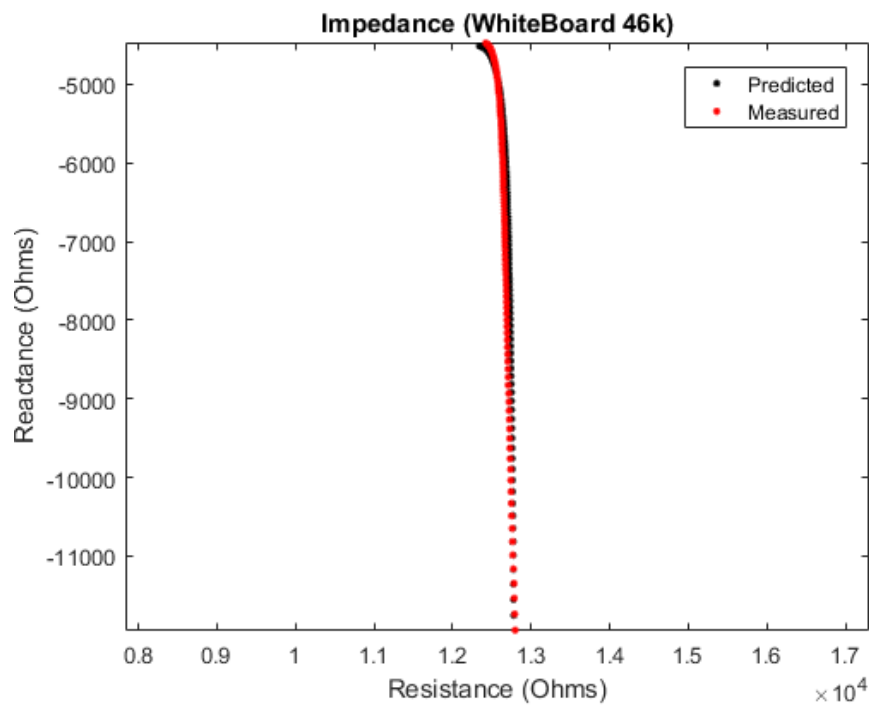


Figure 89: Impedance fitting result of test resistor $46 \times 10^3 \Omega$

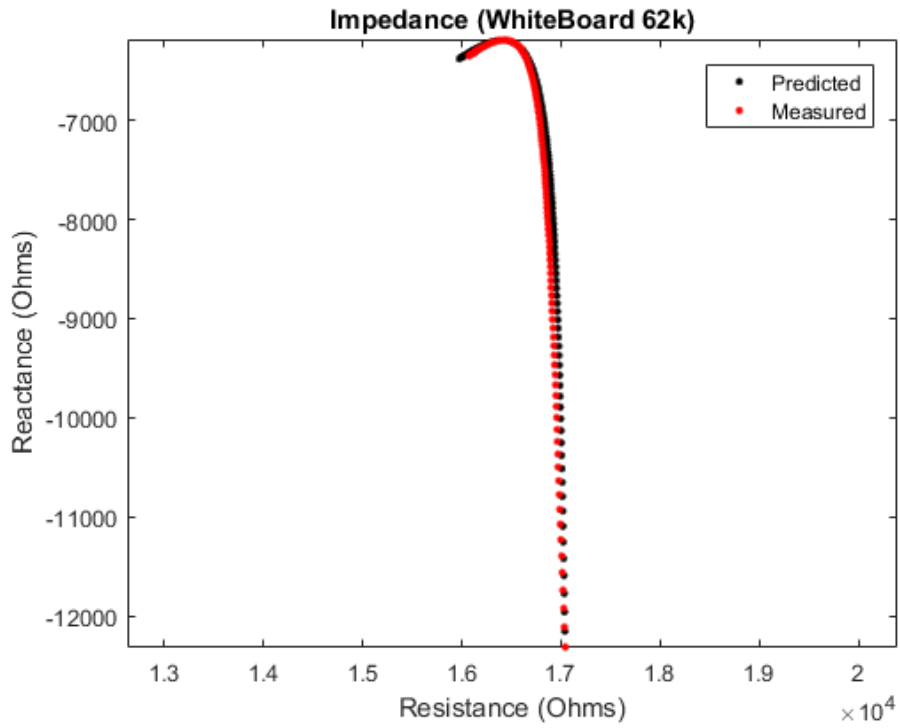


Figure 90: Impedance fitting result of test resistor $62 \times 10^3 \Omega$

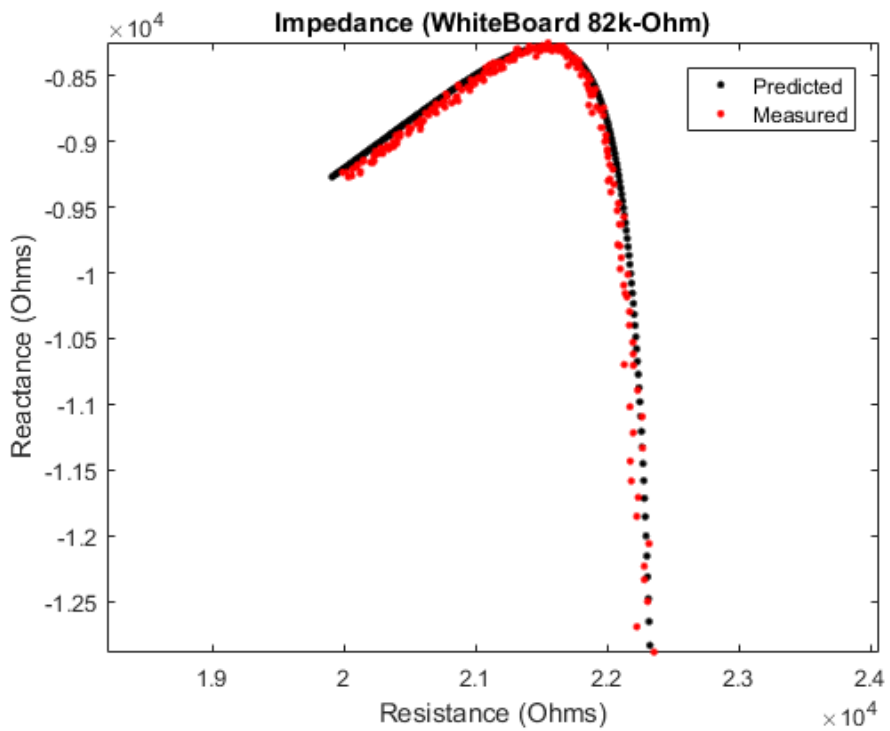


Figure 91: Impedance fitting result of test resistor $82 \times 10^3 \Omega$

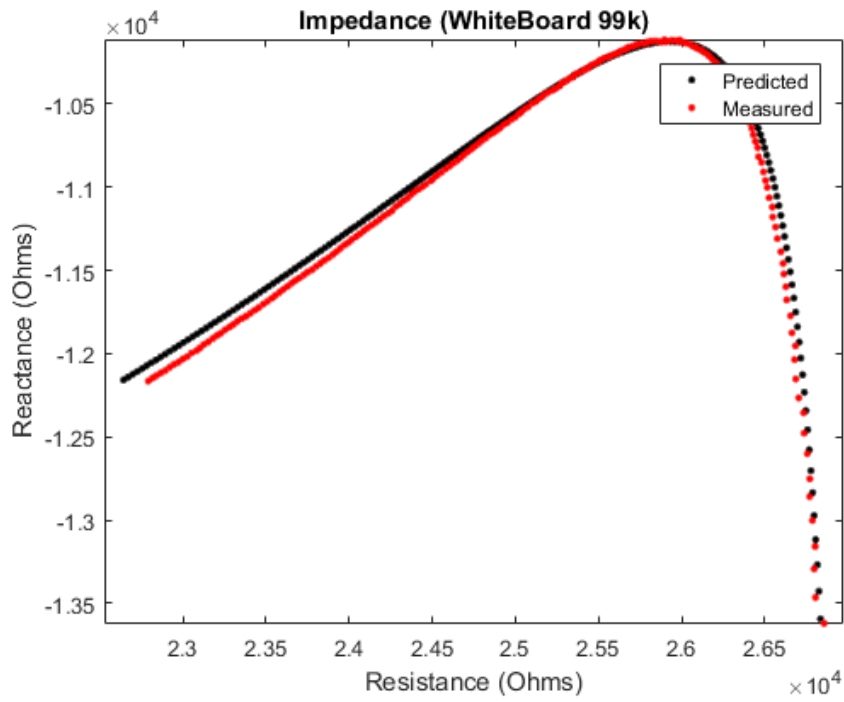


Figure 92: Impedance fitting result of test resistor $99 \times 10^3 \Omega$

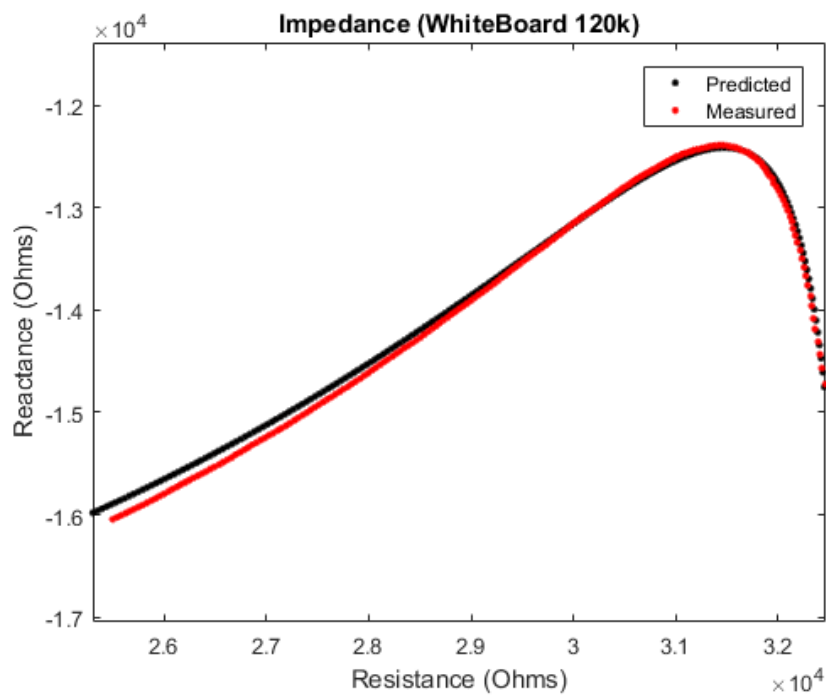


Figure 93: Impedance fitting result of test resistor $120 \times 10^3 \Omega$

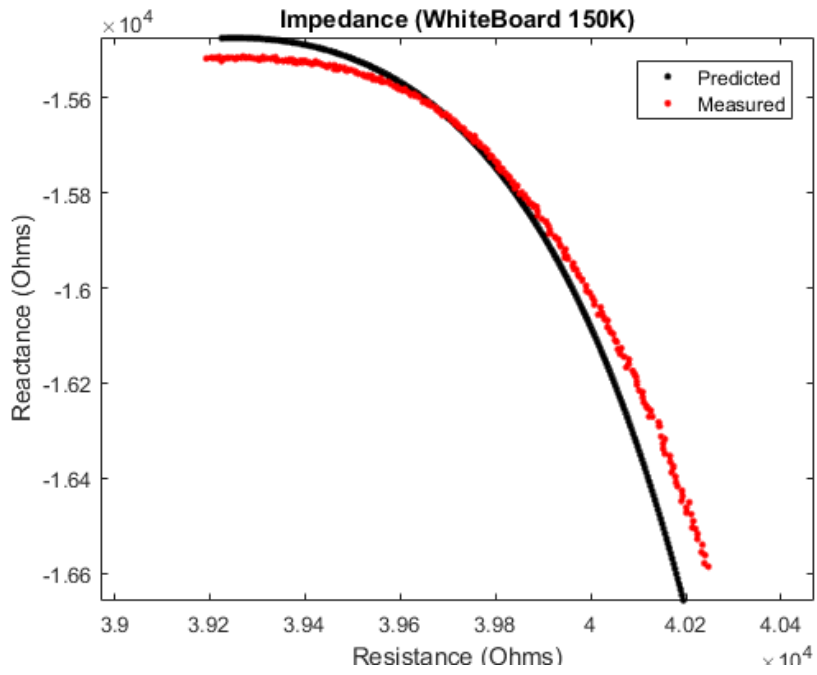


Figure 94: Impedance fitting result of test resistor $150 \times 10^3 \Omega$

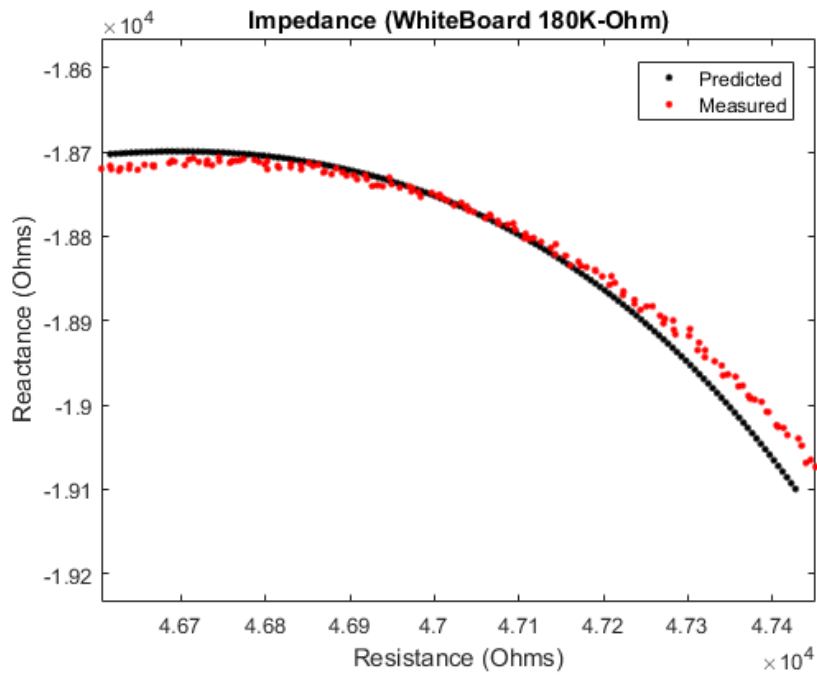


Figure 95: Impedance fitting result of test resistor $180 \times 10^3 \Omega$

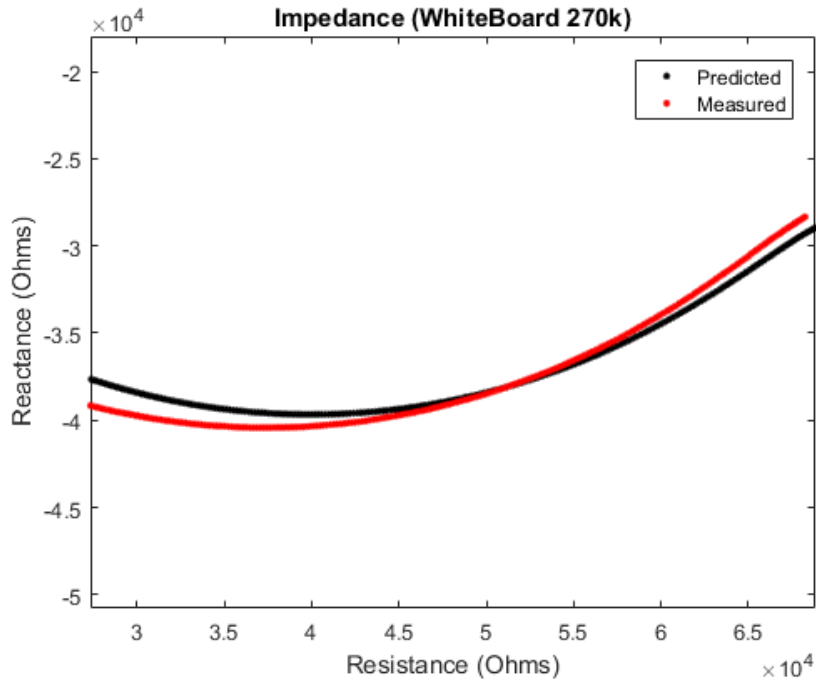


Figure 96: Impedance fitting result of test resistor $270 \times 10^3 \Omega$

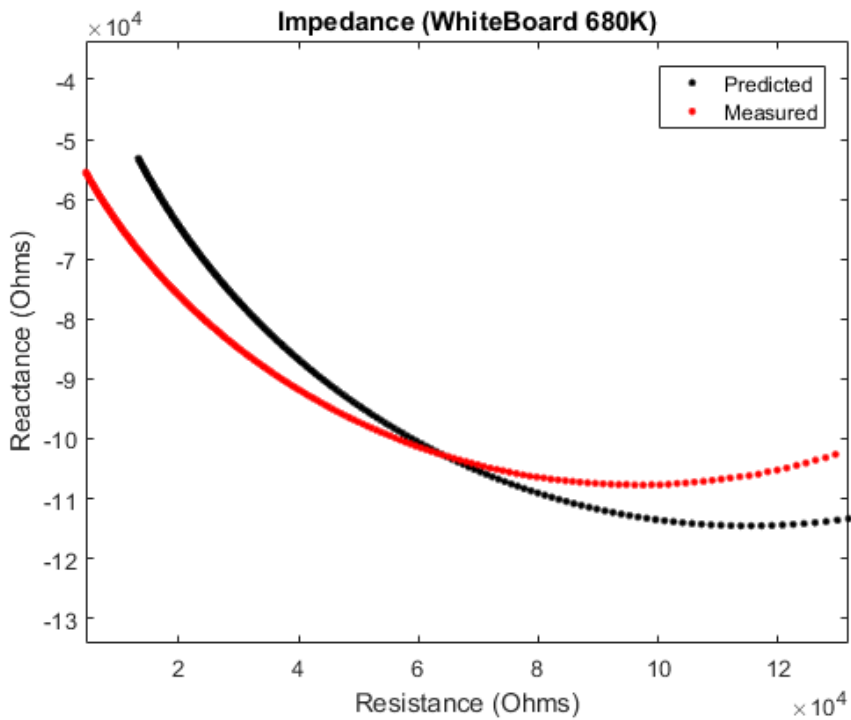


Figure 97: Impedance fitting result of test resistor $680 \times 10^3 \Omega$

Note: All of these impedance fitting results illustrated by Figure 74 to Figure 97 show the same problem, in that the predicted data does not fit very well with the measured impedance at low frequencies (50 Hz to 1 kHz). However, the predicted impedance is in good agreement with the measured impedance at high frequencies from 1 kHz to 21 kHz.

The reason for this situation is possibly because of the boundary layer capacitance associated with the yellow polypropylene dielectric sheet at the bottom and the poor signal-to-noise ratio at low frequencies. For example, a basic circuit model of a non-ideal dielectric material is illustrated in Figure 18. This circuit model changes when associated boundary layer capacitors are included, as shown in Figure 98. Zero frequency leakage currents have been ignored within this model.

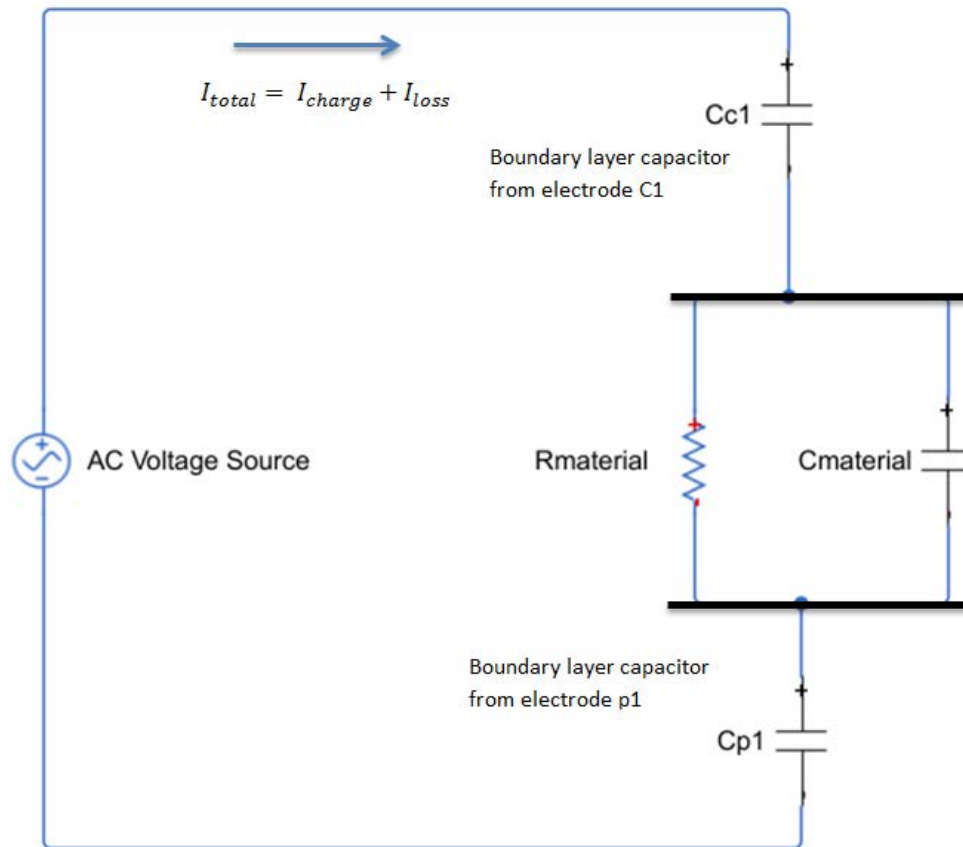


Figure 98: Circuit model of pavement materials with the addition of boundary layer capacitors

Figure 98 illustrates the inclusion of two extra boundary layer capacitors of large value, associated with the two sensor electrodes C1 and P1 used in the mirrored system. When the system operates at low frequencies (50 Hz to 1 kHz), the capacitance Cmaterial may be ignored because of the dominant boundary layer capacitors Cc1 and Cp1. In practice, there are also leakage currents associated with the boundary layer capacitors. Thus, a new circuit model is generated and shown in Figure 99.

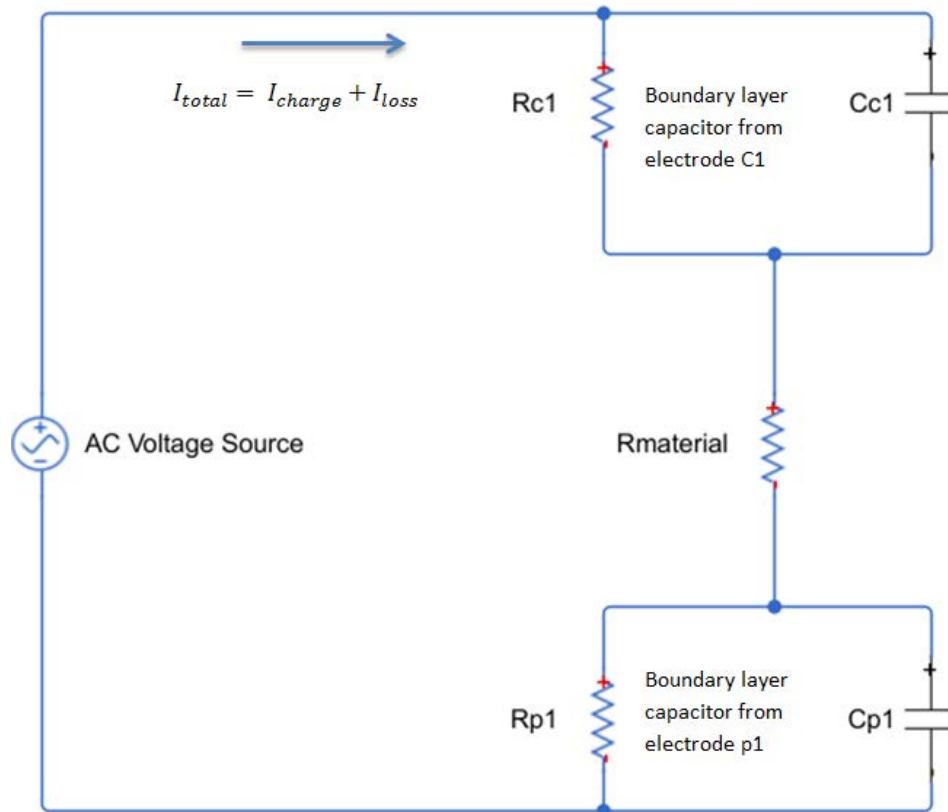


Figure 99: Circuit model of pavement materials with the addition of boundary layer capacitors and associated leakage currents

Figure 99 illustrates a model with three resistors and assumes that the low operating frequency signal is blocked by the boundary layer capacitors. Hence, the measured resistance becomes $R_{c1} + R_{p1} + R_{material}$ instead of a single resistance value $R_{material}$. For experiments using the test resistors, such parasitic factors are not considered within the analytical model or the network method. Therefore, it is likely that the experiments yield higher measured resistance values than the predicted resistance values when the system operates at low frequencies (50 Hz to 1 kHz). Moreover, at very low frequencies such as 50 Hz the ambient power-line interference may also play an important part in increasing the uncertainty of measured values.

These fitting results are based on the fixed components listed in Table 7. The predicted resistances of these test resistors are illustrated in Figure 100. This relationship curve has the same tendency as that generated from the analytical model and the resistor-capacitor network method. The geometric factors derived from this experimental method by using 26 test resistors are calculated by equation (4-69).

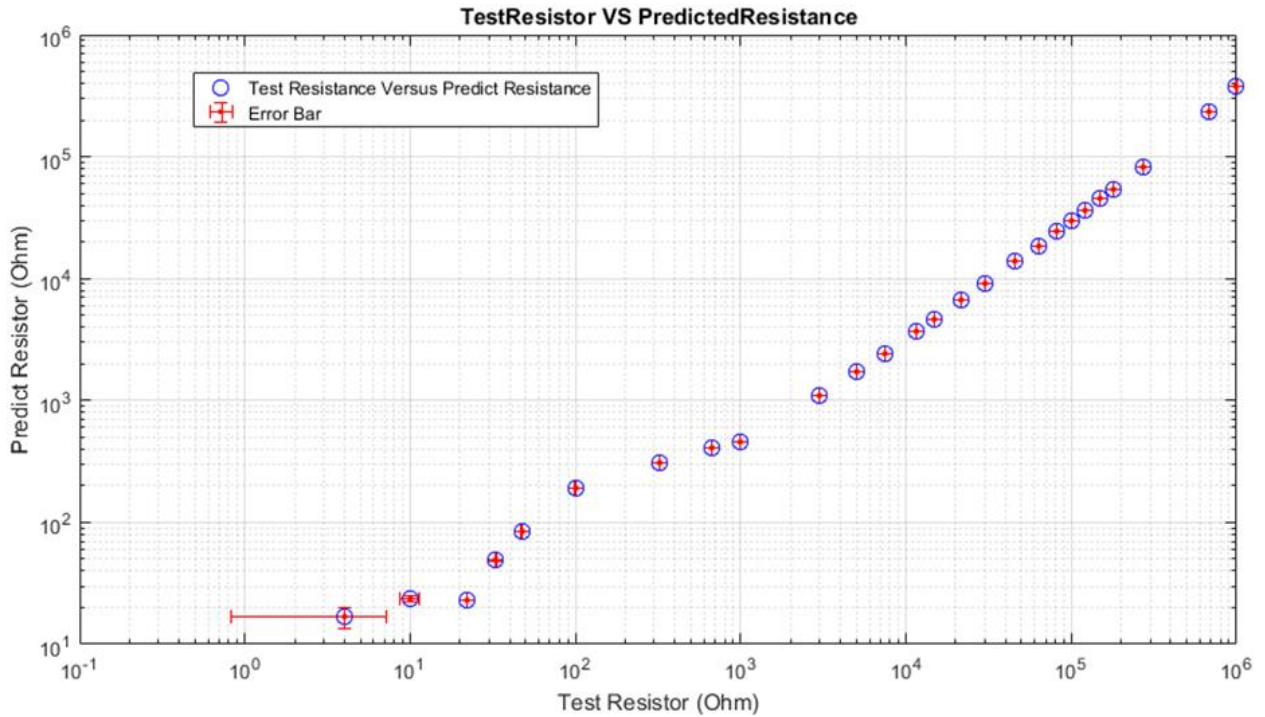


Figure 100: Relationship curve of the predicted resistance of the test resistors and their practical resistance (RMS value of test resistors is $2.5 \times 10^5 \Omega$; RMS value of predict resistance is $0.9 \times 10^4 \Omega$)

To confirm the accuracy of the geometric factors and the efficacy of the circuit model, COMSOL models of the capacitive-coupled resistivity system with 26 discrete test resistors have been built and results are discussed below.

4.3.3 COMSOL modelling of a mirrored capacitive-coupled resistivity system using test resistors

The mirrored circuit of the capacitive-coupled resistivity system measuring the discrete test resistors was modelled using COMSOL. The equivalent model of the capacitive-coupled resistivity system on the foamed PVC board with fixed copper sheets is shown in Figure 101.

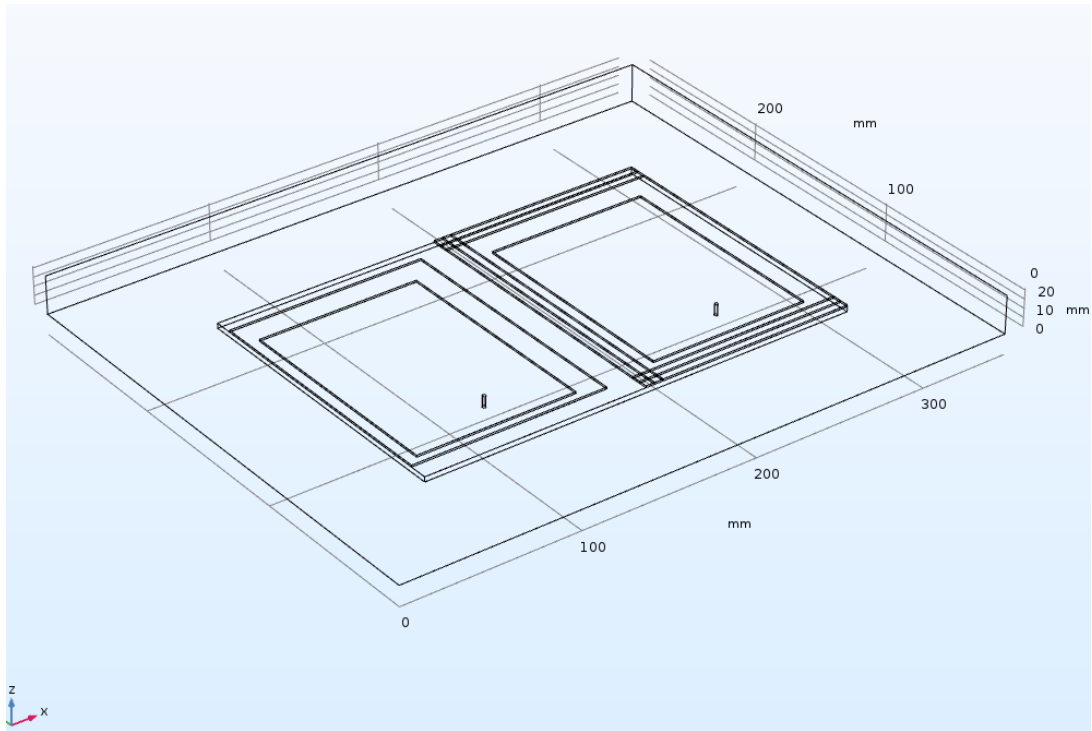


Figure 101: COMSOL model of mirrored capacitive-coupled resistivity system using discrete test resistors at a frequency of 5 kHz

COMSOL Settings

A COMSOL model using the dimensions of the practical system, an operating frequency of 5 kHz and the same components and test resistors as the real capacitive-coupled resistivity system was configured. Electrodes C1 and P1 had a length of 145 mm and a width of 110 mm. The electrode separation between C1 and P1 was 25 mm. The guard ring with a width of 5 mm was placed around the potential electrodes. The separation between the guard ring and the electrode P1 was 5 mm. All electrodes were placed on a polypropylene sheet with a dielectric constant of 2.283 and thickness of 2.273 mm.

The potential on the electrode C1 was connected to a voltage source (peak-peak voltage of 19.9 V). The voltage source was connected to a series resistor of 5 k Ω . To model the NI 9239 ADC internal resistance and internal capacitance, a resistor of 1 M Ω and a capacitor of 4 pF were shunt connected to the series protection resistor. The potential on the electrode P1 was set as a floating potential connected via a 100 M Ω resistor to the earth. A shunt capacitor of 13 pF was connected to the ADC input resistor. Two additional copper plates with a width of 90 mm and a length of 125 mm were set as floating potentials which

were connected to the test resistors to simulate the foamed PVC test fixture. The potential of the material surface was also set as a floating potential. This hidden circuit connection used in the COMSOL model of the capacitive-coupled resistivity system (Figure 101) is given in Figure 102.

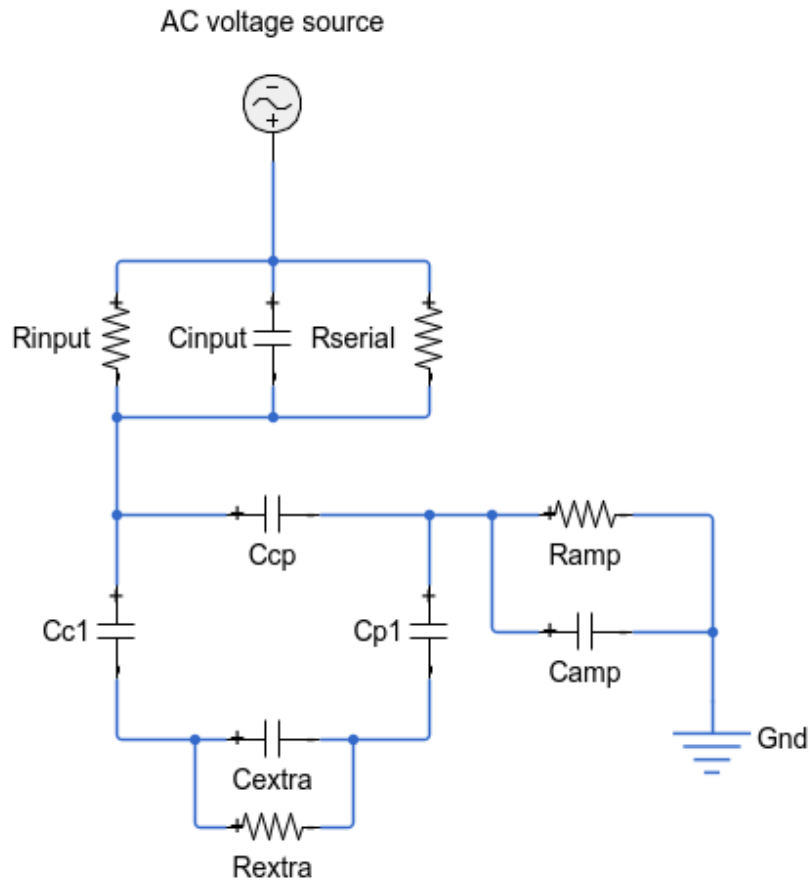


Figure 102: Extra circuit connection hidden in the COMSOL model

Figure 103 illustrates a slice of the electrical potential spatial distribution of the mirrored system.

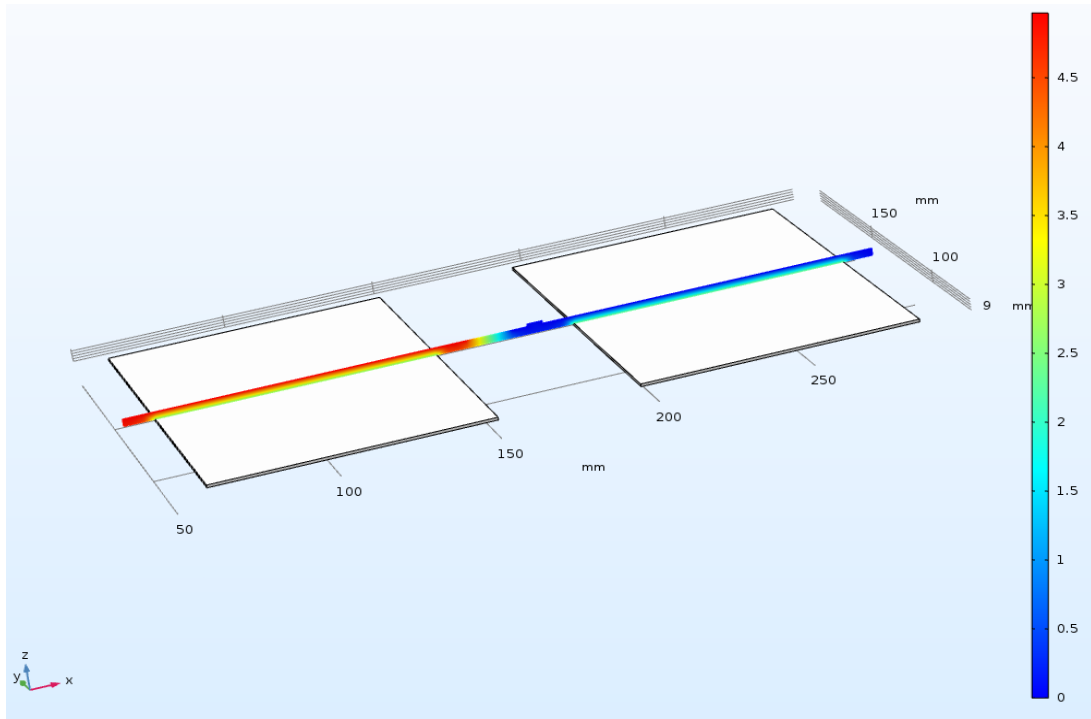


Figure 103: Electric potential spatial distribution of a slice of the mirrored capacitive-coupled resistivity system used to measure test resistors at 5 kHz

The relationship curve between the predicted resistances obtained by COMSOL modelling and the value of the test resistors is illustrated in Figure 104.

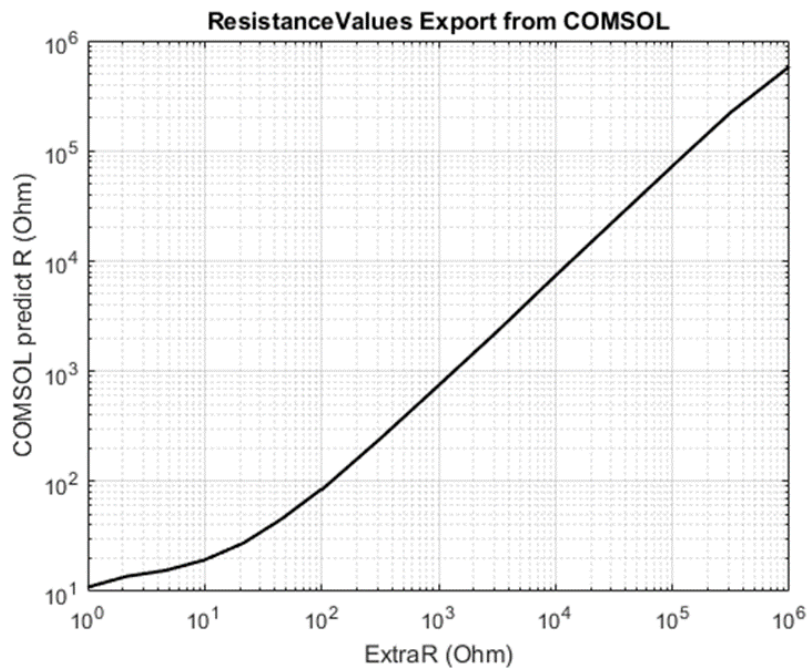


Figure 104: The relationship curve between the predicted resistances using COMSOL modelling and the value of the test resistors at 5 kHz

In Figure 104, the X and Y-coordinates represent the value of the test resistances and the predicted measured resistances. The relationship curve generated by the least square fitting method using practical data, the circuit impedance analysis formula and the COMSOL modelling results are combined together in Figure 105.

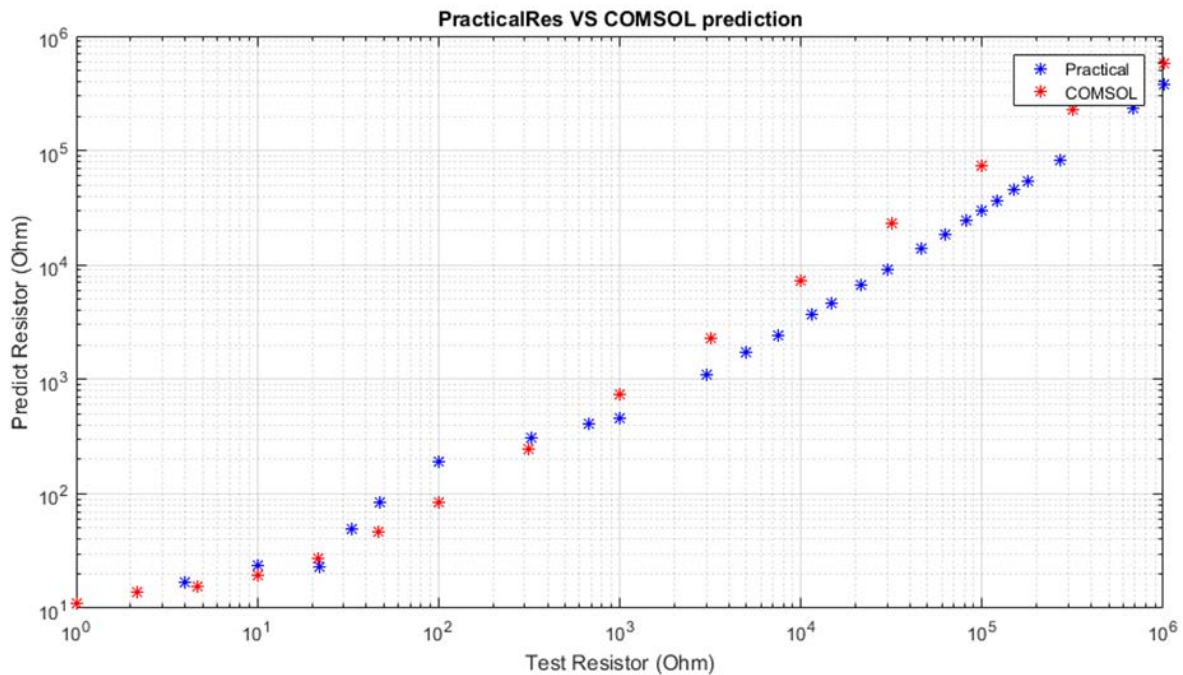


Figure 105: Relationship curves of the test resistances and the predicted measured resistance obtained by two methods (blue curve-from practical experiments; red curve-from COMSOL modelling) at 5 kHz

The error between these two curves is between 2% and 12%. The equivalent geometric factor of test resistors ranging from 0.1 k Ω to 1 M Ω is around 0.4609. It is believed that the circuit model and the resistor-capacitor network method are reasonably effective. Thus, for measured data estimates obtained using this capacitive-coupled resistivity system on pavements, the apparent resistivity values could be predicted by applying the relationship curve illustrated in Figure 105. This is the equivalent of a geometric factor that is a non-linear function of the resistivity value of the material.

4.3.4 Four-rods experiment using black foam and its COMSOL model

4.3.4.1 Practical experiment using four rods

In this research, 5 cm thick black conductive foam was utilised as an alternative physical model of the pavement layer. Before undertaking field surveys, some experiments were

conducted on black conductive foams to verify the geometric factors discussed in previous sections. First, a practical experiment, using four rods placed in a Wenner electrode configuration, was conducted to estimate the electrical resistance of the black foam (Figure 106). The four rods were connected to the HP4921 impedance analyser. The two rods placed at the two ends act as the current sources and other two rods are the potential electrodes.

Table 8: Configuration of practical experiment using four rods

Rod length (cm)	Rod electrode separation (cm)	Rod diameter (cm)	Layer thickness (cm)
50	24	2	5

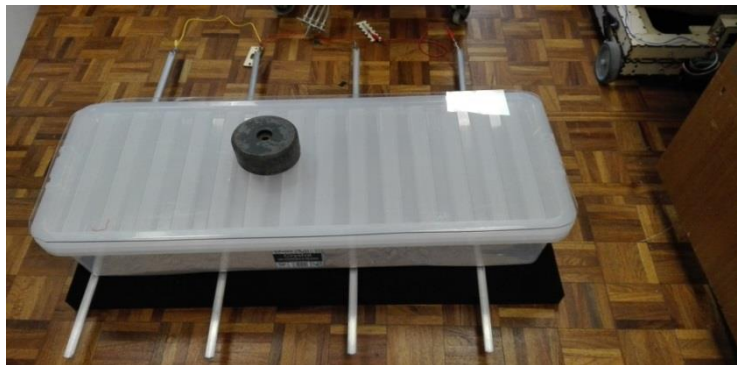


Figure 106: Experiment using four rods weighted on 5 cm thick conductive foam

The four rods were weighted by a box of sand and an iron block to ensure galvanic contact with the foam. The HP4921 was used to measure the impedance of the black foam using a classical four-terminal configuration. The relationship curve of the measured resistance to the operating frequency is shown in Figure 107.

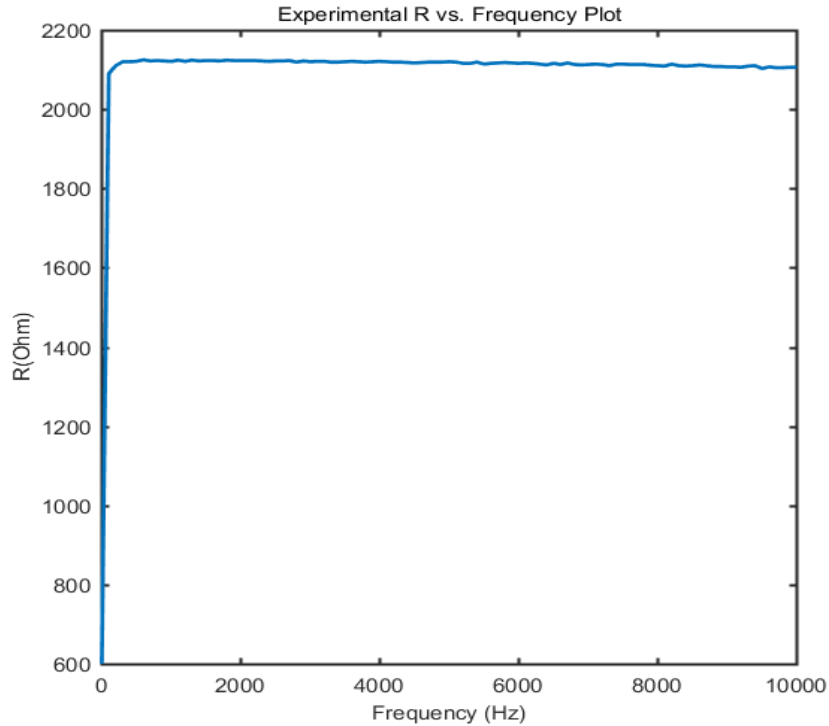


Figure 107: Measured resistance value of the foam by using four rods vs. operating frequency (the spiking value at very low frequency could be the internal resistance of the instrument itself)

The resistance $R_{\text{MeasureFoam}}$ is around 2100Ω at frequencies from 1 kHz to 10 kHz. To calculate the resistivity of this foam, COMSOL was used to model the experiment to predict the geometric factor of four rods deployed in a Wenner electrode configuration.

4.3.4.2 Four rods experiment modelling in COMSOL

A COMSOL model of the experiment using four rods placed on foam of 10 cm thickness was built and is illustrated in Figure 108. In this model the resistivity of the foam is assumed to be $10^4 \Omega\text{m}$. This COMSOL model uses the same dimensions as the practical experiment.

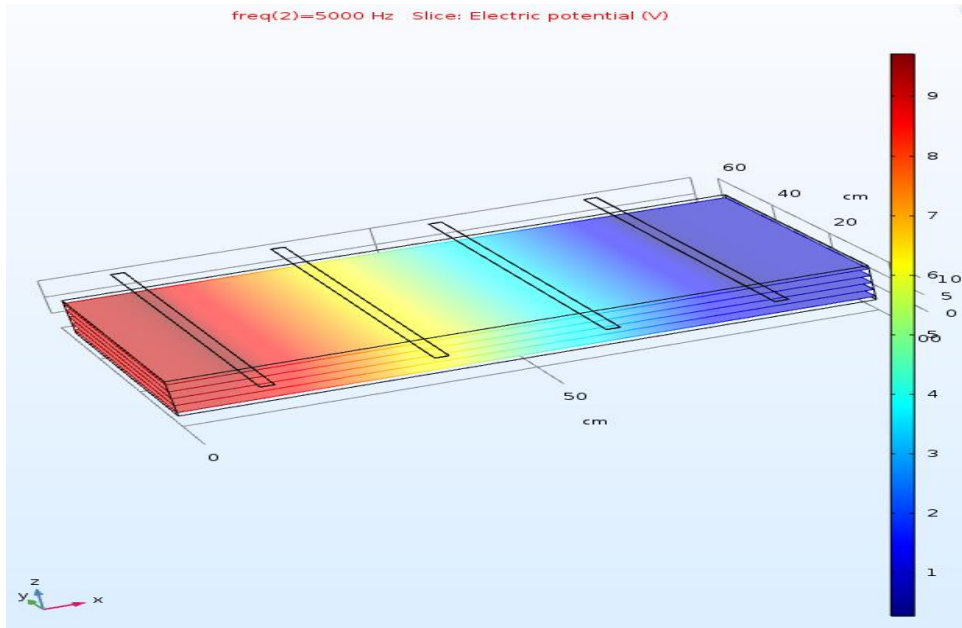


Figure 108: COMSOL model of the experiment using four rods placed on 10 cm thick conductive foam (5 kHz)

The electrical resistance of the foam was calculated by COMSOL. The predicted resistance of the foam layer was 47722 Ω , 47524 Ω , and 47271 Ω when evaluated by COMSOL at frequencies of 1 kHz, 5 kHz and 10 kHz.

Combining these evaluated resistance values and the configured electrical resistivity value, the geometric factor of the experiment using four rod electrodes at the frequency of 5 kHz in a Wenner electrode array configuration is given by

$$k_{\text{rods}} = \frac{\rho}{R} = \frac{1}{\sigma R} = \frac{1}{10^{-4} * 47524} = 0.2104 \quad (4-71)$$

Applying this geometric factor to $R_{\text{MeasureFoam}}$, the apparent resistivity of the black foam is

$$\rho_{\text{blackfoam}} = k_{\text{rods}} R_{\text{MeasureFoam}} = 2100 * 0.2104 = 441.882 \Omega\text{m} \quad (4-72)$$

4.3.5 Capacitive-coupled resistivity system on black foam and its COMSOL model

4.3.5.1 Practical experiment using the capacitive-coupled resistivity system on the black foam

The capacitive-coupled resistivity system was placed on the black conductive foam to test its resistivity r using the least squares network fitting method discussed earlier. The same fitting scheme as used in the free space and copper sheet experiments was used. The measured impedance and predicted impedance are shown in Figure 109.

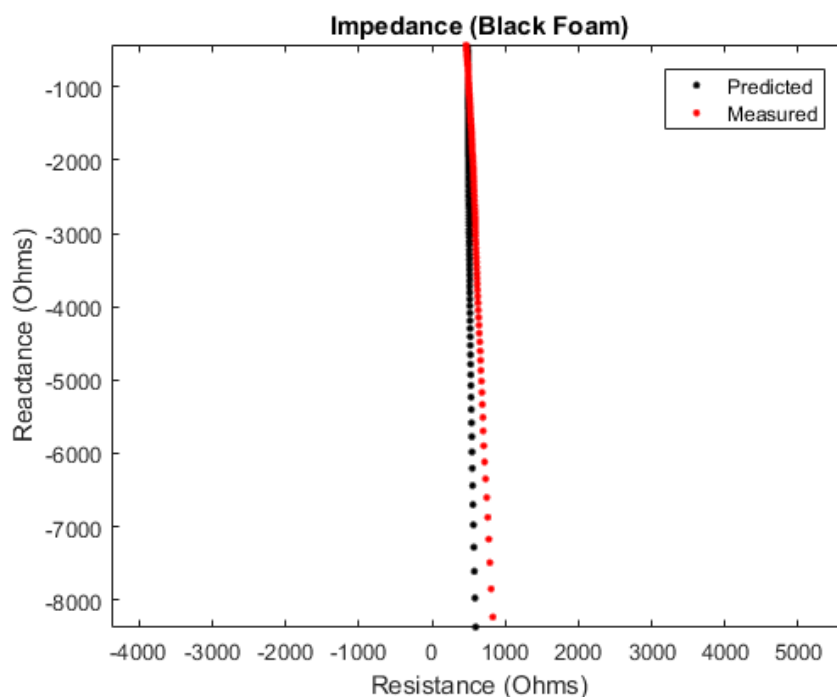


Figure 109: Measured impedance and predicted impedance curves when the capacitive-coupled resistivity system is placed on the conductive foam (10 cm)

The measured foam resistivity using the capacitive-coupled resistivity technique is $480.7259 \Omega\text{m}$. The error between this fitted foam resistivity and measured resistivity using the four-rods' experiment of $441.882 \Omega\text{m}$ is 8.79%. Thus it can reasonably be assumed that the device operates in an acceptable manner when placed on materials with resistivity values similar to those expected from an asphalt pavement.

4.3.5.2 COMSOL model (capacitive-coupled resistivity system measurement on the black foam)

A model of the experiment where the capacitive-coupled resistivity system was placed on the black conductive foam with a thickness of 10 cm was built in COMSOL using the practical system configuration and components' dimensions, as illustrated in Figure 110.

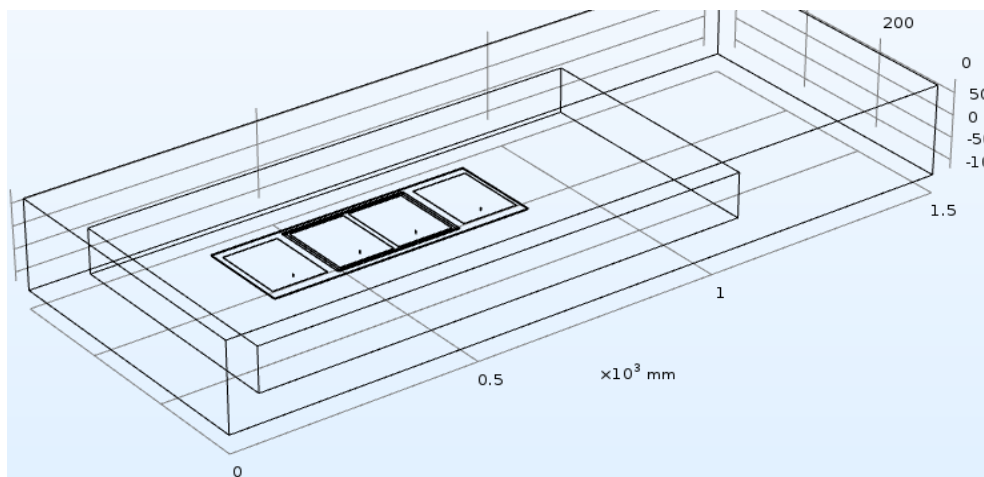


Figure 110: COMSOL model of the capacitive-coupled resistivity system measurement when placed on the black foam with a thickness of 10 cm

The resistances of the material layer as predicted using the COMSOL model were 590.79Ω , 985.28Ω and 1054.1Ω at frequencies of 1 kHz, 5 kHz and 10 kHz. From the relationship curve shown in Figure 105 between the predicted resistances and the practical resistances (the geometric factor of 0.4609), the electrical resistivity of the black foam tested by the capacitive-coupled resistivity system at the frequency of 5 kHz is around $454.1156 \Omega m$. The error between this resistivity and the measured resistivity using the four rods is 2.77%.

In summary, a non-invasive, capacitive-coupled resistivity technique, implemented using four large in-line sensor electrodes was applied to the moisture related (the poor pavement with an old-dry area and an old-wet area of moisture-laden mosses, behind the Gisbert Kapp Building) condition assessment of shallow layers of the pavement. Since pavement materials are generally of high resistivity, the measured impedances become complex impedances caused by displacements of bound charges and some migrating charge carriers referred to as energy loss. In order to recognize pavement materials as a “good conductor”, the operating frequency should be smaller than 25 kHz. A stepped-frequency

continuous wave signal at multi-frequencies (5 kHz, 7.5 kHz, and 10 kHz) was applied during practical surveys. This capacitive-coupled resistivity technique was carried out by an automated vehicle to form a non-destructive, rapidly surveying, labour saving and repeatable device. The investigation depth depends on the electrode array configuration and the electrical resistivity of the pavement materials. One limitation is that the sensor electrodes of this system are of fixed dimensions and fixed electrode separations. Thus, the investigation depth is limited to the shallow layer where the thickness is less than half of the separation of the current injection electrodes. To calculate the apparent resistivity, analytical methods, experimental tests and COMSOL modelling have been applied in this work to calculate and verify the geometric factors of the electrode array configuration of the capacitive-coupled resistivity technique used in this research. The relationship curves obtained by three methods show the same tendencies and verify the accuracy of relatively simple analytical resistor-capacitor network methods. Some errors are introduced by using 1D resistor-capacitor network methods instead of 2D or 3D finite element methods, the use of low-frequencies, ambient noise and low-value parasitic parameters. These are the potential reasons for errors occurring between the measured geometric factor (measured resistivity) and the predicted geometric factor (predicted resistivity).

As mentioned in previous chapters, the output voltage or impedance transfer function is very sensitive to capacitance, including the coupling capacitance of the parallel-plate capacitor and the equivalent capacitance of the materials. The surface roughness impacts on the capacitance and the leakage current, and thus have to be discussed because of variations in the texture of pavement surfaces.

References

- [1] R. V. Hippel, *Dielectric Materials and Applications*, Artech House, 1952.
- [2] CMPT 468: Frequency Modulation Synthesis. Tamara Smyth, School of computing science. Oct 16, 2013
- [3] R. Grard and A. Tabbagh, "A mobile four electrode array and its application to the electrical survey of planetary grounds at shallow depths," in *Journal of geophysical research*, Vol. 96, No.B3, (1991), pp. 4117-4123.
- [4] T. Dahlin, "The development of DC resistivity imaging techniques," in *Computers and Geosciences*, Vol 27 (2001), pp. 1019 – 1029.
- [5] W.M. Telford, *Applied Geophysics*, Cambridge University Press, Cambridge, London, 1976.
- [6] D.J. Griffiths, *Introduction to electrodynamics*, Prentice-Hall Inc, 1981.
- [7] T. Sakurai and K. Tamaru, "Simple formulas for two and three dimensional capacitances," in *IEEE transactions on electron devices*, Vol. 30, No. 2 (1983).
- [8] M.I. Elmasry, "Capacitance calculations in MOSFET VLSI," in *IEEE Electron device letters*, Vol 3, No. 1 (1982).
- [9] G. Shomalnasab and L. Zhang, "New analytical model of coupling and substrate capacitance in nanometre technologies," in *Transactions on very large scale integration (VLSI) systems*, Vol 23, No 7 (2015).
- [10] A.W. Lotfi and F.C. Lee, "Two dimensional skin effect in power foils for high frequency applications," in *Transactions on magnetics*, VOL 31, No 2 (1995).
- [11] J. Larsson, "Electromagnetics from a quasi-static perspective," in *American Journal of Physics*, Vol 75, No. 230 (2007).
- [12] O. Kuras, "The capacitive resistivity technique for electrical imaging of the shallow subsurface," Ph.D dissertation, University of Nottingham, 2002.
- [13] C. Rucker and T. Gunther, "The simulation of finite ERT electrodes using the complete electrode model", in *Geophysics*, Vol 76, No. 4, P. F227-F238, 2011

CHAPTER 5

SURFACE ROUGHNESS EFFECTS ON CAPACITIVE COUPLED RESISTIVITY SYSTEM

Three stages of data acquisition, data processing and data interpretation, are necessary for the majority of geophysical techniques. The data acquisition system of the capacitive coupled resistivity system and a part of the data processing including the required systematic corrections and the geometric factors are discussed and verified in the fourth chapter of this thesis. Considering the sensitivity of the output voltage to the boundary layer capacitance and the surface roughness effects on capacitance and leakage current values, it is proposed that the pavement surface roughness has to be taken into account when processing the measured data. Thus, roughness correction factors will be analysed and applied to the electrical impedance estimates obtained by the capacitive coupled resistivity system derived following field surveys. In order to measure the height distributions of the pavement surfaces, a laser profiling instrument with an along-track resolution of 0.125 mm and a typical height resolution of 50 μm was utilised (Figure 111) during field surveys.



Figure 111: Height distribution measurement of an area of degraded pavement behind the Gisbert Kapp building using a laser profiling instrument

It is practically impossible to measure accurately the surface height roughness distribution of pavement surfaces as only a small fraction of the surface may be interrogated using currently available sensors. An assumption is made that, within a survey field without



apparent rutting or serious surface damage, the surface roughness height distribution measured in 2D space has the same distribution as a line-profiling in 1D. This represents the classical requirement of statistical stationarity. The properties of the surface roughness and the parameters describing a rough surface will be introduced first. After that, surface roughness effects on the capacitance and the impacts on pavement surveys will be discussed.

5.1 Surface roughness

5.1.1 Surface roughness model

The surfaces of the roads that we walk on every day in our lives, are either smooth or rough depending on the scale we look at: from a high altitude, it can be assumed that almost all road surfaces are smooth whilst when using a microscope, their roughness are non-negligible. In this work of placing a non-invasive capacitive coupled technique system directly onto the surfaces of the pavements, the surfaces are considered to be rough. A rough surface is categorized into a self-similar fractal pattern (e.g. snowflakes) and a self-affine surface pattern (e.g. Brownian process, Gaussian distribution) [1] [2] [3]. The fractal geometry assumes a highly irregular framework with a simple process repeated many times at various scales but with the same spatial directions for each repeatable instance. A self-similar pattern, of isotropic transformation type, is a repeatable process of itself obtained by scaling with the same ratio in different directions. A self-affine pattern, of anisotropic transformation type, is a repeatable process of itself obtained by scaling with different ratios in different directions. An affine transformation is more common than a similarity, in that it can elongate objects [2]. For example, an affine transformation can transform circles into ellipses while a self-similar transformation keeps circles as circles or rectangles as rectangles, as shown in Table 9. A summary of the properties of these two patterns is given in Table 9.

Table 9: A summary of the properties of the self-similar rough pattern and the self-affine rough pattern

	Self-similar pattern	Self-affine pattern
Transformation Type	Isotropic transformation type	Anisotropic transformation type
Example	e.g. a square scaled with same ratio in all directions 	e.g. Up/Down direction increases with a larger ratio than Left/Right for a circle 

5.1.2 The mechanisms of the self-affine rough pattern

There are a few mechanisms leading to a self-affine roughness including the deposition process, erosion, or etching and the propagation through other media. According to Barabasi [3], a deposition process is generally categorized into a random deposition and the ballistic deposition such that:

- “The random deposition (RD) is a process that assumes a particle falls vertically from a randomly chosen site over the surface that is higher than the maximum height of the surface, until this particle reaches the top of the column under it where this particle is deposited.
- According to the description of the growth process of a ballistic deposition introduced as a model of colloidal aggregates, it is known that the ballistic deposition (BD) is about such a situation. A particle is released from a randomly chosen position above the surface and this particle follows a straight vertical trajectory until it reaches the surface where it sticks.”

From those two definitions, the most important difference relates to the distance travelled by the particle. Particles following the random deposition mechanism are uncorrelated with its neighbouring particles along the interface, while, for the mechanism of the ballistic deposition, particles are correlated to their neighbouring particles by sticking to the edges of neighbouring particles which leads to the lateral growth. The properties of these two deposition models are summarized in Table 10 based on Barabasi’s research [3]. Furthermore, it is stated that landscape hill terrains, snowflakes aggregations, the surfaces

of the earth and road surfaces are examples of the self-affine rough pattern [1] [2] [4] [5]. Therefore, the investigated pavement surfaces described in this research are recognized to have the self-affine pattern following a ballistic deposition process mechanism [1] [2] [3] [4] [5].

Table 10: A summary of random deposition models and ballistic deformation models from fractal theories [1] [2] [3] [4] [5]

Deposition model	Random deposition model (RD)	Ballistic deposition model (BD)
Roughness Type	Self-similar	Self-affine
Mean height of the surface	$\bar{h}(t) = \frac{1}{L} \sum_{i=1}^L h(i, t)$	$\bar{h}(t) = \frac{1}{L} \sum_{i=1}^L h(i, t)$
Correlation Length ϵ	Zero	Non-zero
Correlation	Un-correlate	Correlated
Width of the interface w	Non-saturation $w(t) \sim t^{\frac{1}{2}}$	Saturation $w(L, t)$ $= \sqrt{\frac{1}{L} \sum_{i=1}^L (h(i, t) - \bar{h}(t))^2}$ $w(L, t) \sim t^\beta \quad t \ll t_x$ $w(L) \sim L^\alpha \quad t \gg t_x$
Scaling relation	No	$w(L, t) \sim L^\alpha f(t/L^z)$
Crossover time	No	$t_x \sim L^z$
Growth exponent	$\frac{1}{2}$	β
Roughness exponent	No	α
Dynamic exponent	No	$z = \frac{\alpha}{\beta}$

Notes: t is the time with units of seconds; w is the width of the interface with units of metres; L is the lateral length of the surface; the surface is defined as a set of particles with the highest particle in each column defining the surface height; β is a growth exponent which describes the time-dependent dynamics of the roughening process; α is a roughness exponent which describes the roughness of a saturated interface; z is a dynamic exponent which describes the crossover time from non-saturation to saturation.

5.1.3 Parameters describing pavement surface roughness

5.1.3.1 Finite and effective parameters

In order to assess roughness effects on the electrical impedance measurements, the surface has to be modelled. Theoretically, it is impossible to use a finite number of parameters to design a general model for surfaces because of the infinite number of road surface textures encountered. Practically, the only reasonable approach available to characterize the rough surfaces of manmade or natural pavements is to use a random structure describing the falling process of particles using a finite number of effective parameters [6]. Gadelmawla [7] illustrated 59 roughness parameters expressing the global and local roughness of different scales. Among these parameters, the main effective parameters are the root mean square (RMS) roughness, the arithmetic average height, the maximum height of peaks, the maximum depth of valleys, the amplitude density function (ADF), the correlation length, the roughness exponent and the auto correlation function (ACF). Definitions and formulas of these main parameters are explained in Appendix 1. In this work, two pavements of good condition (the surface is visually smooth and without cracks; that pavement area was recently maintained, updated and put into service before the field surveys) and poor condition (there were moisture-cracks on the surface even on dry days; for the old-wet area in this poor pavement, there are plants e.g. mosses usually preferring wet growing conditions; that pavement area was not updated for many years) are investigated. The laser profiling instrument was deployed on both pavements during the field surveys to collect the height distributions of the pavement surfaces. 8800 data points (see Figure 149: five-line investigations by using the capacitive system with step-size of 10 cm) were collected on the good pavement with a total survey length of 1.1 m. 17600 data points (see Figure 150: around seven-line investigations by using the capacitive system with step-size of 10 cm) were collected on the poor pavement with a total survey length of 2.2 m. The height distribution data was computed from the surface profiling of both pavements and is illustrated in Figure 112 and Figure 113.

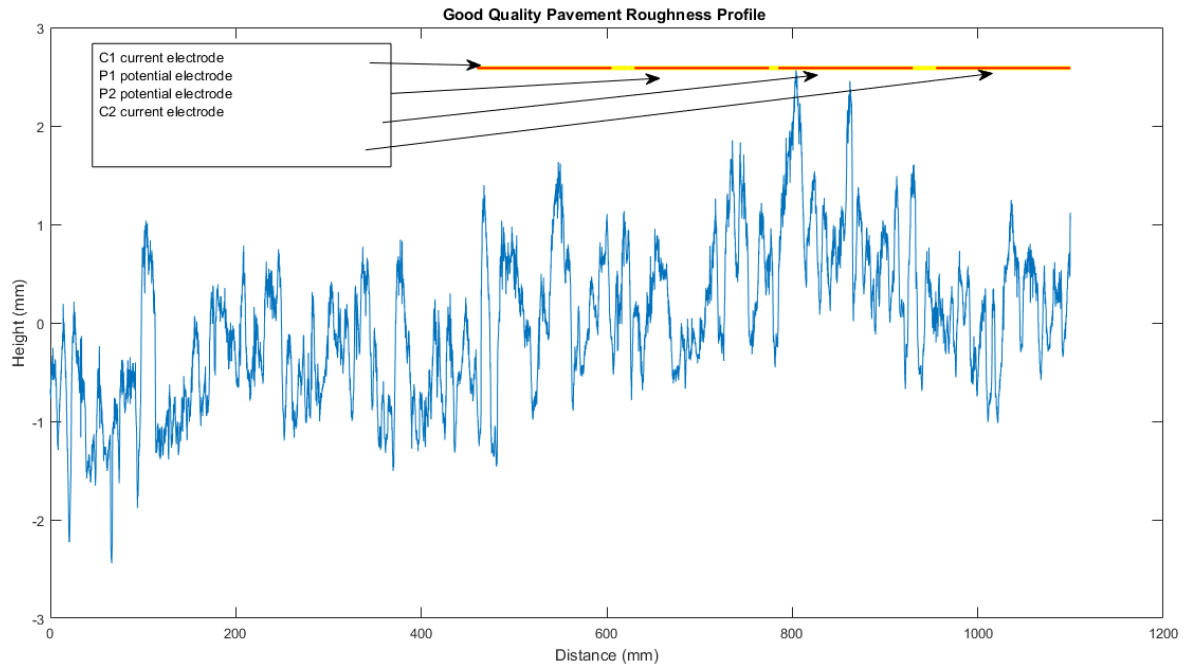


Figure 112: Surface height distribution of the good pavement between the North Car Park and the Gisbert Kapp building

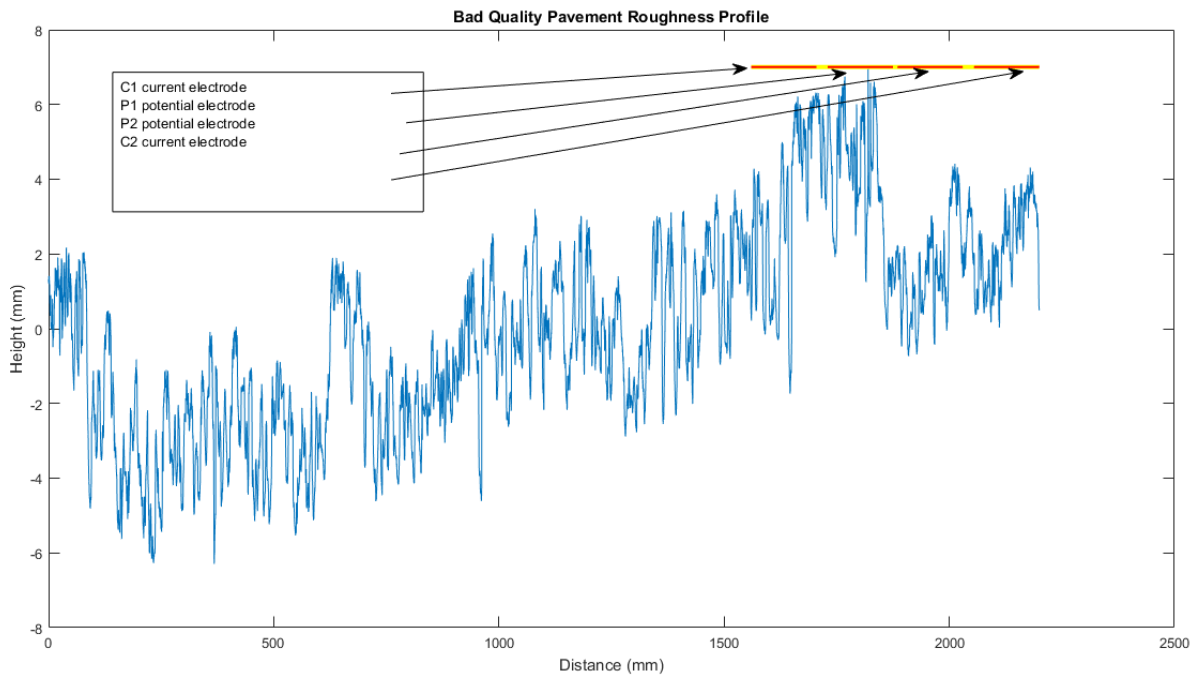


Figure 113: Surface height distribution of the poor pavement behind the Gisbert Kapp building

The blue curves represent the height distributions of the pavement surfaces; the red lines represent the four electrodes of the capacitive coupled resistivity system (for spatial comparison purposes); the yellow lines are the electrode separations. For comparison

purposes, their amplitude cumulative distribution functions, numerically obtained from data used in Figure 112 and Figure 113, are given in Figure 114.

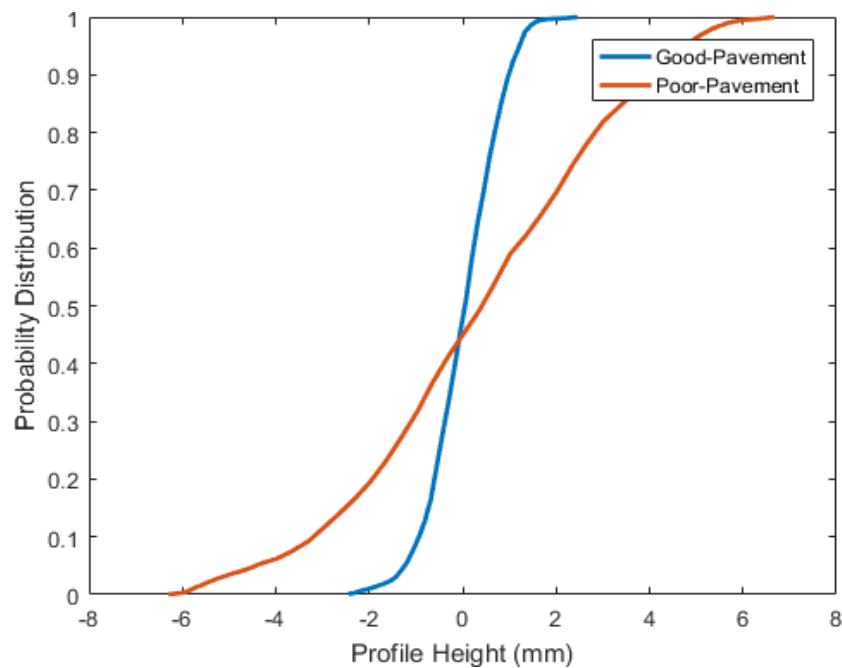


Figure 114: Cumulative distribution function of the amplitude surface roughness of a good pavement and a poor pavement, numerically obtained from data used in Figure 112 and Figure 113

The surface of the poor pavement is much rougher than the surface of the good pavement: 40% of the surface of the poor pavement has a height variation greater than 2 mm which is the maximum height variation of the good pavement. The maximum height variation of the poor pavement is 6 mm which is three times that of the good pavement. The main effective parameters are calculated based on the measured height distribution data (denoted by Y_i) and are summarized in Table 11.

Table 11: Main effective parameters describing the roughness of a good and a poor pavement (Y_i : measured raw height distribution data)

Roughness Parameter (Whole profile)	Mathematic definition	Good-Quality pavement (mm)	Poor-Quality pavement (mm)
Mean line	$\bar{Y} = \frac{\sum_{i=1}^n Y_i}{n}$	29.8	29.9
Reference line	$Y_{ref} = Y_1$	29.1	31.2
Arithmetic average height	$R_a = \frac{\sum_{i=1}^n Y_i - \bar{Y} }{n}$	0.6	2.2
Standard deviation of the roughness profile	$STD = \sqrt{\frac{\sum_{i=1}^n (Y_i - \bar{Y})^2}{n}}$	0.7	2.7
RMS of the roughness profile	$R_{rms} = \sqrt{\frac{\sum_{i=1}^n (Y_i - Y_1)^2}{n}}$	1.0	3.0
Roughness profile	$y_i = Y_i - \bar{Y}$	Figure 112	Figure 113
Max Height of Peaks (local sub-section)	$R_p = \max(y_i)$	1.0, 0.8, 1.6, 2.5, 1.6	2.1, 1.8, 3.2, 6.3, 7.0
Max Height of Valleys (local sub-section)	$R_v = \min(y_i)$	2.4, 1.5, 1.4, 0.6, 1.0	6.2, 5.5, 4.6, 2.5, 0.7
Mean slope	$\bar{k} = \frac{\sum_{i=1}^{n-1} (y_{i+1} - y_i) / \Delta l}{n}$	0.0049 mrad	0.0015 mrad
Correlation Length ε	Shortest distance in which the value of the ACF drops to 36.8% of the zero-shift value	12.1 mm	8.6 mm
ADF (amplitude probability density function)	$P(h) = \text{probability}(y_i \leq h)$	Figure 115	Figure 117
ACF (autocorrelation function)	$\frac{\sum_{i=1}^{N-k} (y_i - \bar{y})(y_{i+k} - \bar{y})}{\sum_{i=1}^N (y_i - \bar{y})^2}$	Figure 116, Figure 119	Figure 118, Figure 120
PSD (power spectral density)	$\frac{(\int_0^L y_i \exp(-jwx) dx)^2}{L}$	Figure 125	Figure 126

From Table 10, it can be stated that both surfaces of the good pavement and the poor pavement have self-affine rough patterns because of their non-zero correlation lengths. The root-mean-square height and the arithmetic average height of the poor pavement are

almost three times those of the good pavement. Both heights are very important parameter affecting the capacitance between an electrode and the material on which it rests. The amplitude probability density function of both pavements is displayed in Figure 115 and Figure 117. The auto correlation function of both pavements is shown in Figure 116 and Figure 118. The correlation lengths of both pavements are derived from the auto correlation functions.

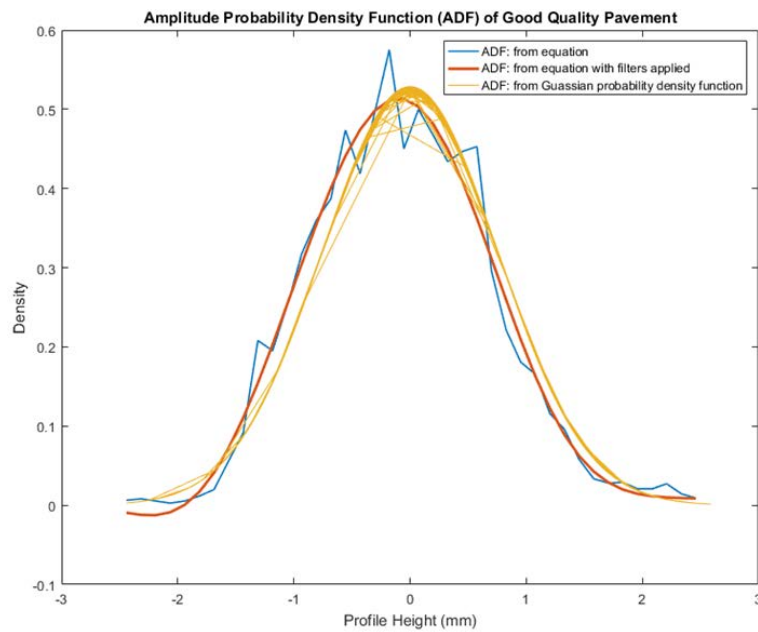


Figure 115: Amplitude probability density function of a good pavement

The blue curve is the amplitude-probability-density-function calculated from the data. The red curve is a filtered version of the blue curve. The yellow curve is a Gaussian distribution function fitted using a MATLAB function. The Gaussian distribution of the heights of these two pavements will be discussed in the following sections.

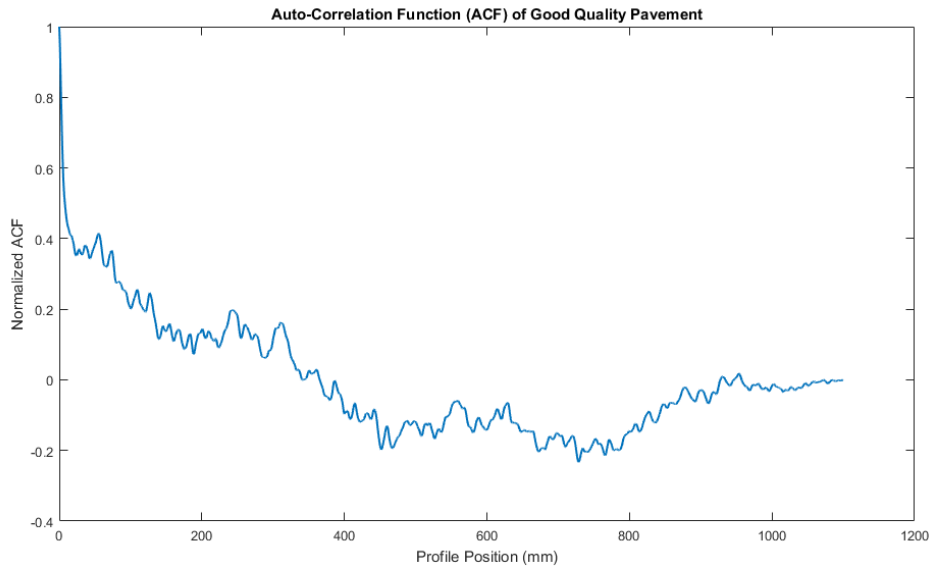


Figure 116: Global autocorrelation function (ACF) of a good pavement

From the Figure 115, for the good pavement, 50% of the surface height measurements lie within 1 mm of the mean value. The peak-to-peak amplitude is smaller than 4 mm. The correlation length of 12.1 mm is derived from the 36.8% ($1/e = 36.8\%$ was used [8]) value of the auto correlation function (Figure 116) of the good pavement.

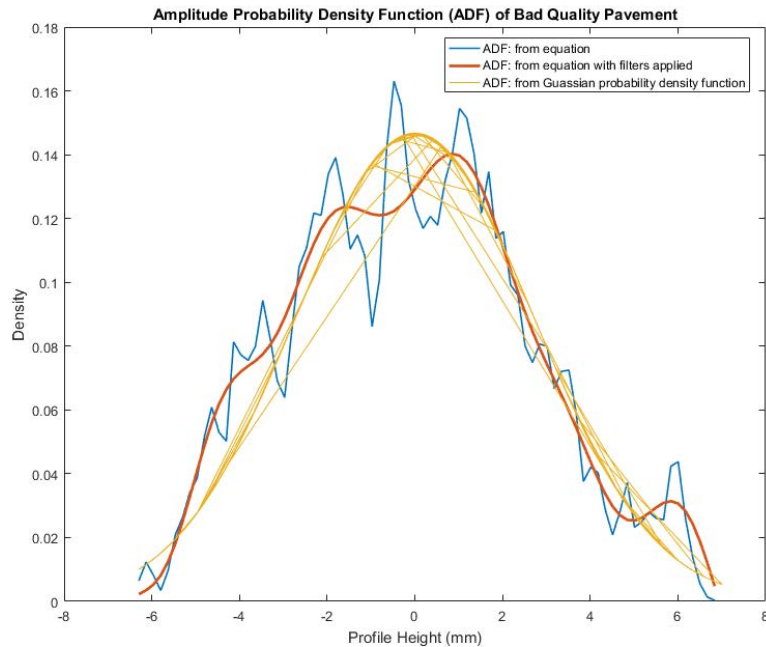


Figure 117: Amplitude probability density function of a poor pavement

The blue curve is the amplitude-probability-density-function calculated from the data. The red curve is a filtered version of the blue curve. The yellow curve is a Gaussian distribution

function fitted using a MATLAB function. The Gaussian distribution of the heights of these two pavements will be discussed in the following sections.

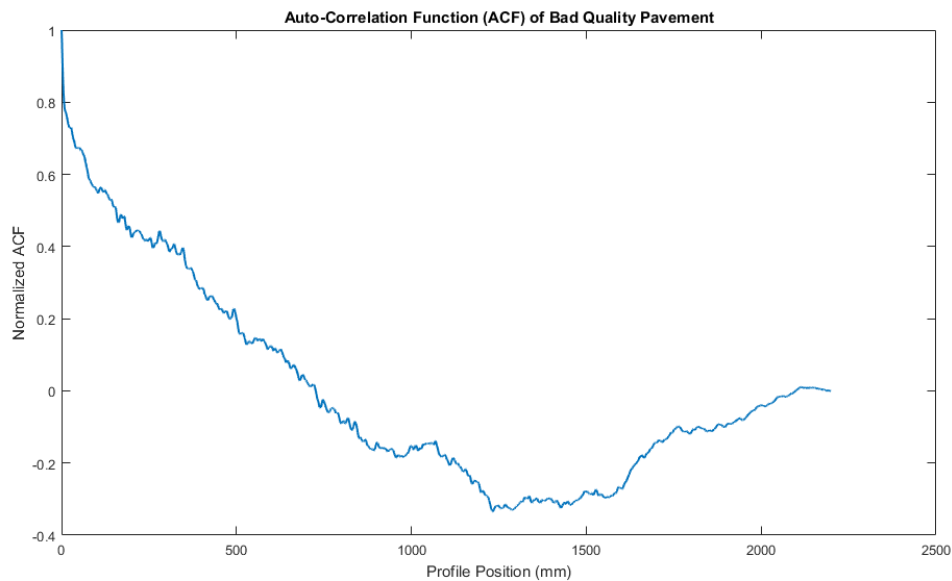


Figure 118: Autocorrelation function (ACF) of a poor pavement

From Figure 117, for the poor pavement, 50% of the surface height measurements lie within 2 mm of the mean value. The peak-to-peak amplitude is smaller than 12 mm. The correlation length 8.6 mm is deduced from the 36.8% ($1/e = 36.8\%$ was used [8]) value of the auto correlation function (Figure 118) of the poor pavement. This correlation length compared to the global peak-to-peak amplitude indicates the poor pavement has more rocky surface profiles and larger surface resistance than the pavement of good condition.

Whitehouse [8] concluded in his research studying a large number of surfaces that random waveform descriptions of manufactured surfaces can be characterised by an autocorrelation function (ACF) and a height distribution. Furthermore, he stated that models of a great number of manmade surfaces have Gaussian height distributions and exponential autocorrelation functions. The height distributions of both pavements are discussed in section 5.1.3.4. Exponential autocorrelation functions describing manmade surfaces are also verified by experiments of the good pavement and the poor pavement in Figure 116 and Figure 118. As roughness effects on the capacitances have to be considered during data processing, a local (computed from a sub-section of the data set) auto correlation function and local correlation length are also predicted. The autocorrelation functions of both pavements are discussed in section 5.1.3.2.

5.1.3.2 Autocorrelation function (ACF)

The autocorrelation describes a correlation relationship between a surface profile and the same profile but shifted by a length parameter. The correlation length, defined as the length when the autocorrelation function magnitude drops down to a value of between 10% and 50% (here $1/e = 36.8\%$ was used) of the maximum value at a shifted length parameter of zero [8], is used to characterize the lateral properties of the pavement surface. Peklenik [9] proposed four classifications of the autocorrelation function as a scale to classify a suitable group of surface roughness characteristics, which includes the types of exponential decay plus cosine, exponential decay plus sine, exponential decay plus cosine and sine, and exponential decay. Two local auto correlation functions corresponding to the surface data collected at specific locations of both pavements, are displayed in Figure 119 and Figure 120. The autocorrelation function has been calculated for locations corresponding to the positions of the C1, P1, P2 and C2 electrodes used during the resistivity surveys revealing similar correlation function widths. The local auto correlation functions of the surfaces of both pavements correspond to exponential decays with cosine or sine modulation. The X-coordinate represents the scanning distance with units of mm. The Y-coordinate is the local normalized autocorrelation function.

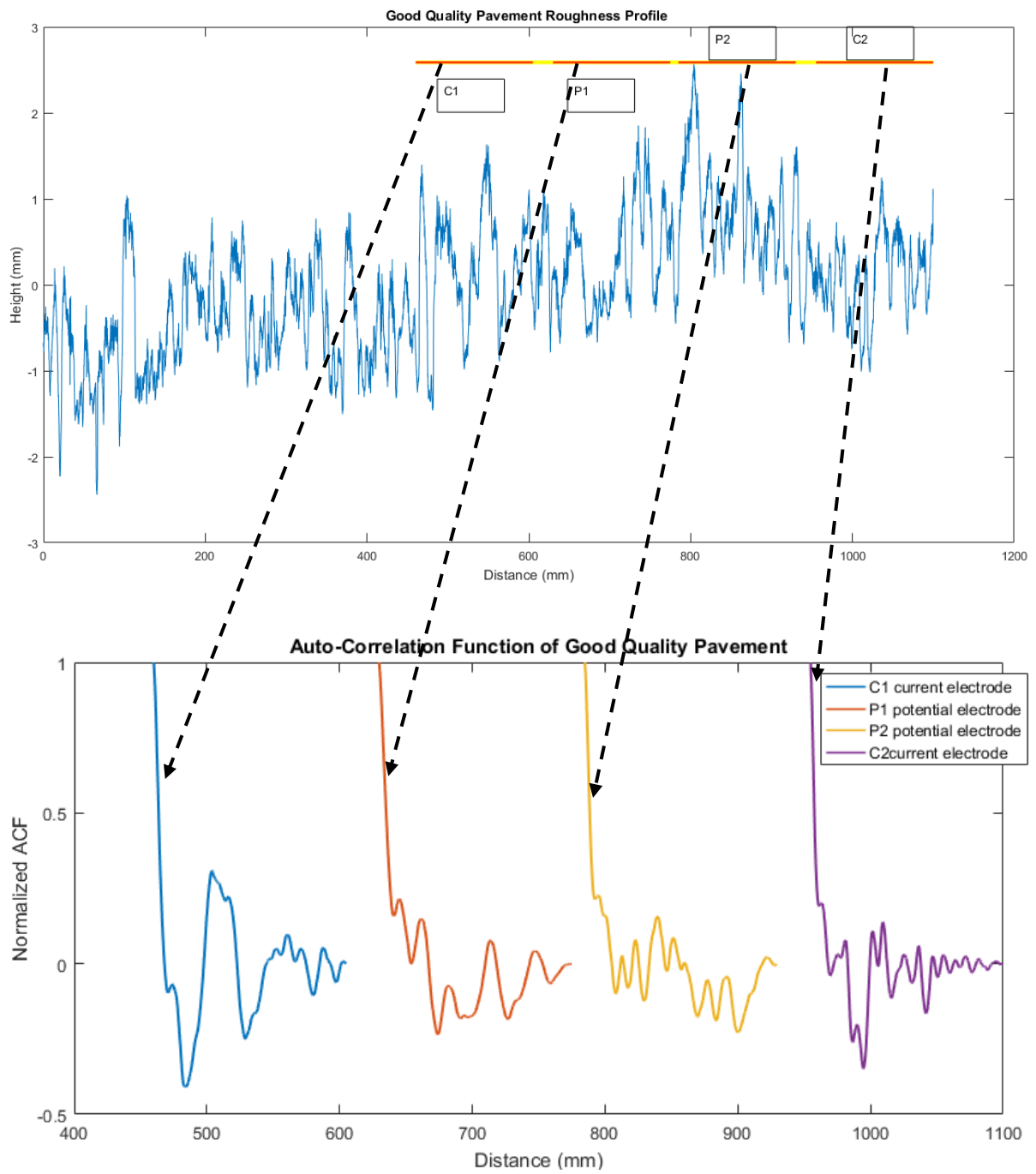


Figure 119: One example of a local autocorrelation function of a good pavement in final survey position where four electrodes are placed in Figure 112

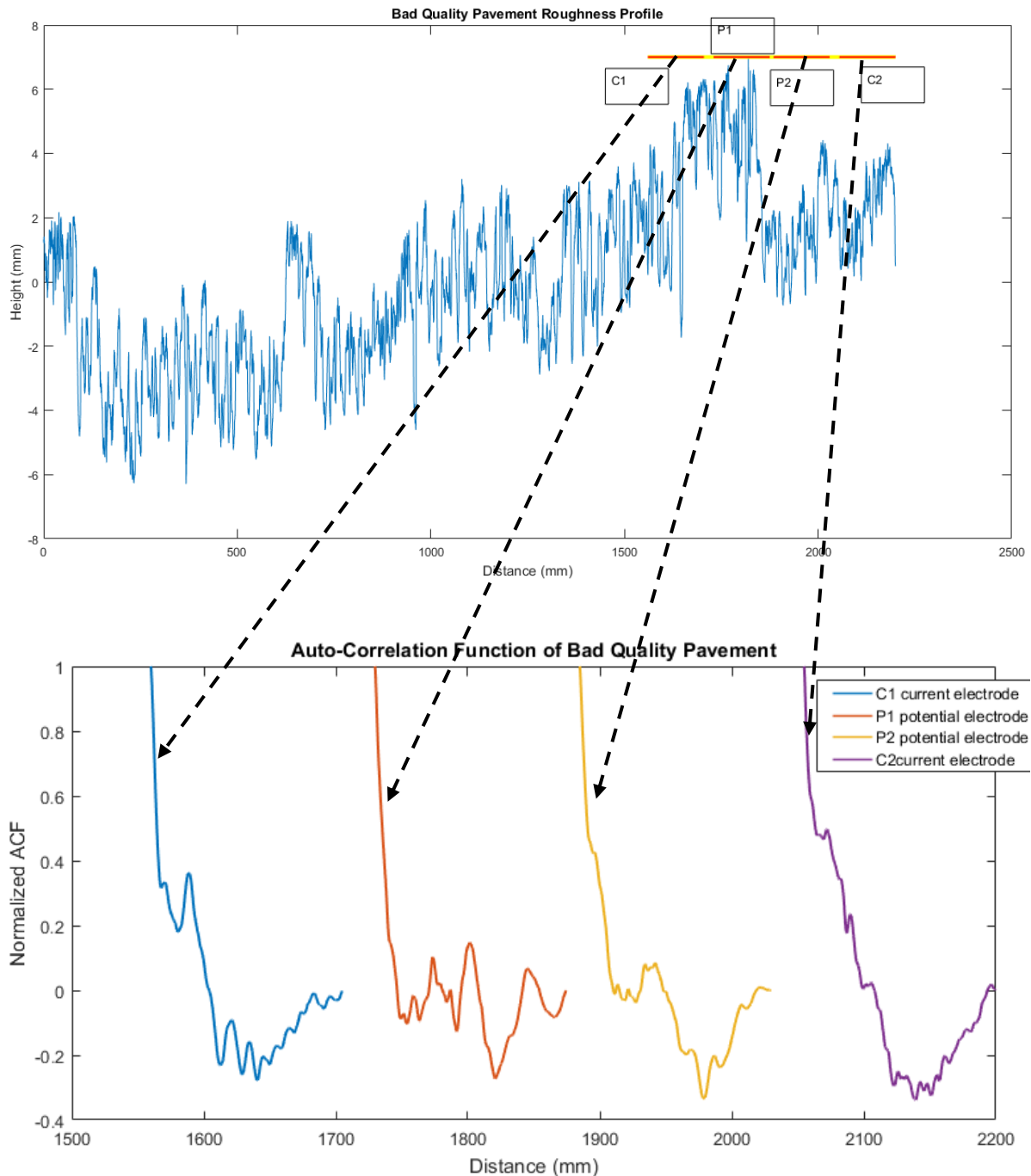


Figure 120: One example of a local autocorrelation function of a poor pavement in final survey position where four electrodes are placed in Figure 113

Note: the four colour curves in Figure 119 and Figure 120 represent local normalized autocorrelation functions corresponding to the surface data collected at a specific location (when the capacitive system moves to the final survey position, seen in Figure 112 and Figure 113) of both pavements (blue curve: from the corresponding surface data of electrode C1; red curve: from the corresponding surface data of electrode P1; yellow curve:

from the corresponding surface data of electrode P2; purple curve: from the corresponding surface data of electrode C2). The X-axis of four local normalized ACFs is limited by the length (110 mm) of the electrode plates. The spacing between the normalized ACFs corresponds to the spacing between the electrode plates.

The curves displayed in these two figures (Figure 119 and Figure 120) show that for both pavements the local autocorrelation functions decrease monotonically with increased length parameter. The local autocorrelation functions have maximum values when the shifted length parameter is of zero value and they converge asymptotically to zero. For every investigation position, there are four corresponded correlation lengths corresponding to the surface areas related to the four electrodes. All these local correlation lengths correspond to the magnitude of the local autocorrelation functions dropping to $1/e$ of its maximum value. These local correlation lengths are given in Figure 121 and Figure 122. Different colours represent the different electrodes and the local roughness varies along the field survey direction.

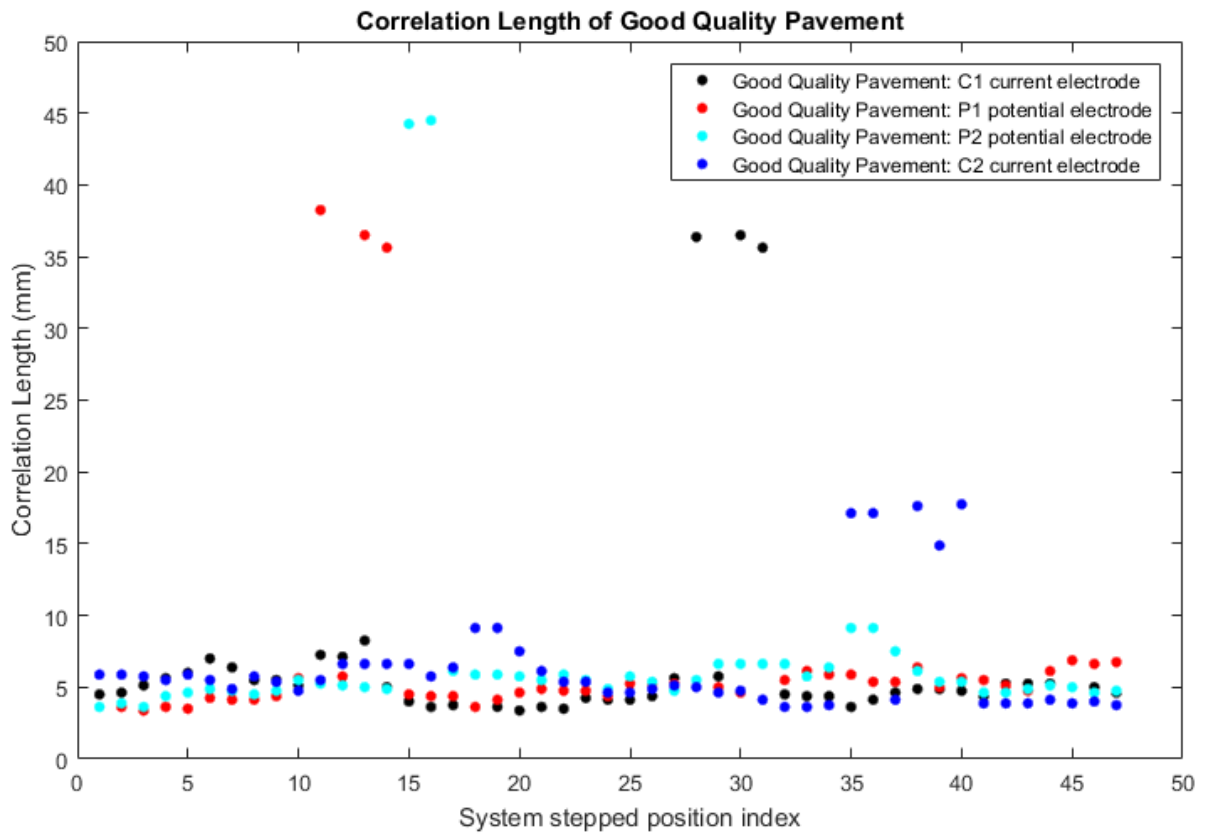


Figure 121: Local correlation lengths of a good pavement

The X-coordinate is the position index related to the step-increment of the system during the profiling measurement. The Y-coordinate is the local correlation length. Four colour markers respectively represent local correlation lengths, corresponding to the electrode dimensions of the good quality pavement which are calculated at every investigation position.

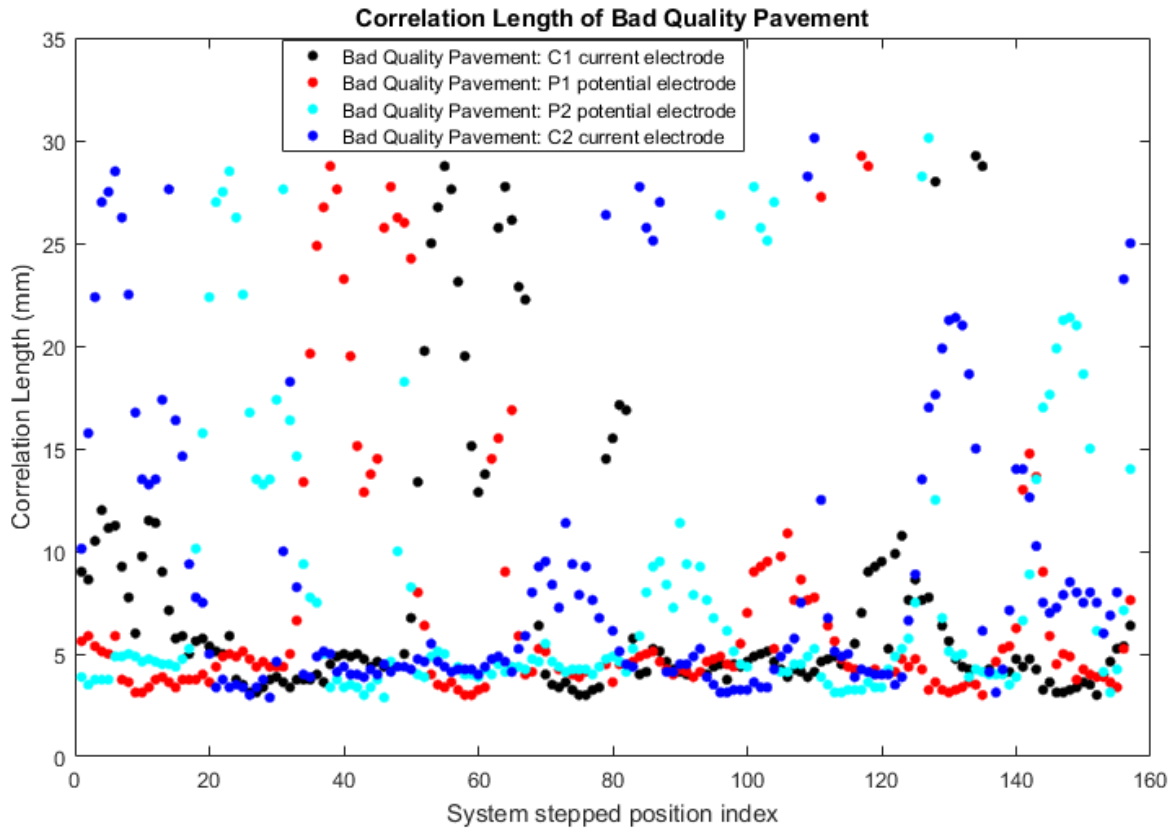


Figure 122: Local correlation lengths of a poor pavement

The X-coordinate is the position index relating to the step-increment of the system during the profiling measurement. The Y-coordinate is the local correlation length. Four colour markers respectively represent local correlation lengths, corresponding to the electrode dimensions of the bad quality pavement which are calculated at every investigation position.

Note: Four colours markers in Figure 121 and Figure 122 represent four corresponding correlation lengths (denoted by Good Quality Pavement: C1 current electrode, P1 potential electrode, P2 potential electrode, C2 current electrode for the good pavement; denoted by Bad Quality Pavement: C1 current electrode, P1 potential electrode, P2 potential electrode, C2 current electrode for the poor pavement) corresponding to the surface areas related to the four electrodes (C1, P1, P2 and C2) at every investigation position. For example, for the 1st step of the profiling measurement, the capacitive system is placed at the beginning position (1st X-value on the X-axis) of the survey area. The four electrode plates have their corresponding dimensions and hence, four local correlation lengths (four circles of different colours) are calculated.

It is seen that generally the local correlation lengths of the poor pavement are often larger than those of the good pavement, as the smaller particles tend to be stripped out. The mean correlation lengths are summarized in Table 12. This table gives us a rough idea of the local correlation lengths of both pavements. To achieve accurate analysis results during data processing, a single local correlation length needs to be used corresponding to the immediate survey area. It is seen that the average local correlation lengths of the poor pavement is a little larger than those of the good pavement.

Table 12: Mean correlation length for each electrode in all survey positions

	Mean Correlation length (C1)	Mean Correlation length (P1)	Mean Correlation length (P2)	Mean Correlation length (C2)
Good quality pavement	6.8 mm	7.8 mm	7.1 mm	6.5 mm
Bad quality pavement	7.7 mm	7.4 mm	8.4 mm	9.0 mm

5.1.3.3 Power spectral density function (PSD)

The power spectral density is linked to the autocorrelation function by the Fourier transformation. The power spectral density function is given by

$$PSD(f) = \frac{1}{L} \left(\int_0^L h(x) e^{2\pi f x} dx \right)^2 \quad (5-1)$$

Where L is the width of each electrode with units of metres; x is the scan length and f is the spatial frequency.

A random pavement surface, recognized to have the self-affine roughness model, exhibits a power-law decay power spectral density relationship $PSD(f) = B f^\beta$ in a finite range of spatial frequencies [4] [6] [10] [11] [12]. B is a constant of dimensions of length in metres and β is a dimensionless constant.

Applying the power spectral density function to every survey area, a number of power spectral density results are calculated. Here, only the local power spectral density for the last scan and the global power spectral density of both pavements combined are given in Figure 123, Figure 124, Figure 125 and Figure 126.

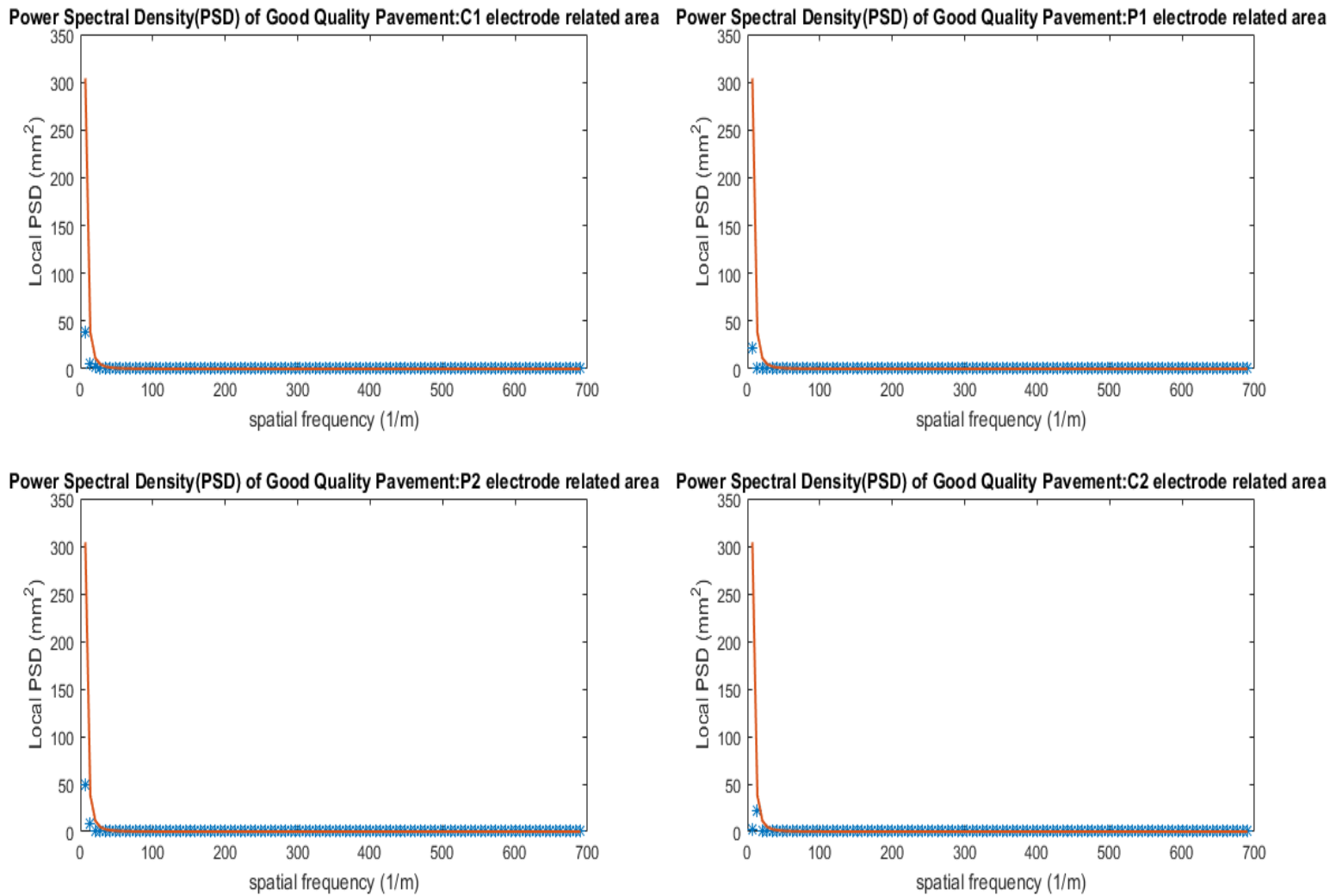
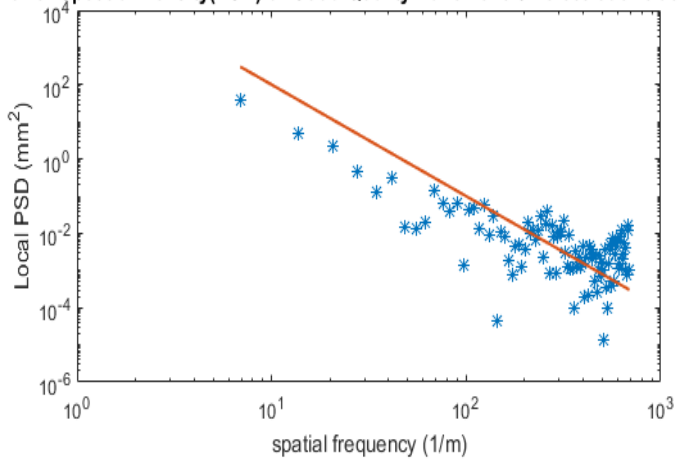
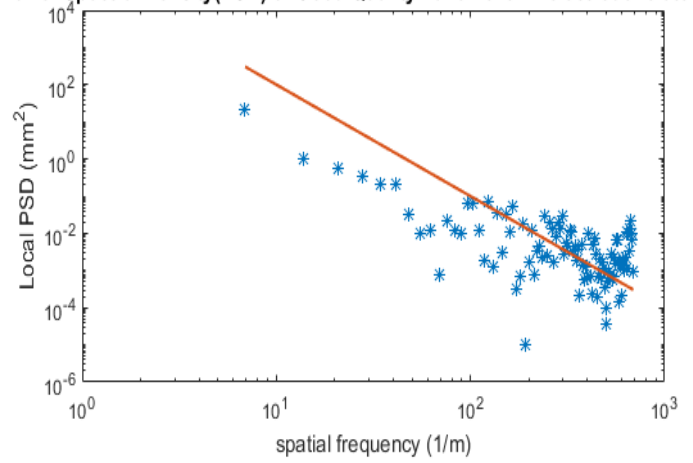


Figure 123(a): Local power spectral density (in linear-linear scale) of good pavement surface profiles covered by each electrode for the last scan

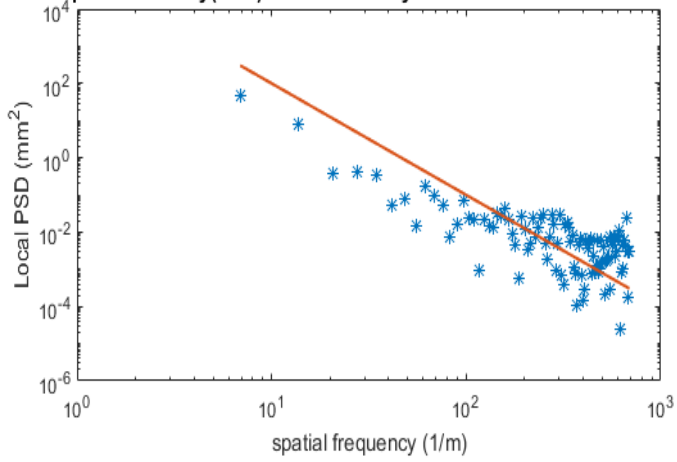
Power Spectral Density(PSD) of Good Quality Pavement:C1 electrode related area



Power Spectral Density(PSD) of Good Quality Pavement:P1 electrode related area



Power Spectral Density(PSD) of Good Quality Pavement:P2 electrode related area



Power Spectral Density(PSD) of Good Quality Pavement:C2 electrode related area

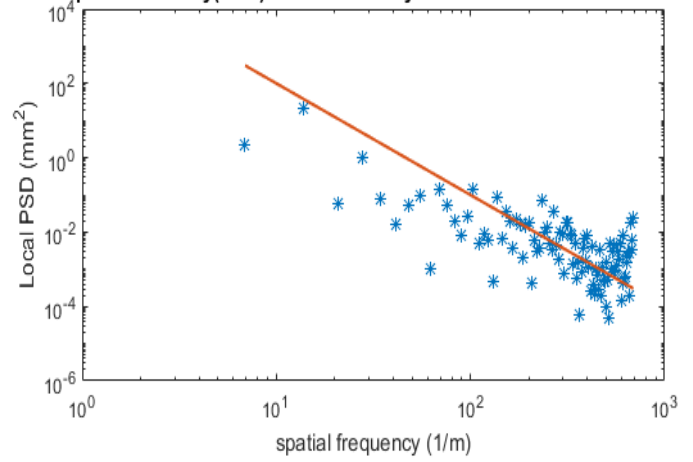


Figure 124(b): Local power spectral density (in log-log scale) of good pavement surface profiles covered by each electrode for the last scan

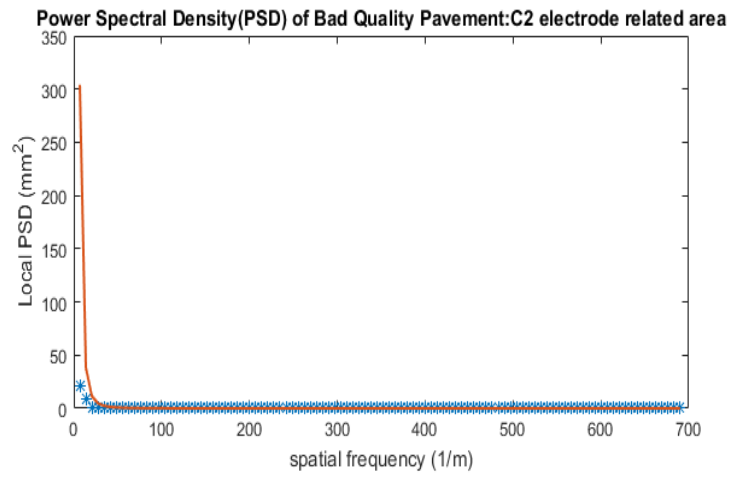
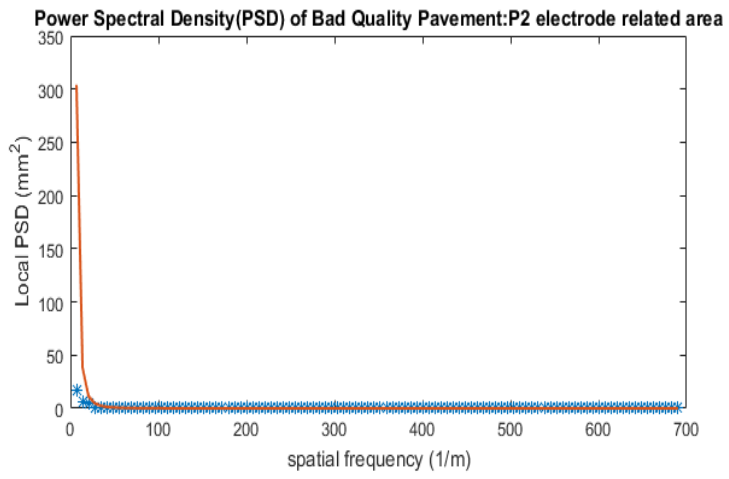
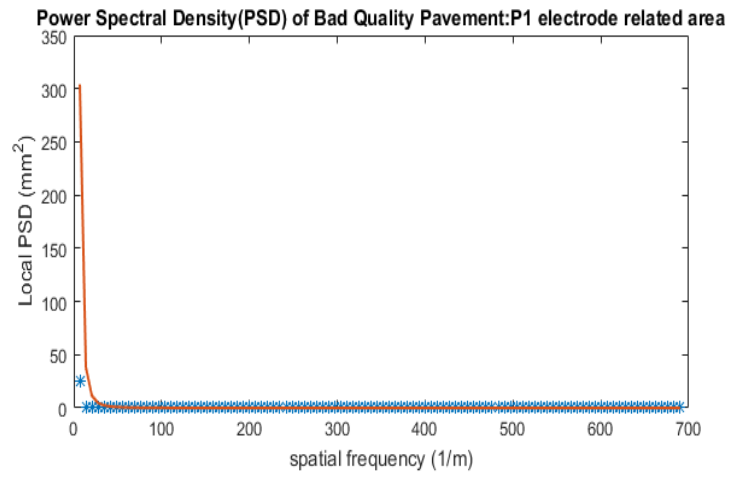
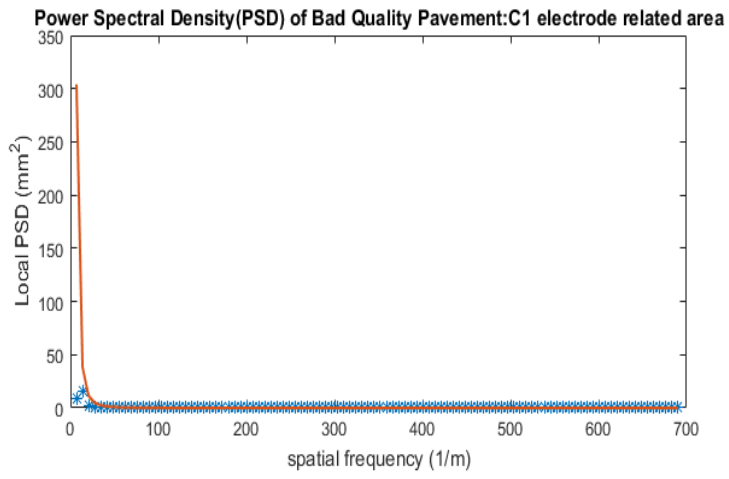


Figure 125 (a): Local power spectral density (in linear-linear scale) of bad pavement surface profiles covered by each electrode for the last scan

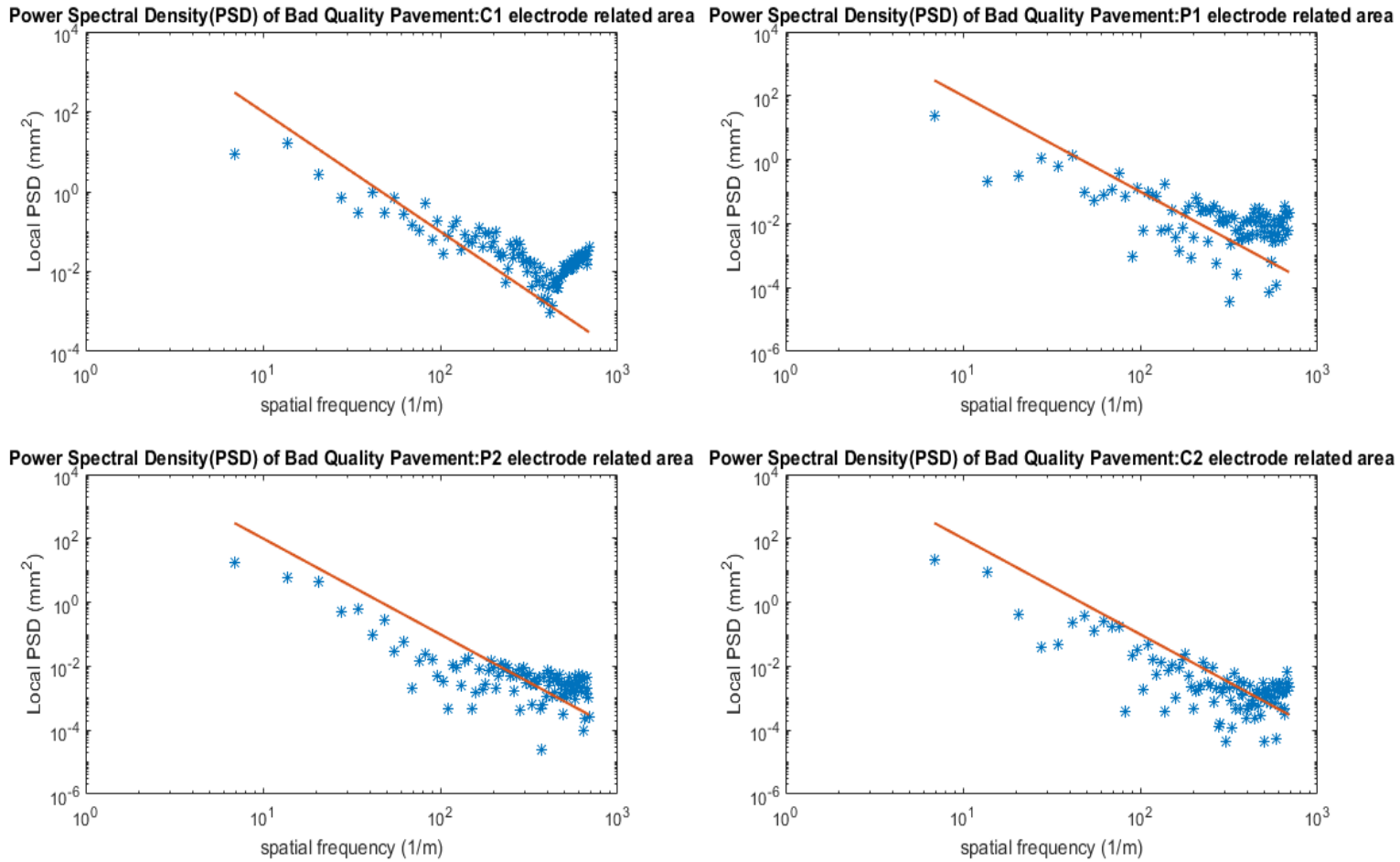


Figure 126 (b): Local power spectral density (in log-log scale) of bad pavement surface profiles covered by each electrode for the last scan

These figures from the left to the right are the local power spectral density of the surface areas related to the electrodes C1, P1, P2 and C2 of the good pavement and the bad pavement.

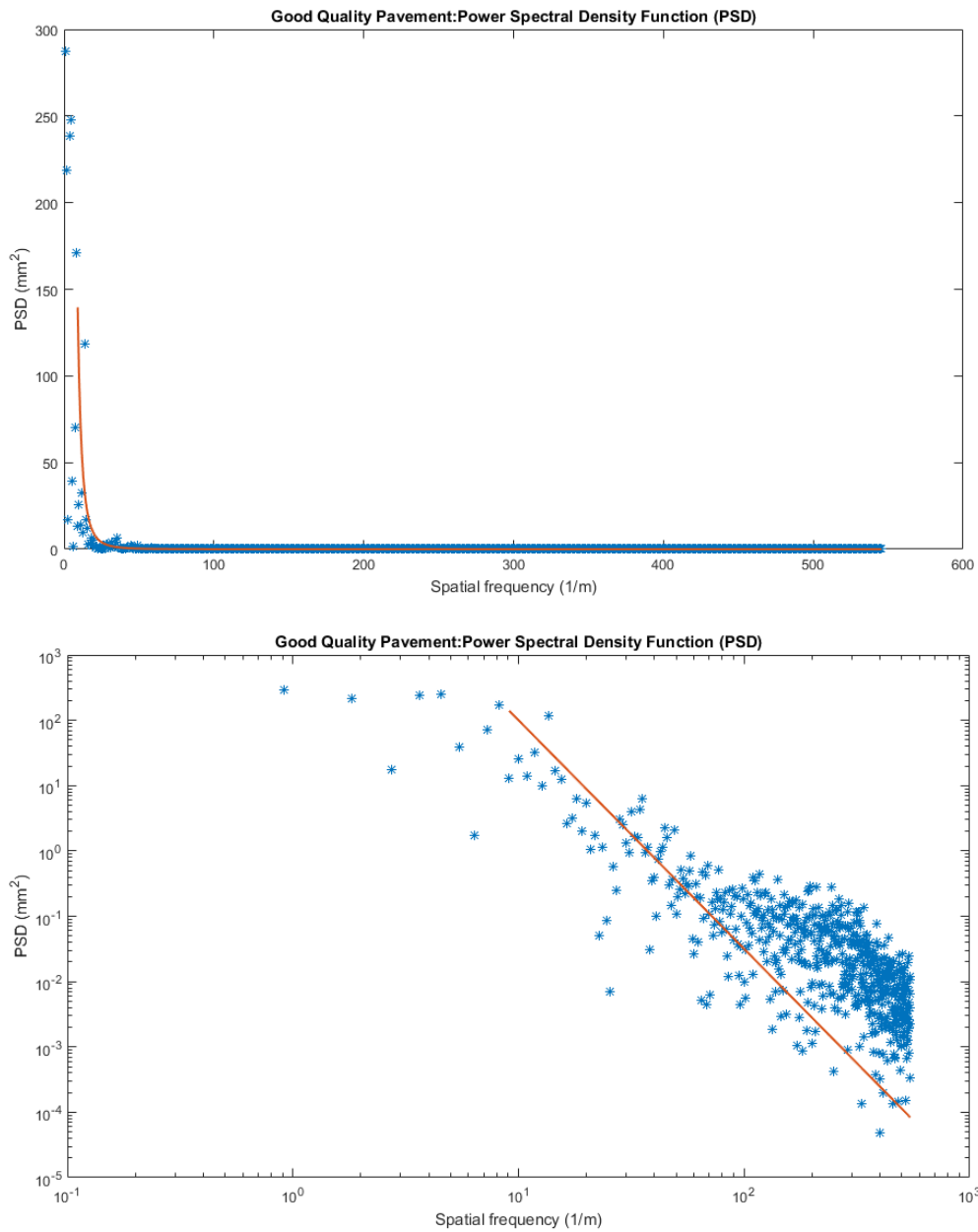


Figure 127: Global power spectral density of a good pavement surface profile (Upper: X and Y are in linear scale; Lower: X and Y are in log-log scale)

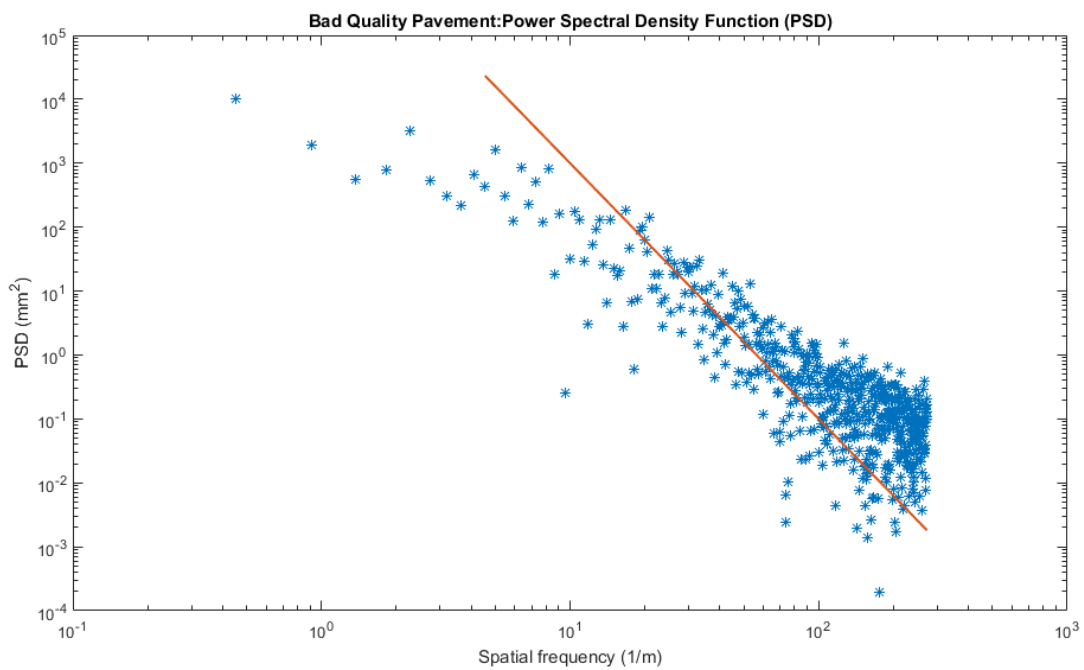
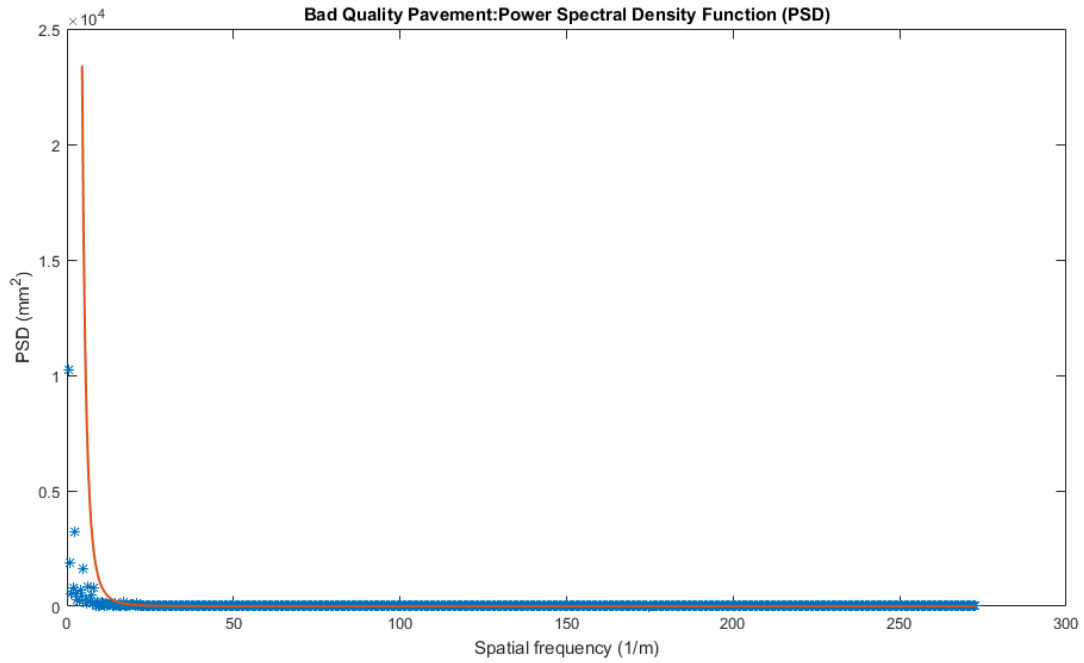


Figure 128: Global power spectral density of a poor pavement surface profile (Upper: X and Y are in linear scale; Lower: X and Y are in log-log scale)

The blue points are the calculated power spectral densities at different spatial frequencies obtained by using the power spectral density function of equation (5-1). The red curves are fitted curves assuming a power-law decay equation. Local measurement data and global measurement data are fitted by the power-law decay function. Using this fitting scheme, the constants of B and β of both pavements are obtained from the global power spectral

densities and given in Table 13. These two constants will be used in the following sections calculating the roughness impacts on the impedance.

Table 13: Two constants of power law decay function obtained from the global power spectral density ($PSD(f) = B f^\beta$)

Global PSD	B	β
Good pavement	1e-5	-3.5
Poor pavement	1e-5	-4

5.1.3.4 Gaussian height distribution

Based on the measured heights of both pavements and their probability density functions (Figure 127), a hypothesis has been proposed that the surface height distributions of both pavements may be modelled by a Gaussian distribution [8]. This hypothesis of the Gaussian distribution will be tested by the Z-test and K-S test in the following sections (see Kolmogorov-Smirnov test and Z-test).

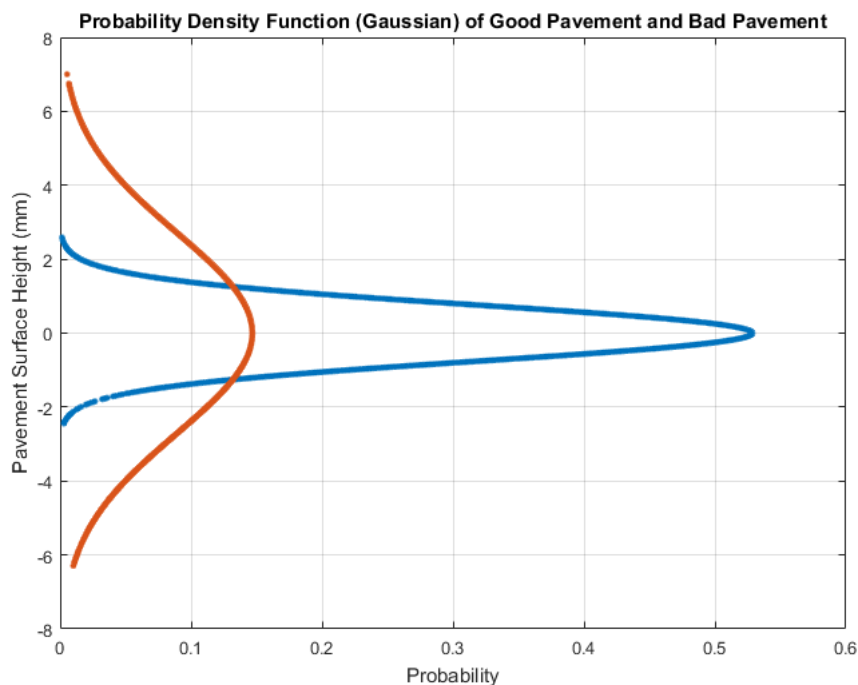


Figure 129: Probability density function of both pavements (X-coordinate represents current height probability and Y-coordinate describes current height)

In order to see if this hypothesis can be accepted or rejected, statistical tests are conducted and discussed below. Each statistical test includes the following procedure of stating a null hypothesis H_0 , choosing a statistical test to test that null hypothesis, defining parameters of the significance level and the size of samples, assuming the sampling distribution of the statistical test under the null hypothesis (a hypothesis of no difference), defining the region of rejection and finally seeing if the value of the statistical test is within the region of rejection or not. If it is within the rejection region, then the null hypothesis should be rejected. Otherwise, on failure to reject the null hypothesis an alternative hypothesis H_1 should be accepted. Such a decision of rejection or acceptance depends on the significance level which is generally set to either 0.01 or 0.05. When the probability under the statistical test is equal or less than the determined significance level value, then the null hypothesis is false which should be rejected [13]. A test of the goodness of fit has to be applied to see if the pavement surface heights meet with the Gaussian distribution. Some statistical tests, independent of the parameters of the samples, have been popularly used in goodness-of-fit approaches. These statistical tests are defined as non-parametric statistical tests e.g. the chi-square test and the Kolmogorov-Smirnov test (KS-test). Compared to the chi-square test, the Kolmogorov-Smirnov test is used because of its independency on the number of samples processed [13] [14] [15].

Kolmogorov-Smirnov test

The Kolmogorov-Smirnov test is one test method of the goodness of fit between pavement surface heights and the Gaussian distribution hypothesis. It operates on the cumulative frequency distribution function and is independent of the number of samples processed. For instance, for any specified profile height, the value of height cumulative frequency function relates the proportion of heights having values less than, or equal to, a specified height. The null hypothesis assumes that the surfaces of both pavements have Gaussian height distributions with their own mean heights of μ and their own standard deviations of σ . The number of samples available of the good pavement is 8800 and number of samples available of the poor pavement is 17600. The significance level is set as 0.05 such that the null hypothesis should be rejected if the probability is smaller or equal 0.05. The Kolmogorov-Smirnov test results of both pavements are given in Table 14.

Table 14: Kolmogorov-Smirnov test of both pavements

	Hypothesis test result (h: 1 or 0)	Test-state	Critical value
Good pavement	0	0.066	0.210
Poor pavement	0	0.062	0.149

The critical value is called the significance level of the test. In Table 14, the significance levels of both pavements are both much larger than the significance level of 0.05. The hypothesis test result of 0 indicates the null hypothesis is accepted. Thus, the height distributions of both pavement surfaces are assumed to meet with the Gaussian distribution hypothesis.

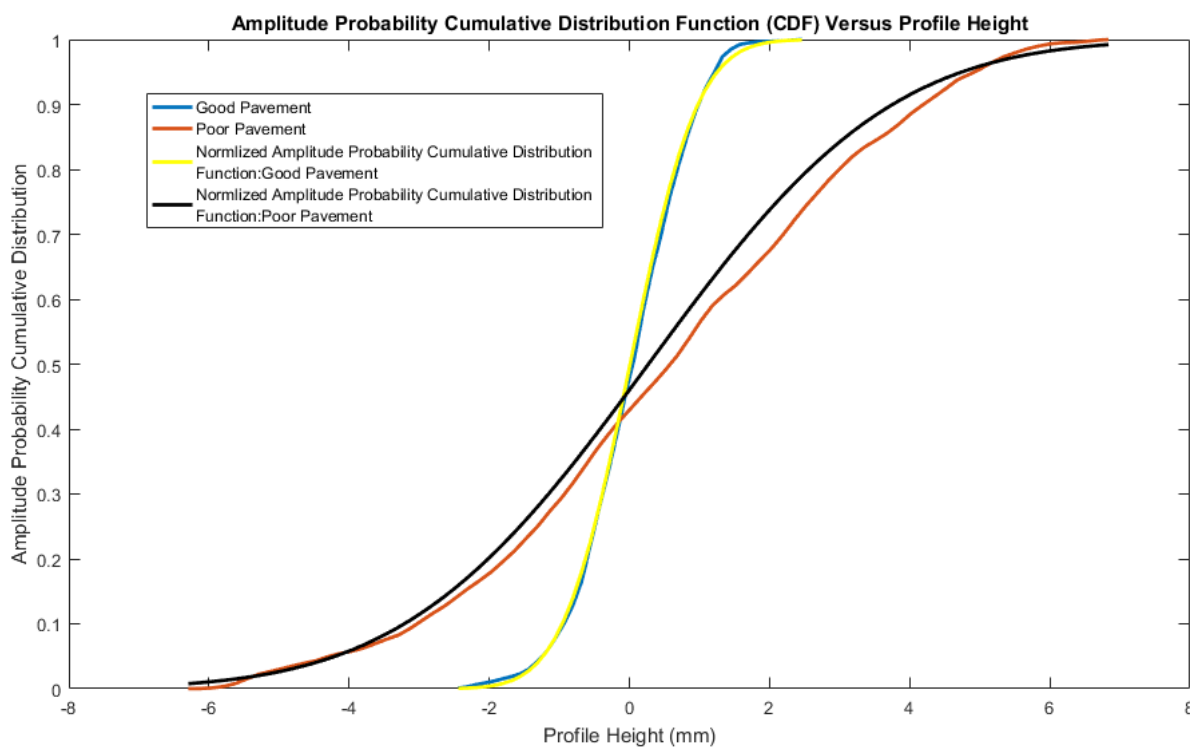


Figure 130: Amplitude probability cumulative distributions of a good pavement and a poor pavement (The four colour curves represent the analytical and measured results of both pavements)

Note: The amplitude probability cumulative distributions of both pavements are shown in Figure 128. The blue curve and the yellow curve are for the good pavement. The red curve and the black curve are the cumulative distributions of the poor pavement. The blue and the red curves are computed using the definition of the cumulative frequency distribution

function from measured data. The yellow and the black curves are produced using the internal modelled distribution functions of MATLAB.

Z-test

The null hypothesis is that the heights of both pavements are in agreement with the standard Gaussian distribution. Beside the non-parametric statistical test, a hypothesis test using a parametric test method known as the Z-test is applied to both pavement data sets to see if the null hypothesis is accepted or not. The output arguments (Table 15) illustrate the test results.

Table 15: Parametric Z-test of both pavements

	Hypothesis test result (h: 1 or 0)	Confidence interval
Good pavement	0	29.8 mm, 29.8 mm
Poor pavement	0	29.9 mm, 30.0 mm

The hypothesis test result of 0 indicates the null hypothesis is accepted at the default 5% significant level implying that the heights of both pavements may be modelled by a Gaussian distribution. The 95% confidence interval between the height of 29.8 mm and 29.8 mm includes the hypothesized mean height of 29.8 mm for the good pavement; that confidence interval between the height of 29.9 mm and 30.0 mm includes the hypothesized mean height of 29.9 mm for the poor pavement.

Normal probability plots of both pavements are often used to indicate Gaussian height distributions as shown in Figure 129 and Figure 130.

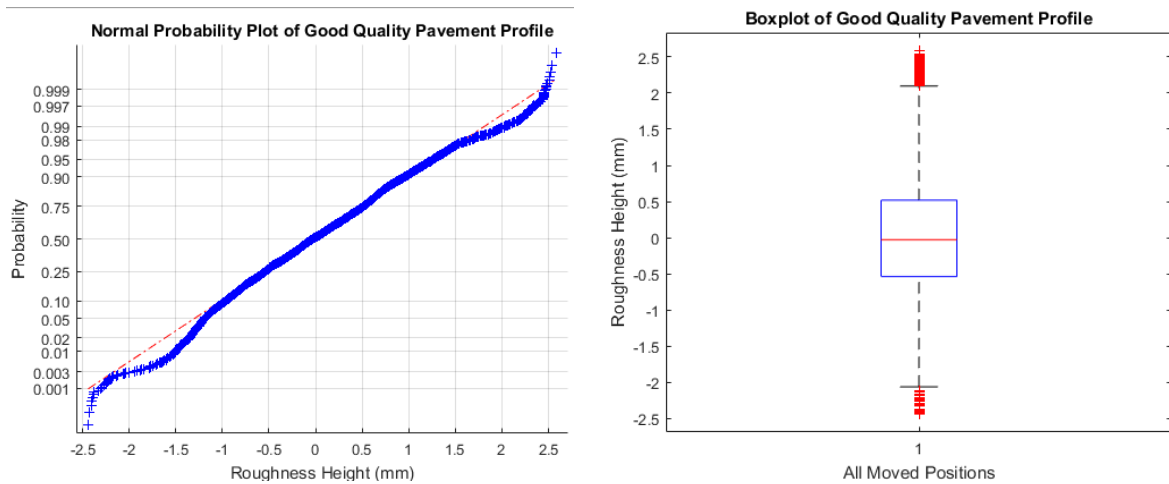


Figure 131: Normal probability plots of a good pavement (Left side: normal probability plot; Right side: a Z-test box-plot)

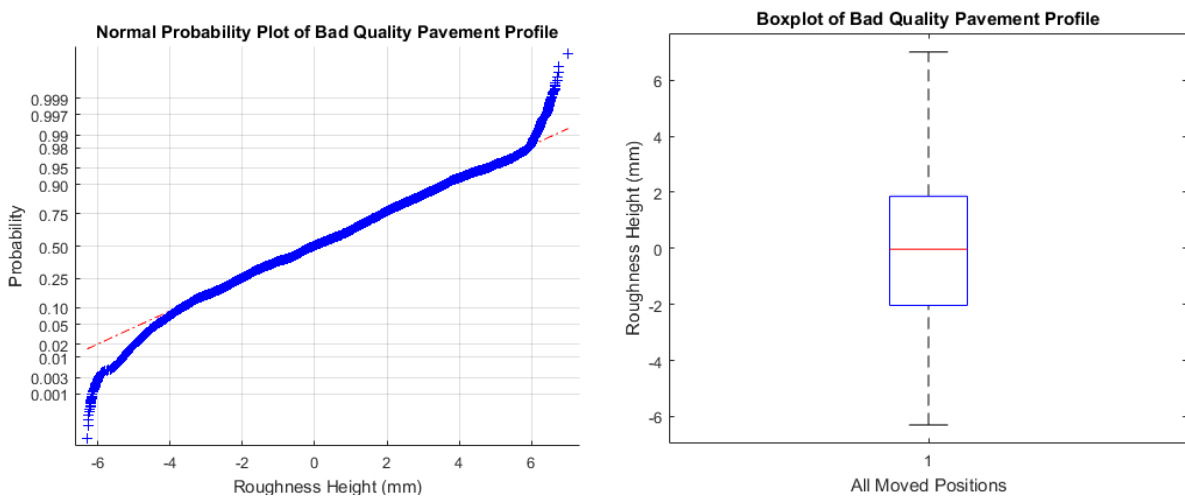


Figure 132: Normal probability plots of a poor pavement (Left side: normal probability plot; Right side: a Z-test box-plot)

The height data of both pavements, represented by the blue dots on the left side of both figures, approximately following straight lines. For comparison, a normal distribution will follow a straight line as represented by the red dotted lines on the left side of both figures. Both pavements show slight deviations from a normal distribution at the two extremes of the normal probability plots. The boxplots, on the right sides of both figures, are used to display the distribution of the samples around their medians of zero. Small red whiskers represent data outliers. It is assumed that these two pavements have random surface heights that follow a Gaussian distribution and may be modelled using an exponential autocorrelation function.

5.1.3.5 Error sources identification by Allan Variance

The autocorrelation function and the power spectral density function rely on the statistics of the surface height distribution being assumed stationary. The distance over which this stationarity assumption is valid may be assessed by the statistical method of determining the Allan variance. The Allan variance is commonly used for the analysis of error sources of any precision measurement instruments. Typical error sources, reflected by the Allan variance, are given in Figure 131, which include the quantization noise due to the nature of the sensors, the random walk angle due to various small drift mechanisms, the sinusoidal modulation resulting from oscillations in the active devices, or the slow motion of the measurement platform, the bias instability due to the electronics, or other components susceptible to $1/f$ noise, the rate of random walk and the rate ramp because of deterministic errors [16] [17].

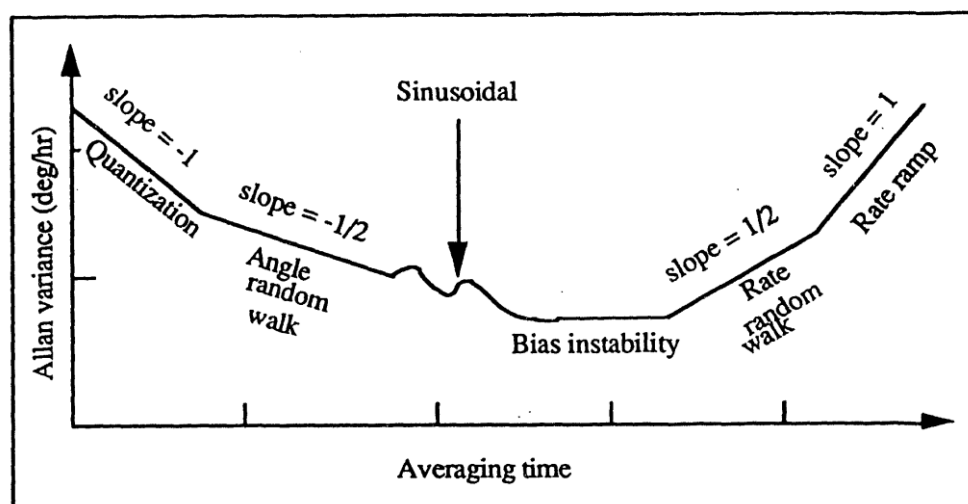


Figure 133: Typical Allan variance analysis results [16] [17]

The quantization noise can be significantly reduced by averaging. During the measurement using an active source, sensor system errors, bias instability noise and sinusoidal noise are assumed as dominant noises. The Allan variances of both pavements are predicted by using a cluster analysis method containing five stages:

- Divide the measured data set into several subsets. Each subset has the same number of data samples. The equivalent length of every subset is defined as the correlation length.

- Average the data contained in each subset.
- Take the variance of each two successive averaged-values.
- Average all the variances calculated in the previous stage.
- Repeat all procedures again but using a different correlation length.

Hence, for each specific correlation length, there will be a related variance. Such a variance is called an “Allan variance”. Allan variances of both pavements are illustrated in Figure 132 and Figure 133. The X-coordinate is the correlation length (the number of the data samples in each subset) with units of mm. The Y-coordinate is the Allan variance with units of *deg/mm*. The black curve illustrated in Figure 132 is an Allan variance statistic description of the good pavement. The red curve illustrated in Figure 133 is an Allan variance statistic description of the poor pavement. Possible noise types are identified by comparing the slopes of the curves with the typical Allan variance curve shown in Figure 131. For both pavements, the quantization noise, the random walk angle, and the sinusoidal modulation are main characteristics identified when measuring the surface height distribution using the laser profiling instrument.

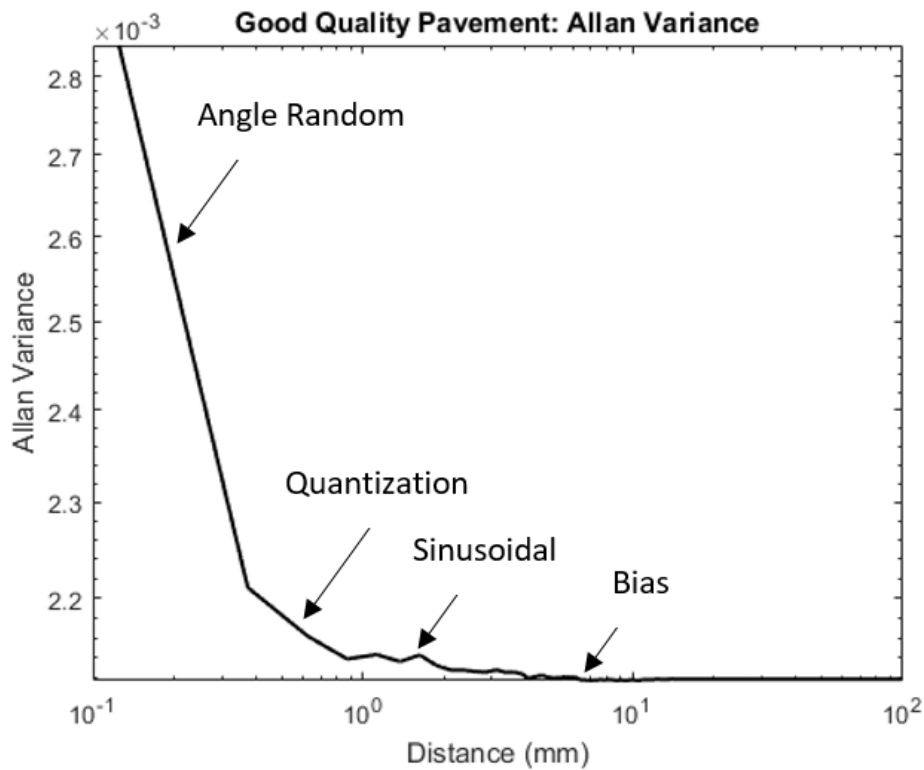


Figure 134: Allan variance analysis result of a good pavement

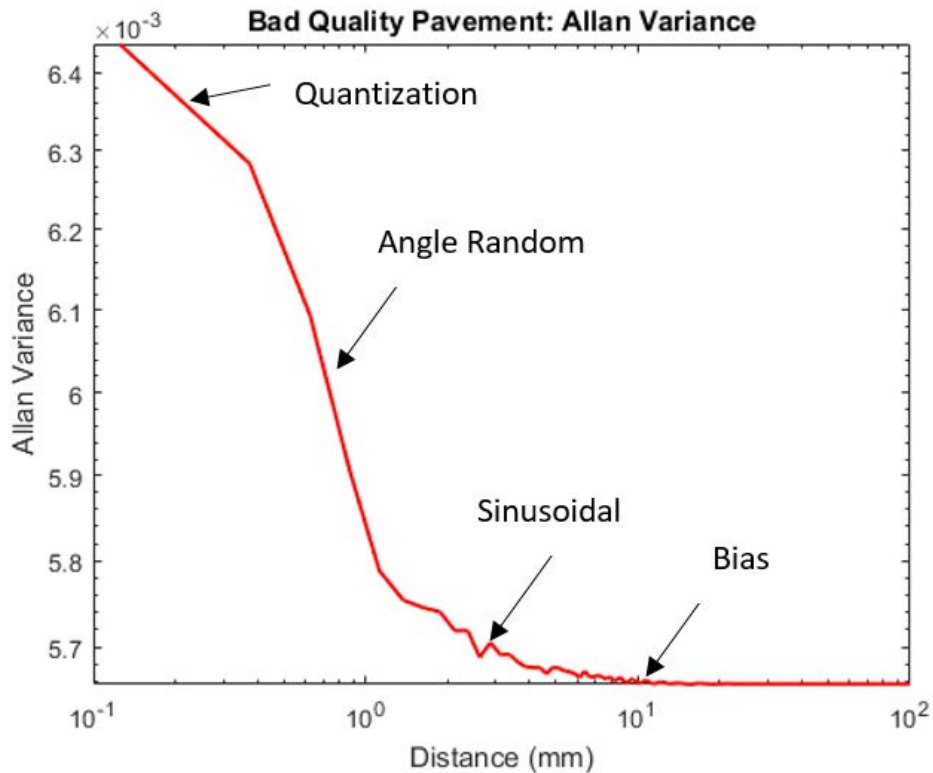


Figure 135: Allan variance analysis result of a poor pavement

In both figures, at very short correlation lengths, the Allan variance decreases rapidly because of the quantization noise and the random walk angle. At long correlation lengths, the Allan variance tends to a small, constant value. For the good pavement, the Allan variance becomes stable after 6.1 mm (averaged local correlation distance of the good pavement is around 7 mm) and for the poor pavement (averaged local correlation distance of the bad pavement is around 8 mm), the Allan variance becomes stable after 9.1 mm. Thus for both good and poor pavements, the surface roughness will be averaged over multiple correlation lengths as a result of the size of the C1, P1, P2 and C2 electrodes. Thus the effects of surface roughness will be reduced by the equivalent spatial filtering operation.

5.2 Roughness impacts on the capacitance

Roughness effects, in scientific areas including Very-Large-Scale-Integrated-Circuits (VLSI) and Micro-Electro-Mechanical-Systems (MEMS), have been theoretically researched and modelled using MATLAB or COMSOL for many years [10] [18] [19] [20]. Zhao [10] and Jamali [20] proposed a 1D model of surface roughness, provided detailed theoretical equations and illustrated the relationship of the capacitance to the correlation length of the

rough surface. Such theoretical analysis is based on a rule used to transform the capacitor with a rough electrode surface, or with defects on an electrode surface, to a parallel-plate capacitor with flat electrode surfaces. This transformation method of solving the roughness effects on the capacitance is referenced in this geophysical research. The capacitance between the flat electrode and the rough surface is defined as a rough-capacitance. To derive the surface roughness effects on a rough-capacitance and the impedance estimated made by the capacitive coupled resistivity system, some theoretical analysis will be given, which is based on Zhao and Palasantzas's detailed mathematical equations [10] [11] using finite parameters calculated in previous sections to model the roughness. Experimental tests have also been conducted to verify the theoretical predictions.

5.2.1 Analytical equations

A simple diagram of the capacitive coupled resistivity technique system placed on the pavement with a rough surface is illustrated in Figure 134.

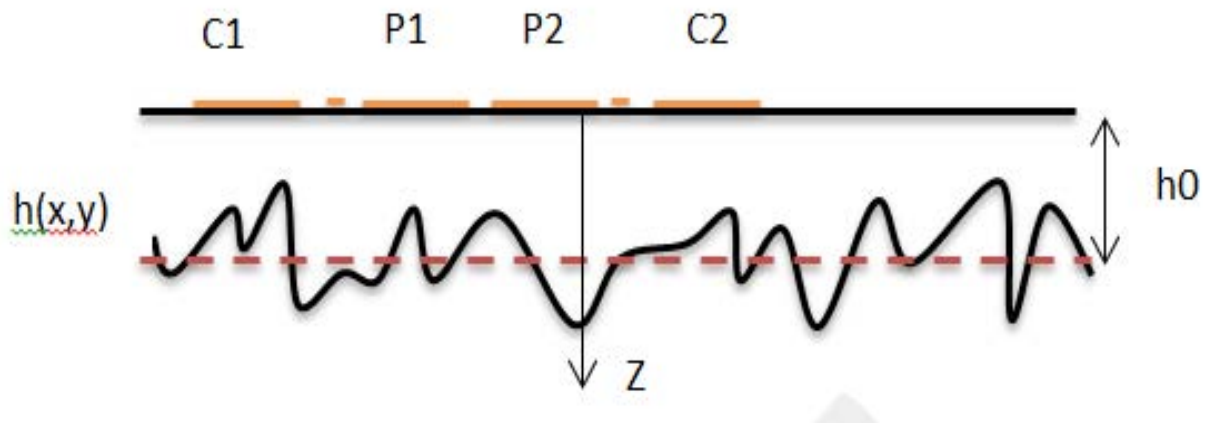


Figure 136: Diagram of the capacitive coupled resistivity technique system placed on the pavement with a rough surface (a side view)

In this figure, the horizontal upper black line represents the dielectric sheet under the four electrodes. The four long, yellow lines represent the four electrode plates C1, P1, P2 and C2. The short yellow lines between the current electrodes and the potential electrodes are the guard rings. The potential on the electrode C1 is annotated by V_C . h_0 is the reference height between the electrode C1 and the rough surface. $V_{MeanLine}$ is assumed as the potential at the transformed flat electrode surface with the Z-coordinate of h_0 . $h(x,y)$ is the surface height fluctuation function in the X-Y coordinate plane. \emptyset describes the

electrostatic potential of the rough capacitor. k and ρ in the following equations represents the radian spatial frequency and the position vector on the X-Y coordinate plane. α is a roughness exponent, ε is a correlation length and λ is the roughness wavelength. Here, the rough-capacitor of the electrode C1 and its related local surface roughness area are taken as an example to discuss the effects on the rough-capacitance introduced by the roughness.

According to detailed theoretical equations (in Appendix 3) by Zhao and Palasantzas [10] [11], the potential of the rough capacitor is given by equation (5-2)

$$\begin{aligned} \Phi \cong & \\ & V_c + \frac{(V_{MeanLine} - V_c)z}{h_0} + \frac{1}{2\pi} \int \left(-\frac{V_{mc}}{h_0} \widehat{h}(k) \frac{\sinh(kz)}{\sinh(kh_0)} \right) \exp(-ik\rho) d\rho + \\ & \frac{1}{2\pi} \int \left(\frac{V_{mc}}{h_0} \int \frac{\cosh(k'h_0)\sinh(kz)}{\sinh(k'h_0)\sinh(kh_0)} k' \widehat{h}(k') h(k - k') dk' \right) \exp(-ik\rho) dk \end{aligned} \quad (5-2)$$

Substitute Φ into the equation of $E = -\nabla\Phi = -\frac{\partial\Phi}{\partial z} - \frac{\partial\Phi}{\partial\rho}$

$$\begin{aligned} E = & \\ & -\frac{(V_{MeanLine} - V_c)}{h_0} - \frac{1}{2\pi} \int \left(-\frac{V_{mc}}{h_0} \widehat{h}(k) \frac{\cosh(kz)}{\sinh(kh_0)} \right) k \exp(-ik\rho) d\rho + \\ & \frac{1}{2\pi} \int \left(-\frac{V_{mc}}{h_0} \widehat{h}(k) \frac{\sinh(kz)}{\sinh(kh_0)} \right) ik \exp(-ik\rho) d\rho - \\ & \frac{1}{2\pi} \int \left(\frac{V_{mc}}{h_0} \int \frac{\cosh(k'h_0)\cosh(kz)}{\sinh(k'h_0)\sinh(kh_0)} kk' \widehat{h}(k') h(k - k') dk' \right) \exp(-ik\rho) dk + \\ & \frac{1}{2\pi} \int \left(\frac{V_{mc}}{h_0} \int \frac{\cosh(k'h_0)\sinh(kz)}{\sinh(k'h_0)\sinh(kh_0)} ik k' \widehat{h}(k') h(k - k') dk' \right) \exp(-ik\rho) dk \end{aligned} \quad (5-3)$$

The rough surfaces of both pavements are categorized into the self-affine roughness models with Gaussian height distributions. Furthermore, the roughness height spectrum of the self-affine models is given by the power law [10] [11]:

$$mean \left(\left| \widehat{h} \left(\frac{k}{2\pi} \right) \right|^2 \right) = \begin{cases} \left(\frac{k}{2\pi} \right)^{-2-2\alpha} & \varepsilon \gg \frac{2\pi}{k} \\ const & \varepsilon \ll \frac{2\pi}{k} \end{cases} \quad (5-4)$$

Using the parameters described in Table 13, the power law decay function of the good pavement surface is:

$$PSD_{GoodPavemetn} = \begin{cases} 10^{-5} f^{-3.5} & f \gg f_{\varepsilon g} \\ 10^2 & f \ll f_{\varepsilon g} \end{cases} \quad (5-5)$$

$$f_{\varepsilon g} = \frac{1}{\varepsilon_{good}} = 81.6$$

Where ε_{good} is the correlation length of the good pavement; the power law decay function of the poor pavement surface is:

$$PSD_{BadPavemetn} = \begin{cases} 10^{-5} f^{-4} & f \gg f_{\varepsilon b} \\ 10^4 & f \ll f_{\varepsilon b} \end{cases} \quad (5-6)$$

$$f_{\varepsilon b} = \frac{1}{\varepsilon_{bad}} = 115.9$$

f is the spatial frequency, ε_{bad} is the correlation length of the poor pavement. Comparing equation (5-5) and equation (5-6) with the equation (5-4), the roughness exponent of both pavements are $\alpha_{good} = 0.75$ and $\alpha_{bad} = 1$. These two exponents show us that the good pavement surface is more jagged than the poor pavement surface. It is known that the mean slopes of both pavements are much smaller than unity and the RMS roughness amplitudes are much smaller than the reference heights of both pavements. Such cases could be recognized as weakly rough surfaces. For weak roughness, the electrostatic potential equation becomes:

$$\phi = V_c + \frac{(V_{MeanLine} - V_c)z}{h_0} + \frac{(2\pi)^3 z V_{mc}}{Area h_0^2} \int \frac{\cosh(k'h_0)}{\sinh(k'h_0)} k' mean(|\widehat{h(k')}|^2) dk' \quad (5-7)$$

The electric field of such a parallel plate capacitor with a smooth electrode and a rough surface becomes

$$E = -\frac{(V_{MeanLine} - V_c)}{h_0} - \frac{(2\pi)^3 V_{mc}}{Area h_0^2} \int \frac{\cosh(k'h_0)}{\sinh(k'h_0)} k' mean(|\widehat{h(k')}|^2) dk' \quad (5-8)$$

The average capacitance of such a capacitor is given by

$$C = \varepsilon \frac{Area}{h_0} \left(1 + \frac{\Delta^2 L^2}{(2\pi)^5} \int_0^{q1} \frac{q^2 \cot(q) h_0}{\left(1 + \frac{L^2 q^2}{2\alpha}\right)^{1+\alpha}} dq + \frac{\Delta^2 L^2}{(2\pi)^5} \int_0^{q2} \frac{2q^2 h_0}{\left(1 + \frac{L^2 q^2}{2\alpha}\right)^{1+\alpha}} dq \right) \quad (5-9)$$

Where $\Delta = \frac{w}{h_0}$ $L = \frac{\xi}{h_0}$ $q = kh_0$ ξ : lateral correlation length

For both pavements, a dielectric material of a yellow polypropylene sheet is placed at the bottom of the electrodes. Air is filled between this yellow polypropylene sheet and the rough surface of the pavement. Hence, the capacitances between the electrodes and the rough surface are going to be a series capacitance incorporating two parts of C_{yellow} and C_{space} .

$$C_{serial} = \frac{C_{yellow} * C_{space}}{C_{yellow} + C_{space}} \quad (5-10)$$

$$C_{yellow} = \epsilon_{yellowsheet} \epsilon_0 \frac{Area}{h_{yellowsheet}} \quad (5-11)$$

$$C_{space} = \epsilon_0 \frac{Area}{h_{RoughSpace}} \left(1 + \frac{\Delta^2 L^2}{(2\pi)^5} \int_0^{q1} \frac{q^2 \cot(q) h_{RoughSpace}}{\left(1 + \frac{L^2 q^2}{2\alpha}\right)^{1+\alpha}} dq \right. \\ \left. + \frac{\Delta^2 L^2}{(2\pi)^5} \int_0^{q2} \frac{2q^2 h_{RoughSpace}}{\left(1 + \frac{L^2 q^2}{2\alpha}\right)^{1+\alpha}} dq \right) \quad (5-12)$$

Where $h_{yellowsheet} = 2.73 \text{ mm}$ $\epsilon_{yellowsheet} = 2.83$ $h_{RoughSpace}$ is the RMS height of the rough surface to the bottom of the yellow sheet.

The capacitance as a function of different rough surfaces can be predicted using these formulae. The larger the RMS height and the rougher the surface is, the smaller the capacitance will be. Figure 135 gives us a basic idea of the impact on the capacitance as a function of the reference heights (the clearance between the electrode and the transformed surface). An example is illustrated in Figure 135 of applying these formulae to a rough-capacitor where the rough surface is assumed to have a reference height ranging from 3.7 mm to 12.7 mm, the RMS height of 1.0 mm, the upper cut-off spatial frequency of 80 rads/m, the lateral correlation length of 12 mm and the roughness exponent of 0.75.

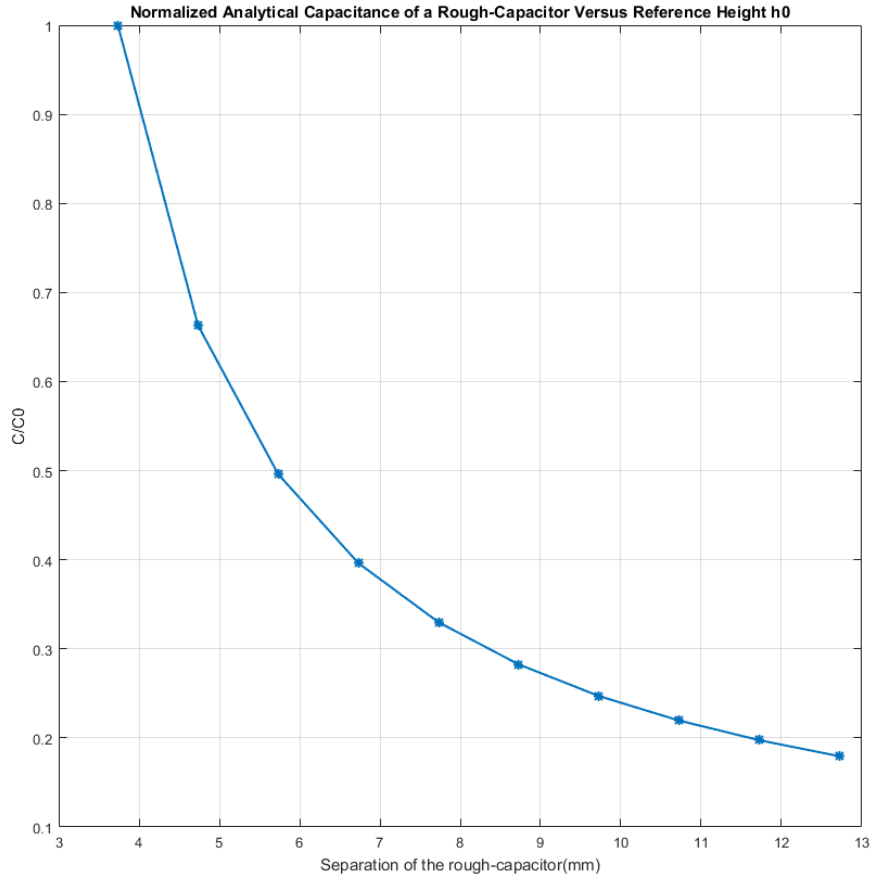


Figure 137: An example of the effects of the reference heights on the capacitance of a rough-capacitor

The X-coordinate represents the reference height of h_0 ; the Y-coordinate represents the normalised capacitances. It is seen that the rough-capacitance greatly depends on the reference heights of the rough surface. As the reference height becomes larger, the normalized capacitance decreases following an exponential law. Once the RMS height is above a threshold level (1 cm in this example), the capacitance ratio becomes approximately constant. Below this threshold level, the capacitance is very sensitive to the RMS height, typically to variations much less than 1 mm.

5.2.2 Experimental tests

To test the efficacy of the analytical model, a number of experimental tests were conducted. The first experimental test was to place the capacitive coupled resistivity system onto a thick foam layer that included various additional dielectric layers between the bottom yellow sheet and the thick foam layer. Secondly, the capacitive coupled resistivity system was placed on the thick foam but with a square, perforated, rough dielectric layer.

5.2.2.1 Vary heights using multiple dielectric-layers

It is known that the rough-capacitance (C_{rough}) can be transformed to the capacitance of a flat capacitor (C_{flat}).

$$C_{flat} = \frac{\epsilon_r \epsilon_0 Area}{h_0} \quad (5-13)$$

$$C_{rough} = k_{rough} C_{flat} = \frac{\epsilon_r \epsilon_0 Area}{\frac{h_0}{k_{rough}}} \quad (5-14)$$

h_0 is the reference height of the rough capacitor; k_{rough} is the transformation coefficient. An experiment based on changing heights was conducted to simulate the impacts of the reference heights on the normalized capacitances and the measured impedance results as illustrated in Figure 136.

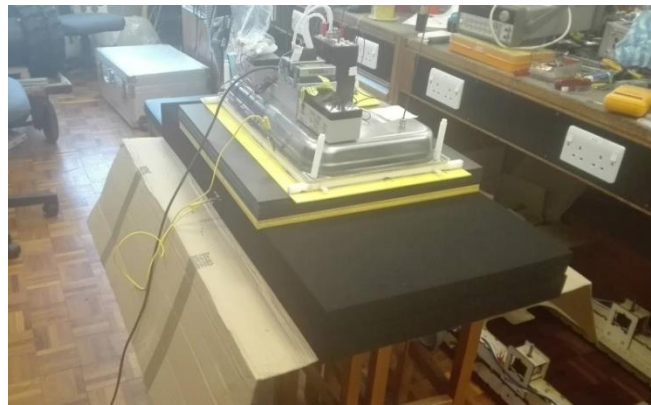


Figure 138: Varying surface heights by using multiple dielectric-layers

In this experiment, the dielectric layer height ranged from 1 mm to 73 mm. The dielectric constant of these dielectric layers was around 2.283. The operating frequency was from 2 kHz to 15 kHz. Each experiment used a different dielectric-thickness and was conducted with the same configuration. The relationship curve of the measured reactance to the measured resistance at 5 kHz is shown in Figure 137. The red line is a polynomial fitting curve to the practical data points.

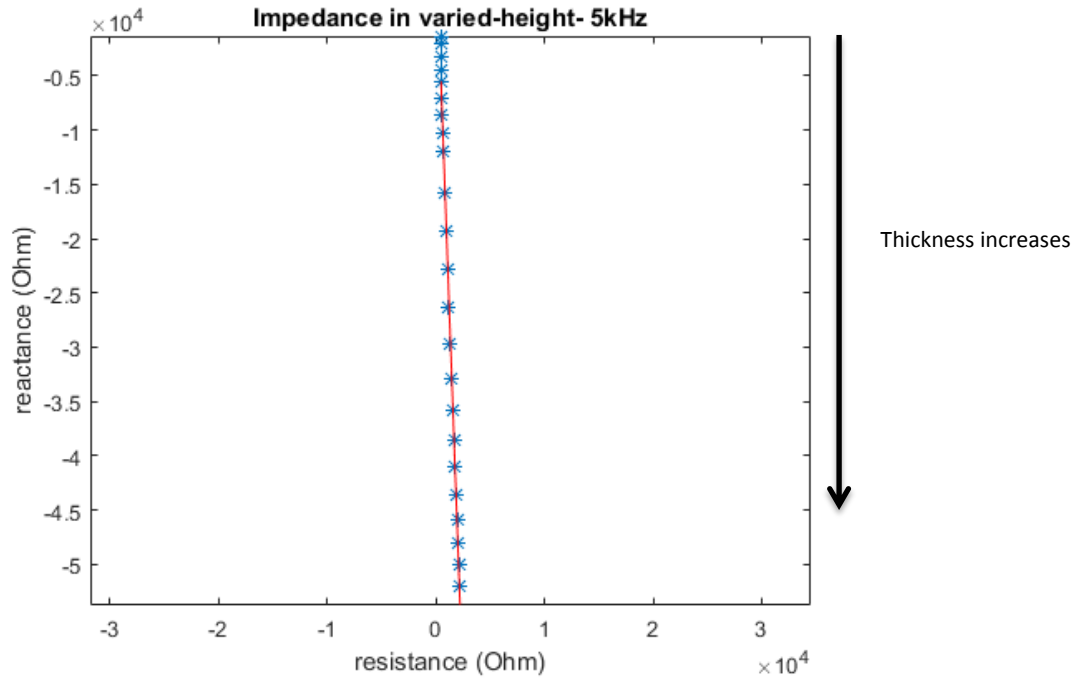


Figure 139: The relationship curve between the reactance and the resistance of a varying dielectric-layer-thicknesses at 5 kHz

Figure 137 illustrates that the height variation has dominant and significant impacts on the reactance. The resistance value also changes with increasing thickness because of unavoidable current leakage through the boundary layer capacitor (this was discussed in Chapter 4), such influence is small and may be ignored. A polynomial equation representing this curve is predicted as

$$X = -27.5R + 7548 \quad (5-15)$$

The slope of the curve is $k_{XR} = 27.5$.

Next the height variation was added into the system circuit fitting by using the resistor-capacitor network method. In this fitting scheme, the resistivity of the thick foam and the lateral capacitance between electrode C1 and electrode P1 are unknown values. The fitting result is presented in Figure 138 and shows that the analytical data and the measured data are in a good agreement. The unknown parameters are predicted and summarized in Table 16.

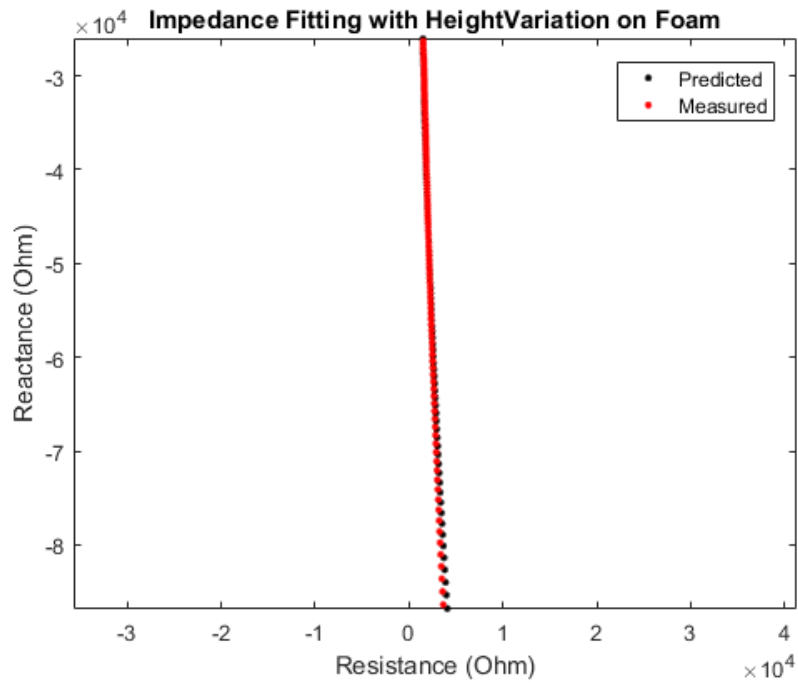


Figure 140: Measured impedance data on foam at various heights fitted with analytical data using the resistor-capacitor network method

Table 16: Predicted foam resistivity and foam equivalent capacitance

Foam resistivity (Ωm)	Foam capacitance (pF)	C_{tx} (pF)
516.8	6.5512	0.3488

Compared with the measured foam resistivity of $484 \Omega m$ and C_{tx} 0.32 pF derived in Chapter 4, the error of the foam resistivity is 6% and that of C_{tx} is 9%. The relationship curve of the normalized capacitance to various heights is illustrated in Figure 139.

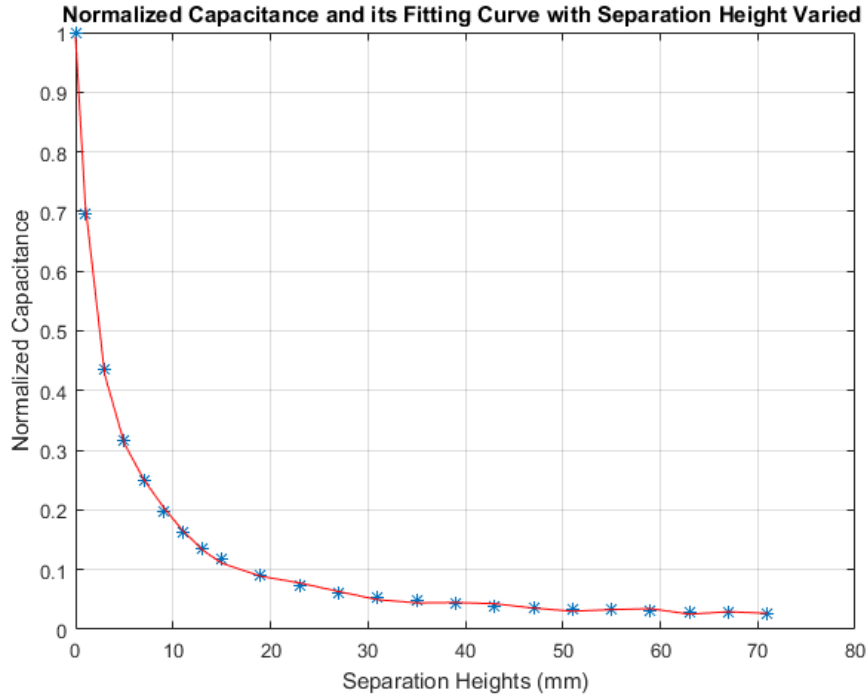


Figure 141: Normalized capacitance on the foam at various heights at 5 kHz

The relationship curve of the normalized capacitance to various heights using the measured impedance, as illustrated in Figure 139, has the same curve tendency as the curve of the analytical model illustrated in Figure 135. Figure 139 also indicates that the height factor has significant impact on the measured reactance or its relevant capacitance when the height is less than 1 cm. Once the height is larger than 1 cm, the height effects on the capacitance can be ignored. From equation (5-13) and equation (5-14), it can be proposed that the relationship curve of the normalised capacitance to the roughness should have the same tendency as the relationship curve of the normalised capacitance to the varied heights.

From equation (5-14), the first differentiation of capacitance to the height becomes

$$\frac{dC_{rough}}{dh_0} = -\epsilon_r \epsilon_0 Area \frac{k_{rough}}{h_0^2} \quad (5-16)$$

The normalised first differentiation at different heights is

$$NormalisedDifferentiation1 = \frac{h_0^2}{h^2} \quad (5-17)$$

For a rough-capacitor, the dielectric constant of the dielectric material and the area of the capacitor are constants. The roughness coefficient k_{rough} and the RMS height h_0 change as the variation of the roughness level of the surface. Hence, for this case, the normalised differentiations at different roughness levels would become

$$NormalisedDifferentiation2 = \frac{k_{rough}}{k_{rough0}} \frac{h_{rms_rough0}^2}{h_{rms_rough}^2} \quad (5-18)$$

Equation (5-18) can be transformed to the equation (5-17) with a normalized coefficient describing the compared-roughness level. Replacing the constant $\frac{k_{rough0}}{k_{rough}}$ by k_0^2 , the equation becomes

$$NormalisedDifferentiation2 = \frac{h_{rms_rough0}^2}{\left(\frac{h_{rms_rough}}{k_0}\right)^2} \quad (5-19)$$

Equations (5-17) to (5-19) indicate that the relationship of the capacitances to the roughness level should share the same form as that of the capacitances to varied clearances, but with shifted equivalent RMS heights because of the k_0 value. These normalised first differentiations of the capacitances to the varied heights are illustrated in Figure 140.

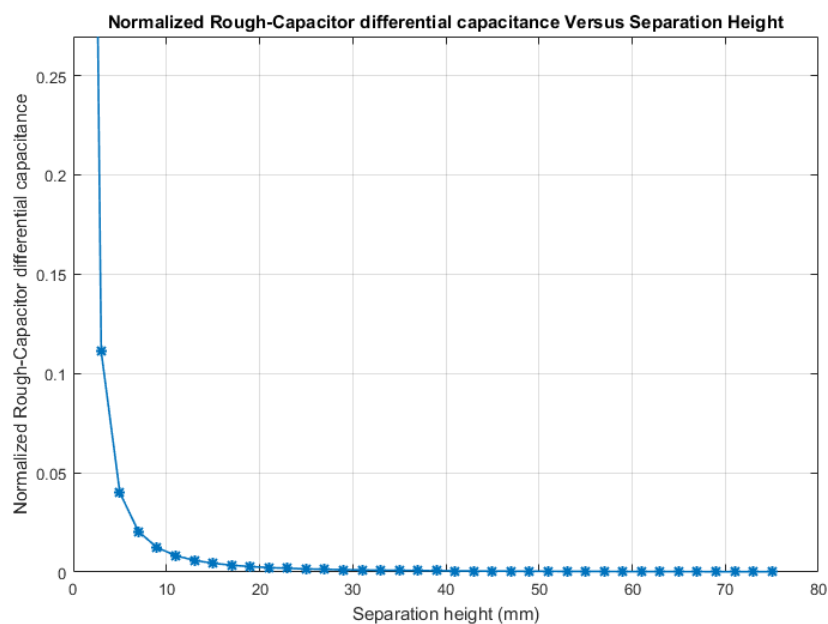


Figure 142: Normalised first differentiation of rough capacitance to the height

The X-coordinate is the varied RMS height. The Y-coordinate is the normalised differentiated capacitance. The relationship curve illustrated in Figure 140 should be suitable for all capacitors with rough electrodes. Hence, it is proposed that the factor of the roughness has significant impact on the reactance estimate obtained by the capacitive coupled resistivity technique system when the rough surface has its RMS height divided by the coefficient k_0 smaller than 1.5 cm.

5.2.2.2 Roughness impacts on capacitance obtained by experiments

To model the roughness impacts on the capacitance value, a number of laboratory tests were conducted to model the roughness layer.

- One method was to place sand into a vacuum plastic bag; then locate this sand-filled-bag on a number of acrylic perforated-sheet-layers (as shown in Figure 141) to model surface roughness layers. The sheet dimensions are given in Table 17. In this research, one-rough-layer, two-rough-layers and three-rough-layers were applied. The reference heights of these layers were 2.7 mm, 5.4 mm and 8.1 mm.

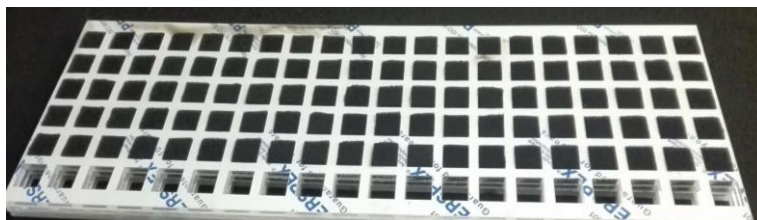


Figure 143: Sand bag located on an acrylic squared, perforated sheet to model a surface roughness layer

Table 17: Polypropylene squared sheet's dimension

Dimensions	Value
Length of Sheet	60.8 cm
Width of Sheet	20 cm
Thickness of Sheet	0.5 cm
Length of Square	2.15 cm
Width of Square	2.15 cm
Left Edge Length	0.41 cm
Right Edge Length	0.38 cm
Space between squares in X direction	0.84 cm
Space between squares in Y direction	0.88 cm
Number of Squares in each row	20
Number of Squares in each Column	6

- The second method was to place one acrylic sheet on the soft foam; then place both of them into a vacuum bag; finally extracted the air inside the bag to leave a rough surface layer as illustrated in Figure 142.



Figure 144: Acrylic squared, perforated sheet placed on the soft foam inside a vacuum bag and used to model a rough surface layer

Both methods were invalid because of a number of reasons.

- The topography of a sand-filled rough surface analogue is quite difficult to measure by laser profiling: the ideal situation is to have each perforated square space filled equally by the same sand volume in the vacuum bag. However, this is impossible because the weight distributed on each square is different from each other. Unfortunately, the sand, plastic sheet and vacuum plastic bag are non-reflective, thus cannot be measured reliably using the laser profiling instrument.

- The sand contained in the bag, or the foam sheet placed in the bag, cannot completely fill each square perforation. Thus it is very difficult to form multi-roughness layer models.
- The sand is not easy to manipulate and the weight distorts the acrylic sheets.

To solve these problems, a test method using copper tape glued to squared-sheet-roughness layers was developed as shown in Figure 143. Experimental test procedures were:

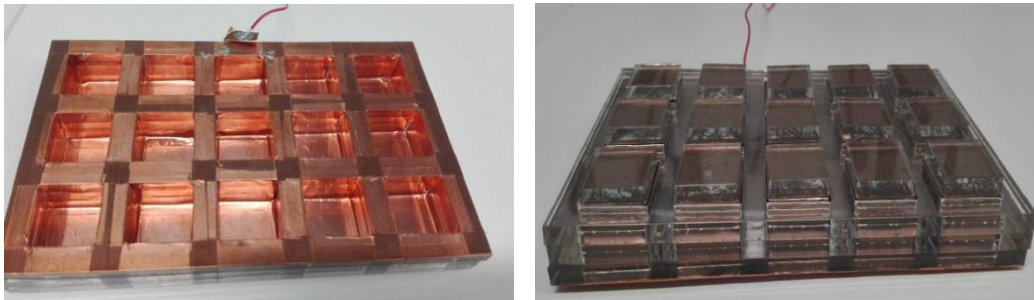


Figure 145: Three-square-layers with copper tapes to model deeper roughness (left side: front view; right side: back view)

- The dimension of a single layer roughness-model is given in Table 18.

Table 18: The dimension of a single layer roughness-model

Dimensions	Value
Length of Sheet	15.8 cm
Width of Sheet	9.85 cm
Thickness of Sheet	0.5 cm
Length of Square	2.15 cm
Width of Square	2.15 cm
Left Edge Length	0.88 cm
Right Edge Length	0.88 cm
Space between squares in X direction	0.84 cm
Space between squares in Y direction	0.88 cm
Number of Squares in each row	5
Number of Squares in each Column	3

- The yellow polypropylene dielectric sheet was placed on the top of the roughness-model, where the sheet has the same thickness and same dielectric constant as the dielectric sheet used as the base layer of the capacitive coupled resistivity technique system.
- A copper plate was placed on the top of the yellow polypropylene sheet and weighted to ensure good contact with the roughness model surface (Figure 144). A rough-capacitor was formed by a squared-roughness-model and the copper plate.
- The rough-capacitor was connected to the HP4921 impedance analyser to measure the impedance and analyse the impact of roughness on the capacitance.



Figure 146: Rough capacitor formed by a square-roughness-model and copper plate connected to the HP4921

- The air-filled separation between the copper plate and the roughness-model surface was then increased in stages by using washers. The air separation was changed from 0 mm to 12 mm in steps of 2 mm. The settings of six experiments are listed in Table 19.

Table 19: Various air-filled separation configurations above a single square-roughness-layer

Heights of single roughness-layer	Configuration (from top to bottom)
0 mm space height	Copper plate; yellow sheet; one rough-layer
2 mm space height	Copper plate; yellow sheet; 2 mm space height; one rough-layer
4 mm space height	Copper plate; yellow sheet; 4 mm space height; one rough-layer
6 mm space height	Copper plate; yellow sheet; 6 mm space height; one rough-layer
8 mm space height	Copper plate; yellow sheet; 8 mm space height; one rough-layer
12 mm space height	Copper plate; yellow sheet; 12 mm space height; one rough-layer

Based on these experimental configurations, the impedances and capacitances of these six experiments were collected using an HP4921 at frequencies from 1 kHz to 1 MHz. Normalised capacitance values are illustrated in Figure 145.

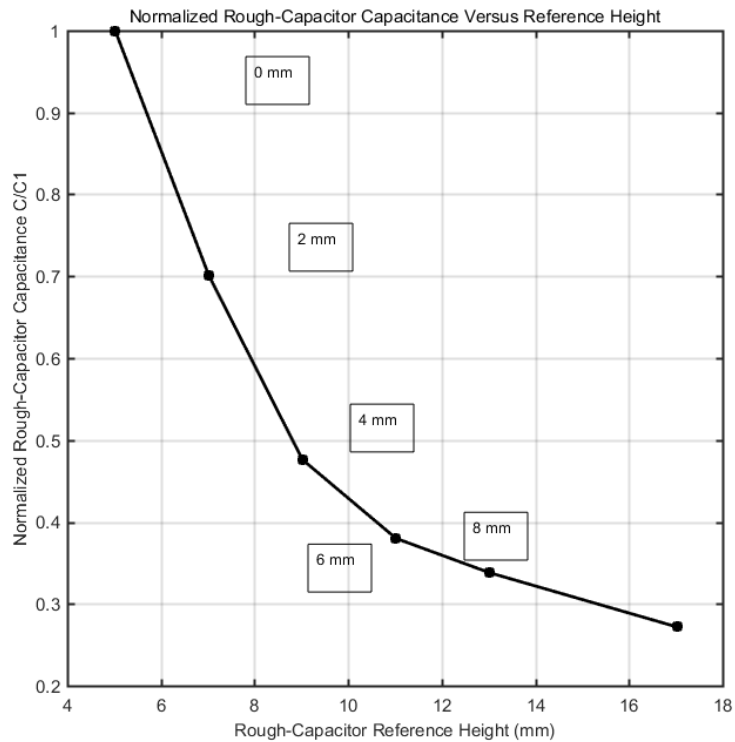


Figure 147: Normalised capacitance of one-layer-roughness-model with spacer heights

In this Figure 145, the X-coordinate represents the varied height including the thickness of the yellow polypropylene sheet, the air space heights and the RMS height of 2.7 mm of the single roughness-model. Hence, the X-coordinate ranges from 5 mm to 18 mm. The Y-coordinate is the normalised capacitances, where all measured capacitances are divided by the capacitance of the rough-capacitor with zero air space height. The normalized capacitance exponentially decreases at first and then becomes constant as the height increases.

To use the analytical equation (5-12) for the capacitance of a rough-capacitor, values of relevant parameters for this single-layer-roughness-model are given in Table 20.

Table 20: Roughness parameters of the single-layer-roughness-model

Parameters	Values
h_0	0.0027 m
f_{cutoff}	33.4 rad/m
ξ	0.02999 m
w	0.0027 m
f	2.2:2.2:33.4 rad/m
$q = fh_0$	0.0061:0.0061:0.0909
$L = \frac{\xi}{h_0}$	10.99
$\Delta = \frac{w}{h_0}$	0.97

The rough capacitance of a single-rough-layer with varying air space heights is annotated by C_{rough} . Because of the yellow dielectric sheet, the total capacitance of this roughness-model is:

$$C_{mix} = C_{rough} C_{yellow} / (C_{rough} + C_{yellow}) \quad (5-20)$$

The predicted capacitances of this single-layer-roughness-model of varied heights are illustrated and compared with the measured capacitances in Figure 146.

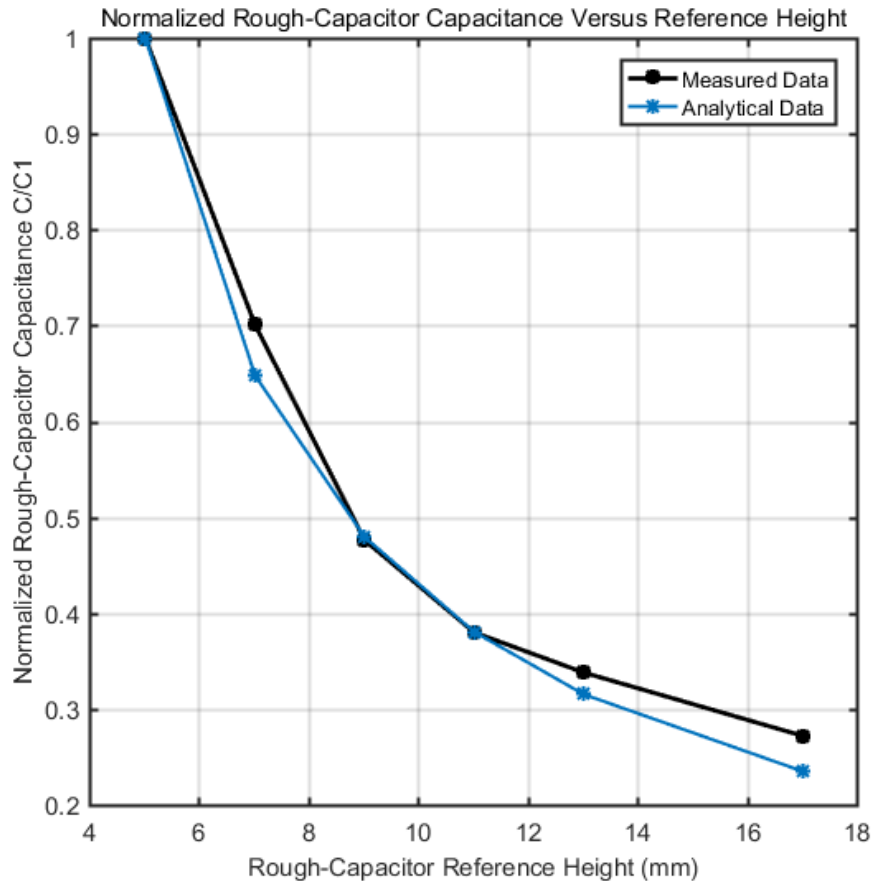


Figure 148: Comparison between the predicted capacitances of a single-layer-roughness-model of varied heights and the measured capacitances

The blue curve represents the measured data and the black curve is derived from the analytical formula. The fitting of these two curves shows a good agreement.

- Next, the impedance measurements corresponding to three layer-roughness models without air space heights were conducted. For the experiments described in this section, the yellow dielectric sheet is placed on the single-layer-roughness-model, the two-layer-roughness-model and the three-layer-roughness-model as shown in Figure 143. These models are of different roughness levels. Finally, a copper plate is placed on the yellow dielectric sheet of these three models.
- The impedances and the capacitances of these three roughness models were measured using the HP4921.

The normalised capacitances of these three layer-roughness models are displayed in Figure 147. The three normalised capacitances are of value 1, 0.98 and 0.94 with respect to the reference height h_0 .

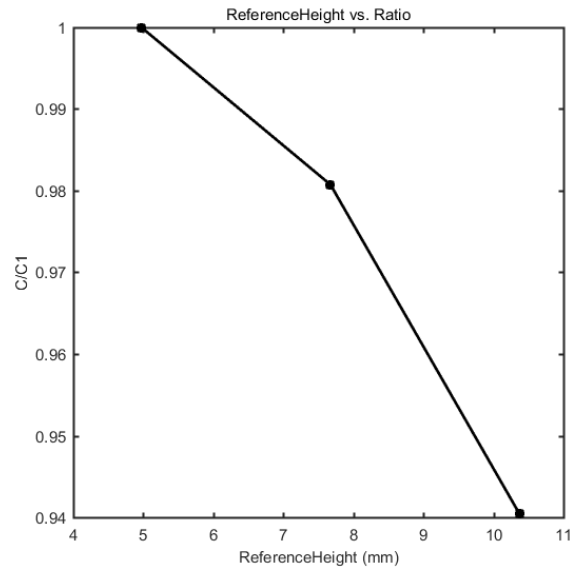


Figure 149: The normalised capacitances of three layer-roughness models using copper tapes

Comparing the results presented in Figure 147 and Figure 146, it is seen that the relationship curve of the normalised capacitances to the reference height in Figure 147 is quite different to that shown in Figure 146. The possible reason is because the equivalent RMS height is shifted, implying that the roughness coefficient k_{rough} is greater than unity. The reference heights h_0 for the three roughness models are 4.97 mm, 7.67 mm and 10.37 mm. Following the transformation, the equivalent reference heights of the double roughness-layer and the three roughness-layer models are much smaller than the original values.

The impedance results of these three roughness models are illustrated in Figure 148. The red point represents the impedance of the single-layer-roughness-model.

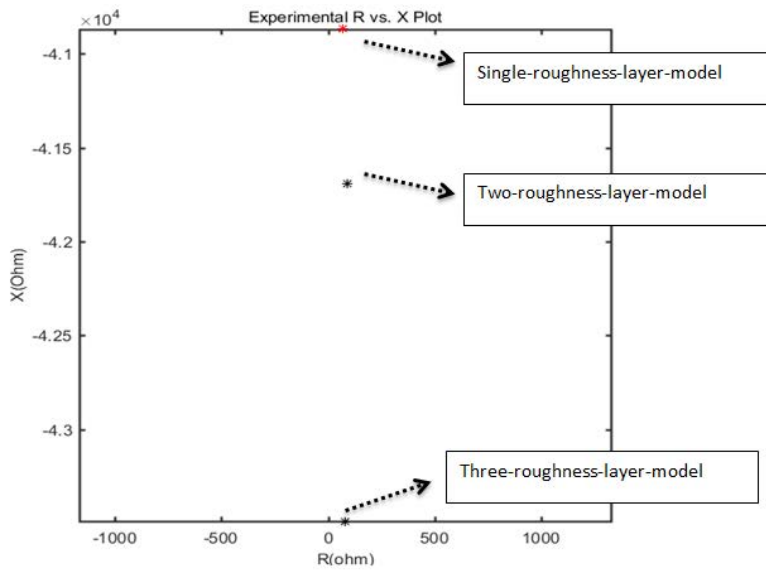


Figure 150: The impedance results of three roughness models

Note: three star-points in the Figure 148 indicate relationships between measured resistance and measured reactance of three roughness models (red – single roughness layer model; the second black star point – two roughness layers model; the third black star point – three roughness layers model).

The resistance values are almost constant whilst the reactance values change significantly as the surface becomes rougher. Therefore, the roughness has a dominant effect on the electrical reactance compared to its effects on the resistance. As reported earlier, the gradient between the reactance and the resistance is around 27.5 for the experimental data measured on an asphalt surface.

5.3 Field surveys and a summary

Following the theoretical study and experimental tests conducted within the laboratory, the influence of the roughness factor on data collected during field surveys has to be considered. The surface height distributions and the impedance measurements were conducted on a good pavement shown in Figure 149 and a poor pavement shown in Figure 150. The poor pavement can be visually categorized into areas of dry old pavement and wet old pavement. To verify the efficacy of the measurement system for moisture-related condition assessment operations, investigations were conducted on the good

asphalt pavement, the dry old asphalt pavement and the wet old pavement. These surveys were conducted during October 2018 at operating frequencies from 1 kHz to 20 kHz.



Figure 151: Field survey on good pavement between the North Car Park and the Gisbert Kapp building

Note: the left image shown in Figure 149 shows an example of one field survey conducted on a good pavement. The capacitive sensor system was carried by an automatic positioning vehicle moving with a step-size of 10 cm. The position-fixing data was obtained using a Leica Total Station. The right image shown in Figure 149 illustrates the measurement positions. In total, five-line investigations were conducted in the enclosed area of the good pavement.

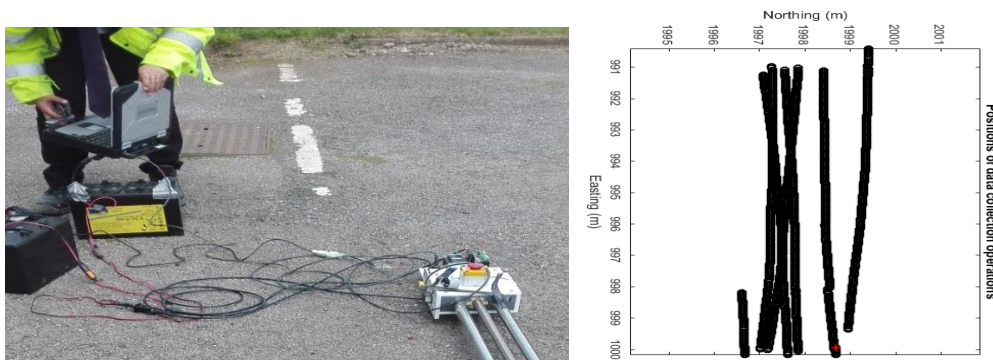


Figure 152: Field survey on the poor pavement at the rear of the Gisbert Kapp building

Note: the left image shown in Figure 150 shows an example of one field survey conducted on a poor pavement. The capacitive sensor system was carried by an automatic positioning vehicle moving with a step-size of 10 cm. The position-fixing data was obtained using a Leica Total Station. The right image shown in Figure 150 illustrates the measurement

positions. In total, seven-line investigations were conducted in the enclosed area of the poor pavement.

For display purposes, the measured impedances at an operating frequency of 5 kHz are selected. The raw data is displayed in Figure 151 and fitted using a polynomial method.

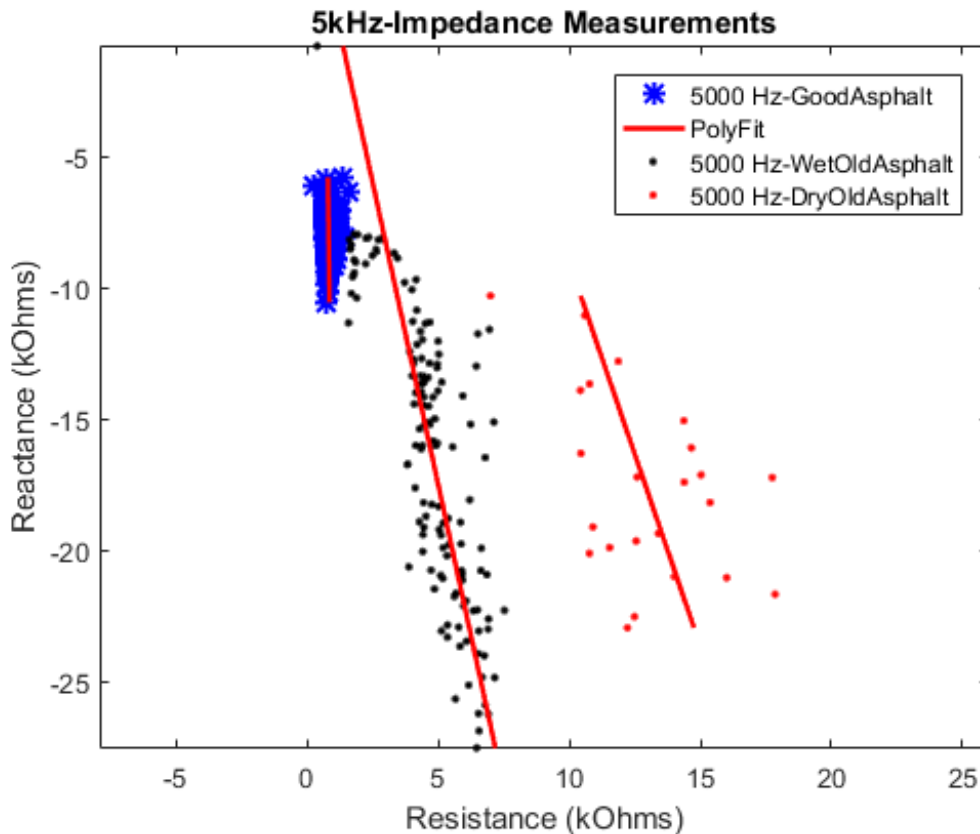


Figure 153: Raw impedance data collected on a good asphalt pavement, a dry old asphalt pavement and a wet old pavement with overlaid polynomial curve fits

The black and the red points are the measured impedance values of the same poor pavement area. The difference is that of moisture content, the black points represent the wet poor pavement and the red points represent the dry poor pavement. The blue points are the measured impedance values of the good pavement area. Apparently, the results illustrated in Figure 151 indicate that the good asphalt has a smoother surface than the poor asphalt. The measured reactance of the good pavement is 2 to 5 times smaller than that of the poor pavement. As discussed in previous sections, a smaller reactance indicates a larger capacitance and a smoother surface. Figure 152 illustrates the corrected raw

impedance (using the input data shown in Figure 151) after applying the roughness correction factor.

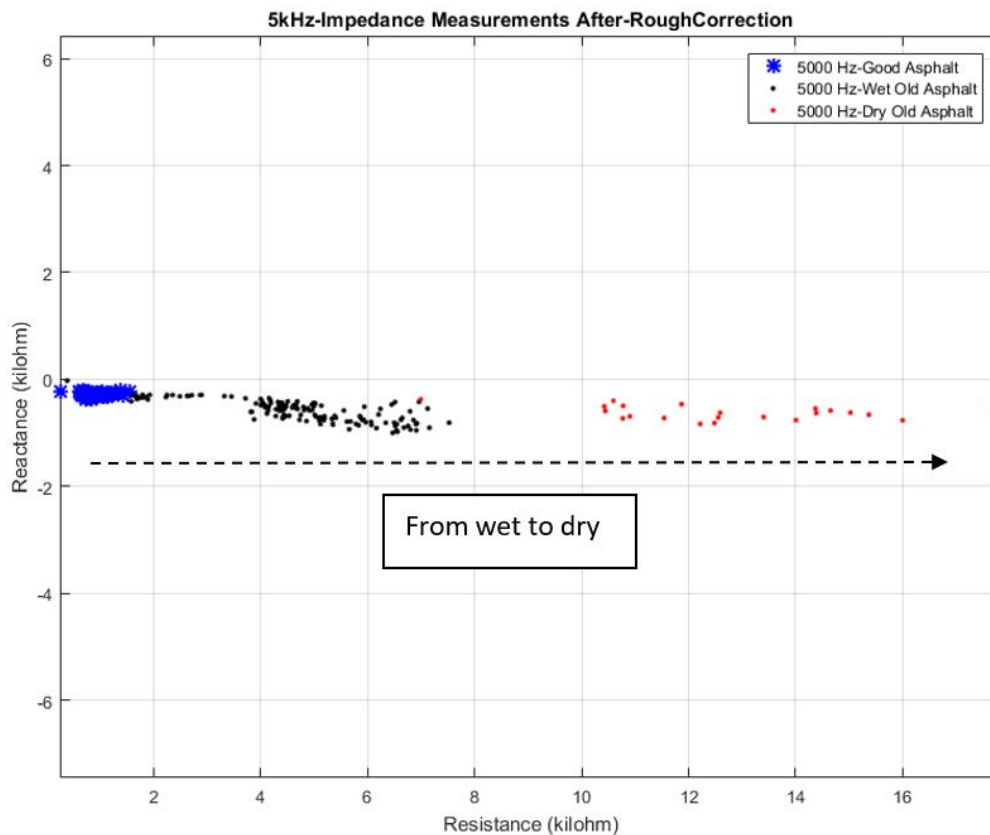


Figure 154: Corrected impedance data collected on a good asphalt pavement, a dry old asphalt pavement and a wet old pavement after applying a roughness correction factor

Note: in Figure 152, all these marker-data points are from the Figure 151 with roughness correction factors applied on the measured reactance (blue star markers: from the good asphalt pavement; black and red markers come from same dataset: respectively from the wet-old pavement with poor conditions, and the dry-old pavement with poor conditions). It is seen that after applying roughness corrections factors, the reactance of different investigated pavements are similar while the resistance of difference investigated pavements are apparently varied from each other. Reactance values are a reasonably indicator of the roughness level of the surface profile. The higher the reactance, the rougher the surface is expected to be.

By inference from the data presented in Figure 151, the pavement materials have resistances ranging from 1 kΩ to 20 kΩ. Using the results presented earlier in this thesis,

the geometric factor is approximately 0.46, when the measured resistances of the materials are within that value range. Applying this geometric factor to the data presented in Figure 152, the apparent resistivities of both pavements are illustrated in Figure 153. Wet-old pavement samples have much smaller resistance values than the dry-old pavement which is a reasonably indicator of the effectiveness of this system for measuring the moisture content.

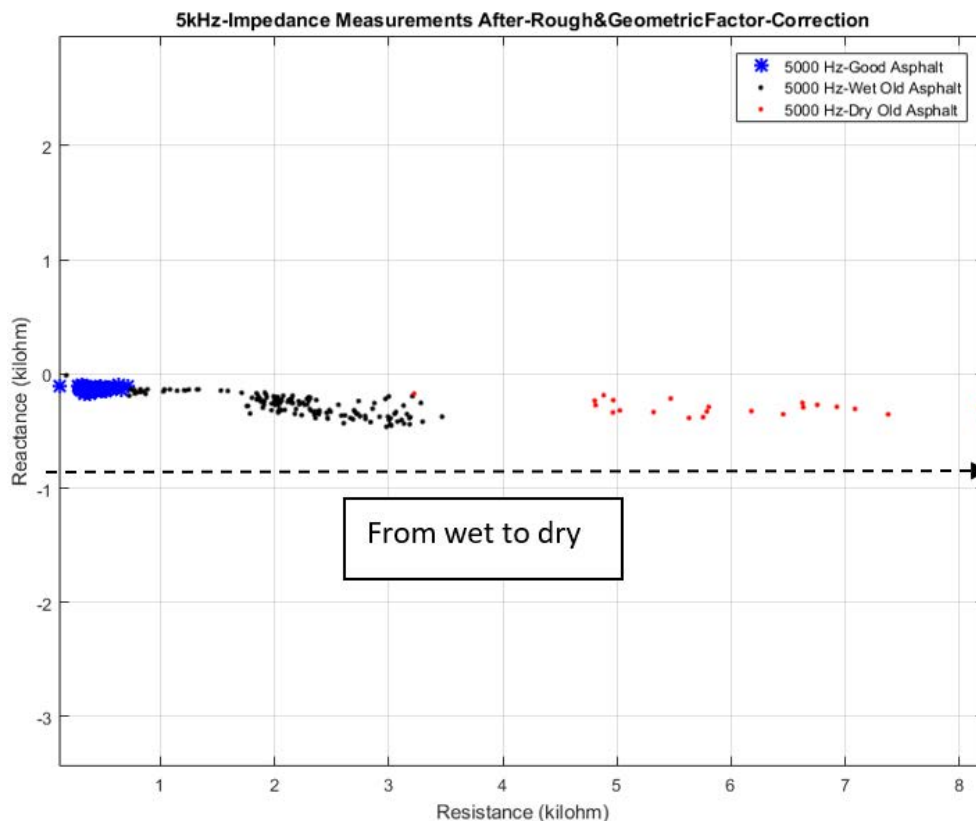


Figure 155: Corrected impedance data collected on a good asphalt pavement, a dry old asphalt pavement and a wet old pavement by roughness correction factor and geometric factor

Examining Figure 151, Figure 152 and Figure 153 indicates that the resistance of the dry old pavement is much larger than that of the wet old pavement and the reactance of the good pavement is much smaller than the reactance of the poor pavement. The resistivity of the pavement materials varies from 1 $k\Omega m$ to 8 $k\Omega m$. This phenomenon meets the hypothesis that the electrical resistance decreases when the moisture level increases, the capacitance reduces and the reactance increases when the surface becomes rougher. The good pavement is very likely to contain more conductive materials than the poor pavement.

In summary, according to the laboratory experiments and the field surveys conducted on pavements of different conditions, it is concluded that the capacitive coupled resistivity technique system used in this research is effective in evaluating the moisture level of the shallow surfacing layers of the pavements and estimating the roughness level of the pavement surfaces. The results presented in Figure 151, Figure 152 and Figure 153 indicate that old-dry poor pavement has a higher resistance value while the old-wet poor pavement has a lower resistance value. This indicates that the system could effectively provide indicative measures of the moisture conditions of the wearing layer of the asphalt pavement.

References

- [1] L. Goehring, A. Nakahara, S. Kitsunezaki, S. Tarafdar and T. Dutta, *Desiccation cracks and their patterns: formation and modelling in science and nature*, 1st edition, Wiley-VCH Verlag GmbH&Co. KGaA, 2015.
- [2] K.J. Falconer, *Fractals: a very short introduction*, Oxford university press, 2013.
- [3] A.L. Barabasi and H.E. Stanley, *Fractal concepts in surface growth*, 1st edition, Cambridge University press, 1995.
- [4] T.R. Thomas, *Rough surfaces*, 2nd edition, Imperial college press, 1999.
- [5] B.B. Mandelbrot, *The fractal geometry of nature*, W.H.Freeman and Company, 1982.
- [6] O.I. Yordanov and K. Ivanova, "Description of surface roughness as an approximate self-affine random structure," in *Surface Science*, Vol 331-333 (1995), pp. 1043-1049.
- [7] E.S. Gadelmawla, M.M. Koura, T.M.A. Maksoud, I.M. Elewa and H.H. Soliman, "Roughness parameters," in *Journal of materials processing technology*, 123 (2002), pp. 133-145.
- [8] D.J. Whitehouse, "The properties of random surfaces of significance in their contact," Ph.D dissertation, University of Leicester, Feb 1971.
- [9] J. Peklenik, "Investigation of the surface typology," in *Ann.CIRP*, Vol 15, No. 381 (1967).
- [10] Y.P. Zhao, G.C. Wang, T.M. Lu, G. Palasantzas and J.T.M.D. Hosson, "Surface roughness effect on capacitance and leakage current of an insulating film," in *Physical review B*, Vol 60, No 12 (1999), pp. 9157-9164.
- [11] G. Palasantzas, "Roughness spectrum and surface width of self-affine fractal surfaces via the K-correlation model," in *Physic Review B*, Vol 48, No 19 (1994), pp. 14472-14478.

- [12] A. Majumdar and B. Bhushan, "Role of fractal geometry in roughness characterization and contact mechanics of surfaces," in *Journal of tribology*, Vol 12 (1990).
- [13] S. Siegel, *Nonparametric statistics*, McGRAW-HILL BOOK COMPANY, New York, London, 1956.
- [14] N. Smirnov, "Table for estimating the goodness of fit of empirical distributions," in *Ann.Math.Statist*, 19 (1948), pp. 279-281.
- [15] F.J. Massey, "The Kolmogorove-Smirnov Test for goodness of fit," in *Journal of the American Statistical Association*, Vol 46, No 253 (1951), pp. 68-78.
- [16] L.C. Ng, "On the application of Allan Variance method for ring laser gyro performance characterization," Lawrence Livermore National Laboratory report, Oct 1993.
- [17] D.W. Allan, "Clock characterization tutorial," Time and Frequency Division, National Bureau of standards, Boulder, Colorado 30303.
- [18] G.J. Sloggett and N.G. Barton, "Surface defects in parallel plate capacitors," in *Journal of physics A: mathematical and general*, (1988), pp. 3695-3702.
- [19] A.B. Yu, X.Z. An, R.P. Zou, R.Y. Yang and K. Kendall, "Self-assembly of particles for densest packing by mechanical vibration," in *Physical review letters*, Dec 2006.
- [20] T. Jamali, S. V. Farahani, M. Jannesar, G. Palasantzas and G.R. Jafari, "Surface coupling effects on the capacitance of thin insulating films," in *Journal of applied physics*, 117, 175308(2015), pp. 1-5.
- [21] D. Saupe, *The science of fractal images*, Springer-Verlag New York, USA, 1988.

CHAPTER 6

PAVEMENT DATA INTERPRETATION BY DEBYE MODEL

6.1 Introduction

It is known that natural asphalt pavements are composed of heterogeneous and complicated dispersions of dielectric materials including rocks, fillers, and pores. Strictly speaking, dielectrics are those materials that only contain bound charges, whilst in reality free charges exist in all subsurface materials including asphalt pavement mixtures and rocks. Such dielectrics are notated as lossy dielectrics which are defined by Jol [1]. The occurrence of free charges result in signal attenuation and energy loss which is related to the real part of the complex conductivity. Bound charges store energy and are related to the imaginary part of the complex conductivity. Pores inside the pavements are usually filled by combinations of water, salt solutions, or air. Levitskaya stated that different polarization processes could be generated if an electric field is applied to the rocks [2] [3] [4]. It is also mentioned by Tabbagh that an induced polarization occurs in heterogeneous materials that contain both conductive and resistive particles embedded with each other. This induced polarization, “an underlying phenomenon that most commonly used surface mineral prospecting techniques are based on, corresponds to the presence of a quadrature component and a frequency dependent variation of electrical resistivity in the frequency domain” [5]. Furthermore, as pointed out by Shang [6] in research on bearing and wearing courses of a dry asphalt pavement and a wet asphalt pavement, various phenomena of polarizations would be caused by the application of an electric field at different operating frequencies. The complex permittivity and complex conductivity of asphalt pavement materials can be described by various empirical models (e.g. Debye model or Cole-Cole model) depending on the operating frequencies (different polarization mechanisms of the Maxwell Wagner; the dipole; the atomic and electronic exist at varying frequencies). The relaxation time of the Debye model or Cole-Cole model quantifies the dielectric dispersion of the asphalt pavement materials resulted from the polarization process. Therefore, an electric field at a specific frequency range applied to an asphalt pavement mixture is

assumed to cause polarization processes. The response of that polarization, in the form of the complex permittivity or complex conductivity, can be interpreted by phenomenological models e.g. Dias model [3] [4], Warburg model [7], Debye model [7] [8] or Cole-Cole model [9].

The phenomena of dispersion and absorption occur in homogeneous dielectrics and also in heterogeneous dielectrics such as asphalt pavement mixture due to several kinds of electrical polarization mechanisms. The dispersion describes a phenomenon that is generally a decrease of the dielectric constant from a high static dielectric constant ϵ_0 to a small dielectric constant tested at very high frequency ϵ_∞ ; and during the transition of the dielectric constant, a loss factor ϵ'' occurs in a bell-form. Such properties of the dielectrics are described in the terms of a complex conductivity or a complex permittivity

$$\epsilon^*(\omega) = \epsilon'(\omega) - j\epsilon''(\omega) \quad (6-1)$$

Or

$$\sigma^*(\omega) = \sigma'(\omega) + j\sigma''(\omega) \quad (6-2)$$

Where $\epsilon^*(\omega)$ denotes the relative complex permittivity; $\epsilon'(\omega)$ represents frequency-dependent relative permittivity; $j = \sqrt{-1}$; $\epsilon''(\omega)$ is a frequency-dependent loss factor; $\omega = 2\pi f$ is the angular frequency; $\sigma^*(\omega)$ denotes the complex conductivity; $\sigma'(\omega)$ is a frequency-dependent conductivity corresponded to free charges; $\sigma''(\omega)$ is related to bound charges.

The phenomena of the dispersion and the absorption from different polarization mechanisms, have the same curve tendencies as illustrated in Figure 154 (derived from the Debye equation). This has been shown by Cole and Cole in their research on the dispersion and absorption effects in dielectrics that “the fact that so many otherwise dissimilar dielectric materials exhibit the same characteristic form of dispersion” [9].

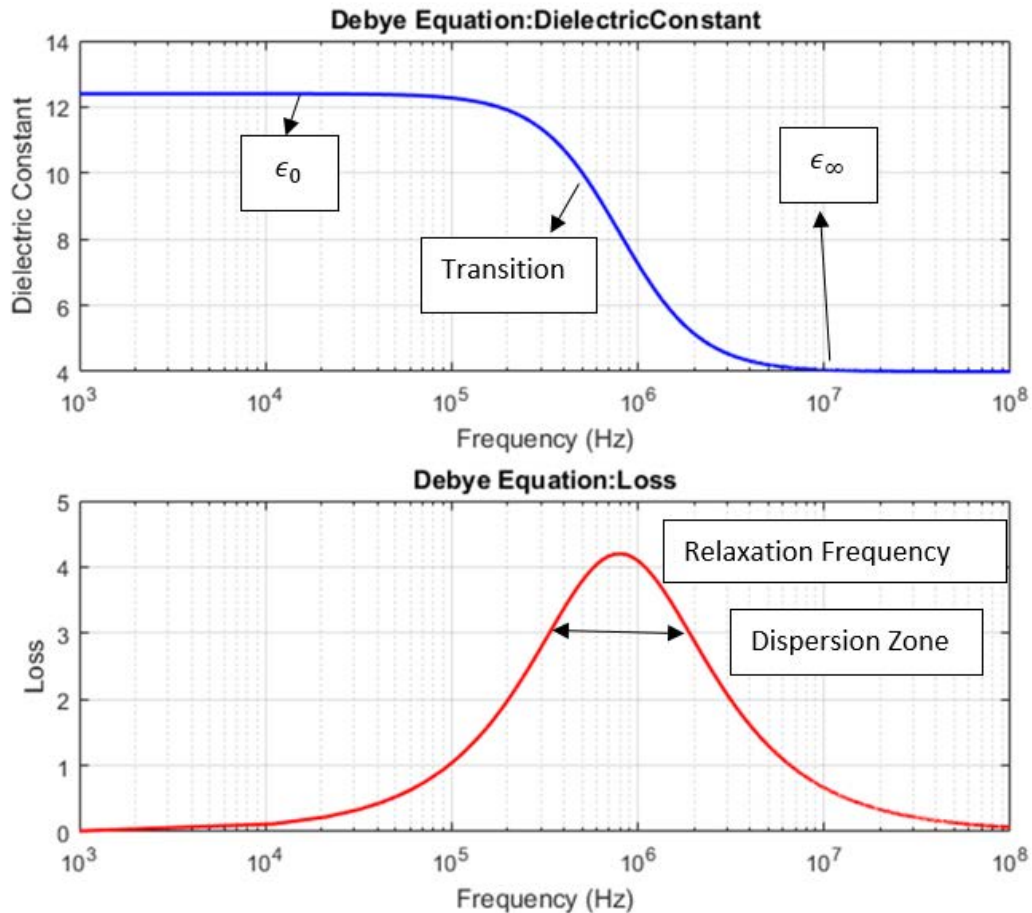


Figure 156: Debye model describing typical dispersion phenomenon (derived from the Debye equation: the relaxation frequency may change with the dielectric materials; the complex permittivity and complex conductivity of asphalt pavement materials can be described by Debye model and may have same curve tendency as this example depending on the operating frequencies)

In Figure 154, ϵ' tends to be a high constant ϵ_0 at very low frequencies and a small constant ϵ_∞ at very high frequencies. At intermediate frequencies, ϵ' tends to decrease in the transition area. Within that transition, ϵ'' tends to increase and then decrease such that a maximum value of ϵ'' appears at a specific frequency which is named as the relaxation frequency. For abnormal dispersion, the only difference is the dielectric constant at very high frequencies would increase and then be constant. Such dispersion is due to the polarization in the dielectric materials.

There are four recognised polarization mechanisms: that of the Maxwell Wagner; the dipole; the atomic and the electronic. The dipole polarisation is available in dielectric materials possessing ions and permanent dipoles; the atomic polarization only occurs in a

dielectric material that has an ionic structure; all non-conducting materials are capable of electronic polarisation at suitably high frequencies. These three polarization mechanisms result from the orientation or displacement of bound charge carriers. The Maxwell-Wagner polarisation is due to the accumulation of mobile charges, or free ionic charges, in water or on structural grain surfaces. Furthermore, the Maxwell-Wagner polarization only occurs on hetero-structures or heterogeneous dielectric matter (e.g. asphalt pavement mixture) with free ionic charges. Atomic polarization and electronic polarization are due to the effects of an external electric field on electrons and atoms at very high frequencies which usually refer to the optical frequency range. At low-to-intermediate frequencies (< 1.5 GHz), dipole polarization and Maxwell-Wagner polarization commonly occurs in dielectrics. It is stated that two physical processes of the Maxwell-Wagner and the electrochemical are used to describe the polarization phenomena in heterogeneous disperse dielectrics. These two processes are dependent on the state of the solid, whether it is considered to be a dielectric or a conductor [1] [2] [3] [4] [5] [6] [10].

- **Electrochemical process**

The electrochemical process includes α -polarisation or Electrical Double Layer polarisation (EDLP). An Electrical Double Layer is a structure that appears on the surface of an object when it is exposed to a fluid (e.g. pore water-solid matrix interface). The α -polarisation corresponds to the polarisation of the Electrical Double Layer (EDL) coating around particles (e.g. silica grains) illustrated in Figure 155 [11] [12]. The Electrical Double Layer polarisation depends on the mobility of the ions in a solution and the pore gap length and may exist at very low frequencies (<1 kHz). There is a potential difference between the Stern layer and the diffuse layer causing double layer polarisation (definitions of the Stern layer and the diffuse layer: seen from the 'Note' section after the Figure 155). As an external electric field is applied, the cations move in the direction of the electric field while the anions move in the opposite direction. Due to the pore gap between two silica grains, the fractions of total free charges passed by the counter-ions are different in the bulk electrolyte and in the Electrical Double Layer [12]. As a result, the salt concentrations on both sides of a boundary are different: the salt concentration on one side with same direction as the

electric field increases and the other side where the salt concentration decreases. Thus, a diffuse potential occurs.

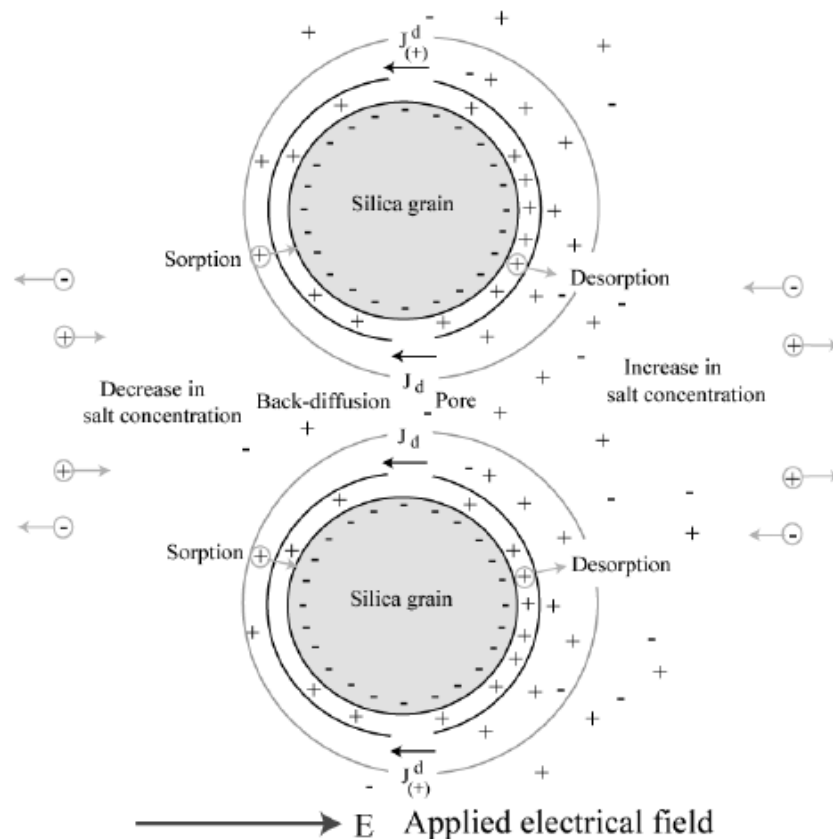


Figure 157: Sketch of three polarizations of a pore between two grains [11] [12]

Note: generally, a medium with lower dielectric constant carries negative surface charge when this medium disperses in a fluid of very high dielectric constant such as water [13]. Water contains several kinds of ions: some conductive ions are from the dissolved solvent such as the salt; some are from inorganic materials such as alkalis, chlorides, sulphide and carbonate compounds. These ions are attracted by the lower dielectric constant media surface and they will form an organized layer. This structured immovable layer is a Stern layer. However, as large water molecules surround those ions, the negative surface charges of the media are not going to be completely cancelled by them. We call those negative surface un-cancelled charges as remaining surface charges. The remaining surface charges continue to attract other cationic charges that are further away from the surface. As the distance between the media surface and the continually attracted cationic charges

increases, the physical force becomes weaker. These cationic charges, attracted by the remaining negative charges, form the second layer called as diffuse layer that is the outer part of the Electrical Double Layer [11] [12].

- **Maxwell-Wagner polarisation**

Maxwell-Wagner polarisation (typically at frequencies from 1 kHz to 10 MHz) is an interfacial polarization caused by ion displacements that are restricted to the scale of pores or particles. It relates to the accumulation of free charges at material surfaces shown in Figure 156 [1]. Maxwell Wagner polarization can be quantified by the Cole-Cole model. Its relaxation time depends on the pore fluid, the pore space size, the free charge density, the porosity and so on. The moisture level is the dominant factor influencing its relaxation time [1] [5] [11] [14].

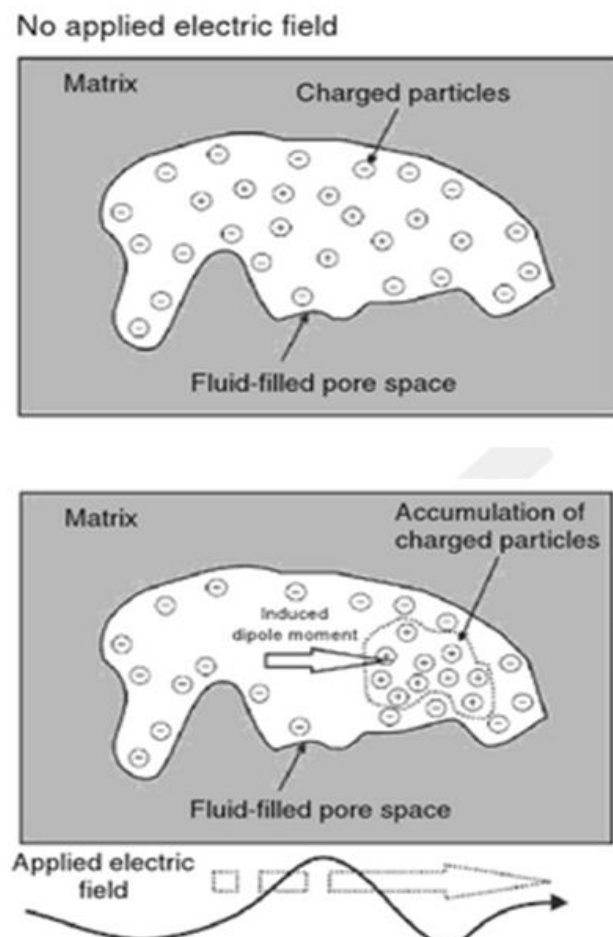


Figure 158: Conceptual diagram illustrating the process of interfacial polarization [1]

Note: the fluid here may be water or any other fluid. The upper figure has no electric field applied (positive free charges are distributed randomly within the pore fluid). In the lower figure, an external electric field is applied at low frequencies (<10 MHz). As mentioned in the previous section, the surface of the matrix grains is negatively charged after it is dispersed into water. Following the application of the electric field, positive free charges accumulates to one side to form a net induced dipole moment.

According to the investigation conducted by Lesmes [10] in their research on dielectric spectroscopy of sedimentary rocks (water-wet mixture), electrochemical polarization controls the dielectric response when the applied frequency is very low (<0.1 Hz) and Maxwell-Wagner polarization dominates the dielectric response when radio frequencies are applied (<0.1 GHz). Tabbagh [5] proposed that the Maxwell-Wagner effect is sufficient to explain the disperse phenomenon in clayey heterogeneous materials (with different water contents) at frequencies ranging from 1 kHz to 1 MHz, though both Maxwell-Wager polarization and electrochemical polarization may exist at the same time. Moreover, Kemna and Jol mentioned that in heterogeneous porous mixed media, Maxwell Wagner polarization dominates among all polarization mechanisms at frequencies from 1 kHz to 1 MHz [1] [12]. This statement was based on investigations of different dominant polarization mechanisms (Electrical Double Layer, diffuse layer polarization or Maxwell-Wagner) in three types of porous materials, as illustrated in Figure 157. Kemna concluded that in the first case of colloidal suspension, Electrical Double Layer, diffuse layer polarization and Maxwell-Wagner polarization co-exist. In the second case of a granular porous media, the diffuse layer polarization does not exist. Therefore, Electrical Double Layer and Maxwell-Wagner exist at the same time. For the third case of continuous solid phase, only Maxwell-Wagner space polarization occurs. Taking asphalt pavement mixtures into account, it can be categorized into any case illustrated in Figure 157 that the Maxwell-Wagner polarization exists.

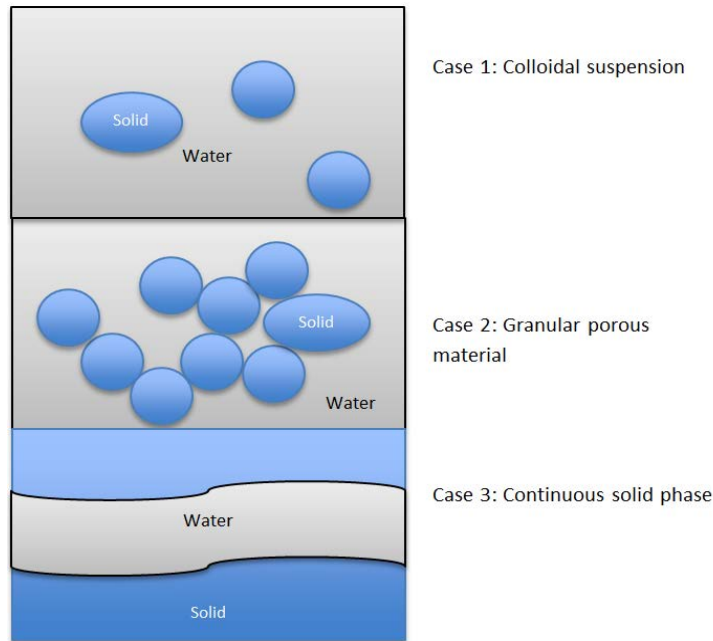


Figure 159: A sketch view of polarization mechanisms in different porous dielectrics

Therefore, the main polarisation mechanism in an asphalt pavement mixture is thought to be Maxwell-Wagner polarisation at frequencies from 1 kHz to 1 MHz. Furthermore, as pointed out by Bottcher [15] and Shang [6], at radio frequencies (3 kHz to 100 MHz), the dielectric properties of experimental asphalt pavement mixture could be expressed by an empirical Debye model which was originally used to describe the dipole polarization mechanism in a homogeneous polar liquid such as water and organic crystalline solids.

6.2 Empirical models used to describe Maxwell-Warburg polarization in the asphalt pavement mixture

Debye [8] published a model equation, commonly known as the Debye model, based on experiments conducted on simple dilute solutions of dipolar molecules in a non-polar liquid.

$$\varepsilon^*(\omega) = \varepsilon_{\infty} + (\varepsilon_0 - \varepsilon_{\infty}) / (1 + j\omega\tau_0) \quad (6-3)$$

And

$$\rho^*(\omega) = \rho_s \left(1 - m \left[1 - \frac{1}{1 + j\omega\tau_0} \right] \right) \quad (6-4)$$

Where,

ε_0 is the static dielectric constant and ε_∞ is the dielectric constant at infinite frequency; τ_0 is the relaxation time which is the reverse of relaxation frequency; $\rho^*(\omega)$ is a frequency-dependent complex resistivity; ρ_s is a static resistivity; $m = \frac{\rho_s - \rho_\infty}{\rho_s}$ is the chargeability;

The Debye permittivity equation yields:

$$\varepsilon^*(\omega) = \varepsilon_\infty + \frac{\varepsilon_0 - \varepsilon_\infty}{1 + (\omega\tau_0)^2} - j \frac{(\varepsilon_0 - \varepsilon_\infty)\omega\tau_0}{1 + (\omega\tau_0)^2} \quad (6-5)$$

Comparing equation (6-5) with the equation (6-1):

$$\varepsilon'(\omega) = \varepsilon_\infty + \frac{\varepsilon_0 - \varepsilon_\infty}{1 + (\omega\tau_0)^2} \quad (6-6)$$

$$\varepsilon''(\omega) = \frac{(\varepsilon_0 - \varepsilon_\infty)\omega\tau_0}{1 + (\omega\tau_0)^2} \quad (6-7)$$

From those two equations (6-6) and (6-7), the relaxation time can be calculated if the complex dielectric constant and the dielectric constant at very high frequency are given:

$$\tau_0 = \frac{\varepsilon''(\omega)}{(\varepsilon'(\omega) - \varepsilon_\infty)\omega} \quad (6-8)$$

The Debye model was originally proposed and tested by Debye using experiments in homogeneous dielectrics and was used in Shang's research [6] on dielectric dispersion effects of asphalt pavement materials of both dry and wet condition at radio frequencies (0.1 MHz to 1.5 GHz). 70 asphalt aggregate samples (measured at 100 MHz) from wearing and bearing courses of the asphalt pavement were collected and tested by Shang using non-destructive technique which indicates the efficacy of the Debye model on heterogeneous dielectrics such as asphalt pavement mixture. Meanwhile, experimental data and relaxation parameters of relaxation time and static dielectric constant of those 70 samples were listed. These results provided a reference for the analysis of the measured data. However, it was stated by Cole and Cole [9] that the Debye model was not sufficient (as seen in Figure 158) to describe a few coexisting polarization phenomena in heterogeneous materials such as rocks and the asphalt pavement mixtures. In Cole and Cole's experimental research, it was shown that the observed experimental behaviour cannot be exactly quantified by the Debye model as the observed behaviour curves fit much better with a broader frequency range of dispersion and absorption and a smaller maximum value

of $\epsilon''(\omega)$ than predicted from the Debye equation. The curves illustrated in Figure 158 describe the relationships of the real and imaginary parts of the complex permittivity with respect to frequency. The black curve is from the Debye model and the red curve is assumed to come from observed data.

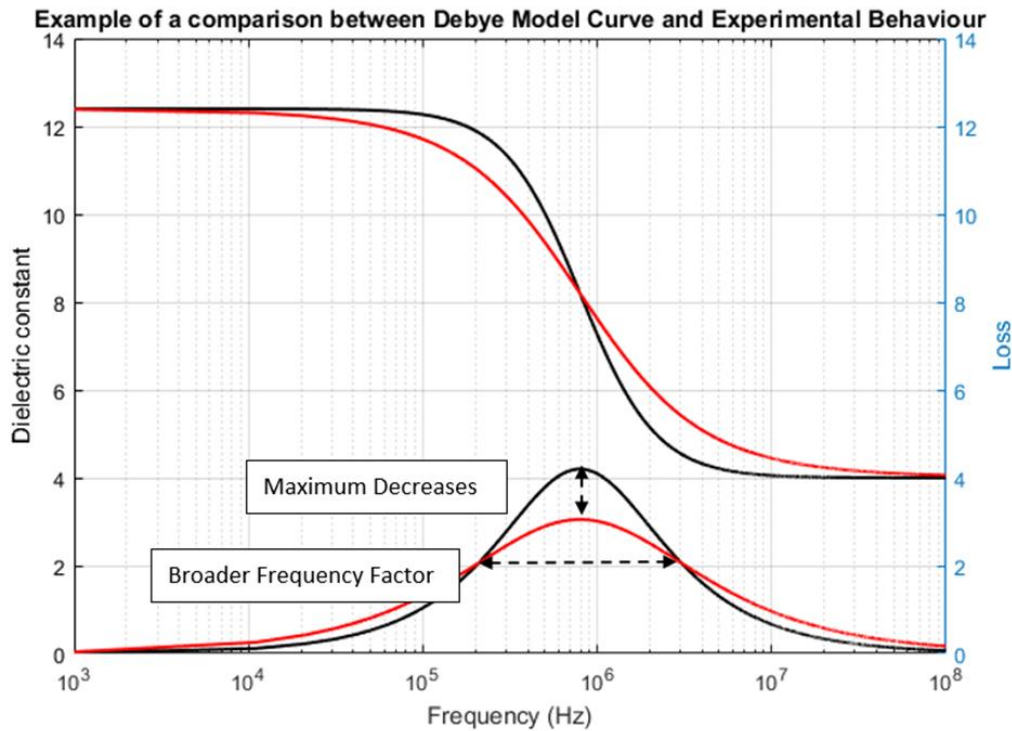


Figure 160: Example of comparison between Debye curve and experimental behaviour (both curves were derived from synthetic data to illustrate results from the literature [9])

Therefore, Cole and Cole developed a Cole-Cole model by introducing a broader frequency range factor α inside the Debye model equation to express possible dispersion effects by a few types of polarization mechanisms in heterogeneous media [9]. The Cole-Cole model has been applied to experiments by many researchers [3] [4] [7] [16] [17] [18]. For example, Dias considered models for sedimentary rocks at frequencies from a few hertz to 1 MHz by trying twelve currently studied empirical models which were used to describe the dispersion effects and the polarization phenomena. Dias concluded that the multi-Cole-Cole and Dias models are the only two models that fit well with the available experimental data [3]. The Cole-Cole model (CCM) is an empirical model [9] extended from the Debye model, which is usually successful in describing natural liquids, rocks, solids and heterogeneous mixtures. From this point, the Cole-Cole model is proposed to be a good approximation of

the complex conductivity behaviour of most of the subsurface materials. The Cole-Cole model equation is given by Cole and Cole:

$$\varepsilon^*(\omega) = \varepsilon_\infty + (\varepsilon_0 - \varepsilon_\infty)/(1 + (i\omega\tau_0)^{1-\alpha}) \quad (6-9)$$

$$\rho^*(\omega) = \rho_s \left(1 - m \left[1 - \frac{1}{1+(j\omega\tau_0)^{1-\alpha}}\right]\right) \quad (6-10)$$

Complex resistivity $\rho^*(\omega)$ or complex permittivity $\varepsilon^*(\omega)$ are related to the complex conductivity by $\sigma^*(\omega) = \frac{1}{\rho^*(\omega)} = i\omega\varepsilon^*(\omega)$ [25]. Comparing the Cole-Cole model equation with the Debye formula, it is known that the Cole-Cole model becomes the Debye model when the parameter of the broader frequency range factor α is assigned as zero.

It is assumed that the Debye model and the Cole-Cole model are both effective in describing the Maxwell-Wagner polarization phenomena in porous dielectric materials such as an asphalt pavement mixture, but of different accuracies. Dielectric dispersion effects and the polarization phenomena are tested by experiments in the following section.

6.3 Dielectric dispersion experiments at frequencies (0.1 kHz – 0.1 MHz)

To test the dispersion effects, epoxy spheres surrounded by water were used to mimic the asphalt pavement aggregates. Epoxy fillers with high resistivity are considered as the solid dielectric.

- 1) A capacitor filled by Epoxy fillers and tap water

A parallel-plate cylindrical capacitor (its geometry given in Table 21) was formed by pasting copper tape on its top and bottom sides.

Table 21: Cylinder geometry

Material	Diameter/m	Thickness/m	Water content	Frequency range
Epoxy Filler	0.0468	0.0175	Around 20%	100 Hz-13 MHz

An HP4921 LF impedance analyser was used to measure the impedance of the experimental test-rig. Before the test, only the epoxy fillers were placed into the plastic container. Then, the void spaces were 50% filled with water. Finally, the void spaced were 100% filled with water (see Figure 159).



Figure 161: Test rig including epoxy fillers surrounded by water

The relationships of the cylindrical capacitance and the conductance with respect to frequency are illustrated in Figure 160.

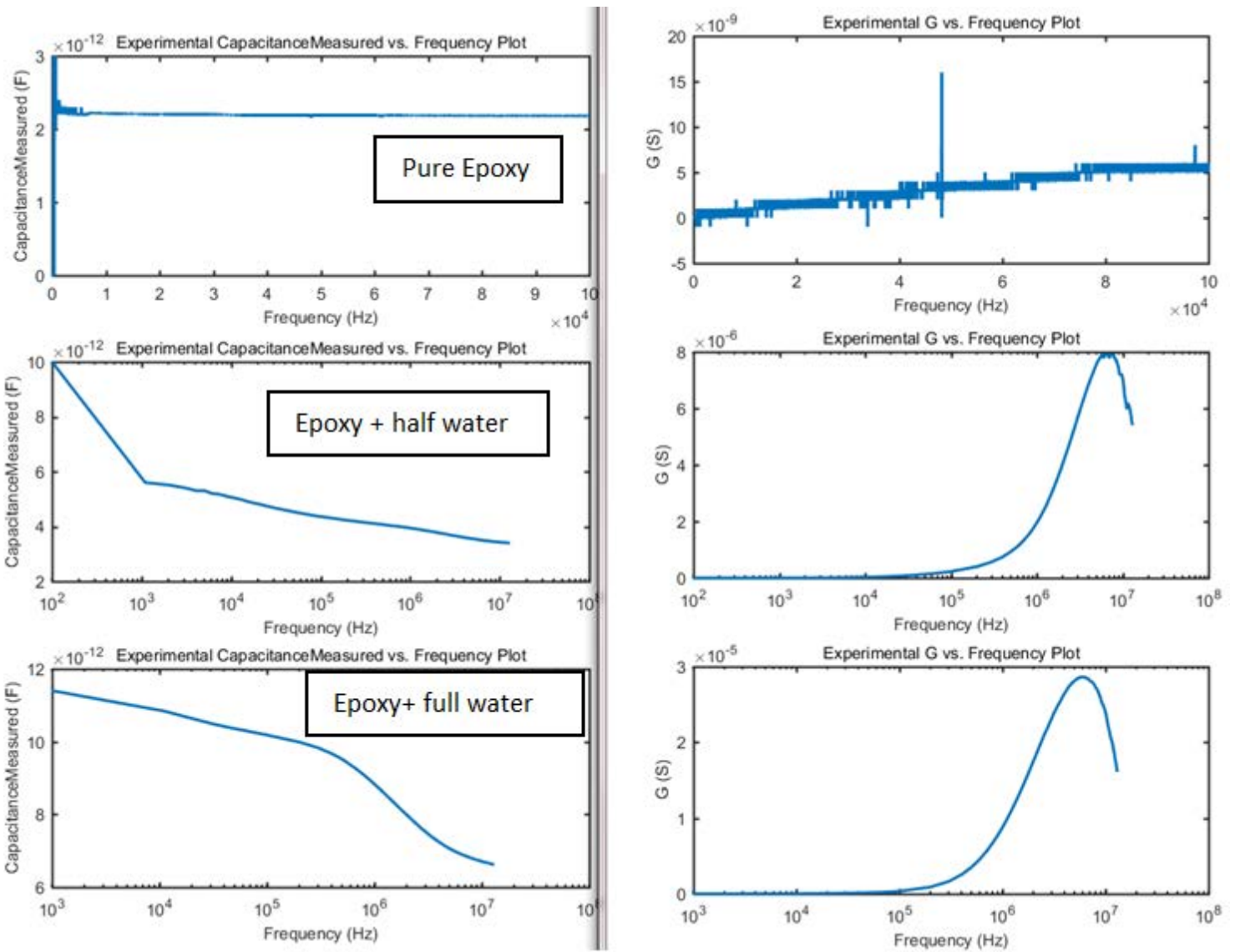


Figure 162: Experimental capacitance and conductance of epoxy experiment

In Figure 160, the X-coordinate is the operating frequency and the Y-coordinate of the figures on left side is the measured capacitance. The Y-coordinate of figures on right side is the measured conductance. The dielectric constant should be proportional to the capacitance and the loss should be a function of the measured conductance. When the epoxy fillers were dry, the capacitance is a constant of 2.2 pF. At low frequencies, all curves vary slightly due to the extremely high values of reactance measured and the ambient electric fields present. For the half-filled water case, the capacitance varies from 10 pF to 3.4 pF whilst the curve changes slightly at low frequencies. For the fully-filled water case, the capacitance varies from 12 pF to 6.7 pF. These experiments verify the existence of the dispersion and absorption effects at frequencies from a few hundred hertz to 100 MHz caused by the Maxwell-Wagner polarization, and possibly the electrochemical effect at very low frequencies because the capacitances measured with water present are nearly 6 times that when only the epoxy spheres are present. The moisture content does have a dominant influence on the permittivity. Further experiments were conducted and their results are shown in Figure 161 to Figure 163.

2) A capacitor filled by Epoxy fillers, some minerals (pure copper powder), and tap water
 The experiments described above were repeated with the addition of some copper powder. In this situation, three difference materials are mixed together.

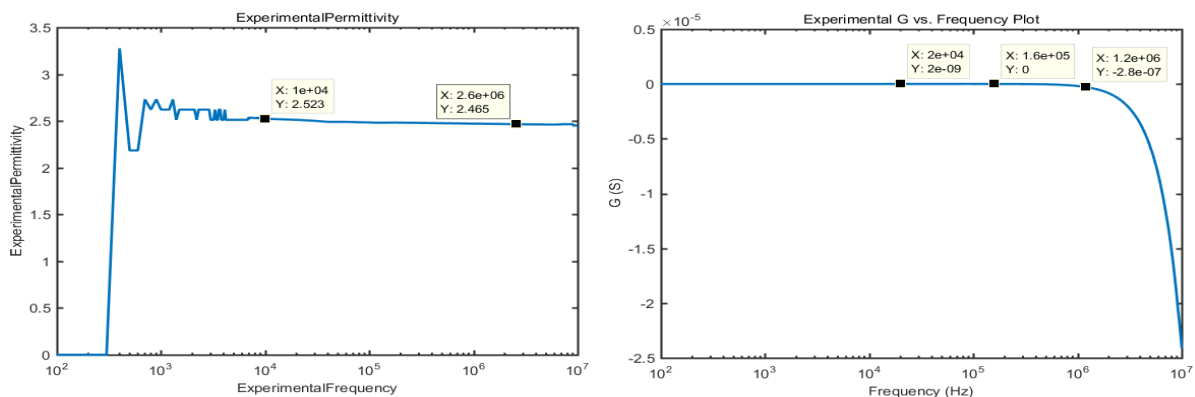


Figure 163: Case 1-using epoxy and copper powder

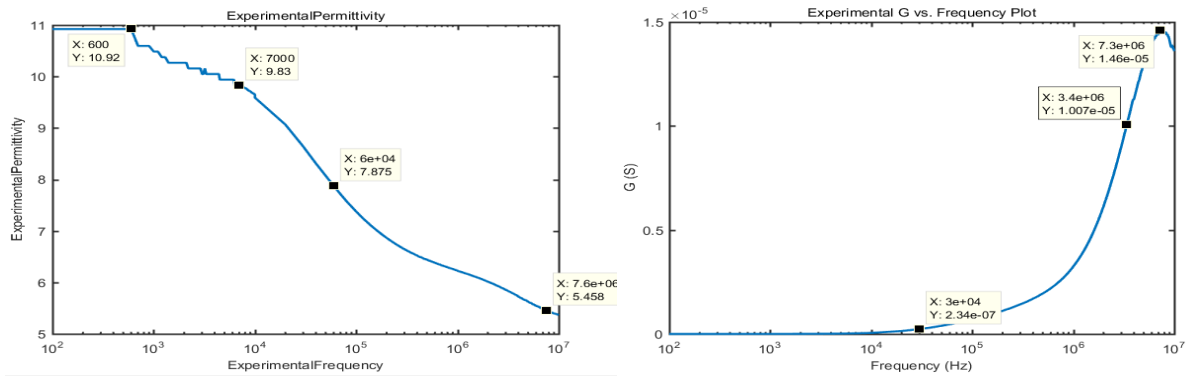


Figure 164: Case 2-using epoxy, copper powder and 50% water-fill

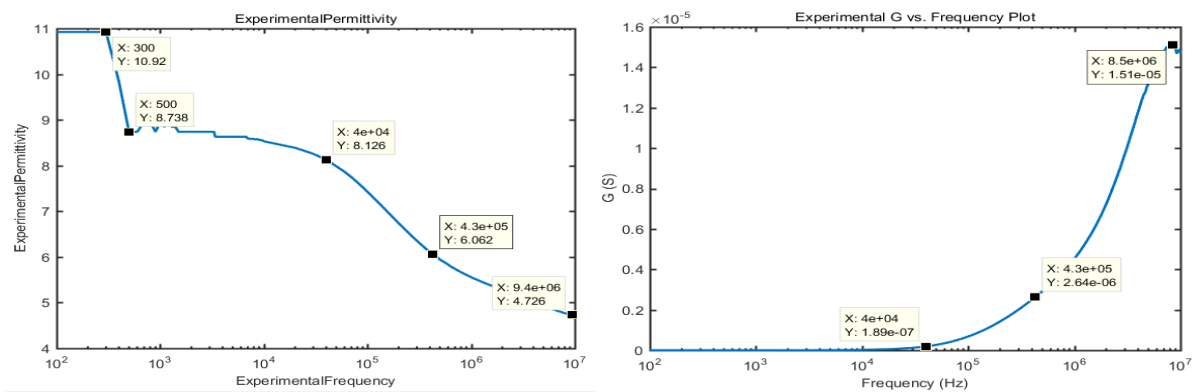


Figure 165: Case 3-using epoxy, copper powder and 100% water-fill

Comparing the figures that come from experimental datasets (Figure 160, Figure 161, Figure 162 and Figure 163) with the previous figures that come from analytical equations (Figure 154 and Figure 158), it is seen that all the experimental dataset-derived curves show the same tendency as the analytical Debye model or the Cole-Cole model. “The complex permittivity and complex conductivity of asphalt pavement materials can be described by various empirical models (e.g. Debye model or Cole-Cole model) depending on the operating frequencies [1] [2] [3] [4] [5] [6]. The relaxation time of the Debye model or Cole-Cole model quantifies the dielectric dispersion of the asphalt pavement materials resulted from the polarization process”. At very low frequencies, the dielectric constant tends to be very high, which is five or six times higher than the value at high frequencies. This is probably because of the Electrical Double Layer (EDL) polarization at very low frequencies. Revil [11] [12] [19] [20] [21] made a conclusion deriving from his investigations that the permittivity resulting from the Electrical Double Layer (EDL) or the electrochemical potential is five or six times larger than the permittivity measured at high frequencies. The Cole-Cole

model with the broader frequency range factor α of zero (the Debye model) is applied to one of these experiments (epoxy fillers with 100% water-fill) to see the fitting results between the measured dataset and the analytical model (Figure 164).

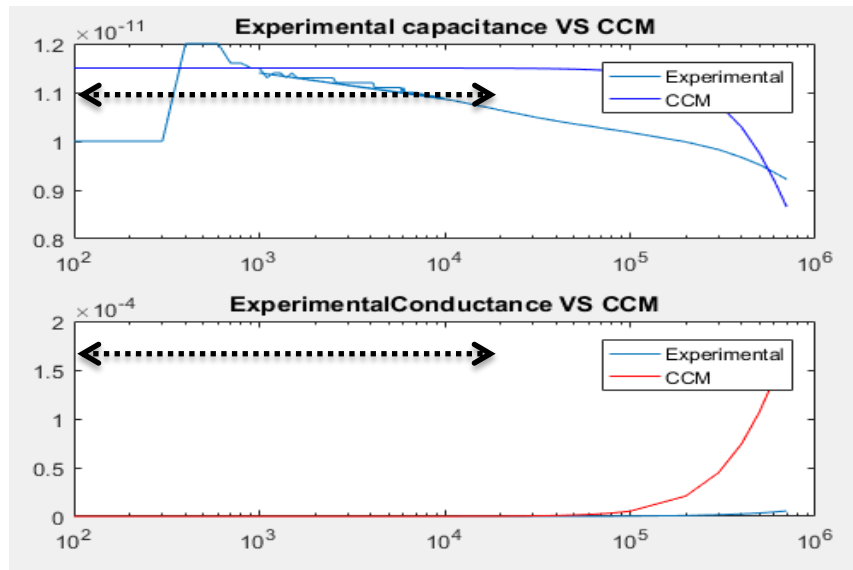


Figure 166: Fitting results between the dataset from the epoxy experiment (epoxy fillers with 100% water-fill) and the analytical Cole-Cole model (broader frequency range factor set as zero; X-axis: operating frequency in unit of Hz; Y-axis of the upper figure: Experimental Capacitance in unit of Farads; Y-axis of the lower figure: Experimental Conductance in unit of Siemens)

The Y-coordinate in the upper figure represents the capacitance and the Y-coordinate in the lower figure represents the conductance. Both the dielectric constant and the loss-related components are fitted by applying the special Cole-Cole model with the broader frequency range factor α of zero (the Debye case). This experiment expresses the same conclusion as Cole and Cole stated in their research work [9] that “there is a considerable amount of experimental evidence to indicate that the Debye model is not a sufficiently correct description of the observed frequency dependence of the polarization processes” as evidence by the results presented in Figure 158. It can be reasonably stated that, the Cole-Cole model with a non-zero broader frequency range factor has to be added to describe the Maxwell-Wagner polarization in heterogeneous porous media of an asphalt pavement mixture in the bearing and wearing course when the frequency is very high (> 20 kHz). However, at low frequencies (black arrows of dashed line in Figure 164), the peak amplitude error between the experimentally measured capacitance and the analytical capacitance is within 10% and the experimental conductance could be recognized as similar to the

analytically derived conductance from the Debye model. As the capacitive coupled resistivity system used to assess the sub-surfacing condition of asphalt pavement in this research has an operating frequency less than 20 kHz, the Debye model is considered to be effective in interpreting collected impedance data from asphalt pavements.

Above all, as stated previously, an electric field at a specific frequency range applied to an asphalt pavement mixture is assumed to cause polarization processes. The response of the polarization can be interpreted by phenomenological models e.g. Dias model [3] [4], Warburg model [7], Debye model [7] [8] or Cole-Cole model [9]. Also according to completed-experiments using different mixture compositions e.g. epoxy fillers, it is reasonably considered that the Debye model and the Cole-Cole model are both effective in describing the Maxwell-Wagner polarization phenomena in porous dielectric materials such as an asphalt pavement mixture. Hence, the Debye model and a fitting scheme are applied to the corrected measured data (the raw measured impedance data after taking geometric factors and roughness correction factors into account) collected from the field surveys of the good asphalt pavement and the poor asphalt pavement to derive the parameters values e.g. relaxation time and resistivity.

6.4 Field survey data interpretation (asphalt pavement)

Apparent resistivities are derived from systematically corrected measured impedance data by application of the geometric factor and the roughness factor (see chapter 4 and chapter 5).

$$Z_{SystemCorrect} = R_{SystemCorrect} + jX_{SystemCorrect} \quad (6-11)$$

$$\rho_{correct} = R_{SystemCorrect} k \quad (6-12)$$

$$X_{Correct} = X_{SystemCorrect} k / RoughFactor \quad (6-13)$$

Where $Z_{SystemCorrect}$ is the measured impedance after applying the systematic correction factors on the raw data; $\rho_{correct}$ is the resistivity after applying the geometric factor on the measured resistance; $X_{Correct}$ is the value after applying the geometric factor and the roughness factor. In this section, measured data collected at an operating frequency of 10 kHz is used. The Debye model is utilised as the analytical model to interpret the

measured impedance of the good pavement and the poor pavement. For data collected on all survey locations, a least square fitting search method with three unknown parameters of “the resistivity ρ_{DC} at DC frequency”, “the resistivity ρ_{∞} at very high frequency” and “relaxation time” is applied to predict the values of these parameters. Initially ρ_{DC} is set as five times of the $\rho_{correct}$ considering the DC effect and the electrochemical polarization at frequencies of a few hertz [11] [12] [19] [20] [21]. The high frequency resistivity ρ_{∞} is set as 1.2 times less than the $\rho_{correct}$ value. Initial relaxation times are predicted by using equation (6-8). For the poor pavement, the fitting scheme is separately applied on the data collected from 161 survey locations. Fitting results and the relaxation time are given in Figure 165, Figure 166 and Figure 167. In all of these figures, the X-coordinate of the “profile” represents the survey locations. From the experiments conducted on different asphalt samples used to predict their relaxation times by Shang [6], it was seen that the relaxation times of wet samples are generally higher than those of the same samples but in dry condition.

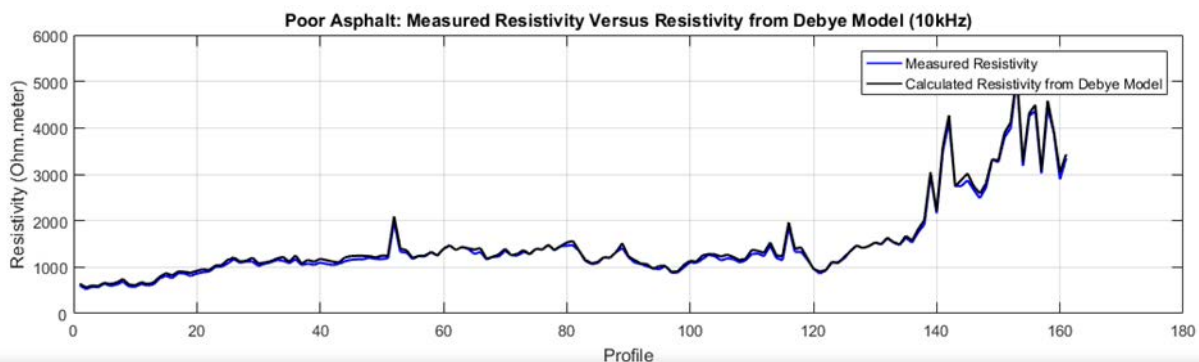


Figure 167: Fitting results between the measured resistivity of a poor asphalt pavement and analytical resistivity predicted using the Debye model at 10 kHz

The Y-coordinate is the resistivity. The standard deviation is $868.05 \Omega m$ and the root mean square is $1708 \Omega m$ (the values differ because of the non-zero-mean characteristics of the data). The standard deviation error between the measured resistivity of a poor asphalt pavement and the analytical resistivity predicted using the Debye model is $36.7 \Omega m$. The root mean square error is $57.8 \Omega m$. The data points, collected from the 138th location to the 161th location of the poor asphalt pavement, are of higher resistivity than the surrounding data points. These data points correspond to the dry areas, assessed through

visual observation and previous weather conditions. The remaining data points are from the wet areas, assessed through visual observation and previous weather conditions.

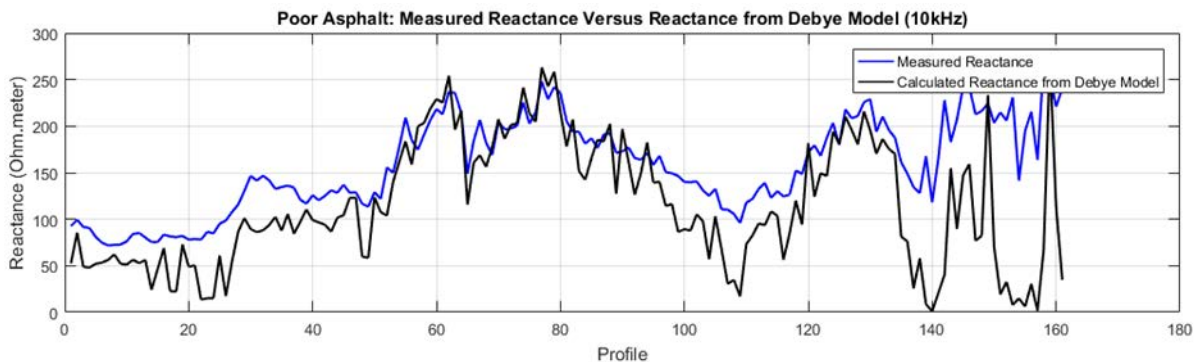


Figure 168: Fitting results between the measured reactance of a poor asphalt pavement (after applying geometric factor and roughness factor) and calculated reactance predicted by the Debye model at 10 kHz

The Y-coordinate is the imaginary part of the complex resistivity. The standard deviation is $49.8 \Omega m$ and the root mean square is $165.28 \Omega m$. The standard deviation error is $50.2 \Omega m$ and the root mean square error is $66.0 \Omega m$.

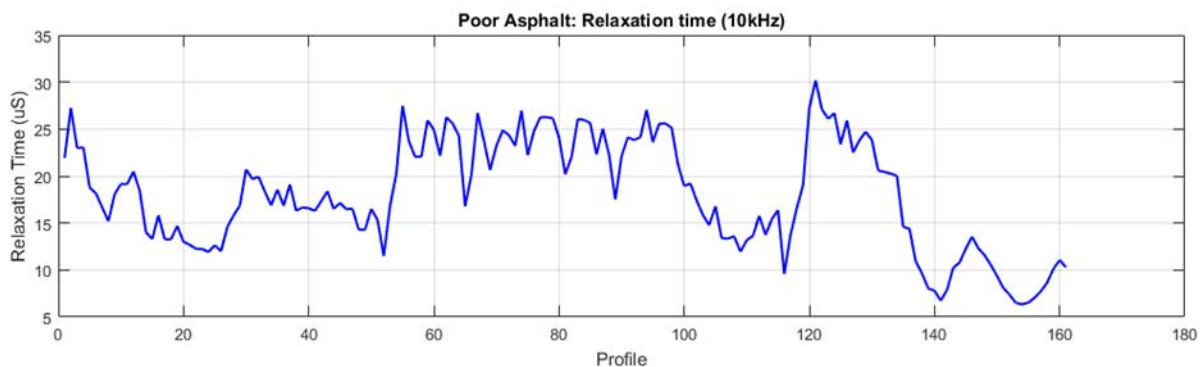


Figure 169: Relaxation time of a poor asphalt pavement at 161 positions predicted by the Debye model at 10 kHz

The Y-coordinate is the relaxation time with units of μS . It is apparent that the relaxation times of the data points, collected from the dry area of the poor pavement (the 138th location to the 161th location), are smaller than the relaxation times of other pavement material samples. The mean relaxation time is $18.7 \mu S$.

For the good pavement, there are 164 survey locations. The fitting results and the relaxation times are given in Figure 168, Figure 169 and Figure 170.

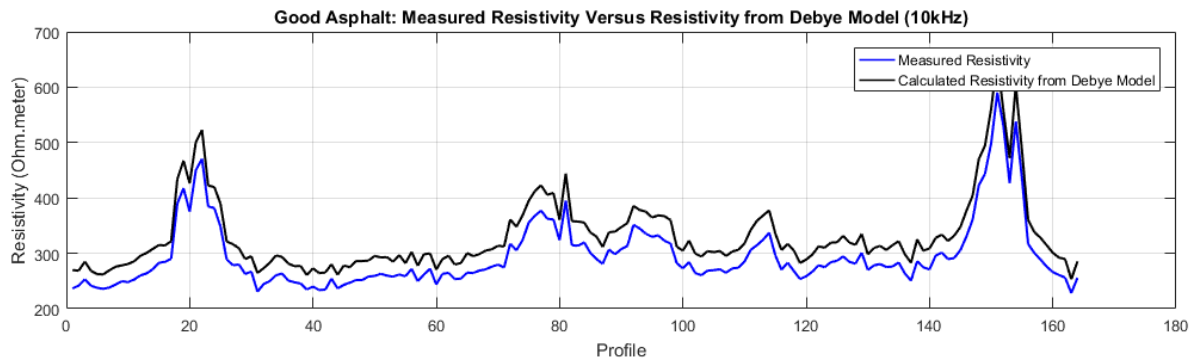


Figure 170: Fitting results between the measured resistivity of a good asphalt pavement and analytical resistivity predicted using the Debye model at 10 kHz

The Y-coordinate is the real part of the complex resistivity. The standard deviation is $61.48 \Omega m$ and the root mean square is $302.12 \Omega m$. The standard deviation error is $7.2 \Omega m$ and the root mean square error is $36.3 \Omega m$.

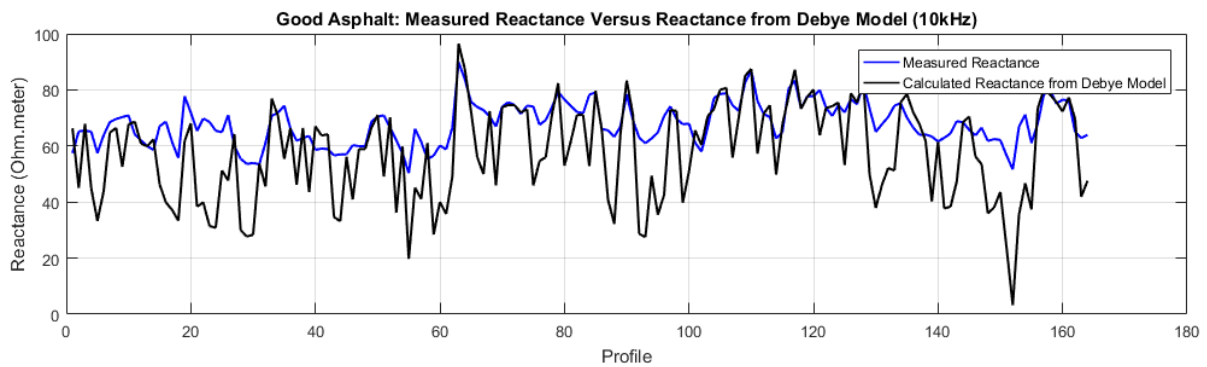


Figure 171: Fitting results between the measured reactance of a good asphalt pavement (after applying geometric factor and roughness factor) and calculated reactance predicted by the Debye model at 10 kHz

The Y-coordinate is the imaginary part of the complex resistivity. The standard deviation is $7.55 \Omega m$ and the root mean square is $68.33 \Omega m$. The standard deviation error is $13 \Omega m$ and the root mean square error is $16.6 \Omega m$.

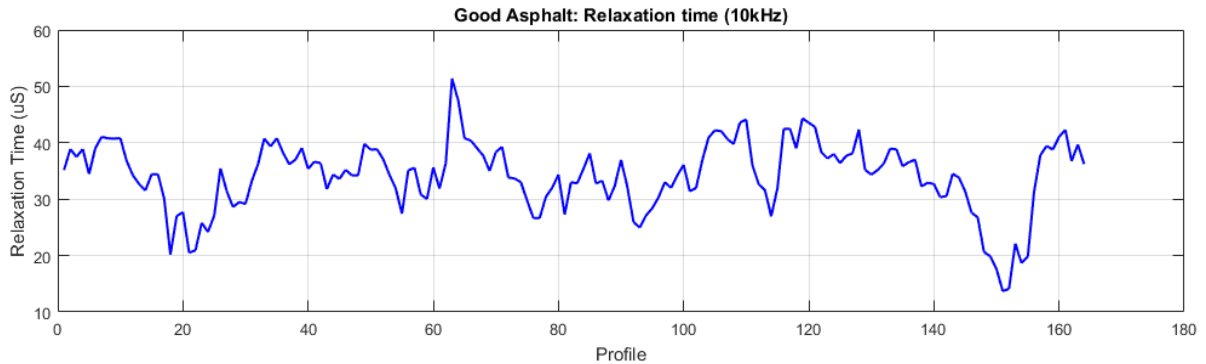


Figure 172: Relaxation time of a good asphalt pavement at 164 positions predicted by the Debye model at 10 kHz

The Y-coordinate is the relaxation time with units of μS . The mean relaxation time of the good pavement is $33.1 \mu S$ which is larger than the poor pavement.

In summary, the poor pavement was visually and qualitatively divided into a dry area and a wet area (through visual observation and previous weather conditions) in order to verify the results obtained by using the capacitive coupled resistivity system. All results presented for the resistivities and the relaxation times verify the visual-division assumption. The relaxation times of the samples in the good pavement are generally a little higher than those in the poor pavement areas. It is possible that there are more conductive materials in the good pavement areas than in the poor pavement areas because of different pavement design processes.

References

- [1] H.M. Jol, "Ground Penetrating Radar: Theory and Applications," in ELSEVIER, 2009.
- [2] T.M. Levitskaya and B.K. Sternberg, "Polarization processes in rocks 1. Complex dielectric permittivity method," in Radio Science, Vol 31, No. 4 (1996), pp. 755-779.
- [3] C.A. Dias, "Developments in a model to describe low frequency electrical polarization of rocks," in Geophysics, Vol. 65, No. 2 (2000), pp. 437-451.
- [4] C.A. Dias, "Analytical model for a polarizable medium at radio and lower frequencies," in Journal of geophysical research, Vol. 77, No. 26 (1972).

- [5] A. Tabbagh, P. Cosenza, A. Ghorbani, R. Guerin, and N. Florsch, "Modelling of Maxwell-Wagner induced polarization amplitude for clayey materials," in *Journal of applied geophysics*, October 2008.
- [6] J.Q. Shang and J.A. Umana, "Dielectric constant and relaxation time of asphalt pavement materials," in *J.Infrasturcture.Syst.*, Vol 5, No. 4 (1999), pp. 135-142.
- [7] W.H. Pelton, S.H. Ward, P.G. Hallof, W.R. Sill and P.H. Nelson, "Mineral discrimination and removal of inductive coupling with multifrequency IP," in *Geophysics*, 43 (1978), pp. 588–609.
- [8] P. Debye., *Polar Molecules*, Chemical Catalog Company, New York, 1929.
- [9] K.S. Cole and R.H. Cole, "Dispersion and absorption in dielectrics 1: Alternating Current Characteristics," in the *journal of chemical physics*, Vol 9, No. 341 (1941).
- [10] D.P. Lesmes and F.D. Morgan, "Dielectric spectroscopy of sedimentary rocks," in *Journal of geophysical research*, Vol. 106,No.B7 (2001).
- [11] A. Revil, "Effective conductivity and permittivity of unsaturated porous materials in the frequency range 1 mHz – 1 GHz," in *Water resources research*, Vol. 49 (2013).
- [12] A. Kemna, A. Binley, G. Cassiani, E. Niederleithinger, A. Revil, L. Slater, K.H. Williams, A.F. Orozco, F.H. Haegel, A. Hordt, S. Kruschwitz, V. Leroux, K. Titov and E. Zimmermann , "An overview of the spectral induced polarization method for near surface applications", in *Near surface geophysics*, Vol 10, No. 6 (2012).
- [13] M. Skold, A. Revil and P. Vaudelet, "The pH dependence of spectral induced polarization of silica sands: Experiments and modelling," in *Geophysical research letters*, Vol 38, No. 12 (2011).
- [14] A. Tabbagh, A. Hesse and R. Grard, "Determination of electrical properties of the ground at shallow depth with an electrostatic quadrupole: field trials on archaeological sites," in *Geophysical prospecting*, 41 (1993).
- [15] C.J.F. Bottcher, *Theory of electric polarization: dielectrics in static fields*, 2nd ed, 1973.
- [16] N. Florsch, C. Camerlynck and A. Revil, "Direct estimation of the distribution of relaxation times from induced-polarization spectra using a Fourier transform analysis," in *Near surface geophysics*, 2012.
- [17] A. Binley, L.D. Slater, M. Fukes and G. Cassiani, "Relationship between spectral induced polarization and hydraulic properties of saturated and unsaturated sandstones," in *Water resource research*, Vol. 41 (2005).
- [18] K. Koch, "Impact of changes in grain size and pore space on the hydraulic conductivity and spectral induced polarization response of sand," in *Hydrology and earth system sciences*, Vol 15 (2011).

- [19] A. Revil, N. Florsch and C. Camerlynck, "Spectral induced polarization porosimetry," in *Geophysical journal international*, 198 (2014).
- [20] A. Revil, M. Karaoulis, T. Johnson and A. Kemna "Review: Some low-frequency electrical methods for subsurface characterization and monitoring in hydrogeology," in *Hydrogeology journal*, Vol 20 (2012).
- [21] A. Revil, "On charge accumulation in heterogeneous porous rocks under the influence of an external electric field," in *Geophysics*, Vol 78 (2013), pp. 271-291.
- [22] C.J.F. Bottcher and P. Borderwijk, *Theory of electric polarization*, 2nd Ed, McGraw-Hill, New York, 1973.
- [23] A. Ghorbani, P. Cosenza, M. Zamora, M. Schmutz, N. Florsch and D. Jougnot, "Non-invasive monitoring of water content and textural changes in clay-rocks using spectral induced polarization: A laboratory investigation," in *Applied clay science*, 43 (2009).
- [24] M. Weigand and A. Kemna, "Relationship between Cole-Cole model parameters and spectral decomposition parameters derived from SIP data," in *Geophysical journal international*, 205 (2016).
- [25] K. Zonge, J. Wynn and S. Urquhart, "Resistivity, induced polarization and complex resistivity," in *Near surface geophysics*, 2005.
- [26] T. Kremer, M. Schmutz, P. Leroy, P. Agrinier and A. Mainault, "Modelling the spectral induced polarization response of water-saturated sands in the intermediate frequency range (100 Hz-100 kHz) using mechanistic and empirical approaches," in *Geophysical journal international*, 207 (2016).
- [27] D.W. Davidson and R.H. Cole, "Dielectric relaxation in glycerol, propylene glycol and n-propanol," in *Journal of Chemical Physics*, Vol 29 (1951), pp. 1484-1490.
- [28] L.D. Slater and D. Lesmes, "IP interpretation in environmental investigations," in *Geophysics*, Vol 67 (2002), pp. 77-88.

Conclusion

A non-invasive electrical resistivity technique using an automated capacitive coupled resistivity system, to assess the moisture condition of the wearing layer of a pavement by measuring the geophysical quantities of electrical resistivity, has been developed and applied to investigations of good pavements and poor pavements. This capacitive coupled resistivity system, operating at frequencies of 5 kHz, 7.5 kHz and 10 kHz, has four in-line electrodes C1, P1, P2 and C2 operating in a Wenner electrode configuration. Electrodes C1 and C2, act as the current source coupling the transmit signal into the paved area. The other two electrodes P1 and P2 measure the voltage induced in the media. Electrodes C1, P1, P2 and C2 are of large dimensions and small electrode separations and so cannot be treated as point sources. To predict the true electrical resistivity of pavement materials, the combination of methods including an analytical resistor-capacitor network, experimental tests and COMSOL modelling was applied in this research work.

- The system is sensitive to the equivalent capacitance of the pavement materials and the boundary layer capacitance including fringing capacitances. Guard rings are required to reduce the fringing effects.
- The system may be effectively modelled by a resistor-capacitor network. This was verified by experimental resistor-tests and COMSOL modelling. The geometric factor is around 0.46 for high resistivity pavement materials.
- The geometric factor of this capacitive coupled resistivity technique system is a function of the materials to be measured when these materials are of resistivities from $1 \Omega m$ to $1e^{10} \Omega m$.
- Errors may be introduced by using a 1D resistor-capacitor network method instead of 2D or 3D network methods. Current leakage within the boundary layer capacitor is likely to be the main error source at low frequencies. The boundary layer capacitor formed by the electrodes and the surface of the pavement results in a higher measured resistance at low operating frequencies than the true resistance. This impact exists in all experimental tests.

Pavement surface roughness and the electrode clearance have significant impacts on the electrode-boundary layer capacitance. According to experiments and field surveys conducted on the good pavement and the poor pavement, it is found that this capacitive coupled system described in this work is effective in evaluating pavement surface texture and indicating the moisture condition of the shallow-underlying (< 50 mm) layers.

- The measured reactance is an indication of the pavement surface roughness. The rougher the pavement surface, the larger the measured reactance will be. There is a significant variation of the measured reactance when the average surface peak-to-peak height of the pavement is smaller than 1.2 cm.
- The rougher surface texture indicates aging pavements and possible water ingress from the surface to the bottom surfacing layer.
- The roughness factor, describing the surface roughness influences on the capacitance, is around 27.5 for the instrument described within this thesis.
- The measured resistances and true apparent resistivities, obtained by this capacitive coupled resistivity system, effectively reflect the moisture condition of the shallow layer e.g. the wearing layer of the pavement, due to the induced energy taking the easiest route that is likely to be near the surface. The wetter the area in the shallow layer is, the smaller the resistivity becomes.

By applying the geometric factor and the roughness factor to form a systematically corrected measured impedance, the resistivity of the pavement material is estimated. A linear least square inversion method and the Debye model are used to extract the parameters e.g. relaxation time over frequency range (< 1 MHz).

- For heterogeneous and disperse dielectric materials comprising the asphalt pavement mixture, the phenomena of dispersion and absorption are due to several electrical polarization mechanisms. At operating frequencies from 1 kHz to 1 MHz, the Maxwell-Wagner interfacial polarization, due to the accumulation of free charges, is the dominant mechanism to be considered within the analysis.
- The dielectric properties of the material mixture is defined by the terms of complex conductivity or complex permittivity. The Cole-Cole model (CCM) is an empirical model that is generally used to describe natural liquids, rocks, solids and

heterogeneous mixtures such as an asphalt pavement. The Cole-Cole model with a non-zero broader frequency range factor has to be added to describe the Maxwell-Wagner polarization in heterogeneous porous media such as an “asphalt pavement mixture” in the bearing and wearing course when the frequency is very high (> 20 kHz).

- At low frequencies (<20 kHz), the error between the experimentally measured capacitance and the analytically predicted capacitance is within 10% and the experimental conductance could be recognized as the same as the analytically predicted conductance from the Debye model. Hence, the Debye model is assumed to be effective within the interpretation of measured complex conductivity of an asphalt pavement material mixture. This is because the capacitive coupled resistivity system used to assess the moisture condition of asphalt pavements described in this thesis operates at frequencies of less than 20 kHz.
- The relaxation time parameter derived from the Debye model is said to be dominantly affected by pore moisture content. Therefore, the relaxation time is assumed to be an indication of water content in the asphalt layer of the pavement.

Appendix 1: Main roughness parameters

Arithmetic average height

It is defined as the average value of the absolute standard deviation of the surface heights $h(x + \Delta x, y)$, which shift from the mean height of same sampling period Δx . The mathematic formula is

$$R_a = \frac{1}{m*n} \sum_{k=0, j=0}^{m,n} |h(x + k \Delta x, y + j \Delta y)|$$

Root mean square roughness

This RMS parameter describes the standard deviation of the irregular heights of the roughness surface. It gives us more information of shift from the mean line especially when the deviation is very large. The mathematic formula is

$$R_q = \sqrt{\left(\frac{1}{m} \sum_{k=0}^m (|h(x + k \Delta x, y)|)^2 \right)}$$

The maximum height of peaks

Given a length duration and divide the whole profile into N sections. For each section, there is a peak of a local maximum height. Thus, for these N sections, there are N local maximum peaks. The peak of the maximum height among those peaks is named as the global maximum height of peaks.

The maximum depth of valleys

Given a length duration and divide the whole profile into N sections. For each section, there is a valley of a local maximum depth. Thus, for these N sections, there are N local maximum valleys. The valley of the maximum depth among those valleys is named as the global maximum depth of valleys. This parameter and maximum height of peaks introduces a basic understanding of vertical range. Other parameters e.g. mean depth of valleys, mean height of peaks can be calculated.

Amplitude density function (ADF)

The ADF defines the profile heights distribution histogram. This parameter indicates a statistical understanding of the probability density of the roughness amplitudes on the vertical direction.

Auto correlation function (ACF)

ACF can be quantitatively used to measure the similarity between a laterally shifted and an un-shifted version of the profiles (Gadelmawla, 2002). The mathematical formula is

$$ACF(\Delta x) = \frac{1}{m-1} \sum_{i=1}^m h(x_i, y) * h(x_i + \Delta x, y)$$

Where Δx is the shifted length; $h(x_i, y)$ is the un-shifted version while $h(x_i + \Delta x, y)$ is the shifted version of the profile. The ACF is a very effective tool to detect the periodic components of the roughness surface even when there are many random elements.

Correlation length

A completely random process has a correlation length of zero. A periodic wave has an infinite correlation length. T.R. Thomas says in his book that the correlation length is defined as the length over which it decays to some fraction of its initial value, sometimes taken as a tenth, sometimes as $1/e$. It is considered that the pairs of data points are independent if the separation gap between these two data pairs is larger than the correlation length (T.R. Thomas, 1982). The ACF always starts from unit value as this corresponds to zero lag. In Gadelmawla's paper, it says that usually correlation length is defined as the shortest distance in which the value of the ACF drops to a certain fraction and this fraction is usually chosen as 10% of the zero-lag ACF value.

Appendix 2: Key Codes

```

%% CW: Continuous Wave Signal
clear
%
StartFrequency = 500; %Hz
Vmax = 9;
InputSamplingRate = double(50000);
OutputSamplingRate = InputSamplingRate;
InputSamplesPerChannel = 2^16;
OutputSamplesPerChannel = InputSamplesPerChannel;
T_OutputSampling = 1/OutputSamplingRate; % sampling period
T_InputSampling = 1/InputSamplingRate; % sampling period
TXIndex = (0:OutputSamplesPerChannel-1)*T_OutputSampling; % time vector
RXIndex = (0:InputSamplesPerChannel-1)*T_InputSampling; % time vector

SteppedFrequencies = 5000 + 2500*floor(10*(TXIndex./TXIndex(end)));
TXCWSignal = Vmax.*exp(1i.*(2*pi.*(SteppedFrequencies).*TXIndex);
if ~isreal(TXCWSignal)
% Convert back to a real signal (start at zero voltage as a sine wave)
TXCWSignal = -imag(TXCWSignal);
end
TXCW_FFT = fft(TXCWSignal,InputSamplesPerChannel);
TXCWSignalFFT = TXCW_FFT./InputSamplesPerChannel; TX_CWSignalFFT_SignalSide = TXCWSignalFFT(1:InputSamplesPerChannel/2+1);
TXIndex_CWSignalFFT_SignalSide = TXIndex(1:InputSamplesPerChannel/2+1);
SamplingFrequencies = InputSamplingRate.*(0:InputSamplesPerChannel-1)/InputSamplesPerChannel;

% Linear Frequency Modulation signal
%
StartFrequency = 100; %Hz
Bandwidth = 10e3;
Vmax = 9;
InputSamplingRate = double(50000);
OutputSamplingRate = InputSamplingRate;
InputSamplesPerChannel = 2^16;
OutputSamplesPerChannel = InputSamplesPerChannel;
T_OutputSampling = 1/OutputSamplingRate;
T_InputSampling = 1/InputSamplingRate;
TXIndex = (0:OutputSamplesPerChannel-1)*T_OutputSampling; % time vector
RXIndex = (0:InputSamplesPerChannel-1)*T_InputSampling; % time vector

SteppedFrequencies = 5000 + 2500*floor(10*(TXIndex./TXIndex(end)));
TXLFMSignal = Vmax.*exp(1i.*(2*pi.*(StartFrequency.*TXIndex+ pi.*(TXIndex).^2*Bandwidth*InputSamplingRate/InputSamplesPerChannel));
LFmFrequencies = StartFrequency + TXIndex.*Bandwidth.*OutputSamplingRate./InputSamplesPerChannel;
DeviationInstantaneousFrequency = TXIndex.*Bandwidth.*OutputSamplingRate./InputSamplesPerChannel;
if ~isreal(TXLFMSignal)
TXLFMSignal = -imag(TXLFMSignal);
end

TXLFM_FFT = fft(TXLFMSignal,InputSamplesPerChannel);
TXLFMSignalFFT = TXLFM_FFT./InputSamplesPerChannel;
TX_LFMSignalFFT_SignalSide = TXLFMSignalFFT(1:InputSamplesPerChannel/2+1);
TXIndex_LFMSignalFFT_SignalSide = TXIndex(1:InputSamplesPerChannel/2+1);
SamplingFrequencies = InputSamplingRate.*(0:InputSamplesPerChannel-1)/InputSamplesPerChannel;

%% Capacitances formulas comparing: parallel capacitor with fringing effects considered
%% Sakurai- simple formula for two-three dimensional capacitances
fprintf('2: Single Plate with Finite dimension on Ground plane\n');
%%%%%%%%%%%%%%%%%%%%%%%%%%%%%%%%%%%%%%%%%%%%%%%%%%%%%%%%%%%%%%%%%%%%%%%% to see Width=0.12m Length=0.2m
Eps = 8.854e-12*2.283;
Width = 0.02:0.01:0.12;
Length = 0.1:0.01:0.2;
Height = 0.00273;
ThickRatioHeight = 0.1;
Thick = Height*ThickRatioHeight;
WidthRatioHeight = Width./Height;
WidthRatioLength = Width./Length;
Area = Width.*Length;
%%%%%%%%%%%%%%%%%%%%%%%%%%%%%%%%%%%%%%%%%%%%%%%%%%%%%%%%%%%%%%%%%%%%%%%%
CircumstanceOfPlate = 2*Width + 2*Length;
Index = 1;
Cplate_standard = Eps*Area./Height;

fprintf('Figure C-plate\n');
Csarukai = Eps*(1.15*Area./Height + 1.40*(ThickRatioHeight).^0.222*(CircumstanceOfPlate) + 4.12*(ThickRatioHeight).^0.728.*Height); % capacitance
between the plate and the ground includes 3D effects
RatioCsarukaiVSstandard = Csarukai./Cplate_standard;
CFringeRatioStandard = (Csarukai-Cplate_standard)./Cplate_standard;
%% M.I.Elmasry: capacitance calculations in MOSFET VLSI (plate)----compare with Mode=2
% while ThickRatioHeight < 10
Celmasry(Index,1) = Cplate_standard.*(1+ 2./WidthRatioHeight.*log(1+ThickRatioHeight) + 2*ThickRatioHeight./WidthRatioHeight.*log(1+Width./(2*(Thick+Height))));
RatioCelmasryVSstandard(Index,1) = 1+ 2./WidthRatioHeight.*log(1+ThickRatioHeight) + 2*ThickRatioHeight./WidthRatioHeight.*log(1+Width./(2*(Thick+Height)));
% G.Shomalnasab equation
Cshomalnasab = Cplate_standard + 4*2*Eps/pi*log10(1+ThickRatioHeight)*(1+1/ThickRatioHeight+0.1*ThickRatioHeight);

%% One point source-Electric Field Map by Iteration Method
% Initialization;
NX = 301;
NY = 301;
V = zeros(NX,NY); % potential distribution matrix
E = zeros(NX,NY);
Q = zeros(NX,NY);
Vtop = 0; % Top Boundary Potential 0V
Vleft = 0;
Vright = 0;
Vbottom = 0;
V(1,:) = Vtop;
V(:,NX) = Vright;
V(:,1) = Vleft;
V(NY,:) = Vbottom;
% define the gap-nodes value (discontinuity there)
V(1,1) = 0.5*(V(1,2)+V(2,1));
V(1,NX) = 0.5*(V(1,NX-1)+V(2,NX));
V(NY,1) = 0.5*(V(NY-1,1)+V(NY,2));
V(NY,NX) = 0.5*(V(NY-1,NX)+V(NY,NX-1));
% create the square-nodes
SquareXMidPoint = NX/2;
SquareYMidPoint = NY/2;
% now 2D: only the Length and Height is considered
NumberIteration = 100;
for iteration = 1:NumberIteration
for i = 2:NX-1
for j = 2:NY-1

```

```

V(cell(SquareXMidPoint),cell(SquareYMidPoint)) = 3;
V(i,j) = (V(i-1,j)+V(i+1,j)+V(i,j-1)+V(i,j+1))/4;
end
end
% figure potential distribution
V = V';
dx = (1:NX)-SquareXMidPoint;
dy = (1:NY)-SquareYMidPoint;
% E-field
[Ex,Ey]=gradient(V);
Ex = -Ex;
Ey = -Ey;
E = sqrt(Ex.^2+Ey.^2);
%%%%%%%%%%%%%%%%%%%%%%%%%%%%%%%%%%%%%%%%%%%%%%%%%%%%%%%%%%%%%%%%%%%%%%%% 2D with two sources
% horizontal-parallel capacitor (top is Sensor; Bottom is Copper)
SensorLength = 21; % plate-length: cm
SensorWidth = 5; % plate width: cm
SensorThickness = 0.02;
HalfSensorLength = SensorLength/2;
Space = 1;
CopperWidth = 2*SensorWidth + Space;
CopperThickness = 0.5;
HalfCopperWidth = CopperWidth/2;
HalfSpace = Space/2;

Plate1RangeLeft = SquareXMidPoint - HalfCopperWidth;
Plate1RangeRight = SquareXMidPoint - HalfSpace;
Plate1RangeFront = SquareXMidPoint - HalfSensorLength;
Plate1RangeBack = SquareXMidPoint + HalfSensorLength;
Plate2RangeLeft = SquareXMidPoint + HalfSpace;
Plate2RangeRight = SquareXMidPoint + HalfCopperWidth;
Plate2RangeFront = SquareXMidPoint - HalfSensorLength;
Plate2RangeBack = SquareXMidPoint + HalfSensorLength;

% now 2D: only the Length and Height is considered
NumberIteration = 100;
for iteration = 1:NumberIteration
    for i = 2:NX-1
        for j = 2:NY-1
            V(Plate1RangeLeft:Plate1RangeRight,Plate1RangeFront:Plate1RangeBack) =
            V(Plate2RangeLeft:Plate2RangeRight,Plate2RangeFront:Plate2RangeBack) = 3;
            V(i,j) = (V(i-1,j)+V(i+1,j)+V(i,j-1)+V(i,j+1))/4;
        end
    end
end
%%%%%%%%%%%%%%%%%%%%%%%%%%%%%%%%%%%%%%%%%%%%%%%%%%%%%%%%%%%%%%%%%%%%%%%% 3D with two sources
Vtop = 0; % Top Boundary Potential 5V
Vleft = 0; % Left Boundary Potential 0V
Vright = 0; % Right Boundary Potential 0V
Vbottom = 0; % Bottom Boundary Potential 0V
Vfront = 0;
Vback = 0;
V(:,1,:) = Vtop;
V(NX, :, ) = Vright;
V(1, :, ) = Vleft;
V(:, :, NZ) = Vbottom;
V(:,1,:) = Vfront;
V(:,NY,:) = Vback;
% define the gap-nodes value (discontinuity there)
V(1,1,1) = (V(1,2,1)+V(2,1,1)+V(1,1,2))/3;
V(NX,1,1) = (V(NX-1,1,1)+V(NX,2,1)+V(NX,1,2))/3;
V(1,1,NZ) = (V(1,1,NZ-1)+V(1,2,NZ)+V(2,1,NZ))/3;
V(NX,1,NZ) = (V(NX-1,1,NZ)+V(NX,2,NZ)+V(NX,1,NZ-1))/3;
V(NX,NY,NZ) = (V(NX-1,NY,NZ)+V(NX,NY-1,NZ)+V(NX,NY,NZ-1))/3;
V(NX,NY,1) = (V(NX-1,NY,1)+V(NX,NY-1,1)+V(NX,NY,2))/3;
V(1,NY,1) = (V(2,NY,1)+V(1,NY-1,1)+V(1,NY,2))/3;
V(1,NY,NZ) = (V(2,NY,NZ)+V(1,NY-1,NZ)+V(1,NY,NZ-1))/3;
%% create the square-nodes
SquareXMidPoint = ceil(NX/2);
SquareYMidPoint = ceil(NY/2);
SquareZMidPoint = ceil(NZ/2);
SensorLength = 85;
SensorWidth = 110;
SensorThickness = 0.5;
HalfSensorLength = floor(SensorLength/2);
Height = 10;
Space = 25;
CopperLength = 2*SensorLength + Space; % X-Direction
CopperWidth = SensorWidth; % Y-Direction error previous: 2*sensorwidth
CopperThickness = 0.5;
HalfCopperLength = floor(CopperLength/2);
HalfSpace = floor(Space/2);
HalfHeight = floor(Height/2);

SensorZPosition = SquareZMidPoint + HalfHeight;
CopperZPosition = SquareZMidPoint - HalfHeight;
Plate1RangeLeft = SquareXMidPoint - HalfCopperLength;
Plate1RangeRight = SquareXMidPoint - HalfSpace;
Plate1RangeFront = SquareYMidPoint - HalfSensorLength;
Plate1RangeBack = SquareYMidPoint + HalfSensorLength;
Plate2RangeLeft = SquareXMidPoint + HalfSpace;
Plate2RangeRight = SquareXMidPoint + HalfCopperLength;
Plate2RangeFront = SquareYMidPoint - HalfSensorLength;
Plate2RangeBack = SquareYMidPoint + HalfSensorLength;

NumberIteration = 25;
InitialIteration = 0;
for iteration = 1:NumberIteration
    for k = 2:NZ-1
        for j = 2:NY-1
            for i = 2:NX-1
                V(SensorZPosition,Plate1RangeLeft:Plate1RangeRight,Plate1RangeFront:Plate1RangeBack) = -3;
                V(SensorZPosition,Plate2RangeLeft:Plate2RangeRight,Plate2RangeFront:Plate2RangeBack) = 3;
                V(CopperZPosition,Plate1RangeLeft:Plate2RangeRight,Plate1RangeFront:Plate1RangeBack) = 0;
                V(i,j,k) = (V(i-1,j,k)+V(i+1,j,k)+V(i,j-1,k)+V(i,j+1,k)+V(i,j,k-1)+V(i,j,k+1))/6;
            end
        end
    end
end

%% Extracting data and applying systematic correction factor
for FileNameIndex = 1:NumberOfRecords
    PossibleFileDateNum = datenum(PossibleFileNameList(FileNameIndex).date);
    if (PossibleFileDateNum >= StartDateNumber) && (PossibleFileDateNum <= StopDateNumber)
        LoadFileName = PossibleFileNameList(FileNameIndex).name;
        if exist(LoadFileName,'file')
            load(LoadFileName);
            if FirstFileFound == 0
                FirstFileFound = 1;
            end
        end
    end
end

```

```

TXTimeIndex = (0:(InputSamplesPerChannel-1))/OutputSamplingRate;
RXTimeIndex = (0:(InputSamplesPerChannel-1))/OutputSamplingRate;
DisplayFrequencyIndex = (0:(InputSamplesPerChannel-1))*OutputSamplingRate/InputSamplesPerChannel;
SteppedFrequencies = CWStartFrequency + (0:(CWNumberOfSteps-1))*CWStepFrequency;
Amplifier_A_Model = polyval(Amplifier_A_Coefficients,SteppedFrequencies);
Amplifier_B_Model = polyval(Amplifier_B_Coefficients,SteppedFrequencies);
FrequencySelectionIndices = zeros(1,CWNumberOfSteps);
for TXIndex = 1:length(SteppedFrequencies)
    [~, FrequencySelectionIndices(TXIndex)] = min(abs(DisplayFrequencyIndex - SteppedFrequencies(TXIndex)));
end
fprintf('%s\n%s\n%s\n',Comment1,Comment2,Comment3);
end

RecoveredDataFFT = fft(RecoveredData(:,AdditionalSamplesRequired:end),InputSamplesPerChannel,2)./InputSamplesPerChannel;
Amplifier_A_Corrected_Output = RecoveredDataFFT(2,FrequencySelectionIndices) ./ Amplifier_A_Model;
Amplifier_B_Corrected_Output = RecoveredDataFFT(3,FrequencySelectionIndices) ./ Amplifier_B_Model;
DifferentialOutput = Amplifier_A_Corrected_Output - Amplifier_B_Corrected_Output;
Impedance(FileNameIndex,:) = Rs .* DifferentialOutput ./ RecoveredDataFFT(1,FrequencySelectionIndices);
else
fprintf('File does not exist %s \n',LoadFileName)
return
end
end
end

%% Poly-fit
CoefficientsGood = polyfit(imag(Impedance(:,1))/1000,real(Impedance(:,1))/1000,1);
Curve1 = polyval(CoefficientsGood,imag(Impedance(:,1))/1000);
CoefficientsPoor = polyfit(imag(Impedance(1:138,1))/1000,real(Impedance(1:138,1))/1000,1);
Curve1 = polyval(CoefficientsPoor,imag(Impedance(1:138,1))/1000);
CoefficientsPoor2 = polyfit(imag(Impedance(139:end,1))/1000,real(Impedance(139:end,1))/1000,1);
Curve2 = polyval(CoefficientsPoor2,imag(Impedance(139:end,1))/1000);

%% Debye model to interpret relaxation time on each investigation location
Parameters = zeros(size(Resistivity),1,3);
for index = 1:size(Resistivity,1)
    DCRol = Resistivity(index,FreqIndex)*5; % very low frequency: EDL double layer polarization 5 or 6 times than high frequency
    HighFreqRol = Resistivity(index,FreqIndex)/1.2;
    EvaluatedRelaxationTime = abs(Reactance(index,FreqIndex)...
        ./((Resistivity(index,FreqIndex)-HighFreqRol).*OmegaFrequencies(FreqIndex)));
    RelaxationTimeCole = EvaluatedRelaxationTime;

    initialDebyeParameters = [DCRol HighFreqRol RelaxationTimeCole];
    options = optimset('fminsearch');
    options.TolX = 1e+2;
    options.TolFun = 1e+2;
    options.Display = 'off';
    [DebyeParameters,fval,exitflag,output]
    fminsearch(@CCMFitting11thOct2018SinglePoint,initialDebyeParameters,options,jOmegaFrequencies,SignalImpedance(index,FreqIndex),FreqIndex);

    Parameters(index,:)=DebyeParameters;
end
DebyeParameters = Parameters;

function fCCM = CCMFitting11thOct2018SinglePoint(initialDebyeParameters,jOmegaFrequencies,MeasuredImpedance,FreqIndex)
Chargeability = (initialDebyeParameters(1)-initialDebyeParameters(2))./initialDebyeParameters(1);
DebyeImpedanceFit = initialDebyeParameters(1).*(1-Chargeability).*(1-1./(1+jOmegaFrequencies(FreqIndex)*initialDebyeParameters(3)));
fCCM = sqrt(sum((real(MeasuredImpedance)-real(DebyeImpedanceFit)).^2+(imag(MeasuredImpedance)-imag(DebyeImpedanceFit)).^2));
end

%% WhiteBoard LFM resistor AnalysisFitting using 26 resistors
%%After RC Network_AnalysisCodes to do fitting on data of 4-copper plates
% for R >= 46k
addpath IndividualAmp_Data
load('IndividualAmplifierModels.mat');
Rs = 5e3;
FrequencyStep = 100; % 100
load('WhiteBoard_5kSense_4ohm_3_chans_LFM.mat')
MemberNames = fieldnames(AllRecoveredData);
ValidIndex = find(contains(MemberNames,'RecoveredData'));
DisplayFrequencies = InputSamplingRate.*(0:(InputSamplesPerChannel-1))./InputSamplesPerChannel;
Amplifier_A_Model = polyval(Amplifier_A_Coefficients,DisplayFrequencies);
Amplifier_B_Model = polyval(Amplifier_B_Coefficients,DisplayFrequencies);
StopFrequency = StartFrequency + Bandwidth;
MaxStartFrequency = 4000; % 2000
MinStopFrequency = 20000; % 20000
[~,MinFrequencyIndex] = min(abs(DisplayFrequencies - MaxStartFrequency));
[~,MaxFrequencyIndex] = min(abs(DisplayFrequencies - MinStopFrequency));
WhiteBoardAverageImpedance = 0;
SelectedFrequencyIndex = MinFrequencyIndex:FrequencyStep:MaxFrequencyIndex;
for ResultsIndex = 1:length(ValidIndex)
    SelectedString = [MemberNames{ValidIndex(ResultsIndex)}];
    SelectedIndex = str2double(SelectedString(14:end));
    RecoveredData = getfield(AllRecoveredData,SelectedString);
    RecoveredDataFFT = fft(RecoveredData(:,AdditionalSamplesRequired:AdditionalSamplesRequired+1+2^16),InputSamplesPerChannel,2);
    Amplifier_A_Corrected_Output = RecoveredDataFFT(2,:) ./ Amplifier_A_Model; % A: purple
    Amplifier_B_Corrected_Output = RecoveredDataFFT(3,:) ./ Amplifier_B_Model; % B: grey
    DifferentialOutput = Amplifier_A_Corrected_Output - Amplifier_B_Corrected_Output; % potential
    Impedance = Rs .* DifferentialOutput ./ RecoveredDataFFT(1,:);
    WhiteBoardAverageImpedance = WhiteBoardAverageImpedance + Impedance;
end
WhiteBoardAverageImpedance = WhiteBoardAverageImpedance ./ length(ValidIndex);
%% for data using yellow sheet + four small size plates + white board (T = 0.00273)
disp('-----WhiteBoard--Model using RCNetwork-----')
disp('-----Also fit Camp-----')
SelectedFrequency = DisplayFrequencies(SelectedFrequencyIndex);
InitialParameter = [0.2,9,12]; % R,Cwires,Camp
Cinput = 4e-12;
jOmega = 1i*2*pi*SelectedFrequency;
Rinput = 1e6;
Zs = 1./(1/Rs + 1/Rinput + jOmega*Cinput);
Zshalf = 1./(2/Rs + 2/Rinput + jOmega*2*Cinput);
Ichan0 = RecoveredDataFFT(1,SelectedFrequencyIndex)./Zs;
options = optimset('fminsearch');
options.TolX = 1e-2;
options.TolFun = 1e-2;
options.Display = 'off'; %display--iter; undisplay--off
i = 0;
[WhiteBoardModelParameters,fval,exitflag,output]
fminsearch(@RC_WhiteBoardFitting,InitialParameter,options,WhiteBoardAverageImpedance(SelectedFrequencyIndex),SelectedFrequency,Ichan0);
fprintf('Resistor (kOhm)\t\tWire-Cap(pF)\t Camp(pF)\tIval\n');
% while fval>1e6
while i <= 30
    i = i+1;
while WhiteBoardModelParameters(1) < 0 || WhiteBoardModelParameters(2) < 0 || WhiteBoardModelParameters(3) < 0
InitialParameter = [(1-0.1)*rand(1)+0.1 (20-8)*rand(1)+8 (18-10)*rand(1)+10];
[WhiteBoardModelParameters,fval,exitflag,output]
fminsearch(@RC_WhiteBoardFitting,InitialParameter,options,WhiteBoardAverageImpedance(SelectedFrequencyIndex),SelectedFrequency,Ichan0);

```



```

end
Parameter(i,:) = WhiteBoardModelParameters;
fvalResults(i) = fval;
fprintf('%e\t',WhiteBoardModelParameters);
fprintf('\tse', fval);
fprintf('\n');
Res = Parameter(i,1)*1e3;
Cap = Parameter(i,2)*1e-12;
Camp = Parameter(i,3)*1e-12;
Vg_network = RC_WhiteBoard(SelectedFrequency,Ichan0,Res,Cap,Camp);
Zpredict = 2*Vg_network./Ichan0*(Rs/2)./Zshalf;

Figure51Handle = figure(51);
set(Figure51Handle,'Color','w')
plot(real(Zpredict),imag(Zpredict),'k.','MarkerSize',9)
hold on
plot(real(WhiteBoardAverageImpedance(SelectedFrequencyIndex)),imag(WhiteBoardAverageImpedance(SelectedFrequencyIndex)),'r.','MarkerSize',9);
hold off
title('Impedance (WhiteBoard 47)')
xlabel('Resistance (Ohms)')
ylabel('Reactance (Ohms)')
legend('Predicted','Measured')
axis('equal')
drawnow

InitialParameter = [(1-0.1)*rand(1)+0.1 (20-8)*rand(1)+8 (18-10)*rand(1)+10];
[WhiteBoardModelParameters,fval,exitflag,output]
fminsearch(@RC_WhiteBoardFitting,InitialParameter,options,WhiteBoardAverageImpedance(SelectedFrequencyIndex),SelectedFrequency,Ichan0);
end
fprintf('the loop is end\n');
[~,MinIndex] = min(fvalResults);
ResOfMin = Parameter(MinIndex,1)*1e3
CapOfMin = Parameter(MinIndex,2)*1e-12
Vg_networkMin = RC_WhiteBoard(SelectedFrequency,Ichan0,ResOfMin,CapOfMin,Camp);
ZpredictMin = 2*Vg_networkMin./Ichan0*(Rs/2)./Zshalf;

Figure51Handle = figure(51);
set(Figure51Handle,'Color','w')
plot(real(ZpredictMin),imag(ZpredictMin),'k.','MarkerSize',9)
hold on
plot(real(WhiteBoardAverageImpedance(SelectedFrequencyIndex)),imag(WhiteBoardAverageImpedance(SelectedFrequencyIndex)),'r.','MarkerSize',9);
hold off
title('Impedance (WhiteBoard 47-Ohm)')
xlabel('Resistance (Ohms)')
ylabel('Reactance (Ohms)')
legend('Predicted','Measured')
axis('equal')
drawnow
##### fitting-fuctin: put Camp into fitting
function RCAnalysisFittingOutput = RC_WhiteBoardFitting(InitialParameter,MeasuredValue,SelectedFrequency,Ichan0)
if (InitialParameter(1)<0 || InitialParameter(2)<0 || InitialParameter(3)<0)
RCAnalysisFittingOutput = 1e+18;
return;
end
Res = InitialParameter(1)*1e3;
Cap = InitialParameter(2)*1e-12;
Camp = InitialParameter(3)*1e-12;
Rs = 5e3;
Cinput = 4e-12;
jOmega = 1i*2*pi*SelectedFrequency;
Rinput = 1e6;
Zs = 1./(2/Rs + 2/Rinput + jOmega*2*Cinput);
Vg_network = RC_WhiteBoard(SelectedFrequency,Ichan0,Res,Cap,Camp);
Zpredict = 2*Vg_network./Ichan0*(Rs/2)./Zs;
RCAnalysisFittingOutput = sum(abs(Zpredict - MeasuredValue)).^2;
##### Resistor-capacitor network
function RC_CoupleOutput = RC_WhiteBoard(SelectedFrequency,Ichan0,Res,Cap,Camp)
r = 6.2e-5;
Ctx = 1.68e-12;
RC_CoupleOutput = zeros(1,length(SelectedFrequency));
Eps = 2.283;
Ep0 = 8.854e-12;
Lc1 = 0.09;
Wc1 = 0.125;
Lgap_cp = 0.045;
Lgap_pp = 0.015;
FEMstep = 0.001;
T = 0.00273;
for index = 1:length(SelectedFrequency)
freq = SelectedFrequency(index);
Omega = 2*pi*freq;
Zresistor = 1/(1/Res + 1i.*Omega*Cap); % for extra resistor 100,200,500,1k,5k...used as verify
ResistorExtraCP = Zresistor; % should consider the r-white board
ResistorExtraPP = Zresistor/2;
g = 1i.*Omega*(Eps*Ep0*Wc1/T);
Delta_Z = r*FEMstep;
Delta_g = g*FEMstep;
Delta_Zc = 1./Delta_g;
Nc1 = Lc1/FEMstep;
Ngap_cp = Lgap_cp/FEMstep;
Ngap_pp = Lgap_pp/FEMstep;
Zgap_cp = ResistorExtraCP;
%Zgap_pp = Delta_Z*Ngap_pp;
Zgap_pp = ResistorExtraPP;
Isource = Ichan0(index);
Rg = 100e6;
Zamp = 1./(1/Rg + 1i.*Omega*Camp);
Ztx = 1./(1i.*Omega*Ctx);
%disp('-----network Current distribution-----');
%disp('network-characteristic polynomial solution');
MatrixParameter1 = 2*Delta_Zc + Delta_Z;
MatrixParameter2 = -Delta_Zc;
MatrixParameter3 = Delta_Zc + Zgap_pp + Zamp;
MatrixParameter4 = 2*Delta_Zc + Zgap_cp + Ztx;
MatrixLHS = zeros(2*Nc1+2,2*Nc1+2);
MatrixRHS = zeros(2*Nc1+2,1);
MatrixRHS(Nc1+1) = Isource*Ztx;
MatrixRHS(end) = Isource*Zamp;
MatrixLHS(1,1) = MatrixParameter1;
MatrixLHS(1,2) = MatrixParameter2;
for Index = 2:size(MatrixLHS,1)-1
MatrixLHS(Index,Index-1) = MatrixParameter2;
MatrixLHS(Index,Index) = MatrixParameter1;
MatrixLHS(Index,Index+1) = MatrixParameter2;
end
MatrixLHS(Nc1+1,Nc1) = MatrixParameter2;
MatrixLHS(Nc1+1,Nc1+1) = MatrixParameter4;
MatrixLHS(Nc1+1,Nc1+2) = MatrixParameter2;
MatrixLHS(end,end-1) = MatrixParameter2;
MatrixLHS(end,end) = MatrixParameter3;
CurrentMatrixC1 = MatrixLHS\MatrixRHS;
% eigMatrixC1 is current distribution

```

```

%% so we could have Icp, Ipp
Icp = CurrentMatrixC1(Nc1+1);
Ipp = CurrentMatrixC1(end);
Ig_amp = Isource - Ipp;
%disp('-----network Voltage distribution-----');
% VoltageGapPP = Ipp*(0:Ngap_pp)*Delta_Z;
VoltageGapPP = Ipp*(0:Ngap_pp)*ResistorExtraPP/Ngap_pp;
VoltageGapPP = VoltageGapPP.';
VoltageP = zeros(Nc1+1,1);
VoltageP(end) = VoltageGapPP(end);
for Index = Nc1+1:-1:2
VoltageP(Index-1) = VoltageP(Index) + CurrentMatrixC1(Nc1+Index)*Delta_Z;
end
VoltageGapCP = VoltageP(1)+Icp*(1:Ngap_cp)*ResistorExtraCP/Ngap_cp;
VoltageGapCP = VoltageGapCP.';
VoltageC = zeros(Nc1+1,1);
VoltageC(end) = VoltageGapCP(end);
for Index = Nc1+1:-1:2
VoltageC(Index-1) = VoltageC(Index) + CurrentMatrixC1(Index-1)*Delta_Z;
end
RC_CoupleOutput(index) = Ig_amp*Zamp;
end
end

%% for C1 plate
%%%%%%%%%%%%%%%%%%%%%%%%%%%%%%%%%%%%%%%%%%%%%%%%%%%%%%%%%%%%%%%%%%%%%%%% using equations
Xrange = 0:FEMstep:Lcl;
Xrange_GapCP = 0:FEMstep:Lcl+Lgap_cp-FEMstep;
Xrange_GapCP_GapPP = 0:FEMstep:2*Lcl+Lgap_cp+Lgap_pp-FEMstep;
% Vc2_coefficient = (VoltageC1(end)-VoltageC1(1)*exp(-Beta*Lcl))/(2*sinh(Beta*Lcl));
% Vc1_coefficient = VoltageC1(1)-Vc2_coefficient - VoltageC1(1);
% Vc_equation = Vc1_coefficient.*exp(-Beta.*Xrange) + Vc2_coefficient.*exp(Beta.*Xrange)+VoltageC1(1);
Vc2_coefficient = (VoltageC1(end)-VoltageC1(1)*exp(-Beta*Lcl)-Vtotal*(1-exp(-Beta*Lcl)))/(2*sinh(Beta*Lcl));
Vc1_coefficient = VoltageC1(1)-Vc2_coefficient - Vtotal;
Vc_equation = Vc1_coefficient.*exp(-Beta.*Xrange) + Vc2_coefficient.*exp(Beta.*Xrange)+Vtotal;
Ic_equation = CurrentMatrixC1(end).*sinh(Beta.*Xrange)./sinh(Beta*Lcl);

%%%%%%%%%%%%%%%%%%%%%%%%%%%%%%%%%%%%%%%%%%%%%%%%%%%%%%%%%%%%%%%%%%%%%%%% Resistor-capacitor using equations
Vequation_GapCP = VoltageC1(end) - Isource*Delta_Z*(1:Ngap_cp);
Vequation_C_CP = [Vc_equation(1:end-1),Vequation_GapCP];
Iequation_C_CP = [Ic_equation(1:end-1),Isource(end)*ones(1,Ngap_cp)];
Ig = Isource-Ipp;
Vg = Ig*Rg;
V2 = (Voltage(245)-Vequation_C_CP(end).*exp(-Beta*Lcl)-Vg*(1-exp(-Beta*Lcl)))/(2*sinh(Beta*Lcl));
V1 = Vequation_C_CP(end) - Vg - V2;
i2 = (Ipp-Isource.*exp(-Beta*Lcl))/(2*sinh(Beta*Lcl));
i1 = Isource-i2;
x_P1 = 0:FEMstep:(Lcl-FEMstep);
Vp = V1.*exp(-Beta.*x_P1) + V2.*exp(Beta.*x_P1) + Vg;
Ip = i1.*exp(-Beta.*x_P1) + i2.*exp(Beta.*x_P1);
%% for gap_cp
Vequation_GapPP = Vp(end) - Ipp*Delta_Z*(1:Ngap_pp);
Vequation_GapCP_GapPP = [Vequation_C_CP,Vp,Vequation_GapPP];
Iequation_GapCP_GapPP = [Iequation_C_CP,Ip,Iequation_C_CP(end)*ones(1,Ngap_pp)];

%%%%%%%%%%%%%%%%%%%%%%%%%%%%%%%%%%%%%%%%%%%%%%%%%%%%%%%%%%%%%%%%%%%%%%%% considering copper resistance as the function of the frequency
function CopperResistance = AlumShieldResOffFreq(SelectedFrequency)
% AlumResistance = AlumResistance*1e5; % this is because the fitting codes: there is 1e-5
VacuumPermeability = 4*pi*1e-7; % H/m
ResistivityCopper = 1.68e-8; % ohm.m
freq = SelectedFrequency; % kHz
Omega = 2*pi*freq;
SkinDepth = sqrt(2*ResistivityCopper./(Omega*VacuumPermeability));
Lhalf = 0.5/2;
Whalf = 0.2/2; %copper sheet: 2*Lhalf 2*Whalf
a = 2*Lhalf/sqrt(pi);
b = 2*Whalf/sqrt(pi);
h = sqrt(a^2-b^2);
hTOa = h/a; %K(h/a)
K = ellipke(hTOa);
alpha = 2;
beta = 5;
gamma = 10;
f0 = pi^2.*ResistivityCopper./(4*VacuumPermeability*Whalf^2.*(ellipke(sqrt(1-(Whalf/Lhalf)^2))).^2);
f1 = pi*ResistivityCopper./(8*VacuumPermeability*Whalf*Lhalf);
FBF = (1+(freq./f1).^alpha+(freq./f0).^beta).^1/gamma;
Rdc = K./(pi*a).*sqrt(VacuumPermeability*f0*ResistivityCopper/pi);

Rac = Rdc.*FBF;
CopperResistance = ResistivityCopper./(pi^2*SkinDepth*a)*K.*(1-exp(-2*Whalf./SkinDepth));
semilogx(freq,CopperResistance)
end

%%%%%%%%%%%%%%%%%%%%%%%%%%%%%%%%%%%%%%%%%%%%%%%%%%%%%%%%%%%%%%%%%%%%%%%% After RC_Network_AnalysisCodes to do FreeSpace, CopperSheet, BlackFoam
% and FieldSurvey fitting again
addpath IndividualAmp Data
load('IndividualAmplifierModels.mat');
Rs = 5e3;
%% Free Space (Reference resistor 5K using CW or LFM signal)
% copper sheet
Choice = 0;
FrequencyStep = 100;
while Choice<=2
Choice = input('Choice:\n');
switch Choice
case 1
load('Free_Space_5kSenseRes_3_chans_LFM.mat')
MemberNames = fieldnames(AllRecoveredData);
ValidIndex = find(contains(MemberNames,'RecoveredData'));
DisplayFrequencies = InputSamplingRate.*(0:(InputSamplesPerChannel-1))./InputSamplesPerChannel;
Amplifier_A_Model = polyval(Amplifier_A_Coefficients,DisplayFrequencies);
Amplifier_B_Model = polyval(Amplifier_B_Coefficients,DisplayFrequencies);
StopFrequency = StartFrequency + Bandwidth;
MaxStartFrequency = 4000;
MinStopFrequency = 20000;
[~,MinFrequencyIndex] = min(abs(DisplayFrequencies - MaxStartFrequency));
[~,MaxFrequencyIndex] = min(abs(DisplayFrequencies - MinStopFrequency));
FreeSpaceAverageImpedance = 0;
SelectedFrequencyIndex = MinFrequencyIndex:FrequencyStep:MaxFrequencyIndex;
for ResultsIndex = 1:length(ValidIndex)
SelectedString = {MemberNames{ValidIndex(ResultsIndex)}};
SelectedIndex = str2double(SelectedString(14:end));
RecoveredData = getfield(AllRecoveredData,SelectedString);
RecoveredDataFFT_FS = fft(RecoveredData(:,AdditionalSamplesRequired:AdditionalSamplesRequired-1+2^16),InputSamplesPerChannel,2);
Amplifier_A_Corrected_Output = RecoveredDataFFT_FS(2,:) ./ Amplifier_A_Model;
Amplifier_B_Corrected_Output = RecoveredDataFFT_FS(3,:) ./ Amplifier_B_Model;
DifferentialOutput = Amplifier_A_Corrected_Output - Amplifier_B_Corrected_Output;

```

```

Impedance = Rs .* DifferentialOutput ./ RecoveredDataFFT_FS(1,:);
FreeSpaceAverageImpedance = FreeSpaceAverageImpedance + Impedance;
End
FreeSpaceAverageImpedance = FreeSpaceAverageImpedance ./ length(ValidIndex);
case 2
load('Copper_Sheet_5kSenseRes_3_chans_LFM.mat')
DisplayFrequencies = InputSamplingRate .* (0:(InputSamplesPerChannel-1))./InputSamplesPerChannel;
Amplifier_A_Model = polyval(Amplifier_A_Coefficients,DisplayFrequencies);
Amplifier_B_Model = polyval(Amplifier_B_Coefficients,DisplayFrequencies);
StopFrequency = StartFrequency + Bandwidth;
MinStopFrequency = min(StopFrequency);
MaxStartFrequency = 2000;
[~,MinFrequencyIndex]= min(abs(DisplayFrequencies - MaxStartFrequency));
[~,MaxFrequencyIndex]= min(abs(DisplayFrequencies - MinStopFrequency));
MemberNames = fieldnames(AllRecoveredData);
ValidIndex = find(contains(MemberNames,'RecoveredData'));
CopperSheetAverageImpedance = 0;
SelectedFrequencyIndex = MinFrequencyIndex: FrequencyStep :MaxFrequencyIndex;
for ResultsIndex = 1:length(ValidIndex)
SelectedString = [MemberNames(ValidIndex(ResultsIndex))];
SelectedIndex = str2double(SelectedString(14:end));
RecoveredData = getfield(AllRecoveredData,SelectedString);
RecoveredDataFFT_CS = fft(RecoveredData(:,AdditionalSamplesRequired:AdditionalSamplesRequired+1+2^16),InputSamplesPerChannel,2);
Amplifier_A_Corrected_Output = RecoveredDataFFT_CS(2,:) ./ Amplifier_A_Model;
Amplifier_B_Corrected_Output = RecoveredDataFFT_CS(3,:) ./ Amplifier_B_Model;
DifferentialOutput = Amplifier_A_Corrected_Output - Amplifier_B_Corrected_Output;
Impedance = Rs .* DifferentialOutput ./ RecoveredDataFFT_CS(1,:);
CopperSheetAverageImpedance = CopperSheetAverageImpedance + Impedance;
end
CopperSheetAverageImpedance = CopperSheetAverageImpedance ./ length(ValidIndex);
AverageImpedanceTotal = [CopperSheetAverageImpedance(SelectedFrequencyIndex),FreeSpaceAverageImpedance(SelectedFrequencyIndex)];

disp('-----FreeSpaceModel using RCNetwork-----')
SelectedFrequency = DisplayFrequencies(SelectedFrequencyIndex);
InitialParameter = [0.1,1.68,10];
% 1st: rAir in unit of 1M OHM
% 2nd: Ctx in unit of pF fixed as 1.5pF according to COMSOL prediction
% 3rd: Camp in unit of pF
Cinput = 4e-12;
jOmega = 1i*2*pi*SelectedFrequency;
Rinput = 1e6;
Zs = 1./(1/Rs + 1/Rinput + jOmega*Cinput);
Zshalf = 1./(2/Rs + 2/Rinput + jOmega*2*Cinput);
Ichan0_FS = RecoveredDataFFT_CS(1,SelectedFrequencyIndex) ./Zs;
options = optimset('fminsearch');
options.TolX = 2e-1;
options.TolFun = 1e-1;
options.Display = 'off'; %display--iter; undisplay--off
i = 0;
[FreeSpaceModelParameters,fval,exitflag,output]
fminsearch(@RC_CoupleInsideFSFitting,InitialParameter,options,FreeSpaceAverageImpedance(SelectedFrequencyIndex),SelectedFrequency,Ichan0_FS);
fprintf('rAir(0.1Mhm.meter)\t\t\tCtx(pF)\t\t\tCamp(pF)\n');
% while fval>1e9
while i<=10
i = i+1;
while FreeSpaceModelParameters(1) < 0 || FreeSpaceModelParameters(2) < 0 || FreeSpaceModelParameters(3) < 0
InitialParameter = [(0.3-0.1)*rand(1)+0.1 (20-0.01)*rand(1)+0.01 (20-3)*rand(1)+3];
[FreeSpaceModelParameters,fval,exitflag,output]
fminsearch(@RC_CoupleInsideFSFitting,InitialParameter,options,FreeSpaceAverageImpedance(SelectedFrequencyIndex),SelectedFrequency,Ichan0_FS);
end
Parameter(i,:) = FreeSpaceModelParameters;
fvalResults(i) = fval;
fprintf('%e\t\t\t\t\t',FreeSpaceModelParameters);
fprintf('\n');
rAir = Parameter(i,1)*1e5;
Ctx = Parameter(i,2)*1e-12;
Camp = Parameter(i,3)*1e-12;
Vg_network = RC_CoupleInsideFS(SelectedFrequency,Ichan0_FS,rAir,Ctx,Camp);
Zpredict = 2*Vg_network./Ichan0_FS*(Rs/2) ./Zshalf;
InitialParameter = [(0.3-0.1)*rand(1)+0.1 (20-0.01)*rand(1)+0.01 (15-10)*rand(1)+10];
[FreeSpaceModelParameters,fval,exitflag,output]
fminsearch(@RC_CoupleInsideFSFitting,InitialParameter,options,FreeSpaceAverageImpedance(SelectedFrequencyIndex),SelectedFrequency,Ichan0_FS);
end
return

function RCAnalysisFittingOutput = RC_CoupleInsideFSFitting(InitialParameter,MeasuredValue,SelectedFrequency,Ichan0)
% InitialParameter = rAir,Ctx,Camp
if (InitialParameter(1)<0 || InitialParameter(2)<0 || InitialParameter(3)<0)
RCAnalysisFittingOutput = 1e+18;
return;
end
r = InitialParameter(1)*1e5;
Ctx = InitialParameter(2)*1e-12;
Camp = InitialParameter(3)*1e-12;
Rs = 5e3;
Cinput = 4e-12;
jOmega = 1i*2*pi*SelectedFrequency;
Rinput = 1e6;
Zs = 1./(2/Rs + 2/Rinput + jOmega*2*Cinput);
Vg_network = RC_CoupleInsideFS(SelectedFrequency,Ichan0,r,Ctx,Camp);
Zpredict = 2*Vg_network./Ichan0*(Rs/2) ./Zs;
RCAnalysisFittingOutput = sum(abs(Zpredict - MeasuredValue)).^2;
%% for copper sheet data (similar as the freespace but with different initial parameters)
disp('-----CS--Model using RCNetwork-----')
InitialParameter = [(7-1)*rand(1)+1,0.68,(20-3)*rand(1)+3];

##### rough capacitance analysis : using profile data on 20170810 (good quality and bad quality) to do
addpath RoughnessProfileData scripts
ThickOfDielectric = 2.73; %mm
LoopFlag = 1;
LaserStep = 0.125; %mm
while LoopFlag <=2
Choice = input('type in quality type: 1-good quality 2-bad quality\n');
switch Choice
case 1
load('GK_20170810_113220.mat');
GoodQualityRawData = RawData;
DistanceIndexGQ = DistanceIndex; % mm
clear RawData DistanceIndex;
case 2
load('GK_20170810_122621.mat');
BadQualityRawData1 = RawData;
DistanceIndexBQ1 = DistanceIndex;
clear RawData DistanceIndex;
load('GK_20170810_125349.mat');
BadQualityRawData2 = RawData;
DistanceIndexBQ2 = DistanceIndex; % mm
DistanceIndexBQ2 = DistanceIndexBQ2 + DistanceIndexBQ1(end);
clear RawData DistanceIndex;

```

```

end
LoopFlag = LoopFlag + 1;
end
BadQualityRawData = [BadQualityRawData1;BadQualityRawData2];
DistanceIndexBQ = [DistanceIndexBQ1 DistanceIndexBQ2]; % mm
LengthGQ = length(GoodQualityRawData);
LengthBQ = length(BadQualityRawData);
IndexGQ = 1:LengthGQ;
IndexBQ = 1:LengthBQ;
% to see NAN data points
[QnanRow,QnanCol] = find(isnan(GoodQualityRawData));
[BQnanRow,BQnanCol] = find(isnan(BadQualityRawData));
if isempty(QnanRow)==0
    fprintf('NaN data in GoodQualityGroup!\n');
elseif isempty(BQnanRow)==0
    fprintf('NaN data in BadQualityGroup!\n');
end
BadQualityRawData(BQnanRow(1)) = 25.58;
BadQualityRawData(BQnanRow(2)) = 25.06;
%% Now using raw data to minus M-line to have standard data group
% Roughness basic amplitude parameters
% mean line;
GoodQualityMeanLine = sum(GoodQualityRawData)/LengthGQ;
fprintf('GQ M-line in %f\n',GoodQualityMeanLine);
BadQualityMeanLine = sum(BadQualityRawData)/LengthBQ;
fprintf('BQ M-line in %f\n',BadQualityMeanLine);
% mean line
disp('-----mean line using Arithmetic Average-----')
GQdataMinimumLine = GoodQualityRawData - GoodQualityMeanLine;
BQdataMinimumLine = BadQualityRawData - BadQualityMeanLine;
Ra_GQ = sum(abs(GQdataMinimumLine))/LengthGQ;
Ra_BQ = sum(abs(BQdataMinimumLine))/LengthBQ;
fprintf('Arithmetic mean profile: Ra_GQ=%f(mm)\tRa_BQ=%f(mm)\n',Ra_GQ,Ra_BQ)
%% to achieve some important parameters
% Ten-Point Height (Rz), Maximum height of Peaks and Maximum Depth of Valleys
FifthLegnthPointNum_GQ = LengthGQ/5;
FifthLegnthPointNum_BQ = LengthBQ/5;
MaxFivePeaks_GQ = [max(GQdataMinimumLine((1:FifthLegnthPointNum_GQ),1)),max(GQdataMinimumLine(FifthLegnthPointNum_GQ+1:2*FifthLegnthPointNum_GQ)),...
max(GQdataMinimumLine(2*FifthLegnthPointNum_GQ+1:3*FifthLegnthPointNum_GQ)),...
max(GQdataMinimumLine(3*FifthLegnthPointNum_GQ+1:4*FifthLegnthPointNum_GQ)),...
max(GQdataMinimumLine(4*FifthLegnthPointNum_GQ+1:5*FifthLegnthPointNum_GQ))];
MaxFivePeaks_BQ = [max(BQdataMinimumLine((1:FifthLegnthPointNum_BQ),1)),max(BQdataMinimumLine(FifthLegnthPointNum_BQ+1:2*FifthLegnthPointNum_BQ)),...
max(BQdataMinimumLine(2*FifthLegnthPointNum_BQ+1:3*FifthLegnthPointNum_BQ)),...
max(BQdataMinimumLine(3*FifthLegnthPointNum_BQ+1:4*FifthLegnthPointNum_BQ)),...
max(BQdataMinimumLine(4*FifthLegnthPointNum_BQ+1:5*FifthLegnthPointNum_BQ))];
MaxFiveDepth_GQ = [min(GQdataMinimumLine((1:FifthLegnthPointNum_GQ),1)),min(GQdataMinimumLine(FifthLegnthPointNum_GQ+1:2*FifthLegnthPointNum_GQ)),...
min(GQdataMinimumLine(2*FifthLegnthPointNum_GQ+1:3*FifthLegnthPointNum_GQ)),...
min(GQdataMinimumLine(3*FifthLegnthPointNum_GQ+1:4*FifthLegnthPointNum_GQ)),...
min(GQdataMinimumLine(4*FifthLegnthPointNum_GQ+1:5*FifthLegnthPointNum_GQ))];
MaxFiveDepth_BQ = [min(BQdataMinimumLine((1:FifthLegnthPointNum_BQ),1)),min(BQdataMinimumLine(FifthLegnthPointNum_BQ+1:2*FifthLegnthPointNum_BQ)),...
min(BQdataMinimumLine(2*FifthLegnthPointNum_BQ+1:3*FifthLegnthPointNum_BQ)),...
min(BQdataMinimumLine(3*FifthLegnthPointNum_BQ+1:4*FifthLegnthPointNum_BQ)),...
min(BQdataMinimumLine(4*FifthLegnthPointNum_BQ+1:5*FifthLegnthPointNum_BQ))];
for index = 1:5
MaxFivePeaks_GQ_Index = find(GQdataMinimumLine((index-1)*FifthLegnthPointNum_GQ+1:index*FifthLegnthPointNum_GQ)==MaxFivePeaks_GQ(index));
MaxFivePeaks_BQ_Index = find(BQdataMinimumLine((index-1)*FifthLegnthPointNum_BQ+1:index*FifthLegnthPointNum_BQ)==MaxFivePeaks_BQ(index));
MaxFiveDepth_GQ_Index = find(GQdataMinimumLine((index-1)*FifthLegnthPointNum_GQ+1:index*FifthLegnthPointNum_GQ)==MaxFiveDepth_GQ(index));
MaxFiveDepth_BQ_Index = find(BQdataMinimumLine((index-1)*FifthLegnthPointNum_BQ+1:index*FifthLegnthPointNum_BQ)==MaxFiveDepth_BQ(index));
end
Rz_GQ = (sum(MaxFivePeaks_GQ) - sum(MaxFiveDepth_GQ))/5; % international ISO standard
Rz_BQ = (sum(MaxFivePeaks_BQ) - sum(MaxFiveDepth_BQ))/5; % international ISO standard
%% to achieve Rp and Rv, Rmax, Rtl: maximum peak to valley in local
disp('-----Rp Rv Rmax Rtl-----')
Rp_GQ = max(MaxFivePeaks_GQ);
Rp_BQ = max(MaxFivePeaks_BQ);
Rv_GQ = max(MaxFiveDepth_GQ);
Rv_BQ = max(MaxFiveDepth_BQ);
clear Rz_GQ Rz_BQ Rp_GQ Rv_GQ Rp_BQ Rv_BQ index QnanCol QnanRow BQnanCol BQnanRow
%% to acheive RMS = Rq, skewness= Rsk, kurtoise- Rku
disp('-----RMS, Variance, Skewness and Kurtoise-----')
STD_GQ = sqrt(sum(GQdataMinimumLine.^2)/LengthGQ); % standard deviation to mean line
STD_BQ = sqrt(sum(BQdataMinimumLine.^2)/LengthBQ); % standard deviation to mean line
Rq_GQ = sqrt(sum((GoodQualityRawData-GoodQualityRawData(1)).^2)/LengthGQ); % RMS value : deviation to reference line
Rq_BQ = sqrt(sum((BadQualityRawData-BadQualityRawData(1)).^2)/LengthBQ); % RMS value: deviation to reference line
for index = 1:LengthGQ
Rsk_GQ(index) = sum(abs(GQdataMinimumLine(1:index)).^3)/(index*STD_GQ^3);
Rku_GQ(index) = sum(abs(GQdataMinimumLine(1:index)).^4)/(index*STD_GQ^4);
end
% amplitude density function
%ADF_GQ = sqrt(2*pi*Rq_GQ^2)*exp(-GQdataMinimumLine.^2/(2*Rq_GQ^2));
for index = 1:LengthBQ
Rsk_BQ(index) = sum(abs(BQdataMinimumLine(1:index)).^3)/(index*STD_BQ^3);
Rku_BQ(index) = sum(abs(BQdataMinimumLine(1:index)).^4)/(index*STD_BQ^4);
end
% amplitude density function
disp('-----GQ & BQ ADF (amplitude density function)-----')
NumberOfBinADF_GQ = 40;
NumberOfBinADF_BQ = 80;
ADF_GQ = MathPDF(NumberOfBinADF_GQ,GQdataMinimumLine);
ADF_BQ = MathPDF(NumberOfBinADF_BQ,BQdataMinimumLine);
% ADF-but try gaussian/normal probability density function
GaussianADF_GQ = exp(-(GQdataMinimumLine).^2/(2*STD_GQ^2))./(STD_GQ*(2*pi)^0.5);
GaussianADF_BQ = exp(-(BQdataMinimumLine).^2/(2*STD_BQ^2))./(STD_BQ*(2*pi)^0.5);
%% try a acf function by myself (ACF or ACVF of a random function)
ACF_GQ = TingACF(GQdataMinimumLine,LengthGQ-1); % vector, lags
ACF_BQ = TingACF(BQdataMinimumLine,LengthBQ-1); % vector, lags
disp('-----MeanSlope and RMS-slope and Average wavelength-----')
Step = 0.125; % mm
diffACF_GQ = diff(ACF_GQ);
diffACF_BQ = diff(ACF_BQ);
Slope_GQ = abs(diffACF_GQ)/Step;
Slope_BQ = abs(diffACF_BQ)/Step;
MeanSlopeGQ = sum(Slope_GQ)/(LengthGQ - 1);
MeanSlopeBQ = sum(Slope_BQ)/(LengthBQ - 1);
MeanWavelength_GQ = (sum(abs(GQdataMinimumLine))/LengthGQ)*2*pi/MeanSlopeGQ; % mm
MeanWavelength_BQ = (sum(abs(BQdataMinimumLine))/LengthBQ)*2*pi/MeanSlopeBQ; % mm
SF_GQ = 2*STD_GQ^2*(1-ACF_GQ);
SF_BQ = 2*STD_BQ^2*(1-ACF_BQ);
disp('-----using ACF to confirm each correlation length (Global)-----')
%ACF fitting
ACFcoefficients_GQ = polyfit(DistanceIndexGQ,ACF_GQ,2);
ACFfitCurve_GQ = polyval(ACFcoefficients_GQ,DistanceIndexGQ);
ACFcoefficients_BQ = polyfit(DistanceIndexBQ,ACF_BQ,2);
ACFfitCurve_BQ = polyval(ACFcoefficients_BQ,DistanceIndexBQ);
% to compare ACFfitCurve_GQ ACFfitCurve_BQ with original-ACF-curves
[~,Cols_GQ] = find(abs(ACF_GQ -ACFfitCurve_GQ)<0.001);
[~,Cols_BQ] = find(abs(ACF_BQ -ACFfitCurve_BQ)<0.001);
CorrLength_GQ = ACFpointSearch(ACF_GQ(1:Cols_GQ(1)),LaserStep); % mm
CorrLength_BQ = ACFpointSearch(ACF_BQ(1:Cols_BQ(1)),LaserStep); % mm
fprintf('CorrLength_GQ=%.3f (mm)\tCorrLength_BQ=%.3f (mm)\n',CorrLength_GQ,CorrLength_BQ)
clear Slope_GQ Slope_BQ diffACF_GQ diffACF_BQ

```

```

disp('-----plotting ADF based on filtfilt-----')
d1 = designfilt('lowpassfir','FilterOrder',12, ...
    'HalfPowerFrequency',0.15,'DesignMethod','butter');
%% Kolmogorov-Smirnov test (most practical method) and chi-square test and Z-test
% To determine if the distribution is indeed Gaussian (Smirnov,1948; Siegel, 1956; Massey, 1951)
disp('-----Kolmogorov-Smirnov Test to determine if it is indeed Gaussian Distribution (Global)-----')
testCDF_GQ = makedist('Normal','mu',mean(ADF_GQ.CurrentHeight),'sigma',std(ADF_GQ.CurrentHeight));
[hGQ,pGQ,ksstatGQ,cvGQ] = kstest(ADF_GQ.CurrentHeight,'CDF',testCDF_GQ);
testCDF_BQ = makedist('Normal','mu',mean(ADF_BQ.CurrentHeight),'sigma',std(ADF_BQ.CurrentHeight));
[hBQ,pBQ,ksstatBQ,cvBQ] = kstest(ADF_BQ.CurrentHeight,'CDF',testCDF_BQ);
if (hGQ == 0)
    disp('kstest REJECT the null hypothesis at the default 55 significance level (accepted)');
    fprintf('test result: h=%d\n',hGQ);
    disp('GQ-profile has INDEED-Gaussian-Distribution');
end
if (hBQ ==0)
    fprintf('test result: h=%d\n',hGQ);
    disp('BQ-profile has INDEED-Gaussian-Distribution');
end
[hGQ,pvalueGQ,ciGQ,zvalGQ] = ztest(GQdataMinumMline,mean(GQdataMinumMline),std(GQdataMinumMline));
[hBQ,pvalueBQ,ciBQ,zvalBQ] = ztest(BQdataMinumMline,mean(BQdataMinumMline),std(BQdataMinumMline));
%% selection data based on the sensor-width
SensorLength = 145; % mm
Gap1 = 25; % mm
Gap2 = 10; % mm
FourSensorLength = SensorLength*4+Gap1*2+Gap2; % mm
FourSensorPoints = FourSensorLength/LaserStep;
MovingStep = 10/LaserStep; % mm
NumOfBin = 20;
NyquistNumber = 100;
% for GOOD QUALITY
index = 0;
indexMax = ceil((DistanceIndexGQ(end) - FourSensorLength)/(MovingStep*LaserStep));
SelectionVectorInitialGQ = [ones(FourSensorPoints,1);zeros(LengthGQ-FourSensorPoints,1)];
*****
GQ_AverageC1PlateHeight = zeros(indexMax,1);
GQ_AverageP1PlateHeight = zeros(indexMax,1);
GQ_AverageP2PlateHeight = zeros(indexMax,1);
GQ_AverageC2PlateHeight = zeros(indexMax,1);
GQ_rmsC1PlateHeight = zeros(indexMax,1);
GQ_rmsP1PlateHeight = zeros(indexMax,1);
GQ_rmsP2PlateHeight = zeros(indexMax,1);
GQ_rmsC2PlateHeight = zeros(indexMax,1);
*****
PSD_GQ_C1_MainFun = zeros(NyquistNumber,indexMax);
PSD_GQ_P1_MainFun = zeros(NyquistNumber,indexMax);
PSD_GQ_P2_MainFun = zeros(NyquistNumber,indexMax);
PSD_GQ_C2_MainFun = zeros(NyquistNumber,indexMax);
GQ_Selection_K_C1 = zeros(indexMax,1);
GQ_ACFcorrLengthC1 = zeros(indexMax,1);
GQ_ACFcorrLengthP1 = zeros(indexMax,1);
GQ_ACFcorrLengthP2 = zeros(indexMax,1);
GQ_ACFcorrLengthC2 = zeros(indexMax,1);
*****
while index <= indexMax
    SumMovingGQ = index*MovingStep;
    GQSensorPlateSelectionMax = FieldGQSensorSetting(SumMovingGQ,FourSensorLength,GQdataMinumMline,DistanceIndexGQ,SelectionVectorInitialGQ,NumOfBin);
    index = index + 1;
    GQ_AverageC1PlateHeight(index) = GQSensorPlateSelectionMax.AverageC1PlateHeight;
    GQ_AverageP1PlateHeight(index) = GQSensorPlateSelectionMax.AverageP1PlateHeight;
    GQ_AverageP2PlateHeight(index) = GQSensorPlateSelectionMax.AverageP2PlateHeight;
    GQ_AverageC2PlateHeight(index) = GQSensorPlateSelectionMax.AverageC2PlateHeight;
    GQ_rmsC1PlateHeight(index) = GQSensorPlateSelectionMax.rmsC1PlateHeight;
    GQ_rmsP1PlateHeight(index) = GQSensorPlateSelectionMax.rmsP1PlateHeight;
    GQ_rmsP2PlateHeight(index) = GQSensorPlateSelectionMax.rmsP2PlateHeight;
    GQ_rmsC2PlateHeight(index) = GQSensorPlateSelectionMax.rmsC2PlateHeight;
    GQ_SensorPlateSelectionPSD = GQselectionPSD(NyquistNumber,SumMovingGQ,FourSensorLength,GQdataMinumMline,DistanceIndexGQ,SelectionVectorInitialGQ);
    PSD_GQ_C1_MainFun(:,index) = GQ_SensorPlateSelectionPSD.PSD_GQ_C1;
    PSD_GQ_P1_MainFun(:,index) = GQ_SensorPlateSelectionPSD.PSD_GQ_P1;
    PSD_GQ_P2_MainFun(:,index) = GQ_SensorPlateSelectionPSD.PSD_GQ_P2;
    PSD_GQ_C2_MainFun(:,index) = GQ_SensorPlateSelectionPSD.PSD_GQ_C2;
    GQ_Selection_K_C1(index) = GQ_SensorPlateSelectionPSD.GQ_K_C1; % the start spatial freq
    GQ_ACFcorrLengthC1(index) = GQ_SensorPlateSelectionPSD.GQ_ACFcorrLengthC1;
    GQ_ACFcorrLengthP1(index) = GQ_SensorPlateSelectionPSD.GQ_ACFcorrLengthP1;
    GQ_ACFcorrLengthP2(index) = GQ_SensorPlateSelectionPSD.GQ_ACFcorrLengthP2;
    GQ_ACFcorrLengthC2(index) = GQ_SensorPlateSelectionPSD.GQ_ACFcorrLengthC2;
end
% for bad quality
index = 0;
indexMax = ceil((DistanceIndexBQ(end) - FourSensorLength)/(MovingStep*LaserStep));
SelectionVectorInitialBQ = [ones(FourSensorPoints,1);zeros(LengthBQ-FourSensorPoints,1)];
*****
BQ_AverageC1PlateHeight = zeros(indexMax,1);
BQ_AverageP1PlateHeight = zeros(indexMax,1);
BQ_AverageP2PlateHeight = zeros(indexMax,1);
BQ_AverageC2PlateHeight = zeros(indexMax,1);
BQ_rmsC1PlateHeight = zeros(indexMax,1);
BQ_rmsP1PlateHeight = zeros(indexMax,1);
BQ_rmsP2PlateHeight = zeros(indexMax,1);
BQ_rmsC2PlateHeight = zeros(indexMax,1);
*****
PSD_BQ_C1_MainFun = zeros(NyquistNumber,indexMax);
PSD_BQ_P1_MainFun = zeros(NyquistNumber,indexMax);
PSD_BQ_P2_MainFun = zeros(NyquistNumber,indexMax);
PSD_BQ_C2_MainFun = zeros(NyquistNumber,indexMax);
BQ_Selection_K_C1 = zeros(indexMax,1);
BQ_ACFcorrLengthC1 = zeros(indexMax,1);
BQ_ACFcorrLengthP1 = zeros(indexMax,1);
BQ_ACFcorrLengthP2 = zeros(indexMax,1);
BQ_ACFcorrLengthC2 = zeros(indexMax,1);
while index <= indexMax
    SumMovingBQ = index*MovingStep;
    BQSensorPlateSelectionMax = FieldBQSensorSetting(SumMovingBQ,FourSensorLength,BQdataMinumMline,DistanceIndexBQ,SelectionVectorInitialBQ,NumOfBin);
    index = index + 1;
    BQ_AverageC1PlateHeight(index) = BQSensorPlateSelectionMax.AverageC1PlateHeight;
    BQ_AverageP1PlateHeight(index) = BQSensorPlateSelectionMax.AverageP1PlateHeight;
    BQ_AverageP2PlateHeight(index) = BQSensorPlateSelectionMax.AverageP2PlateHeight;
    BQ_AverageC2PlateHeight(index) = BQSensorPlateSelectionMax.AverageC2PlateHeight;
    BQ_rmsC1PlateHeight(index) = BQSensorPlateSelectionMax.rmsC1PlateHeight;
    BQ_rmsP1PlateHeight(index) = BQSensorPlateSelectionMax.rmsP1PlateHeight;
    BQ_rmsP2PlateHeight(index) = BQSensorPlateSelectionMax.rmsP2PlateHeight;
    BQ_rmsC2PlateHeight(index) = BQSensorPlateSelectionMax.rmsC2PlateHeight;
    *****
    BQ_SensorPlateSelectionPSD = BQselectionPSD(NyquistNumber,SumMovingBQ,FourSensorLength,BQdataMinumMline,DistanceIndexBQ,SelectionVectorInitialBQ);
    PSD_BQ_C1_MainFun(:,index) = BQ_SensorPlateSelectionPSD.PSD_BQ_C1;
    PSD_BQ_P1_MainFun(:,index) = BQ_SensorPlateSelectionPSD.PSD_BQ_P1;
    PSD_BQ_P2_MainFun(:,index) = BQ_SensorPlateSelectionPSD.PSD_BQ_P2;
    PSD_BQ_C2_MainFun(:,index) = BQ_SensorPlateSelectionPSD.PSD_BQ_C2;
    BQ_Selection_K_C1(index) = BQ_SensorPlateSelectionPSD.BQ_K_C1; % the start spatial freq
    BQ_ACFcorrLengthC1(index) = BQ_SensorPlateSelectionPSD.BQ_ACFcorrLengthC1;
    BQ_ACFcorrLengthP1(index) = BQ_SensorPlateSelectionPSD.BQ_ACFcorrLengthP1;

```

```

BQ_ACFcorrLengthP2(index) = BQ_SensorPlateSelectionPSD.BQ_ACFcorrLengthP2;
BQ_ACFcorrLengthC2(index) = BQ_SensorPlateSelectionPSD.BQ_ACFcorrLengthC2;
end
%%%%%%%%%%%%%%%%%%%%%%%%%%%%%%%%%%%%%%%%%%%%%%%%%%%%%%%%%%%%%%%%%%%%%%%%%% mean(CorrLength)
disp('GQ-Mean CorrLength from C1 P1 P2 C2: (mm)');
fprintf('%f\t%f\t%f\t%f\n',mean(GQ_ACFcorrLengthC1),mean(GQ_ACFcorrLengthP1),mean(GQ_ACFcorrLengthP2),mean(GQ_ACFcorrLengthC2));
disp('BQ-Mean CorrLength from C1 P1 P2 C2: (mm)');
fprintf('%f\t%f\t%f\t%f\n',mean(BQ_ACFcorrLengthC1),mean(BQ_ACFcorrLengthP1),mean(BQ_ACFcorrLengthP2),mean(BQ_ACFcorrLengthC2));
NyquistNumberWhole = 600;
DistanceStep = 0.125; % mm
GQ_K = 1/(DistanceIndexGQ(end)-DistanceIndexGQ(1)); % GQ_K : spatial frequency
GQ_K_Nyquist = NyquistNumberWhole*GQ_K;
BQ_K = 1/(DistanceIndexBQ(end)-DistanceIndexBQ(1)); % BQ_K : spatial frequency
BQ_K_Nyquist = NyquistNumberWhole*BQ_K;
LengthGQ = length(DistanceIndexGQ);
LengthBQ = length(DistanceIndexBQ);
PSD_GQ = zeros(NyquistNumberWhole,1);
PSD_BQ = zeros(NyquistNumberWhole,1);
PSDindex = 1;
for K=(GQ_K:GQ_K:GQ_K_Nyquist)
PSD_GQ(PSDindex) = 1/DistanceIndexGQ(end).*abs(sum(GQdataMinimumLine'.*...
exp(-1i*2*pi*K*(1:LengthGQ)))).^2;
PSDindex = PSDindex+1;
end
PSDindex = 1;
for K=(BQ_K:BQ_K:BQ_K_Nyquist)
PSD_BQ(PSDindex) = 1/DistanceIndexBQ(end).*abs(sum(BQdataMinimumLine'.*...
exp(-1i*2*pi*K*(1:LengthBQ)))).^2;
PSDindex = PSDindex+1;
end

disp('self-affine power law decay PSD k0*f^(-alpha)');
SelfAffineAnalyticalPSD = 1e-5*(10^GQ_K:GQ_K:GQ_K_Nyquist).^(-3.5);
SelfAffineAnalyticalPSD_BQ = 1e-5*(10^BQ_K:BQ_K:BQ_K_Nyquist).^(-4);
%% roughness capacitance calculation
disp('-----roughness capacitance calculation -----')
GQ_C1_RoughCratio = zeros(length(GQ_AverageC1PlateHeight),1);
GQ_P1_RoughCratio = zeros(length(GQ_AverageC1PlateHeight),1);
GQ_P2_RoughCratio = zeros(length(GQ_AverageC1PlateHeight),1);
GQ_C2_RoughCratio = zeros(length(GQ_AverageC1PlateHeight),1);
BQ_C1_RoughCratio = zeros(length(BQ_AverageC1PlateHeight),1);
BQ_P1_RoughCratio = zeros(length(BQ_AverageC1PlateHeight),1);
BQ_P2_RoughCratio = zeros(length(BQ_AverageC1PlateHeight),1);
BQ_C2_RoughCratio = zeros(length(BQ_AverageC1PlateHeight),1);
for index = 1:length(GQ_AverageC1PlateHeight)
h0_C1 = abs(GQ_AverageC1PlateHeight(index))*0.001; %m
W_C1 = GQ_rmsC1PlateHeight(index)*0.001;
LateralCorrelateLength_C1 = GQ_ACFcorrLengthC1(index)*0.001;
h0_P1 = abs(GQ_AverageP1PlateHeight(index))*0.001; %m
W_P1 = GQ_rmsP1PlateHeight(index)*0.001;
LateralCorrelateLength_P1 = GQ_ACFcorrLengthP1(index)*0.001;
h0_P2 = abs(GQ_AverageP2PlateHeight(index))*0.001; %m
W_P2 = GQ_rmsP2PlateHeight(index)*0.001;
LateralCorrelateLength_P2 = GQ_ACFcorrLengthP2(index)*0.001;
h0_C2 = abs(GQ_AverageC2PlateHeight(index))*0.001; %m
W_C2 = GQ_rmsC2PlateHeight(index)*0.001;
LateralCorrelateLength_C2 = GQ_ACFcorrLengthC2(index)*0.001;
GQ_C1_RoughCratio(index) = RoughEffectOnCapacitance(h0_C1,W_C1,LateralCorrelateLength_C1);
GQ_P1_RoughCratio(index) = RoughEffectOnCapacitance(h0_P1,W_P1,LateralCorrelateLength_P1);
GQ_P2_RoughCratio(index) = RoughEffectOnCapacitance(h0_P2,W_P2,LateralCorrelateLength_P2);
GQ_C2_RoughCratio(index) = RoughEffectOnCapacitance(h0_C2,W_C2,LateralCorrelateLength_C2);
end

for index = 1:length(BQ_AverageC1PlateHeight)
h0_C1_BQ = abs(BQ_AverageC1PlateHeight(index))*0.001; %m
W_C1_BQ = BQ_rmsC1PlateHeight(index)*0.001;
LateralCorrelateLength_C1_BQ = BQ_ACFcorrLengthC1(index)*0.001;

h0_P1_BQ = abs(BQ_AverageP1PlateHeight(index))*0.001; %m
W_P1_BQ = BQ_rmsP1PlateHeight(index)*0.001;
LateralCorrelateLength_P1_BQ = BQ_ACFcorrLengthP1(index)*0.001;
h0_P2_BQ = abs(BQ_AverageP2PlateHeight(index))*0.001; %m
W_P2_BQ = BQ_rmsP2PlateHeight(index)*0.001;
LateralCorrelateLength_P2_BQ = BQ_ACFcorrLengthP2(index)*0.001;
h0_C2_BQ = abs(BQ_AverageC2PlateHeight(index))*0.001; %m
W_C2_BQ = BQ_rmsC2PlateHeight(index)*0.001;
LateralCorrelateLength_C2_BQ = BQ_ACFcorrLengthC2(index)*0.001;
% THESE results are come from Alpha = 0.3;
BQ_C1_RoughCratio(index) = RoughEffectOnCapacitance(h0_C1_BQ,W_C1_BQ,LateralCorrelateLength_C1_BQ);
BQ_P1_RoughCratio(index) = RoughEffectOnCapacitance(h0_P1_BQ,W_P1_BQ,LateralCorrelateLength_P1_BQ);
BQ_P2_RoughCratio(index) = RoughEffectOnCapacitance(h0_P2_BQ,W_P2_BQ,LateralCorrelateLength_P2_BQ);
BQ_C2_RoughCratio(index) = RoughEffectOnCapacitance(h0_C2_BQ,W_C2_BQ,LateralCorrelateLength_C2_BQ);
end
%% call function: AllanVarianceEstimator.m to see correlation distance
% using collected sample data
IntervalNum_GQ_C1 = mean(GQ_ACFcorrLengthC1)/DistanceStep;
IntervalNum_GQ_P1 = mean(GQ_ACFcorrLengthP1)/DistanceStep;
IntervalNum_GQ_P2 = mean(GQ_ACFcorrLengthP2)/DistanceStep;
IntervalNum_GQ_C2 = mean(GQ_ACFcorrLengthC2)/DistanceStep;
IntervalNum_BQ_C1 = mean(BQ_ACFcorrLengthC1)/DistanceStep;
IntervalNum_BQ_P1 = mean(BQ_ACFcorrLengthP1)/DistanceStep;
IntervalNum_BQ_P2 = mean(BQ_ACFcorrLengthP2)/DistanceStep;
IntervalNum_BQ_C2 = mean(BQ_ACFcorrLengthC2)/DistanceStep;
AllanVarianceEstimator(GQdataMinimumLine(1:1000));
[AllanVarianceOutput_BQ,IntervalNumberBQ] = AllanVarianceEstimator(BQdataMinimumLine(1:1000));
disp('GQ-Mean CorrLength from C1 P1 P2 C2: (mm)');
fprintf('%f\t%f\t%f\t%f\n',mean(GQ_ACFcorrLengthC1),mean(GQ_ACFcorrLengthP1),mean(GQ_ACFcorrLengthP2),mean(GQ_ACFcorrLengthC2));
disp('BQ-Mean CorrLength from C1 P1 P2 C2: (mm)');
fprintf('%f\t%f\t%f\t%f\n',mean(BQ_ACFcorrLengthC1),mean(BQ_ACFcorrLengthP1),mean(BQ_ACFcorrLengthP2),mean(BQ_ACFcorrLengthC2));
rmpath RoughnessProfileData scripts

% Allan Variance: describes frequency stability in (clocks, oscillators and amplifiers)
% it is intended to estimate stability due to noise processes instead of
MaxIntervalNum = 800;
i = 1;
for IntervalNumber = 1:2:MaxIntervalNum
Index = 0;
MaxIndex = floor((length(dataMinimumLine)-1)/IntervalNumber)+1;
while Index <= MaxIndex-4
Cluster1Mean = mean(dataMinimumLine(Index*IntervalNumber+1:(Index+1)*IntervalNumber+1));
Cluster2Mean = mean(dataMinimumLine((Index+1)*IntervalNumber+1:(Index+2)*IntervalNumber+1));
Cluster3Mean = mean(dataMinimumLine((Index+2)*IntervalNumber+1:(Index+3)*IntervalNumber+1));
FreqDeviationC1(Index+1) = (Cluster3Mean-2*Cluster2Mean + Cluster1Mean).^2/IntervalNumber^2;
Index = Index + 1;
end
AllanVarianceOutput(i) = 0.5*mean(FreqDeviationC1);
IntervalNo(i) = IntervalNumber;
i = i + 1;

%% mathe equation of PDF
InitialHeight = max(dataMinimumLine);
PeakPeakAmplitude = max(dataMinimumLine) - min(dataMinimumLine);

```

```

BinHeightStep = PeakPeakAmplitude/NumOfBin;
NumOfCurrentHeight = zeros(1,NumOfBin);
CurrentHeight = zeros(1,NumOfBin);
index = 1;
while index <= NumOfBin
    LowerInitialHeight = InitialHeight - BinHeightStep;
    UpperInitialHeight = InitialHeight;
    [Row,Col] = find((dataMinimumMline<=UpperInitialHeight) & (dataMinimumMline > LowerInitialHeight));
    if (isempty(Row) || isempty(Col))
        NumOfCurrentHeight(index) = 0;
    else
        NumOfCurrentHeight(index) = length(Row);
    end
    InitialHeight = LowerInitialHeight;
    CurrentHeight(index) = InitialHeight;
    index = index +1;
end
CurrentHeightProbability = NumOfCurrentHeight/sum(NumOfCurrentHeight);
APD = 0;
for index = 1:length(CurrentHeightProbability)
    APD = APD + CurrentHeightProbability(index);
    AmpProbability(index) = APD;
end
PDF.CurrentHeightProbability = sort(AmpProbability,'descend');
PDF.AmpDensityProbability = CurrentHeightProbability/BinHeightStep; %
PDF.CurrentHeight = CurrentHeight;
PDF.NumOfCurrentHeight = NumOfCurrentHeight;
PDF.SumNumHeight = sum(NumOfCurrentHeight);

```